THÈSE

En vue de l'obtention du

DOCTORAT DE L'UNIVERSITÉ DE TOULOUSE

Délivré par :

Institut National Polytechnique de Toulouse (INP Toulouse)

Discipline ou spécialité :

Science et Génie des Matériaux

Présentée et soutenue par :

M. DENI FERDIAN

le mardi 24 juin 2014

Titre :

EFFET DE LA VITESSE DE REFROIDISSEMENT SUR LA TAILLE DES GRAINS, LA MODIFICATION EUTECTIQUE ET LA PRECIPITATION D'INTERMETALLIQUES RICHES EN FER DANS DES ALLIAGES Al-Si HYPOEUTECTIQUES

Ecole doctorale :

Sciences de la Matière (SDM)

Unité de recherche :

Centre Interuniversitaire de Recherche et d'Ingénierie des Matériaux (C.I.R.I.M.A.T.)

Directeur(s) de Thèse :

M. JACQUES LACAZE

Rapporteurs :

M. ARNE K. DAHLE, JONKOPING UNIVERSITY

M. JULIUS C. SCHUSTER, WIEN UNIVERSITAT

Membre(s) du jury :

M. LORENTZ RATKE, GERMAN AEROSPACE CENTER KOLN, Président

M. BAMBANG SUHARNO, UNIVERSITE D'INDONESIE, Membre

M. FREDERIC MONPIOU, CEMES TOULOUSE, Membre

M. JACQUES LACAZE, INP TOULOUSE, Membre

Mme ANA I FERNANDEZ-CALVO, AZTERLAN DURANGO, Membre

Acknowledgement

This work in performed within the Mécanique, Microstructure, Oxydation et Corrosion (MEMO) of Centre Interuniversitaire de Recherche et d'Ingénierie des Matériaux (CIRIMAT) under the framework of European Space Agency - MICAST IV project, contract No. 4200014347. Financial support from Directorate General of Higher Education - Ministry of Education, Republic of Indonesia, beam time from ESRF and material support from AZTERLAN are highly acknowledged.

First, I would like to express my gratitude to my mentor, Dr. Jacques Lacaze for all the knowledge, guidance, kindness and his patience during this last three years. Not to mention, the big gamble to accept me as a student under his supervision. I also would like to thanks to his family and especially his wife, Mireille, for the lovely conservation over lunches or dinners at their house.

I would like to thank the members of the jury, Prof Lorentz Ratke, as the chairman of jury; Prof. Julius Clemens Schuster and Prof. Arne Dahle as rapporteur for reading through and reviewing my dissertation. Moreover, I also would like to send my gratitude to other members of the jury; Dr. Frédéric Mompiou, Dr. Ana Fernàndez-Calvo and Prof. Bambang Suharno.

I would like to express my appreciation to Prof. Luc Salvo for his help on in-situ X-ray tomography at ESRF. Not to forget, the fruitful discussions over the beta phase growth and interpretation of tomography data. Dr. Christophe Tenailleau and Benjamin Duployer for their help in post-mortem analysis. I also would like to thank Yannick Thebault for EDS and SEM, Claudie Josse, Patrick Nguyen and Nathalie Gey for EBSD, Phillipe de Parseval for EPMA, Nicolas Ratel-Raymond for μXRD, Alexandre Freulon and Ronan Mainguy for metallography preparations and other small things that I asked in the lab for my samples preparations. I also would like to send my gratitude to everyone in AZTERLAN and MICAST team for their material supports.

Dr. Koenraad and Roxana, thank you for the pleasant talks and our small group discussions in solidification. To all CIRIMAT-MEMO team, lecturers, researchers, administration and doctoral students, whom I cannot thank enough for all the helps, friendship and accepting me as a family in the lab.

Last but not least, to my parents, parents in-law, and my wife for their extent supports and encouragements

Table of Content

1. D. Ferdian, B. Suharno, B. Duployer, C. Tenailleau, L. Salvo, J. Lacaze, Differential thermal analysis assessment of beta phase precipitation in Al-6.5Si-1Fe Alloy, Transactions of the Indian Institute of Metals, Volume 65, Issue 6, December 2012, pp 821-825.
2. D. Ferdian, J. Lacaze, I. Lizarralde, A. Niklas, A.I. Fernández-Calvo, Study of the effect of cooling rate on eutectic modification in A356 aluminium alloys, Material Science Forum, Vol. 765- Light Metals Technology 2013, pp. 130-134
3. D. Ferdian, J. Lacaze, Evaluation of (Al)-Si Eutectic Reference Temperature of A3XX alloys, Material Science Forum, Vol. 790-791 (2014) - Solidification and Gravity VI, pp. 367 - 372
4. J. Lacaze, D. Ferdian, I. Lizarralde, A. Niklas, S. Eguskiza, A.I. Fernández-Calvo, Improved grain size prediction in aluminium-silicon alloys by thermal analysis, 71st World Foundry Congress, 19-21 May 2014, Bilbao – Spain.

1. Introduction

1. Foreword

Aluminum is one of the common elements in the earth crust, even though it is in the oxide form and requires further separation process which was developed back in 19th century. Aluminum alloys are widely used today in applications ranging from airplanes, architecture façades to automotive parts. In most of the automotive components, manufacturing by casting method is mainly due to their ability to be formed with different sizes, geometries, and capability for mass production. Aluminum-silicon alloys are the most common aluminum casting alloys produced due to their fluidity characteristic and mechanical and light weight properties.

Due to their high strength and low density characteristics, the consumption of aluminum has increased in automotive industries. By reducing the vehicle weight, a better fuel consumption is achieved and this also reduces the CO_2 emission to the atmosphere. Data have shown an increase of Al content in the automotive part from 50 Kg in 1990 to 140 Kg in 2012 [1]. However, the energy consumption for Al production is one of the highest among others mineral processing. The average of electrical consumption in smelter for Al production ranges from 13 to 16 KWh/kg [2]. Recycling process, only consumes 2.8 KWh, i.e. 18% of the total energy used in primary aluminum production [3]. This huge difference makes the processing of recycled aluminum a lucrative process.

Even though, Al alloys were known for the weight/strength ratio, improving their mechanical strength would allow overtaking the present limit for their application. By increasing the strength, we could reduce the total weight of the material for the same purpose. In general, the metallic material strength increases by decreasing the grain size of the alloy. For Al alloys, increasing the grain number is performed by adding a grain refiner such as titanium-boron. Additionally, the presence of silicon is also affecting the mechanical properties of the alloys. Silicon is known to play a role in casting fluidity, but the faceted morphology of silicon reduces the material ductility greatly. The modification of silicon by adding a modifier element such as strontium is one of the methods normally used in industry and is occasionally complemented with heat treatment to improve the strength. In real casting condition, cooling rate is one of the factors that is not easy to predict, which is related with the geometry of casting part or the casting process itself. Several researchers already studied the effect of cooling rate on the microstructure and mechanical properties of Al alloys. In this work, we try to revisit the cooling rate effect on the morphology changes of microstructure in Al-Si alloys.

Another issue related with recycling is the low quality material due to high level of impurity elements. Iron is known to form intermetallic phases within the Al alloys, especially in the Al-Si grades. Because of its low solid-state solubility, any iron remains in Al alloys form iron bearing phases during solidification. The iron content increases with successive recylings. The intermetallic phases in general have a detrimental effect on the tensile properties of the alloy, however the so-called beta phase is certainly the most detrimental one. Various methods to mitigate the beta phase effect have been developed, such as adding Mn as a so-called neutralizer element or physical methods such as filtering.

1.2. Objective

The primary goal of this study is to establish the relationship between the cooling rate and microstructure features in Al-Si alloys. Cooling rate is one of the parameters most commonly found in the literature and industrial reports. Finite cooling rate leads to solidification under a non-equilibrium conditions, and thus opens the possibility for different phase precipitation within the alloy. Because of that, the effect of cooling rate on the characteristic temperatures of cooling curve records and their relation to grain size and eutectic silicon modification is presented in this work.

Furthermore, the study also includes the effect of cooling rate on the morphology of beta phase. Research on the beta phase in ternary Al-Fe-Si alloys has been conducted by several authors; nevertheless there are some aspects still unknown. The effect of minor elements on the morphology change and the growth mechanism of the beta phase remains under study by many researchers. An attempt to characterize the growth of beta phase was performed through post-mortem and in-situ tomography. In addition, some variations on the solidification path have been observed which are also discussed.

1.3. Outline of the thesis

Chapter 2, Literature review, presents briefly background information regarding grain refinement and eutectic modification. In addition, present knowledge on the Al-Fe-Si ternary system is presented. Emphasis is also put on the beta phase, in particular the modification attempts to alter its shape with various methods. Chapter 3 gives a summary of the experimental procedures and the various techniques employed in the present study. Chapter 4 deals with the effect of cooling rate on the grain size and eutectic modification of a commercial alloy. In the appendix, a modified formula for evaluating the eutectic depression temperature is also proposed. Chapter 5 discusses the beta phase morphology in relation with

the cooling rate and further study by post mortem and in-situ tomography regarding its growth morphology. Chapter 6 shows an interesting finding regarding the appearance of script phase and rosettes.

Reference

1. European Aluminium Association, Aluminium in cars-unlocking the light-weighting potential, 2013, available in http://www.alueurope.eu/wp-content/uploads/2013/10/EAA-Aluminium-in-Cars-Unlocking-the-light-weighting-potential_September2013_03.pdf, accessed 30 June 2014.
2. Z. Luo, A. Soria, Prospective study of the world aluminium industry, European Commission-Joint Research Centre, Institute for Prospective Technological Studies, 2007.
3. J.A.S. Green, Aluminum recycling and processing for energy conservation and sustainability, ASM International, 2007.

2. Literature Review

2.1. Al-Si alloys

2.1.1 Al-Si alloys classification

In general, aluminum silicon alloys can be classified into three groups based on their silicon content which are hypoeutectic, eutectic and hypereutectic alloys as illustrated in Figure 2.1. The International Alloy Designation System (IADS) further classified aluminum alloys as wrought and cast aluminum alloys, where four digit indexes were used for the designation of the alloys [1]. Nevertheless, different methods of classification are still in use by different countries such as Japan with their own nomenclature such as AC4CH (JIS H5202) which is equivalent to A 356.2 alloys.

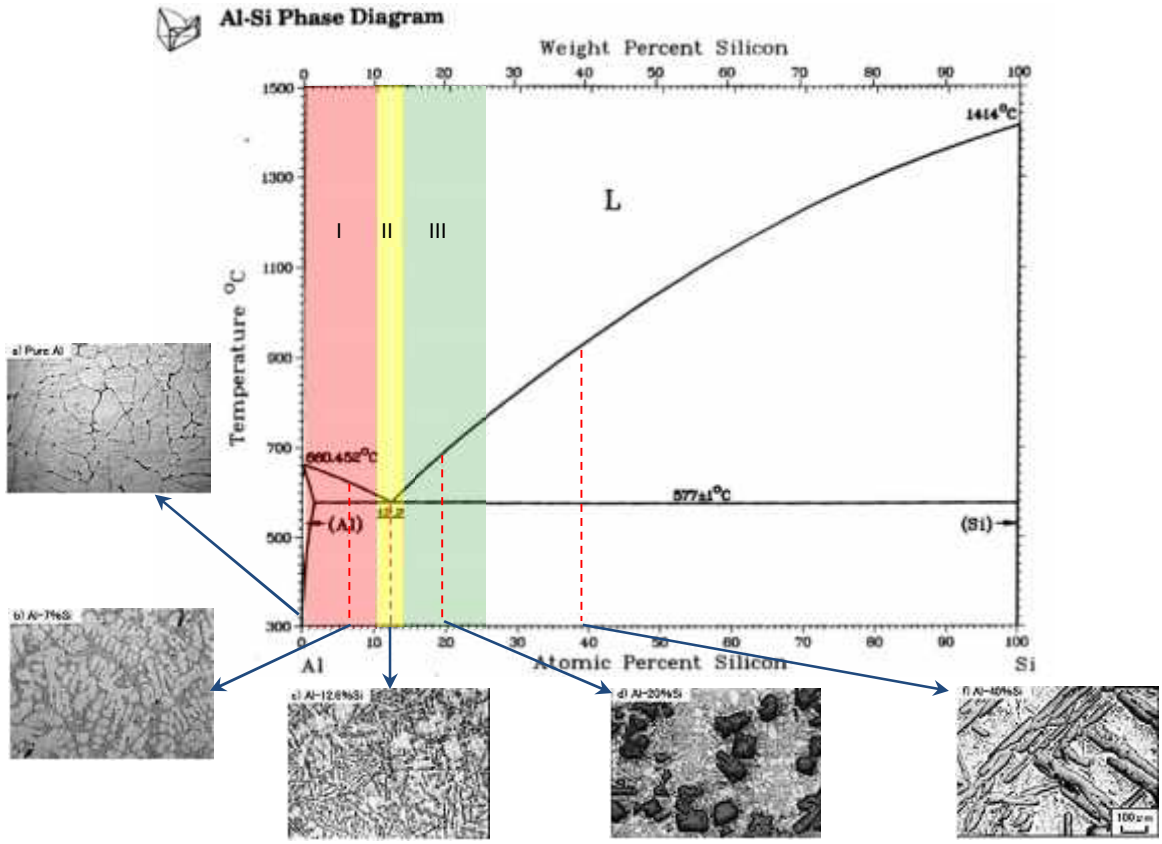

Figure 2.1. Al-Si phase diagram [1] and the silicon content effect to microstructure [2] with typical chemical composition range of (I) hypoeutectic, (II) eutectic, (III) hypereutectic alloys

2.1.2. Role of alloying element

Silicon as the main alloying element increases casting fluidity and reduces shrinkage of aluminium alloys. Other than silicon some elements are added to the alloys and some exist

as trace elements. Elements such as copper, magnesium, manganese are added to improve alloys mechanical properties. Copper could increase the strength through Guinier-Preston (GP) zone [3, 4] after supersaturated solid solution treatment and aging, as well as magnesium that increase the mechanical strength after heat treatment through the precipitate hardening [5]. Addition of minor elements such as strontium or sodium is well known to modify the eutectic silicon and therefore improve the ductility and mechanical strength. Nevertheless, some researchers indicated that the Sr addition also increases the level of porosity within the alloys [6]. Titanium and boron are primarily added for grain refining.

Furthermore, the increasing use of recycled alloys and low quality electrode in aluminum plant has increased the level of impurities in primary Al production. Traces of minor elements such as Ca, Cr, Co V and rare earths are known to have an effect on alloy's microstructure. This addition of trace elements leads to the formation of precipitates phases and modification eutectic silicon. Several researchers have shown the effect of rare earths for changing the eutectic silicon and the morphology of intermetallic phase [7-9].

2.2. Grain refinement

Grain refining is one of the strengthening mechanisms which yield higher mechanical properties of an alloy. The mechanism is hindering the dislocation movement, this is illustrated by Hall-Petch relation [10, 11]. Grain refinement would increase the number of grain and their boundaries therefore increase the yield strength of the material. Grain refinement of aluminum alloys has been used commercially since 1930 by incorporating titanium to the molten alloy [12]. Addition of grain refiner increases the number of nucleation sites, thus promoting equiaxed grain rather than columnar grain growth. Early studies on the grain refinement are shown in extensive work by Cibula [13] and Crosley and Mondolfo [14]. Numerous reviews on grain refinement mechanism can be found in the works by Backerud [15] (Figure 2.2), Mc. Cartney [16], Murty et al. [17], Quested and Greer [18], St John et al. [19, 20].

Several models have been proposed for the nucleation step in the grain refinement mechanism. Maxwell and Hellawell model [21] assumes the grain nucleate throughout the melt and nucleation stops as recalescence occurs or effective nucleants are already consumed. Greer et al. [22] proposed a free growth model taking into account the size distribution of refining particles as a factor for grain refinement. Grain refinement then results from a competition between nucleation and growth of the grains during solidification process.

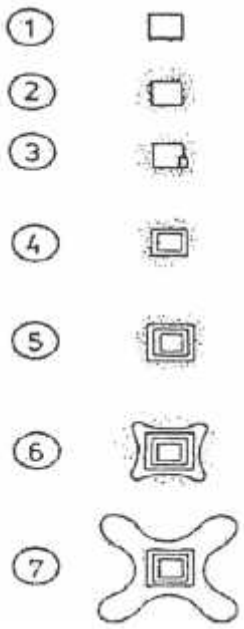

Figure 2.2. Nucleation of Al grain at the surface of $AlTi_3$ [15].

Marcantonio and Mondolfo [23] studied the ternary Al-Ti-B and found the grain refinement due to nucleation of Al by Al_3Ti crystal. Work by Schumacher et al. [24] and Fan [25] have showed the existence of a Al_3Ti layer over the surface of TiB_2 particles which nucleated the primary (Al) grain (Figure 2.3). Work by Iqbal et al. [26] using differential thermal analysis (DTA) and 3D-X-ray diffraction (3D-XRD) revealed the formation of Al_3Ti prior to solidification in the presence of solute Ti and TiB_2 particles. Zhang [27] also conclude the lattice matching of $AlTi_3$ with the primary (Al) which makes this phase a powerful catalyst for nucleation of (Al) grains.

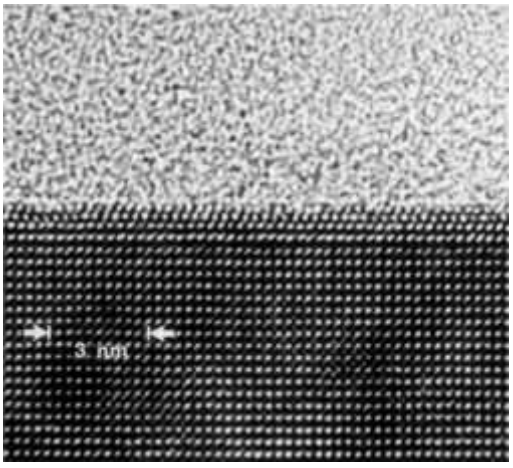

Figure 2.3. Cross section of HR-TEM of TiB_2 particle surface embedded in an Al based glassy matrix [24].

Another factor related to the grain size is growth restriction factor (GRF) [28]. The GRF is seen as the contribution of constitutional factor from all solute elements. Easton et al. [29, 30] suggested the constitutional supercooling associated to solute segregation is essential for effective grain refinement. During solidification, the solute elements play an important role in decreasing the growth of nucleated grain, which is also shown in the work by Fetzer and Kozlov [31]. As seen in A356 alloys, without the addition of Ti as grain refiner, the GRF value for typical A356 alloy approximately is 40, based on the curve by Backerud and Vainik [32] with the smallest obtained grain size is 750 μm. By addition of 0.1-0.2 %Ti, the GFR value is 70-85. In the presence of TiB_2 particle the grain size would have a smaller value due to the presence of nucleation site.

The cooling rates also have an impact to the grain refinement. Easton and StJohn [33] studied the effect of cooling rate to the grain size of Al alloys and correlate their observations with the increasing number of nuclei and restriction factor. Different levels of silicon content also have an effect to the effectiveness of grain refiner. Lee et al. [34] studied showed that the effectiveness grain refiner is better before the transition point (about 3% silicon content in unrefined alloy) and the grain size remain the same regardless the amount of refiner added to the alloy.

2.3. Eutectic modification mechanism

Al-Si eutectic is an irregular coupled eutectic with Si showing a faceted morphology. This faceted appearance has an impact of lowering the alloy mechanical strength. One of the methods to reduce this effect is by modifying the eutectic silicon from coarse flake into fibrous appearance. Modification of silicon can be achieved by adding a modifier element [35-38] or induced by rapid cooling or quench [39]. Further investigation by Lu and Hellawell [40] indicated that the Si modified by Sr or Na shows a high density of twins, while with quenching it is twin free and non-faceted. However, Shamsuzzoha and Hogan [41] suggested that the quench modified silicon eutectic has a higher twin density than the unmodified, and thus is different from strontium modified eutectic. They concluded the twins were created due to large undercooling.

Liu et al. [38] observed that the modification did not affect the thermodynamic parameter of eutectic silicon, hence the modification is believed as a kinetic related problem. Several other elements are known to modify silicon, such as sodium and antimony. Nogita et al. [42] suggested that rare earth has some effect to eutectic modification. Currently, the most commonly used element in industry is strontium due to its low toxicity and low fading.

Early work on the modification of eutectic silicon can be found in patent by Pacz back to early 1920's [43]. Several theories have been proposed to explain the mechanism of silicon modification, among them is twin plane re-entrance edge (TPRE) mechanism [44] and impurity induced twinning (IIT) [45] (Figure 2.4). The presence of modifier would suppress the TPRE growth mechanism of eutectic silicon, while according to IIT theory; impurities change the stacking sequence of silicon during plate growth. Reviews by Gruzleski [46], Makhlouf and Guthy [47], Hedge and Prabhu [48] provide a comprehensive evaluation and information on the aluminum-silicon reaction and its modification. Recent work by Timpel et al. [49] gives further understanding on the role of strontium on silicon modification mechanism through the use of atomic probe tomography and both mechanisms were observed. Nevertheless, the strontium role as a modifier element in eutectic modification is still studied.

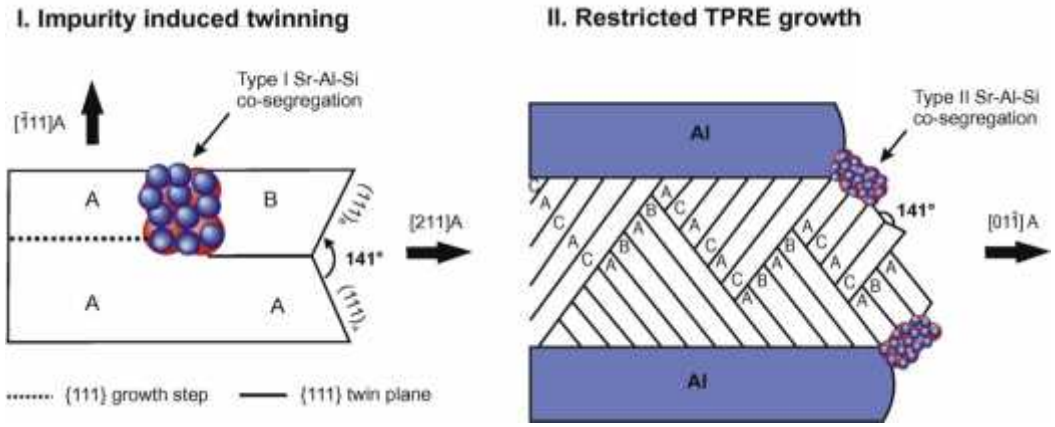

(a). (b).

Figure 2.4. Modification mechanism of eutectic silicon (a). IIT (b). TPRE [49]

In previous paragraph, the modification of silicon was seen as the effect of modifier element to the growth of silicon. Another approach to eutectic modification has been proposed by Yilmaz et al. [50] which elaborated that the modification of silicon is caused by the poisoning of the growth sites rather than by hindering nucleation, and in agreement with older work by Kobayashi and Hogan [51]. AlP is believed to be the nucleation site for eutectic silicon as studied by Ho and Cantor [52], Nogita et al. [53] and recent work by Ludwig et al. [54]. Deactivation of AlP could lead to the modification of eutectic silicon. The role of element such as sodium in neutralizing AlP has been proposed in the early work by Crosley and Mondolfo [55]. Other research also indicated that the strontium could poisoned the nucleation site for silicon (AlP) and in the same way as sodium. Work by Cho et al. [56] proposed that both eutectic silicon and β-$Al_9Fe_2Si_2$ are preferentially nucleated on AlP

particles. By adding Sr element, the formation of beta phase was suppressed by the present of intermetallic Al_2Si_2Sr which causing poisoning effect to AlP.

2.4. Iron in the Al-Si alloys: Al-Si-Fe ternary diagram

One of the minor elements commonly found in commercial Al alloy is iron, which forms iron rich intermetallic phases. The presence of such iron rich intermetallic phases reduces the mechanical properties of the Al Alloys. The high level of iron content mostly originates from the use of scrap in production process. These scraps are used in the foundry production line to cut down the production cost and increase the product competitiveness in the market. Eventually, iron is gradually accumulated for each recycling process performed [57]. Nevertheless, the presence of iron at certain amount is needed in die casting process to prevent the "die soldering phenomenon" of metal product to the metallic mould.

Iron has very small solubility in Al, with only 0.052% at 660°C solid Al phase [1]. Therefore, iron leads easily to the formation of intermetallic phases in interdendritic region. The liquidus projection of the Al-Fe-Si phase diagram is shown in Figure 2.5. The ternary Al-Fe-Si system shows 11 stable ternary compounds (labelled τ_1 to τ_{11}) while several metastable compounds have been reported [58, 59]. Detail information of the stable phases can be seen in Table 2.1.

Review of the Al-Fe-Si system can be tracked back to the work by Gwyer and Philips [60] and to the extensive work by Takeda and Mutuzaki [61]. Furthermore, Rivlin and Raynor [62] re-evaluated it on the basis of published literature to early 80's. While Belov et al. [63] extended the study of the iron effect to several systems of Al alloys. Thermodynamic approach can be seen in the work Du et al. [64] which reviewed the system and compared calculation to experimental data from various authors. Eleno et al. [65] also studied the system on the basis of COST 507 database [66]. Recent work by Marker et al. [67] added a new compound with composition $Al_{48}Fe_{36}Si_{16}$ and labelled as τ_{12}.

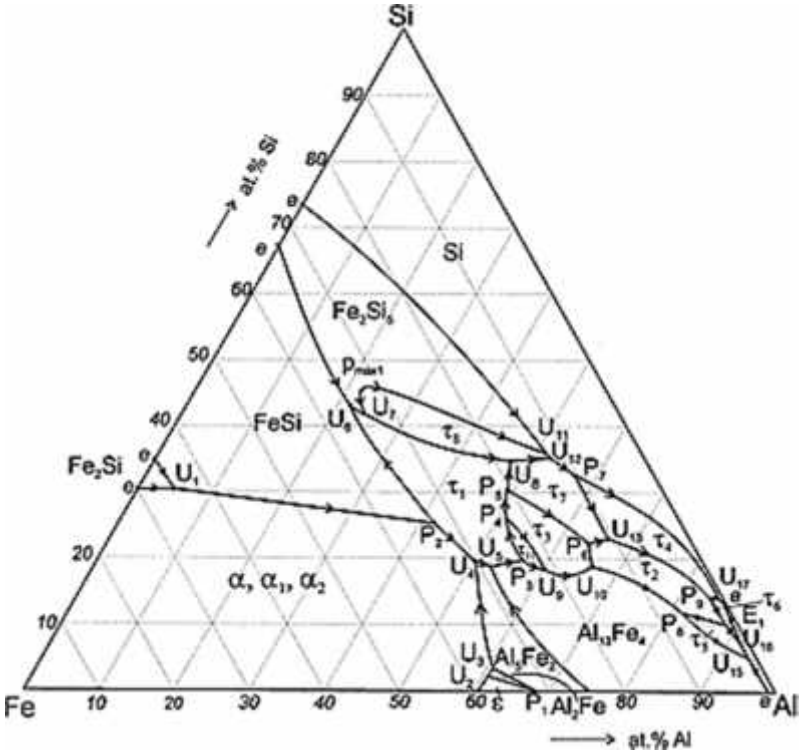

Figure 2.5. Phase Diagram Al-Fe-Si system, Liquidus projection [58].

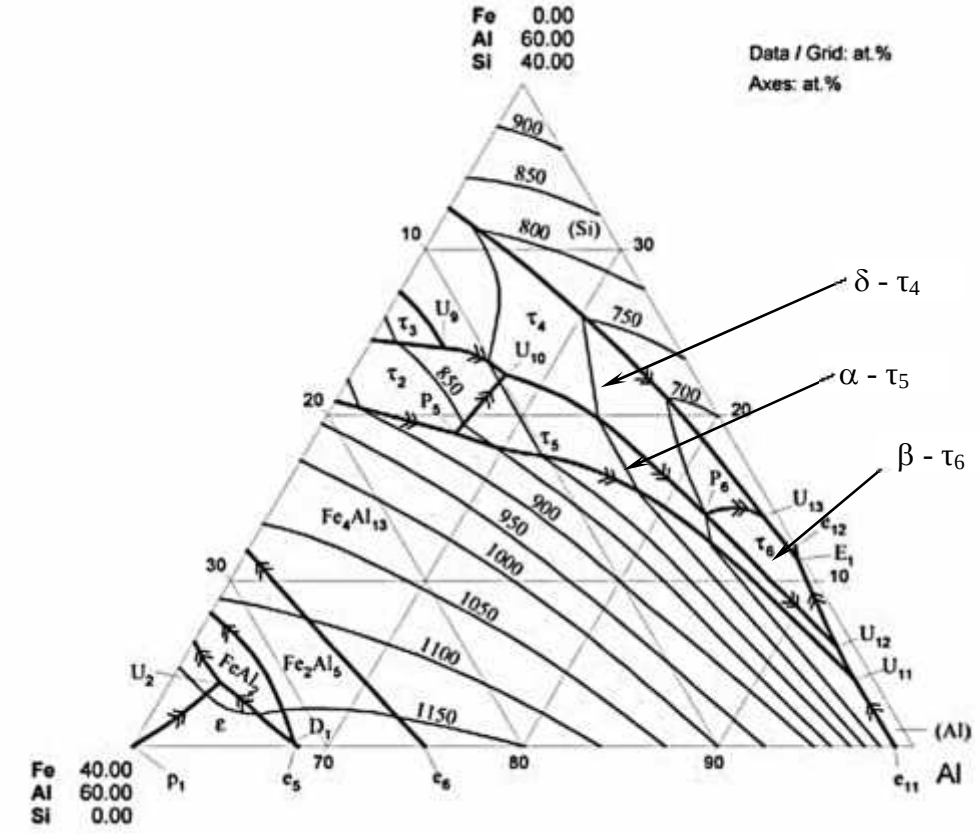

Figure 2.6. Liquidus projection of Al corner of Al-Fe-Si ternary phase diagram [58]

Table 2.1. Ternary Al-Fe-Si Phases: Compositions and Crystallographic data

Phase	Common Name	Chemical composition	Other chemical composition	Crystallography data		Ref
				Lattice parameter (nm)	Pearson symbol/ Space group	
τ_1/τ_9		$Fe_3Al_2Si_3$		a = 0.4623; b = 0.6374; c = 0.7599 α = 102.81°; β = 105.6°; γ = 100.85°	*aP*16 / *P*1	59
τ_2	γ- gamma	Al_3FeSi		a = 0.8893; b = 1.0188, c = 1.7669; β = 132.18°	*mC**	59
τ_3		Al_2FeSi		a = 0.7958; b = 1.5178; c = 1.5237	*oC*128 / *Cmma*	59
τ_4	δ- delta	Al_3FeSi_2		a = 0.6087; c = 0.9536	*tI*24 / *I*4/*mcm*	59
τ_5	α - alpha	Al_8Fe_2Si	α-Al_7Fe_2Si	a = 1.2404; c = 2.6234	*hP*245 / *P*6$_3$/*mmc*	68
τ_6	β - beta	$Al_9Fe_2Si_2$	β-Al_5FeSi, β-$Al_{4.5}FeSi$	a= 0.6161; b = 0.6175; c = 2.0813; β = 90.42°	*C*2/*c* / *m*C52	69
τ_7		$Al_3Fe_2Si_3$		a= 0.7189; b = 0.8317; c = 1.4542; β = 93.48°	*P*2$_1$/*c* / *mP*64	59
τ_8		$Al_2Fe_3Si_4$		a = 0.3669; b = 1.2385; c = 1.0147	oC36 / *Cmcm*	59
τ_{10}		$Al_{12}Fe_5Si_3$		a = 1.5518; c = 0.7297	*hP*28 / *P*6$_3$/*mmc*	59
τ_{11}		$Al_4Fe_{1.7}Si$		a = 0.7509; c = 0.7594	P6$_3$/*mmc*	59
τ_{12}		Al_3Fe_2Si		a= 1.0806	Fd 3m	67

Further investigation will focus on the Al corner of Al-Fe-Si ternary system which is represented in Figure 2.6, where the phases are here designated with their usual name in casting and solidification studies. Table 2.1 shows the correspondence between the names in Figure 2.5 and 2.6. According to the ternary diagram, in the equilibrium condition, one could expect the precipitation of intermetallic phase such as θ–$Al_{13}Fe_4$ (theta phase), α-Al_8Fe_2Si (alpha phase), β-$Al_9Fe_2Si_2$ (beta phase) depending on the alloy chemical composition. Nonetheless, due to the composition of commercial Al-Si alloys, the most commonly found intermetallic phase in Al-Si alloys are alpha phase and beta phases which are presented in more detail in the following section.

The system also shows metastable phases which are related to non-equilibrium solidification process or the presence of trace elements which alter the crystal structure and composition of the stable phases. As an example, several authors reported various metastable variant of the alpha phase: Westengen [70] identified tetragonal alpha phase (α_T), Liu et al. [71] observed an orthorhombic structure (q_1) and Dons [72] that reported a monoclinic alpha phase (α_V). However, further studies indicate that α_T variant of alpha phase is a modified cubic structure [73].

2.5. Iron-rich alpha and beta phases

2.5.1. Alpha phase

The alpha phase was discovered as early as 1919 [74]. Alpha phase is considered to have a hexagonal crystal structure in equilibrium condition [75, 76], and often recognized by its Chinese script morphology in Al-Si alloys. Corby and Black [76] could not differentiate Si and Al atom in the structure and it was assumed to be identical because of their close atomic number. The phase has a range of chemical composition of 30-36% Fe, 6-11% Si [77].

In earlier literature, the crystal structure of alpha phase was considered as a cubic by Phragmen [78] and Cooper [79]. However, investigation by Munson [80] showed that the effect of transition element such as Mn could transform the equilibrium hexagonal structure into $Al_{15}(Fe,Mn)_3Si_2$ cubic structure which is isomorph with the cubic Al_8Mn_2Si phase of the Al-Mn-Si system. Further work by Zheng et al. [81] and work by Kral [82] also showed that the alpha phase with manganese has a cubic crystal structure. Consequently, the hexagonal crystal structure is considered as the structure of alpha phase in high purity Al-Fe-Si ternary alloys. Note that the use of the same name for different phases is very unfortunate. This has led to error in the past and still leads to ambiguities in present literature. Whenever needed, the name of the phases should be complemented with the indication of its crystallographic structure.

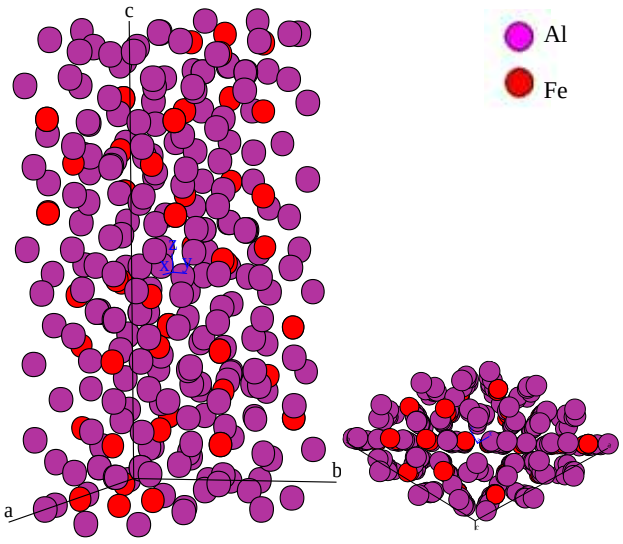

Figure. 2.7. Ball model showing Al and Fe atoms position in alpha phase according to Corby and Black [76]. Crystal structure was drawn in CaRIne crystallography 3.1 [83].

2.5.2. Beta phase

The beta phase is considered to have a monoclinic crystal structure (Figure 2.8), as reported by Rosenhain et al. [84] and showed in the studied by Phragmen [78], Romming et al. [69] and Hansen et al. [85]. However a conflicting result was obtained by Zheng [81] and Carpenter and Page [86] who indicated the beta phase as orthorhombic. Later work by Hwang et al. [87] argues against the hypothesis proposed by Zheng regarding the misperception of crystal structure of beta phase so, that the monoclinic structure will be accepted here. The same problem as in alpha phase, in the work by Romming et al. [69] the Si atom position in beta phase also could not be differentiate from the Al atom position and assumed it was statistically distributed among Al position. Beta phase has the range of chemical composition of 25-30% Fe, 12-15% Si [77].

Beta phase is known to have some detrimental effect compared to other iron-rich intermetallic phases. Studies by Gowri et al. [88] have showed that this intermetallic phase reduces melt fluidity without lowering surface tension. Work by Elsebaei et al. [89] revealed that the beta phase acts as crack initiation site and provide crack propagation path in impact test. Numerous researches also have showed that this harmful effect may be attributed to the beta phase morphology [90-93].

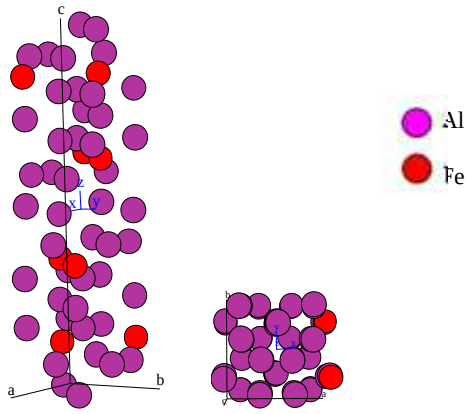

Figure. 2.8. Ball model showing Al and Fe atoms position in beta phase according to Romming et al. [69]. Crystal structure was drawn in CaRIne crystallography 3.1 [81].

Early researcher characterized the morphology of alpha phase as Chinese script and beta phase as needle-like appearance in 2D metallographic observation. However, further development by using deep etching technique and scanning electron microscopy analysis showed that the beta phase actually has a plate-like structure. Work by Dinnis et al. [94] which performing serial sectioning and reconstructing slice of 2D image from metallographic

examination into a 3D image showed this plate like beta phase morphology appeared interconnected, as illustrated in Figure 2.9.

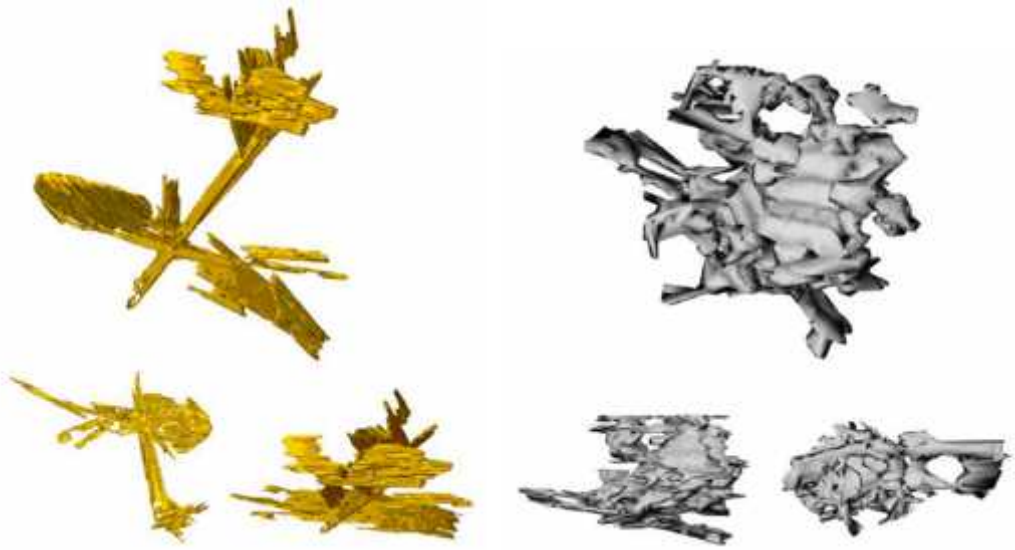

a. **b.**

Figure 2.9. 3D reconstruction from serial sectioning (a) beta phase, (b) alpha phase [92].

2.5.3. Fe/Si ratio of alpha and beta phase

Generally, the intermetallic phase identification was based on their chemical composition and morphology appearance. Classification based on the Fe/Si ratio of the phase showed that α-Al_8Fe_2Si phase (most of Fe/Si ratio > 3) has a higher value than β-$Al_9Fe_2Si_2$ phase (Fe/Si ratio 1.8-2), due to the higher iron and lower silicon content. Nevertheless, works by Kral et al. [82, 95] suggested that the method based on morphology appearance or chemical composition cannot be used solely for intermetallic phase identification. Although, in the work Kral used Al-Fe-Mn-Si which might influence the ratio and the morphology of the alloys.

Table.2.2. List of reference to alpha phase, composition and crystallographic data.

Reference.	Element (wt%)		Lattice parameter (Å)			crystal structure
	Fe	Si	a	b	c	
Dix and Heath, 1928 [96]	30	8				-
Fink and Van Horn, 1931 [97]	30.3	8.3				-
Takeda, Mutuzaki, 1940 [61]	38.1	15.9				-
Pratt and Raynor 1951 [98]	32.1-32.69	8.4-10.3	12.3		26.2	Hexagonal
Nowotny et al., 1951[99]	30.6	10.3				-
Robinson and Black, 1953 [75]	32.5	8.7	12.3		26.2	Hexagonal
Sun and Mondolfo, 1967 [100]	30-33	7.4-11				Hexagonal
Barlock and Mondolfo, 1975[101]	31	8	12.3		26.3	Hexagonal
Corby and Black, 1977 [82]			12.404		26.223	Hexagonal
Stefaniay et al., 1987 [102]	31-35	6-13	12.404		26.234	-
Gringer, 1987 [103]	33.5	8				Hexagonal
Sritharan et al., 2000 [104]	31.6	7.8				-
Pontevichi et.al., 2004 [105]	31-33.3	8.6-10.9				-
Roger et al., 2011 [68]			12.404		26.234	Hexagonal
Mikolajczak and Ratke, 2011 [106]	32.6	9.7				-
Gorny et al., 2013 [107]	33.8	9.4				-

Table 2.3 List of reference to beta phase, composition and crystallographic data.

Reference.	Element (wt%)		Lattice parameter (Å)				crystal structure
	Fe	Si	a	b	c	angle	
Dix and Heath, 1928 [96]	27	15					-
Fink and Van Horn, 1931 [97]	27.3	15					-
Sergeev and Rimmer, 1937 [108]	25.9-29.1	12.8 -14.6					-
Takeda, Mutuzaki, 1940 [61]	29.1	14.6	6.12	6.12	41.48	91	-
Phragmen, 1950 [77]	27.2-27.8	13.5-14	6.12	6.12	41.5	91	monoclinic
Pratt and Raynor, 1951 [98]	26.65-27.30	13.82-14.93					-
Nowotny et al., 1951 [99]	27.2	13.7					-
Obinata and Komatsu, 1954 [109]	23.52-25.75	15.77-18.92	6.12	6.12	41.48	91	-
Sun and Mondolfo, 1967 [100]	25.5-26.5	12.1-14.6					-
Barlock and Mondolfo, 1975 [101]	25	13	6.12	6.12	41.5	91	monoclinic
Stevaniay et al., 1987 [102]	25-29	13-16					-
Romming et al., 1994 [68]	27.22	13.69	6.161	6.175	20.81	90.42	monoclinic
Hansen et al., 1998 [85]			6.167	6.166	20.80	90.42	monoclinic
Sritharan et al., 2000 [104]	27.2	13.3					-
Mikolajczak and Ratke, 2011 [106]	24.2	12.5					-
Gorny et al., 2013 [107]	31.57	15.37					-

Table 2.2 and Table 2.3 show the composition and crystallographic data of alpha and beta phase taken from selected literature in chronicle order. Figure 2.10 is a plot of the Fe/Si ratio with open symbols when the structure has been reported, closed symbols otherwise.

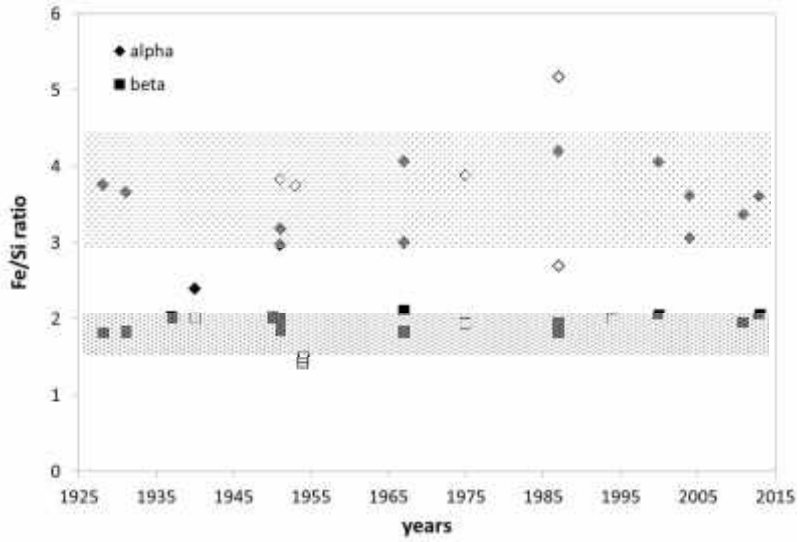

Figure 2.10. Fe/Si ratio of alpha and beta phase in chronicle order

2.5.4. Growth mechanism of beta phase

The formation of iron rich phases is controlled by the chemical composition of the alloys (silicon and iron contents) and by cooling rate. Early work by Mondolfo [76] showed that the higher the iron content in the alloys, the longer and wider the needles of beta phase formed. Investigation by Khalifa et al. [110] confirmed that the volume fraction of iron-bearing intermetallic phases increases with the increase in the amount of Fe. Yaneva et al. [111] reported that changes in silicon content also influence the beta phase fraction and the size beta platelet at high iron levels. Furthermore, work by Dinnis et al. [112] classified the solidification sequence of beta phase as follows:

- Pre-eutectic, after the primary (Al) dendrites, but prior to the (Al)-Si eutectic reaction, in a two phase (Al)-β-$Al_9Fe_2Si_2$ eutectic reaction.
- Post (Al)-Si eutectic, after the (Al)-Si two-phase eutectic as part of a three-phase eutectic (Al)-Si-β-$Al_9Fe_2Si_2$.
- As a three-phases eutectic directly after the dendrites in the case the final liquid composition arrived in eutectic point. For this work, post-eutectic would be renamed as three phase eutectic (3PE) beta phase.

Schematic classification of beta precipitation upon liquidus projection of Al-Fe-Si system in relation to the solidification sequence is illustrated in Figure 2.11. The red line as Fe critical level line acts as the boundary for the beta phase formation region classification. Typical chemical composition ranges of some Al-Si alloys with only taking account Si and Fe content were also superimposed.

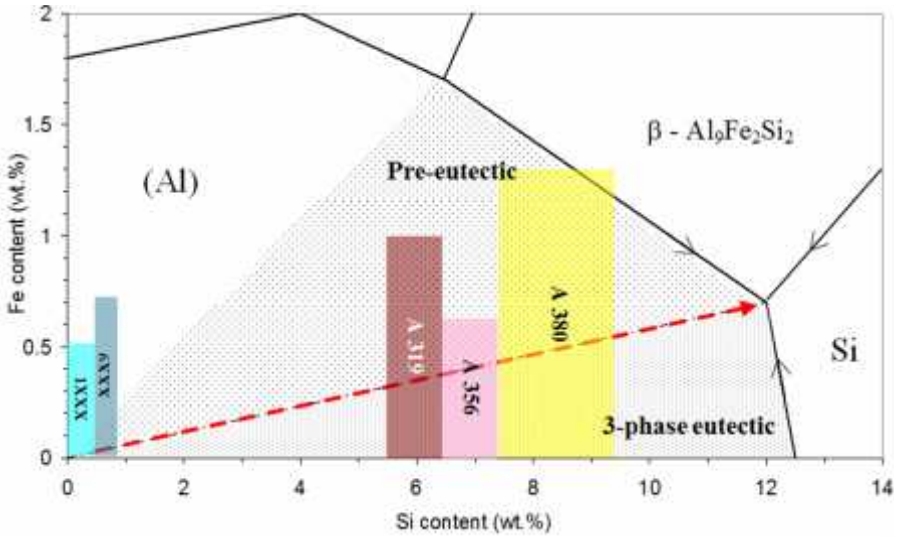

Figure 2.11. Beta phase precipitation classification and typical chemical composition of some Al-Si alloys superimposed upon Al corner of Al-Fe-Si phase diagram

Study by Tang and Sritharan [113] showed that the beta phase was found at the interface between flake silicon and aluminum-rich solution. Increasing the iron level and decreasing the cooling rate causing the β platelets to crystallize independently of silicon. Later, they proposed that two-phase eutectic β platelets which form at high iron levels were efficient nucleant for the eutectic silicon in unmodified and strontium modified alloys. Taylor et al. [114] also stated that the formation of large platelets of beta phase normally occurs as two-phase eutectic beta phase, when the iron level is above the critical level (draw as red line in the Figure 2.11) enables them as nucleation sites for eutectic silicon. Below the critical level, the eutectic silicon nucleates prior to the formation of beta phase. However, work by Lu and Dahle [115] suggests that eutectic (Al)-silicon grains are independent from beta phase, otherwise the distribution and number of eutectic grains would be dictated by the beta phase growth and orientation.

The influence of cooling rate on the growth of beta phase has been described by Khalifa et al. [110]. The volume fraction of beta phase is higher in slow cooling rate condition and large intermetallic precipitates are observed. They also noticed that the solidification range increases as the cooling rate decreases due to the precipitation of 3 phase eutectic beta phase. Narayanan et al. [116] observed that the beta phase start temperature is decreased along with increasing cooling rate. Another study of the effect cooling rate on the precipitation of intermetallic phases has been conducted by Langsurd [117] upon alloys in the 1XXX series. Langsurd reported that a shift occurs in the solidification field of Al_3Fe, Al_8Fe_2Si and $Al_9Fe_2Si_2$ toward lower Si concentration with increasing cooling rate. Therefore,

it suppressed the formation of beta phase from the peritectic reaction. Nevertheless, Narayanan et al. [116] reported that in a Al-6Si-1Fe (wt%) without Mn, the crystallization of alpha phase did not occurred, even with high cooling rate (20°C/s).

Moreover, the nucleation site for beta phase is still on debate. Khalifa et al. [118] looked for potential oxides as nucleation sites. They found CaO could be a favourable nucleation substrate for intergranular intermetallic particles. Another study by Cao and Campbell [119] suggested that oxide films, especially bifilms play an important role in beta phase nucleation.

Finally, the precipitation of beta phase has also been linked to porosity formation inside Al-Si alloys. Moustafa [120] showed that long branched platelets cause shrinkage cavity due to the inability of liquid metal to feed during solidification (Figure 2.12).

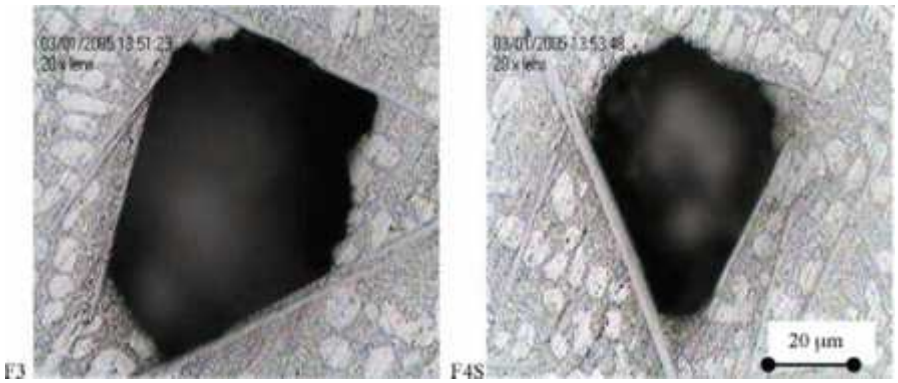

Figure 2.12. Shrinkage hole surrounded by β-phase platelets [120].

2.6. Beta phase modification

Due to the severity of detrimental effect of beta phase, several methods were developed to minimize that effect. Some of them were explained in this section.

2.6.1. Physical

The density difference between (Al) and intermetallic phases open the possibility for separation using gravitational effect. Shabestari and Gruzleski [121] studied this segregation phenomenon occurs when the cooling rate is slow. The results showed that the volume fraction of intermetallic increases with the distance from the melt surface. Work by Serak et al. [122] was also based on settling characteristic of intermetallic phase by holding the furnace temperature between solidus and liquidus for a long time period. However, this method would

be inefficient from the production point of view, due to the prolonged time needed for the intermetallic settling at the furnace bottom.

Moraes et al. [123] studied the possibility for removing intermetallics by physical filtration through ceramic filter. The results showed that by using proper filter along with Mn and Si addition and decreasing the temperature, the intermetallic phase can crystallize and be separated. Investigation by Gao et al. [124] was used $Na_2B_4O_7$ to form iron boride (Fe_2B) that settle at the bottom, thus reducing the iron content inside the liquid. Further study showed that the addition of $Na_2B_4O_7$ with flux could reduce up to 44% of the iron content inside the molten metal [125].

Another technique was developed by using ultrasonic wave to alter the intermetallic phase morphology. Working on ADC 12 alloy, Khalifa et al. [126] used the ultrasonic treatment which was coupled into the shot sleeve of high pressure die casting machine. The result showed that the ultrasonic could change the long plate beta phase into highly compacted fine globular form with dimension < 15 µm. Electromagnetic field effect has also been studied by Li et al. [127]. They used steady magnetic field to separate the intermetallic precipitates from the melt, however the result showed the beta phase morphology was unaffected.

Intensive shearing was developed to achieve fine grain structure under semi-solid condition, and should also affect the intermetallic morphology. Kumar et al. [128] studied the microstructure Al-Mg-Mn-Fe-Cu-Si alloy under intensive shear force and observed dispersed intermetallic precipitates and finer grain size compared to conventional casting. Observation by Kim et al. [129] also confirmed that mechanical melt-shearing treatment could modify the needle-like beta phase into shorter needle morphology.

2.6.2. Thermal treatment

Study on the superheating effect on nucleation can be found in the work by Mondolfo and Barlock [130]. Awano and Shimizu [131] also studied the effect of superheating prior pouring the melt and reported that this leads to Chinese script morphology of intermetallic precipitates without any addition of neutralizing element. Superheating would seemingly increase the iron content needed for beta phase formation. Work by Narayanan et al. [116] on commercial A319 alloys also showed similar effect. The result showed when the melt was superheated 200°C above the liquidus temperature and cooled at 20°C/s, the beta phase would be replaced by script phase as seen in Figure 2.13. Preferential nucleation of hexagonal alpha phase can be caused by the transformation of gamma alumina is into alpha alumina, which is

known as a poor nucleant for beta phase. Nevertheless, no information was given regarding the crystallography data of the observed script phase.

Another study by Jie et al. [132] with Al7Si0.55Mg alloy with very low iron content showed that the superheating could change the morphology of beta phase into small skeleton appearance. The superheat process was conducted for 30 minutes on a temperature range of 720-950°C. Mechanical tests showed the improvement in tensile strength to be higher compared to eutectic modification. However, both high temperature and high cooling rate should be used to insure the modification takes place.

To conclude, the use of superheat in production process could promote the adsorption of hydrogen into the molten metal which may cause porosity. Not to mention, higher temperature will increase the furnace operational cost.

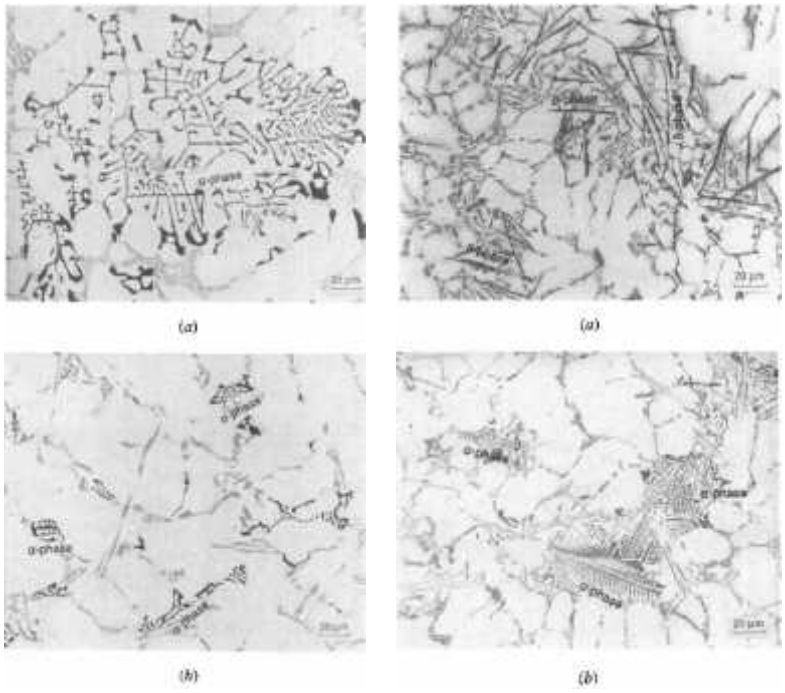

(A) (B)

Figure 2.13. Comparison of optical microstructure of A319 alloys (A) with 0.15% Fe (a) adding manganese, (b) superheated at 850°C (B) alloy with 1%Fe (a) superheated to 750°C (b) superheated to 850°C with cooling rate 10°C/s [116].

Another thermal treatment to reduce the beta phase is through non-equilibrium heat treatment. Villeneuve and Samuel [133] reported that heat treatment could increase the dissolution rate of beta phase. The mechanism occurred due to rejection of silicon from the 3 phase eutectic beta phase needle and decreased the total length of the beta phase.

2.6.3. Chemical neutralization

The most common method to reduce the harmful effect of beta phase is through low-level alloying. Several elements show the capability to alter plate like beta phase into a more compact Chinese script morphology which is less detrimental for mechanical properties.

2.6.3.1. Transition metal (Mn, Cr, Mo, V)

The knowledge that manganese neutralizes the harmful effect of beta phase can be traced back to early work by Philips and Varley [134], who investigated quaternary Al-Fe-Mn-Si alloys. The monoclinic beta phase is replaced by the cubic alpha phase $Al_{15}(Mn,Fe)_3Si_2$ with Chinese script morphology after the addition of manganese. The general assumption for the optimum Mn/Fe ratio is 1:2 [135]. However, other factors such as cooling rate and chemical composition could interfere with the formation of the cubic alpha phase. Narayanan et al. [116] noted that at low cooling rate with Mn addition, cubic alpha phase formed in interdendritic region in A 319 alloys. However, at higher cooling rate (20°C/s) the beta phase was also present. Another work by Seifeddine et al. [136] used a Mn:Fe ratio 2:1 on Al-9%Si alloy; the result showed Mn addition unable to totally hinder the beta phase formation at higher ratio.

Mahta et al. [137] found that Cr and Co are also able to modify beta phase into well distributed fine precipitates of cubic alpha phase. Their work also showed that the addition of Cr or Co promotes the formation of primary Si. An intermetallic phase of Al(Fe,Mn,Cr)Si with mainly polyhedral and star like shape forms by the addition of Cr in AlSi9Cu3 die casting alloy [138]. One problem related with addition of manganese and chromium is the formation of sludge at the bottom of holding furnace which reduced the efficiency process. A formula known as sludge factor (SF) formula (1%Fe + 2%Mn + 3%Cr) has been suggested by Jorstad [139], and this value should be keep such as $1.8<SF<2.1$.[135]

Other elements such as Mo and Ni also have been studied; however documentation regarding their use is limited. Work by Dichtl [140] on Al-Si alloy showed that Mo could convert platelet intermetallic into compact star shape compound. Another study by Nikitina et al. [141] on the effect of alloying on Al-Si-Cu alloy also showed that Mo could create a compacted form of intermetallic phase, thus increasing the impact strength of the cast metal. Moreover, vanadium is also known to modify the beta intermetallic phase as can be seen in work by Skinner et al. [142] and Rao [143].

2.6.3.2 Alkaline earth metal (Be, Ca, Sr)

Murali et al. [144, 145] reported that in the present of Be, the formation of beta intermetallic phases were suppressed. As a result a BeFe phase with Chinese script and polygon shape grows along with the primary Aluminum. They proposed that BeFe phase act as nucleate site for primary (Al) and the BeFe phase is a result of peritectic reaction instead of ternary eutectic reaction. The same result also showed in the work of Wang and Xiong [146] with Al7SiMg alloy. Wang observed that the addition of Be changes the plate like beta phase into Chinese script or polygon alpha phase. All Be-added alloys, individually and combined with Mn and Cr additions, appear to neutralize the detrimental effect of Fe content on mechanical properties [145]. Investigation by Chen et al. [147] also found that Be addition would transform beta plate like phase into script type π phase.

Another element studied in modification of beta phase is calcium. Investigation by Kumari et al. [148] illustrated that the additions Ca have reduced the intermetallic size and modified the eutectic microstructure. Work by Kobayashi et al. [149] also showed similar effect. However, studied by Cadena and Valdes [150] showed the opposite result, that the addition of Ca coarsened the intermetallic phase, even though refinement of the eutectic silicon occurred, as seen in Figure 2.14

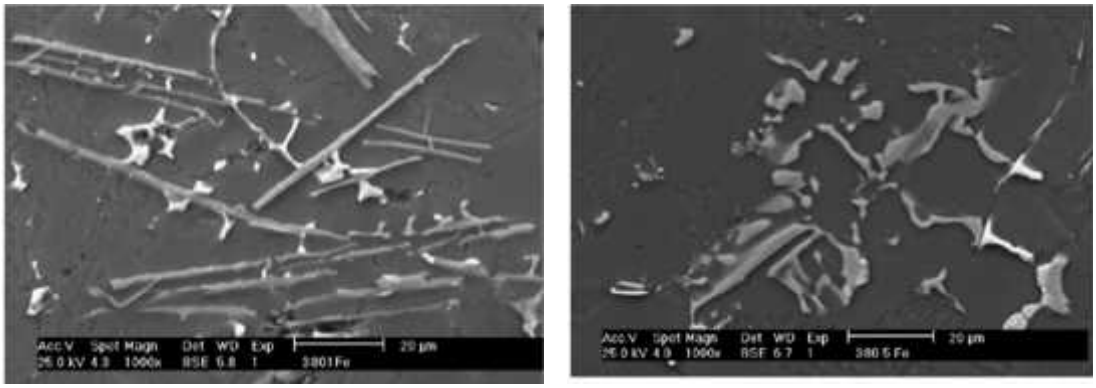

Figure 2.14. Effect of calcium additions on the coarsening morphology of iron-rich phases in an A380 alloy [150].

One of the elements continuously studied for its possible impact on beta phase modification is strontium. Samuel et al. [151] claimed the adsorption of strontium at alpha phase surface is preventing further diffusion of Si and reduces the possible appearance of the beta phase. Mulazimoglu et al. [152] analyzed their results in the same line, as illustrated in Figure 2.15.

Observation by Liu et al. [153] showed that Sr modification leads to fragmentation 3 phase eutectic beta phase, however with increasing iron content this effect diminishes. Investigation by Shabestari et al. [154] on A380 alloy showed that Sr modification delays the formation of intermetallic and sedimentation. Cuadra et al. [155] studied the effect of Sr on A319 alloy. They studied the Sr and cooling rate effect on intermetallic phase formation, and stated that cooling rate plays an important role on the refinement of grain size and intermetallic phase.

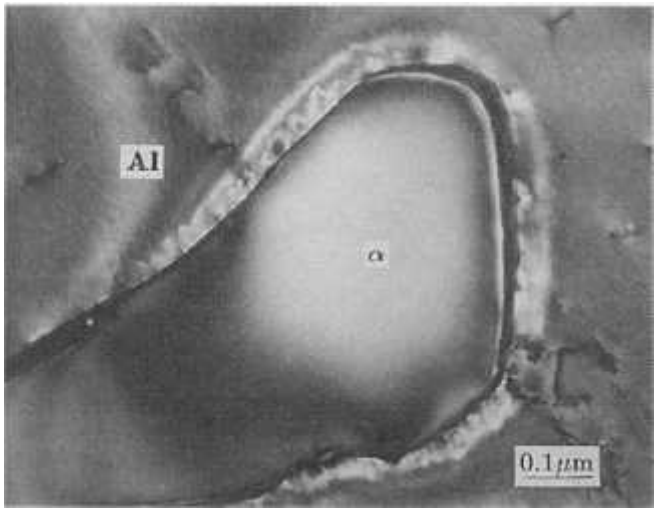

Figure 2.15. Silicon-rich layer surrounding ~-A1FeSi phase in the presence of strontium [152].

2.6.3.3. Alkali metal (Li, K)

Investigation by Asthari et al. [156] showed the capability of K to modify beta phase into alpha phase, as seen from DTA thermogram in Figure 2.16. The work also showed that the element is modified eutectic silicon as well. Another work by Asthari et al. [157] used Li as modification element, the result showed Li addition modified coarse beta phase into finer particle. In their work, the Li element was able to suppress the nucleation of beta phase, however excessive addition resulted a AlLiSi intermetallic.

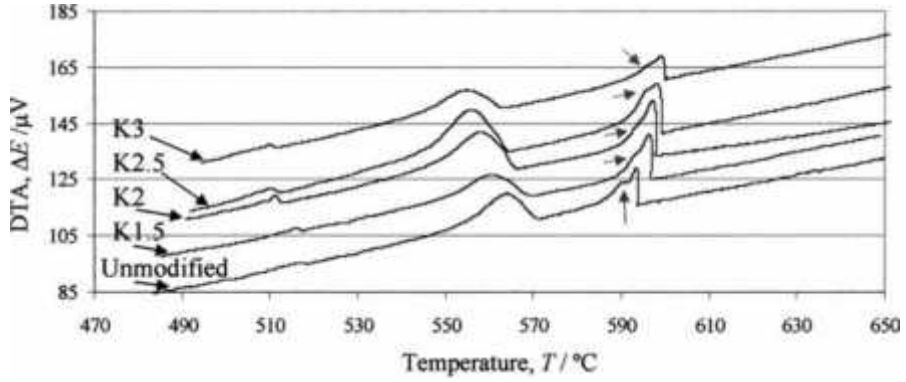

Figure 2.16. DTA thermogram cooled at 4.8°C/min showed the effect of K on beta phase precipitation in A319 alloys. The beta phase thermal arrests are highlighted by arrows [156].

2.6.3.4. Rare earth

Study by Fu et al. [158] on 1XXX alloy series stated that rare earth can modify the beta phase into AlFe(Ce,Nd,La) or AlFeSi(Ce,Nd,La) complex compound with sphere/short stick form. Hosseinifar and Malakov [159] also studied the effect of La and Ce on the intermetallic phase in alloys of 6XXX series (Figure 2.17). The addition of La promotes the formation of Chinese script α-AlFeSi phase and has a grain refinement effect. However, the same changes effects were not shown by Ce addition.

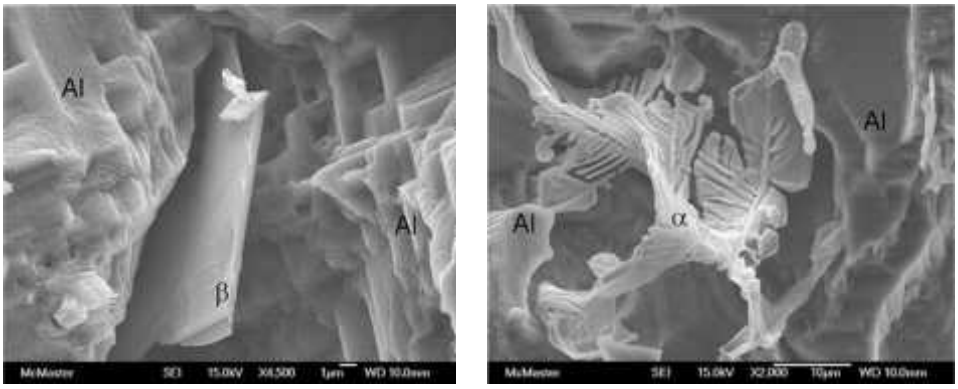

(a) (b)

Figure 2.17. SEM micrograph (a) morphology of the -AlFeSi phase in the as-cast (b) morphology of an ~-AlFeSi intermetallic particle observed in alloy containing 0.2 wt.% La [158].

Reference

1. J.R. Davis, ASM Speciality handbook aluminum and aluminum alloys, ASM International, 2003.
2. S. Goto, Y. Komatsu and S. Aso, Analysis of slurry-erosion Behavior in silicon particles dispersed Al-Si binary alloys, Journal of the Society of Materials Engineering for Resources of Japan, 17, (2004), 13-19.
3. G.D. Preston, The diffraction of X-rays by an age-hardening alloy of aluminium and copper. The structure of an intermediate phase, Phil. Mag., 1938, vol. 26, pp. 855–871.
4. A. Guinier, Structure of Age-Hardened Aluminium-Copper Alloys, Nature, 1938, vol. 142, pp. 569–570.
5. A. Lutts, Pre-precipitation in Al-Mg-Ge and Al-Mg-Si, Acta Metall., 9, 2, (1961), 577-586.
6. A.M. Samuel, F.H. Samuel, Effect of melt treatment, solidification conditions and porosity level on the tensile properties of 319.2 end chill aluminium castings, J. Mat. Sci., 30, (1995), 4823-4833.
7. K. Nogita, S.D. McDonald and A.K. Dahle, Eutectic modification of Al-Si alloys with rare earth metals. Materials Transactions, 45, 2(2004): 323-326.
8. M. Ravi, U. T. S. Pillai, B. C. Pai, A. D. Damodran and E. S. Dwarakadasa, The effect of mischmetal addition on the structure and mechanical properties of a cast Al-7Si-0.3Mg alloy containing excess iron (up to 0.6 Pct), Metall. Mater. Trans A. 33 (2002) 391-400.
9. Y. Rao, H.Yan, Z. Hu, Modification of eutectic silicon and β-Al_5FeSi phases in as-cast ADC12 alloys by using samarium addition, Journal of Rare Earths, 31, (2013), 916-922.
10. E.O. Hall, The deformation and ageing of mild steel: III discussion of results, Proc. Phys. Soc. London B, 64, (1951), p. 747.
11. N.J. Petch, The cleavage strength of polycrystals, J. Iron Steel Inst., 174 (1653), p. 25
12. W. Rosenhain, J. Grogan and T. Schofield, Foundry trade journal, 43, (1930), 177-180.
13. A. Cibula, The mechanism of grain refinement of sand casting in aluminum alloys, J. Inst. Metals, 76, (1949), 321-360.
14. F.A. Crosley, L.F. Mondolfo, Mechanism of grain refinement in aluminum alloys ,Trans. AIME, 191, (1951), 1143-1148.
15. L. Backerud, How does a good refiner work?, Light metal age, 1983, 6-12.
16. D.G. McCartney, Grain refining of aluminium and its alloys using inoculants, International Materials Reviews, 34, (1988), 247-260.
17. B.S. Murty, S. A. Kori, M. Chakraborty, Grain refinement of aluminium and its alloys by heterogeneous nucleation and alloying, International Materials Reviews, 01/2002; 47(1):3-29
18. T.E. Quested and A.L. Greer, Athermal heterogeneous nucleation of solidification, Acta Materialia, 53, (2005), 2683–2692.

19. M. Easton and D. StJohn, Grain refinement of aluminium alloys: Part I. The nucleant and the solute paradigm – A review of the literature, Metall. Mater. Trans. A, 30A, (1999), 1613-1623.

20. D.H. StJohn, M. Qian, M.A. Easton, P. Cao, The interdependence theory: The relationship between grain formation and nucleant selection, Acta Materialia, 59, (2011), 4907-4921.

21. I. Maxwell, A. Hellawell, The constitution of the system Al-Ti-B with reference to aluminum-base alloys, Metallurgical Transaction, 3, (1972), 1487-1493.

22. A.L. Greer, A.M. Bunn, A. Tronche, P.V. Evans, D.J. Bristow, Modelling of inoculation of metallic melts: application to grain refinement of aluminium by Al-Ti-B, Acta Materialia, 48, (2000), 2823-2835.

23. J.A. Marcontonio, L.F. Mondolfo, Grain refinement in aluminum alloyed with titanium and boron, Metallurgical Transaction, 2, (1971), 465-471.

24. P. Schumacher, A.L. Greer, J. Worth, P.V. Evans, M.A. Kearns, P. Fisher, and A.H. Green, New studies of nucleation mechanisms in aluminium alloys: implications for grain refinement practice, Mater.Sci.Technol, 14, (1988), 394-404.

25. Z. Fan, An epitaxial model for heterogeneous nucleation on potent substrates, Metallurgical and Materials Transactions A, 44, (2013), 1409-1418.

26. N. Iqbal, N.H. van Dijk, S.E. Offerman, N. Geerlofs, M.P. Moret, L. Katgerman, G.J. Kearley, In situ investigation of the crystallization kinetics and the mechanism of grain refinement in aluminum alloys, Materials Science and Engineering A, 416, (2006), 18-32.

27. M.X. Zhang, P.M. Kelly, M.A. Easton, J.A. Taylor, Crystallographic study of grain refinement in aluminum alloys using the edge-to-edge matching model, Acta Materialia, 53, (2005), 1427−1438.

28. I. Maxwell, A. Hellawell, A simple model for grain refinement during solidification, Acta Metallurgica, 23, (1975), 229-237.

29. M. Easton, D.StJohn, Grain refinement of aluminum alloys: part II. Confirmation of, and a mechanism for, the solute paradigm, Metallurgical and Materials Transactions A, 30A, (1999), 1625-1633.

30. M. Qian, P. Cao, M.A. Easton, S.D. McDonald, D.H. StJohn, An analytical model for constitutional supercooling-driven grain formation and grain size prediction, Acta Materialia, 58, (2010), 3262-3270.

31. R. Schmid-Fetzer, A. Kozlov, Thermodynamic aspects of grain growth restriction in multicomponent alloy solidification, Acta Materialia, 59, (2011), 6133–6144.

32. L. Backerud, Rein Vainik, Method for optimized aluminum grain refinement, Light metal 2001, 951-954.

33. M.A. Easton, D.H. StJohn, Improved prediction of the grain size of aluminum alloys that includes the effect of cooling rate, Materials Science and Engineering A, 486, (2008), 8-13.

34. Y.C. Lee, A.K. Dahle, D.H. StJohn, J.E.C. Hutt, The effect of grain refinement and silicon content on grain formation in hypoeutectic Al-Si alloys, Materials Science and Engineering A, 259, (1999), 43-52.

35. R.W. Smith, Modification of aluminium-silicon alloys, The Solidification of Metals, The iron and steel institute, London, (1968), 224-237.

36. H. Fredriksson, M. Hillert, N. Lange, The modification of aluminium-silicon alloys by sodium, Journal of the institute of metals, 101, (1973), 285-299

37. D.C. Jenkinson, L.M. Hogan, The modification of aluminium-silicon alloys with strontium, Journal of Crystal Growth, 28, (1975), 171-187.

38. Q. Liu, Q. Li, Q. Liu, Modification of Al-Si alloys with sodium, Acta Metall. Mater, 39, (1991), 2497-2502.

39. S. Khan, R. Elliott, Quench modification of aluminium-silicon eutectic alloys, Journal of Materials Science, 31, (1996), 3731-3737.

40. S.Z. Lu, A. Hellawell, Growth mechanism of silicon in Al-Si alloys, Journal of Crystal Growth, 73, (1985), 316-328.

41. M. Shamsuzzoha, L.M. Hogan, The twinned growth of silicon in chill-modified Al-Si eutectic, Journal of Crystal Growth, 82, (1987), 598-610.

42. K. Nogita, S.D. McDonald, A.K. Dahle, Eutectic modification of Al-Si alloys with rare earth metals, Material Transaction, 45, (2004), 323-326.

43. A.Pacz, US Patent 1387900, (1921).

44. D.R. Hamilton, R.G. Seidensticker, Propagation mechanism of germanium dendrites, Journal of Applied Physics, 31, (1960), 1165-1168.

45. S.Z. Lu, A. Hellawell, The mechanism of silicon modification in aluminum-silicon alloys: Impurity induced twinning, Metallurgical Transactions A, 18, (1987), 1721-1733.

46. J.E. Gruzleski, The art and science of modification*:* 25 years of progress, Transactions of the AFS, 100, (1992), 673–683

47. M.M. Makhlouf, H.V. Guthy, The aluminum–silicon eutectic reaction: mechanisms and crystallography, Journal of Light Metals, 1, (2001), 199–218.

48. S. Hegde, K.N. Prabhu, Modification of eutectic silicon in Al–Si alloys, Journal of Materials Science, 43, (2008), 3009-3027.

49. M. Timpel, N.Wanderka, R.Schlesiger, T.Yamamoto, N.Lazarev, D.Isheim, G.Schmitz, S.Matsumura, J. Banhart, The role of strontium in modifying aluminium-silicon alloys, Acta Materialia, 60, (2012), 3920-3928.

50. F. Yilmaz, O.A. Atasoy, R. Elliott, Growth structure in alumium-silicon alloys II. The influence of strontium, Journal of Crystal and Growth, 118, 1992, 377-384.

51. K.F. Kobayashi, L.M. Hogan, The crystal growth of silicon in Al-Si alloys, Journal of Materials Science, 20, (1985), 1961-1975.

52. C.R. Ho and B. Cantor, Modification of hypoeutectic Al-Si alloys, Journal of Materials Science, 30, (1995), 1912-1920.

53. K. Nogita, S.D. McDonald, K. Tsujimoto, Y. Kazuhiro, and A.K. Dahle, Aluminium phosphide as a eutectic grain nucleus in hypoeutectic Al-Si alloys, Journal of Electron Microscopy, 53, (2004), 361–369.

54. T.H. Ludwig, P.L. Schaffer, L. Arnberg, Influence of phosphorus on the nucleation of eutectic silicon in Al-Si alloys, Metallurgical and Materials Transactions A, 44A, (2013), 5796-5805.

55. P.B. Crosley, L.F. Mondolfo, The modification of aluminum-silicon alloys, AFS Trans. 74 (1966) 53–64.

56. Y.H. Cho, H.-C. Lee, K.H. Oh, A.K. Dahle, Effect of strontium and phosphorus on eutectic Al-Si nucleation and formation of β-Al_5FeSi in hypoeutectic Al-Si foundry alloys, Metallurgical and Materials Transactions A, 39A, (2008), 2435-2448.

57. J.A.S. Green, Aluminum recycling and processing for energy conservation and sustainability, ASM International, 2007.

58. G. Ghosh, Aluminium-iron-silicon, in: Light metal systems: Phase diagrams, crystallographic and thermodynamic data, vol. IV of Landolt-Börnstein (New Series), Springer-Verlag, Berlin, 2008.

59. N. Krendelsberger, F. Weitzer and J.C. Schuster, On the reaction scheme and liquidus surface in ternary system of Al-Fe-Si, Metallurgical and Materials Transactions A,38A (2007), 1681-1691.

60. A.G.C. Gwyer and H.W.L. Phillips, The ternary system: aluminium-silicon-iron in the constitution of alloys with silicon and iron, J. Inst. Metals, 38, (1927), 35-44.

61. H.P. Takeda, K. Mutuzaki, The equilibrium diagram of the iron-aluminium-silicon system (in Japanese), Tetsu to Hagane, 26, (1940), 335–361.

62. V.G. Rivlin and G.V. Raynor, Phase equilibria in iron ternary alloys 4: Critical. evaluation of constitution of aluminium-iron-silicon system, Int. Met., Rev. 26(1981) 133.

63. N.A. Belov, A.A. Aksenov, and D.G. Eskin. Iron in aluminium alloys: impurity and alloying element, Taylor and Francis Inc., London and New York, 2002.

64. Y. Du, Z. Jin, B. Huang, W. Gong, H. Xu, Z. Yuan, J.C. Schuster, F. Weitzer, N. Krendelsberger, A thermodynamic description of the Al-Mn-Si system over the entire composition and temperature ranges, Metall. Mater. Trans. A,. 35, (2004), 1613-1628.

65. L. Eleno, J. Vezelý, B.Sundman, M. Cieslar, J. Lacaze, Assessment of the al corner of the ternary Al-Fe-Si system, Materials Science Forum, vol. 649, (2010), 523-528.

66. I. Ansara, A. Dinsdale, M. Rand, COST 507, Definition of thermochemical and thermophysical properties to provide a database for the development of new light alloys: Thermochemical database for light metal alloys – 1998.

67. M.C. Marker, B. Skolyszewska-Kühberger, H.S. Effenberger, C. Schmetterer, K.W. Richter, Phase equilibria and structural investigations in the system Al-Fe-Si, Intermetallics, 19, (12) (2011), 1919–1929.

68. J. Roger, F. Bosselet, J-C. Viala, X-rays structural analysis and thermal stability studies of the ternary compound α-AlFeSi, Journal of Solid State Chemistry, 184, 5, (2011), 1120-1128.

69. C. Romming, V. Hansen, J. Gjonnes, Crystal structure of β-$Al_{4.5}FeSi$, Acta Crystallogr., Sect. B: Struct. Crystallogr. Crys. Chem., B50 (3), (1994), 307–312.

70. H. Westengen, Formation of intermetallic compounds during DC casting of commercial purity Al-Fe-Si alloy, Z. Metallkd., 73, (1982), 361–368.

71. P. Liu, T. Thorvaldsson, GL. Dunlop, Formation of intermetallic compound during solidification of dilute Al-Fe-Si alloys. Materials Science and Technology, 2, (1986), 1009-1018.

72. A.L. Dons, AlFeSi-particles in commercial pure aluminium, Z. Metallkd., 75, (1984), 170–174.

73. C.L. Jensen, R.K. Wyss, Electron diffraction study of α and α_T-AlFeSi, Metallurgical Transaction A, 19A, (1988), 893-898.

74. L.F. Mondolfo, Metallography of aluminum alloys, Wiley & sons. inc., 1943.

75. K. Robinson, P.J. Black, An X-ray examination of an α-(Al-Fe-Si) ternary compound, Philos. Mag., 44, (1953), 1392–1397.

76. R.N. Corby, P.J. Black, The structure of α-AlFeSi by anomalous dispersion method, Acta Crystallogr. B, 33B, (1977), 3468–3475

77. L.F. Mondolfo, Aluminium alloys, structure and properties, Butterworths, London (1976).

78. G. Phragmen, On the phase occurring in alloys of aluminium with copper, magnesium, manganese, iron and silicon, J. Inst. Met., 77, (1950), 489–552.

79. M. Cooper, The crystal structure of the ternary alloys α-AlFeSi, Acta Crystallogr., 23, (1967), 1106–1107.

80. D. Munson, A Clarification of the phases occurring in aluminium rich aluminium-Iron-silicon alloys with particular reference to the ternary phase α-AlFeSi, J. Inst. Met., 95, (1967), 217–219.

81. J.G. Zheng, R. Vincent, J.W. Steeds, Crystal structure of an orthorhombic phase in β-(Al-Fe-Si) precipitates determined by convergent-beam electron diffraction, Philosophical magazine. A. Physics of condensed matter. Structure, defects and mechanical properties, 80, (2000), 493-500.

82. M.V. Kral, A crystallographic identification of intermetallic phases in Al-Si alloys, Materials Letters, 59, (2005), 2271 – 2276.

83. C. Boudias, D. Monceau, Carine Crystallography 3.1 crystallographic software.

84. W. Rosenhain, S.L. Archbutt, D. Hanson, Some Alloys of Aluminium-Light Alloys, London, 1921

85. V. Hansen, B. Hauback, M. Sundberg, C. Romming, J. Gjonnes, A combined synchrotron powder diffraction, electron diffraction, high-resolution electron microscopy and single-crystal X-ray diffraction Study of a faulted structure, Acta Crystallogr., 54B, (1998), 351–357.

86. G.J.C. Carpenter and Y. Le Page, Revised cell data for the β-FeSiAl phase in aluminum alloys, Scr. Metall. Mater., 28, (1993), 733-736.

87. J.Y. Hwang, H.W. Doty, M.J. Kaufman, Crystallographic studies on the iron-containing intermetallic phases in the 319-type aluminium casting alloys, Philosophical Magazine, 88, 2008, 607-619.

88. S. Gowri, F.H. Samuel, Effect of Alloying Element on the Solidification Characteristics and Microstructure of Al-Si-Cu-Mg-Fe 380 Alloy, Metall. Trans.A., 25, (1994), 437-448.

89. O. Elsebaie, A. M. Samuel and F. H. Samuel, Effects of Sr-modification, iron-based intermetallics and aging treatment on the impact toughness of 356 Al–Si–Mg alloy, Journal of Materials Science, 46, 3027-3045

90. S.Belmares-Perales, M.Castro-Román, M.Herrera-Trejo, L.E Ramírez-Vidaurri, Effect of cooling rate and Fe/Mn weight ratio on volume fractions of α-AlFeSi and β-AlFeSi phases in Al-7.3Si-3.5Cu alloy, Metals and Materials International, 14, (2008), 307-314.

91. S. Murali, K. S. Raman and K. S. S. Murthy, Effect of magnesium, iron (impurity) and solidification rates on the fracture toughness of Al-7Si-0.3Mg casting alloy, Materials Science and Engineering: A, 151, (1992), 1–10.

92. M.A. Moustafa, Effect of iron content on the formation of β-Al_5FeSi and porosity in Al–Si eutectic alloys, Journal of Materials Processing Technology, 209, (2009), 605–610.

93. J.Z. Yi, Y.X. Gao, P.D. Lee, T.C. Lindley, Effect of Fe-content on fatigue crack initiation and propagation in a cast aluminum–silicon alloy (A356–T6), Materials Science and Engineering A, 386 (2004) 396–407.

94. C.M. Dinnis, J.A. Taylor, As-cast morphology of iron-intermetallics in Al–Si foundry alloys Scripta Materialia 53 (2005) 955–958.

95. M.V. Kral, P.N.H. Nakashima, D.R.G. Mitchell, Electron microscope studies of Al-Fe-Si intermetallics in an Al-11% Si alloy, Metall. Mater. Trans A, 37A, (2006), 1987–1997.

96. E.H. Dix Jr., Observations on the occurrence of iron- and silicon in aluminium, Trans.AIME, 69, (1923), 957–971.

97. W.L. Fink, K.R. Van Horn, Constituents of aluminium-iron-silicon alloys, Trans.AIME, Inst. Met. Div., (1931), 383–394.

98. J.N. Pratt, G.V. Raynor, The intermetallic compounds in the alloys of aluminium and silicon with chromium, manganese, iron, cobalt and nickel, J. Inst. Met., 79, (1952), 211–232.

99. H. Nowotny, K. Komerek, J. Kromer, An investigation of the ternary system: aluminium-iron-silicon (in German), Berg- und Huettenmn. Monatsh. Hochsch. Loeben, 96, (1951), 161–169.

100. C.Y. Sun, L.F. Mondolfo, A clarification of the phases occurring in Al rich Al-Fe-Si alloys, J. Inst. Met., 95, (1967), 384.

101. J.G. Barlock, L.F. Mondolfo, Structure of some aluminum-iron-magnesium-silicon alloys, Z. Metallkd., 66, (1975) 605–611.

102. V. Stefaniay, A. Griger, T. Turmezey, Intermetallic phases in the aluminium-side corner of the AlFeSi-alloy system, J. Mater. Sci., 22, (1987), 539–546.

103. A. Gringer, Powder data for the α_H Intermetallic phases with slight variation in composition in the system Al-Fe-Si, Powder Diffr., 2, (1987), 31–35.

104. T. Sritharan, S. Murali, P. Hing, Synthesis of Aluminium-iron-silicon intermetallics by reaction of elemental powders, Mater. Sci. Eng. A, 286, (2000), 209–217.

105. S. Pontevichi, F. Bosselet, F. Barbeau, M. Peronnet, J.C. Viala, Solid-liquid phase equilibria in the Al-Fe-Si system at 727°C, J. Phase Equilib. Diffus., 25(6), (2004), 528–537.

106. P. Mikolajczak, L. Ratke, Intermetallic Phases and Microstructure in AlSi Alloys Influenced by Fluid Flow, TMS 2011 Supplemental Proceedings: General Paper Selections, Volume 3, 2011.

107. A. Gorny, J. Manickaraj, Z. Cai, S. Shankar, Evolution of Fe based intermetallic phases in Al–Si hypoeutectic casting alloys: Influence of the Si and Fe concentrations, and solidification rate, Journal of Alloys and Compounds, 577, 15, (2013), 103-124.

108. L.N. Sergeev, B.I. Rimmer, Constitution of the system aluminium-iron-silicon (in Russian), Metallurg., (9/10), (1937), 112–125.

109. I. Obinata, N. Komatsu, On the Phases occuring in alloys of aluminium with iron and silicon (in Japanese), Nippon Kinzoku Gakkaishi, 19, (1954), 197–201.

110. W. Khalifa, F.H. Samuel, J.E. Gruzleski, Iron intermetallic phases in the Al corner of the Al-Si-Fe system, Metall. Mater. Trans. A, 34, (2003), 807 – 825.

111. S. Yaneva, N. Stoichev, Z. Kamenova, S. Budurov, Quaternary iron-containing phases in Al-Si Cast Alloys, Zeitschrift fuer Metallkunde, 75, (1984), 395-398.

112. C.M. Dinnis, J.A. Taylor, A.K. Dahle, Iron-related porosity in Al–Si–(Cu) foundry alloys, Materials Science and Engineering A, 425, (2006), 286-296.

113. S.K. Tang, T. Sritharan, Morphology of β-AlFeSi intermetallic in Al-7Si alloy castings, Materials Science and Technology, 14, (1998), 738-742.

114. J.A. Taylor, G.B. Schaffer, D.H. StJohn, The role of iron in the formation of porosity in Al-Si-Cu-based casting alloys: Part III. A microstructural model, Metall. Mater. Trans. A, 30A, (1999), 1657–1662.

115. L. Lu, A.K. Dahle, Iron-rich intermetallic phases and their role in casting defect formation in hypoeutectic Al−Si alloys, Metall. Mater. Trans. A, 36 (2005), 819-835.

116. L.A. Narayanan, F.H. Samuel, J.E. Gruzleski, Crystallization behavior of iron-containing intermetallic compounds in 319 aluminum alloy, Metall.Trans, 25A, (1994), 1761-1773.

117. Y. Langsrud, Silicon in commercial aluminium alloys-what becomes of its during DC casting, Key Engineering Material, 44-45, (1990), 95-116.

118. W. Khalifa, F.H. Samuel, J.E. Gruzleski, H.W. Doty, S. Valtierra, Nucleation of Fe-intermetallic phases in the Al-Si-Fe alloys, Metall. Mater. Trans. A, 36, (2005), 1017-1032.

119. X. Cao, J. Campbell, The solidification characteristics of Fe-rich intermetallics in Al-11.5Si-0.4Mg cast alloys, Metall. Mater. Trans. A, 35, (2004), 1425-1435.

120. M.A. Moustafa, Effect of iron content on the formation of β-Al_5FeSi and porosity in Al–Si eutectic alloys, Journal of Materials Processing Technology, 209, (2009), 605-610.

121. S.G. Shabestari, J.E. Gruzleski, Gravity segregation of complex intermetallic compounds in liquid aluminum-silicon alloys, Metall. Mater. Trans. A, 26, (1995), 999 – 1006.

122. J. Šerák, D. Vojtech, P. Novák, K. Dám, T. Janoušek, The influence of annealing conditions on microstructure Of AlSiCuMgFe Alloys, METAL 2009 - 18th International Metallurgical & Material Conference, Hradec nad Moravicí, Czech Republic, May 19-21 2009.

123. H.L. de Moraes, J.R. de Oliveira, D.C. Romano-Espinosa1 and J.A. Soares-Tenório, Removal of iron from molten recycled aluminum through intermediate phase filtration, Materials Transactions, 47, (2006), 1731-1736.

124. J.W. Gao, D. Shu, J. Wang, B.D. Sun, Effects of $Na_2B_4O_7$ on the elimination of iron from aluminum melt, Scripta Materialia, (2007), 57.

125. J.W. Gao, D. Shu, J. Wang, B.D. Sun, Study on iron purification from aluminium melt by $Na_2B_4O_7$ flux, Materials Science and Technology, 25, (2009), 619-624.

126. W. Khalifa, Y. Tsunekawa, M. Okumiya, Effect of ultrasonic treatment on the Fe-intermetallic phases in ADC12 die cast alloy, Journal of Materials Processing Technology, 210, (2010) 2178–2187.

127. T. Li, Z. Xu, B. Sun, D. Shu, Y. Zhou, Electromagnetic separation of primary iron rich phase from aluminum silicon melt, J. Trans Nonferrous Met.Soc.China, 13, (2003), 121-125.

128. S. Kumar, N. Hari Babu, G.M. Scamans, Z. Fan, Influence of intensive melt shearing on the microstructure and mechanical properties of an Al-Mg Alloy with high added impurity content, Metallurgical and Materials Transactions A, 42A, (2011), 3141.

129. B.W. Kim, S. Lee, Melt shearing process for recycling of iron contaminated Al-Si Alloy by modification of harmful morphology of intermetallics, Advanced Materials Research, 421, (2011), 160-163.

130. L.F. Mondolfo and J.G. Barlock, Effect of some superheating on structure aluminum alloys, Metallurgical Transactions B, 6, (1975), 565- 572.

131. Y. Awano, Y. Shimizu, Non-equilibrium crystallization of AlFeSi compound in melt-superheat Al–Si alloy castings, AFS Trans., 98, (1990), 889–895.

132. W. Jie, Z. Chen, W. Reif and K. Müller, Superheat treatment of Al-7Si-0.55Mg melt and its influences on the solidification structures and the mechanical properties, Metall. Mater. Trans. A, 34, (2003), 799-806.

133. C. Villeneuve, F. H. Samuel, Fragmentation and dissolution of β-Al_5FeSi phase during solution heat treatment of Al-13%Si-Fe alloys, International Journal of Cast Metals Research, 2, (1999), pp. 145-160.

134. H.W.L. Phillips, P.C. Varley. JIM, 69, (1943), 317.

135. D.L. Colwell, J.R. Kissling, Die and permanent mold casting aluminum alloy minor elements, AFS Transactions, 69, (1961), 610 – 615.

136. S. Seifeddine, S. Johansson, I.L. Svensson, The influence of cooling rate and manganese content on the β-Al_5FeSi phase formation and mechanical properties of Al–Si-based alloys, Materials Science and Engineering: A, 490, (2008), 385-390.

137. M. Mahta, M. Emamy, A. Daman, A. Keyvani, J. Campbell, Precipitation of Fe rich intermetallics in Cr- and Co-modified A413 alloy, International Journal of Cast Metals Research, 18, (2005), 73-79.

138. G. Timelli, F. Bonollo, The influence of Cr content on the microstructure and mechanical properties of AlSi9Cu3(Fe) die-casting alloys, Materials Science and Engineering: A, 528, (2010), 273-282.

139. J.L. Jorstad, Die Cast. Eng. 11/12 (1986) 30–36.

140. H.J. Dichtl, Use of molybdenum to compensate for the adverse effect of iron in aluminum silicon alloys, Aluminum, 46, (1970), 362–364.

141. E.V. Nikitina, Effect of alloying elements on the structure and properties of secondary Al–Cu–Si alloys produced under nonequilibrium solidification conditions, Russian Metallurgy (Metally), (2005), 180-184

142. D.J. Skinner, R.L. Bye, D. Raybould, A.M. Brown, Dispersion strengthened Al-Fe-V-Si alloys. Scripta Metallurgica, 20, (1986), 867–872.

143. A.K. Prasada Rao, Influence of vanadium on the microstructure of A319 alloy, Trans Indian Ins. Met., 64, (2011), 447-451.

144. S. Murali, K.S. Raman, K.S.S. Murthy, The formation of β-$FeSiAl_5$ and BeFe phases in Al7Si0.3Mg alloy containing Be, Materials Science and Engineering A, 190, (1995), 165-172.

145. S Murali, K.S. Raman, K.S.S. Murthy, Morphological studies on β-$FeSiAl_5$ phase in Al-7-Si-0.3Mg alloy with trace additions of Be, Mn, Cr, and Co, Materials Characterization, 33, (1994), 99-112.

146. Y. Wang, Y. Xiong, Effects of beryllium in Al-Si-Mg-Ti cast alloy, Materials Science and Engineering A, 280, (2000), 124-127.

147. Z. Chen, H. Zhang, R. Zhang, Effect of beryllium and iron addition on iron bearing phase A 357 aluminum alloys, China Foundry, 7, (2010), 275-277.

148. S.S. Sreeja Kumari, R.M. Pillai, B.C. Pai, K. Nogita and A.K. Dahle, Influence of calcium on the microstructure and properties of an Al-7Si-0.3Mg-xFe alloy, Metallurgical and Materials Transactions A, 37, (2006), 2581-2587.

149. T. Kobayashi, H.J. Kim, M. Niinomi, Effect of calcium on mechanical properties of recycled aluminium casting alloys, Materials Science and Technology 13, (1997), 497-502.

150. A.A Zaldivas Cadena, A. Flores Valdes, Prediction and identification of calcium rich phase in Al-Si alloys by electron backscatter diffraction EBSD: SEM, Material Characterization, 58, (2007), 834-841.

151. A.M. Samuel, F.H. Samuel, H.W. Doty, Observations on the formation of β-AlFeSi phase in 319 type Al-Si alloys, Journal of Materials Science, Vol. 31 (1996), 5529-5539.

152. M.H. Mulazimoglu, A. Zaluska, J.E. Gruzleski, F. Paray, Electron microscope study of Al-Fe-Si intermetallics in 6201 Aluminum Alloy, Metallurgical and Materials Transactions A, 27A (1996), 929-936.

153. L. Liu, A.M.A. Mohamed, A.M. Samuel, F.H. Samuel, H.W. Doty, And S. Valtierra, Precipitation of β-Al_5FeSi phase platelets in Al-Si based casting alloys, Metallurgical and Materials Transaction A, 40A, (2009), 2457-2469.

154. S.G. Shabestari, M. Keshavarz, M.M. Hejazi, Effect of strontium on the kinetics of formation and segregation of intermetallic compounds in A380 aluminum alloy, Journal of Alloys and Compounds, 477, (2009), 892-899.

155. J.E. Cuadra, P.G. Acevedo, H.M. Molinar, A. Picado, Effect of Sr and solidification conditions on characteristics of intermetallic in Al–Si 319 industrial alloys, Material and Design, 31,(2010), 343-356.

156. P. Ashtari, H. Tezuka, T. Sato, Modification of Fe-containing intermetallic compounds by K addition to Fe-rich AA319 aluminum alloys, Scripta Materialia, 53, (2005), 937-942.

157. P. Ashtari, H. Tezuka, T. Sato, Influence of Li addition on intermetallic compound morphologies in Al–Si–Cu–Fe cast alloys, Scripta Materialia, 51, (2004), 43-46.

158. G. Fu , F. Su, L. Ren, W. Chen, K. Qian, Modification behaviour of trace rare earth on impurity Ppases in Ccmmercial purity aluminum, J. of Rare Earth, 20, (2002), p 61-66.

159. M. Hosseinifar and D.V. Malakhov, Effect of Ce and La on microstructure and properties of a 6XXX series type aluminum alloy, Journal of Materials Science, 43, (2008), 7157-7164.

3. Materials and Experimental Methods

In this chapter, the studied materials, the experiment preparation and the techniques to characterize microstructure features in Al-Si alloys will be described.

3.1. Material

3.1.1 Commercial A356 Alloys

Aluminum alloys used in this study are a commercial alloy and a synthetic alloy. The commercial alloy is A356 provided by AZTERLAN. A356 grade is classified as hypoeutectic Al-Si-Mg alloy and generally used because of its superior castability and good mechanical properties, especially after heat treatment (T6), owing to a fine precipitation of Mg_2Si. Automotive components such as cast wheels and engine blocks are made from this grade, and this alloy is widely used in permanent die casting process. In the present work, an assessment was performed to a series of A356 samples solidified under different cooling rates. Furthermore, modification of the alloys was made with strontium and varies between 0.003-0.013 wt%, with one sample modified with Na. The final chemical compositions of the A356 alloys used in this study are listed in Table 3.1.

Table 3.1. Chemical composition (wt.%) of studied A356 alloys and their calculated liquidus temperature (°C).

Sample Code	Chemical composition (% wt)											Calculated Liquidus (°C)
	Si	Fe	Cu	Mn	Mg	Cr	Ni	Zn	Ti	Sr	Na	
1	7.26	0.1	<0.01	<0.01	0.41	<0.01	<0.01	<0.01	0.12	<0.003		613.8
2	7.07	0.13	<0.01	<0.01	0.5	<0.01	<0.01	<0.01	0.16	<0.003		615.1
3	6.99	0.16	0.01	<0.01	0.35	<0.01	<0.01	0.02	0.16	0.01		616.1
4	6.62	0.14	<0.01	<0.01	0.28	<0.01	<0.01	<0.01	0.14	<0.003	0.01	618.8
5	6.86	0.19	0.02	0.01	0.39	<0.01	0.01	0.01	0.16	0.009		616.8
6	6.83	0.09	<0.01	<0.01	0.31	<0.01	0.01	<0.01	0.14	0.011		617.4
7	6.3	0.13	0.03	<0.01	0.32	<0.01	<0.01	0.05	0.19	0.013		621.4
8	7.52	0.1	<0.01	<0.01	0.42	<0.01	<0.01	<0.01	0.1	0.008		611.8
9	6.9	0.18	<0.01	0.02	0.53	0.01	<0.01	<0.01	0.14	0.011		615.7
10	6.65	0.17	0.02	<0.01	0.5	<0.01	<0.01	<0.01	0.16	0.013		617.8
11	6.83	0.14	<0.01	<0.01	0.52	<0.01	<0.01	<0.01	0.13	0.013		616.3

The experiment then focused on the grain refinement evaluation and eutectic modification with the role of cooling rate (CR) and other time or temperature parameters related to the phenomena regardless the level of the grain refiner and modifier added. The reference liquidus temperatures were calculated using Thermo-calc TCAl2 database and are reported in Table 3.1.

3.1.2. Synthetic Al-6.5Si-1Fe alloys

The synthetic alloy was prepared by Hydro Aluminium Deutschland GmBH from high purity metals and the samples were then prepared into 10 mm rod by hot extrusion, as seen in Figure 3.1. The alloy contains 6.5Si and 1Fe and its chemical composition analysis is provided in **Appendix 1.**

Figure 3.1. Rod of as received synthetic Al6.5Si1Fe alloy

3.2. Experiments

3.2.1. Thermal Analysis

Thermal analysis became widespread technique for evaluating melt preparation of aluminum alloys in the 1980's [1, 2]. Basically, thermal analysis is performed by pouring the molten metal into a cup equipped with a thermocouple to record the temperature changes against the time. The solidification reactions occurring during the process are detected as changes in thermal profile of the curve. The cooling rate is only controlled by the heat loss by the cup wall to the surrounding environment. Several parameters have been proposed in the literature for characterizing the thermal effects seen on the cooling curves which are associated to nucleation and growth of (Al) phase (grain refinement) and to the (Al)-Si eutectic (eutectic modification) [3-8]. Development of computer aided cooling curve analysis also extended the use of the thermal analysis with the capability to detect minor reaction through the use of cooling curve first derivative [9]. For quaternary alloy or commercial alloy the solidification process continues after the (Al)-Si eutectic until the final reaction where secondary precipitation such as phi phase, Al_2Cu and/or Mg_2Si occurs. With high cooling

rates, the thermal arrest associated with secondary reaction is difficult to detect. Therefore, extrapolation from the final solidification reaction is used to track the end of eutectic plateau.

Grain size prediction in cooling curve thermal analysis is usually linked with undercooling and recalescence during the nucleation phenomena, where no or lack of recalescence indicates a good nucleation which leads to fine grain size assessment [8].

Thermal analysis can also be used to predict the modification level of the alloys by analyzing the cooling and the eutectic temperature depression. Other than temperature parameters, time parameters can be used to characterize the cooling curves, see section 3.2.3.

3.2.2. Instrumented casting

Cooling curve analysis was performed on a series of A356 alloys with chemical composition listed in Table 3.1. Most of the grain size predictions in the cast house are made by using standard thermal analysis cup (quick cup) with very low thermal coefficient, in which the cooling rate is controlled at low or moderate value. However, in real castings, the shape of the casting components varies and this could induce different cooling rates across the part affecting the final grain size and modification of the materials. Therefore, experimental castings were prepared to study the effect of cooling rate.

The cooling curves were recorded using Thermolan®-Al system. The experimental procedure consisted in casting the liquid alloys into sand and metallic moulds with different casting modulus (ratio of outer surface to volume) according to the schematic in Figure 3.2. These moulds were designed for casting cylindrical samples with various thermal moduli (TM) through variation in h = ∅. The TM values and the cooling rates achieved are listed in Table 3.2.

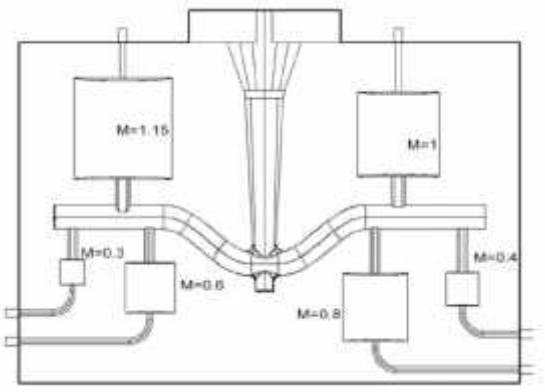

Figure 3.2. Schematic of the mould used showing six cylinders with different thermal moduli.

At the time of casting, a standard cup for thermal analysis (TA) with TM=0.605 cm was also poured and its cooling curve was recorded along with that of other moduli. Type K thermocouple was used in this experiment with temperature error from -0.9 to 1.1 °C.

Table 3.2. Thermal moduli (TM) and ranges of eutectic cooling rate (CR_e) of cylinder test samples.

Sand mould	TM (cm)	1.5	1.15	1	0.8	0.6	0.4	-
	CR_e (°C/s)	0.13-0.20	0.17-0.32	0.21-0.39	0.28-0.72	0.65-1.1	2.4-2.9	-
Metallic mould	TM (cm)	-	1.15	1	0.8	0.6	0.4	0.3
	CR_e (°C/s)	-	1.5-2.8	2.6-3.0	3.5-5.6	4.7-6.5	9.4-12.5	9.9-18.1

3.2.3. Cooling curve analysis

The characteristic parameters obtained from the cooling curves were extracted according to the nomenclature shown in Figure 3.3. All values are listed in **Appendix 2**.

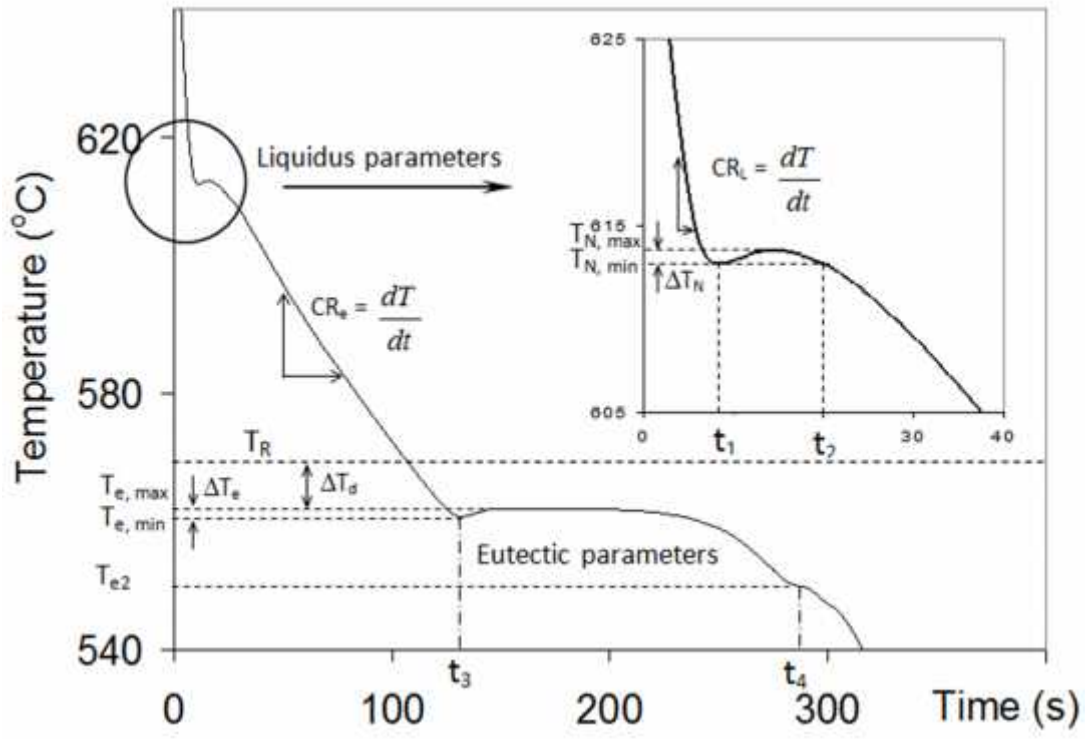

Figure 3.3. Parameters taken from cooling curves for characterizing primary (Al) precipitation and (Al)-Si eutectic. Insert image showed enlarged area of liquidus.

Not all the data from the series was used in the calculation because some of the cooling curves could not be recorded due to thermocouple failure. Moreover, high cooling rate for small modulus is causing a fast heat release by the mould and large time gap interval for thermocouple data acquisition. Thus, the initial solidification temperature of the small cylinders could not be recorded properly. Some parameters related to the whole solidification process were selected to check for the overall reproducibility of the data records. Finally,

some of the data when the initial temperature was less than 620°C were excluded from further analysis. The cooling curve parameters considered in present work are defined as follows:

- For the nucleation of (Al), parameters related to temperature: minimum temperature ($T_{N,min}$), maximum temperature ($T_{N,max}$) and recalescence ($\Delta T_{N=}$ $T_{N,max}$ - $T_{N,min}$), as seen in Figure 3.3. In the case of no nucleation recalescence, the $T_{N,max}$ was obtained from the maximum value of the first derivative of the cooling curve, as seen in Figure 3.4.
- total nucleation time (Δt_N) was measured from the primary (Al) nucleation time start (t_1) to the extrapolation time (t_2)
- V_{max} recalescence was acquired from the maximum value of the first derivative of the cooling curve.
- Absolute nucleation undercooling was obtained from temperature difference between calculated liquidus (T_{liq}) and maximum nucleation temperature, max ($T_{N,max}$).
- Liquid cooling rate (CR_L) was acquired from the slope of the cooling curve (625°C - 620°C) before the primary (Al) nucleation reaction ($T_{N,min}$).
- Eutectic cooling rate (CR_e) was measured from the slope of the cooling curve (600°C to 575°C) after primary (Al) nucleation and prior to the (Al)-Si eutectic reaction.
- t_{coales} was measured from the primary (Al) nucleation start (t_1) to (Al)-Si eutectic start (t_3). In the case of no recalescence, the time was evaluated between the maximum values of the first derivative of the cooling curve, see Figure 3.4.
- t_f was measured from the primary nucleation time start (t_1) to the final solidification reaction (t_4).
- For the eutectic reaction, parameter related to temperature: minimum eutectic temperature ($T_{e,min}$), maximum eutectic temperature ($T_{e,max}$) and the recalescence (ΔT_e= $T_{e,max}$ - $T_{e,min}$). In the case of no eutectic recalescence, the $T_{e,max}$ was obtained from the maximum value of the first derivative of the cooling curve, as seen in Figure 3.4.
- t_{eut} (eutectic time) was measured from the (Al)-Si eutectic start (t_3) to the final solidification reaction (t_4).
- ΔT_d = T_R - $T_{e,max}$, is the eutectic depression, where T_R is the equilibrium eutectic temperature calculated using an equation obtained by updating the one proposed by Mondolfo (**Appendix 3**).

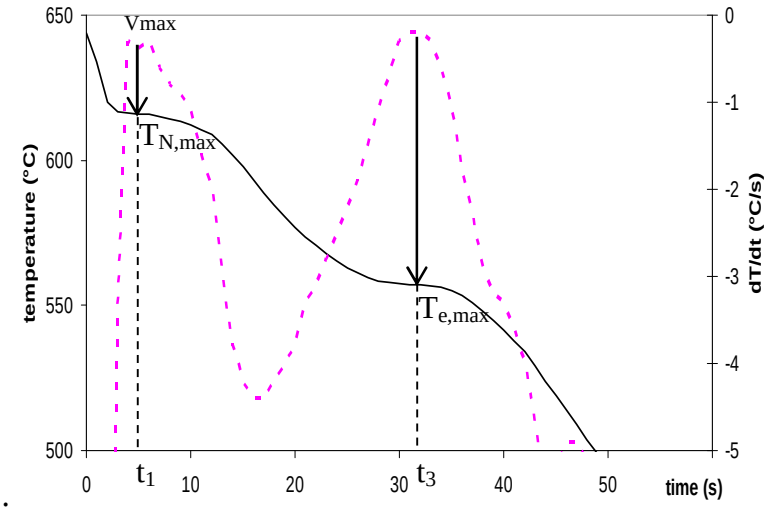

Figure 3.4. Method to extract the characteristic $T_{N,max}$ and $T_{e,max}$ from the cooling curve when no recalescence shows up.

3.2.3. Eutectic reference temperature

Concerning eutectic modification, as already stated before the most used method is to correlate the effectiveness of modification with increased eutectic undercooling or eutectic depression. Evaluation of this undercooling requires the knowledge of a eutectic reference temperature which should be given by the relevant phase diagram and has often been evaluated experimentally as the eutectic temperature of the unmodified alloy. However, in many cases, this latter cannot be obtained in a cast shop due the possibility of prior modification treatment to the alloys or the use of returns in the charge.

One of the most used methods to evaluate the reference temperature of the (Al)-Si eutectic was proposed by Apelian et al. [5] who derived an equation expressing the eutectic temperature as a function of alloy's composition from ternary phase diagrams compiled by Mondolfo [10]. The so-called “Mondolfo’s equation” is still widely accepted as seen in the recent work by Wang and Lu [11]. In this work, we first reconsider the derivation of the equation and then update it according to more recent assessed phase diagram information **(Appendix 3).**

There are several other approaches proposed to calculate the reference eutectic temperature. Study by Joenoes and Gruzleski [12] focused on the magnesium effect and proposed a series of empirical calculations with a coefficient depending on the Si content in the alloys. While those equations only consider one element in the calculation and are limited to one type of chemical composition, Sthuldreier et al. [13] considered 3 major elements, Mg, Cu and Fe, based on their experimental data. A different approach was used by Djurdjevic and collaborators [14, 15] who described the (Al) liquidus with second order polynomial for

binary Al-X systems of interest and then defined a silicon equivalent (Si_{eq}) for each element X. We then review other approaches proposed in the literature and finally compare them to available experimental data from literature. Detailed work can be seen **Appendix 3**.

3.3 Differential thermal analysis

Differential thermal analysis (DTA) has been used for analysing phase transitions in alloys based on their thermal behaviour during heating or cooling process. The DTA method works by detecting the heat release, or more generally any change in Cp due to a reaction event in a sample as compared to an inert reference. This phase change, whether exothermic or endothermic, is recorded as a thermal arrest and may be associated to the temperature when the change occurred. A flow of argon gas is ensured during the process to prevent oxidation. Compared to conventional thermal analysis, DTA has the advantages of higher sensitivity, controlled atmosphere and constant scanning rate.

DTA development can be seen as early as 1887 [16]. Further use of DTA method can be found in Pope and Judd [17] and Wendlandt [18]. A monogram released by National Institute of Standards and Technology (NIST)-USA authored by Boetinger et al. [19] provides guide lines for DTA experiments and result analysis and their relation to phase diagram. By using a series of compositions and cooling rates from the same alloy system, the liquidus and solidus temperatures can be determined and produce the phase diagram, as seen in Figure 3.5. In most cases, the heating scans were used for determining the liquidus and solidus of an alloy to avoid the undercooling effect of solidification (compare Figures 3.5a and b)

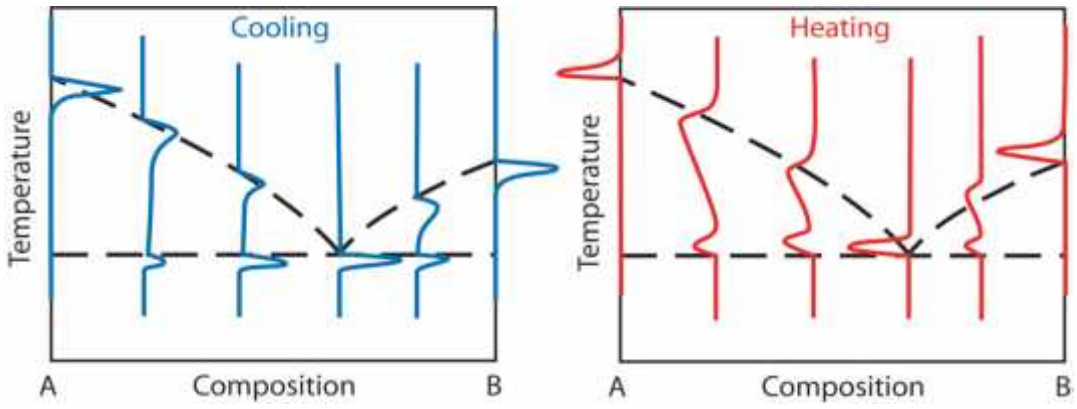

Figure 3.5. Schematic DTA thermograms and correlation with the phase diagram of a binary alloy [19].

A typical DTA thermogram and its relation with sample and reference temperatures are illustrated in Figure 3.6. The application of DTA in the solidification study of Al alloys

can be seen in Chen and co-worker [20, 21]. Martinez et al. [22] also used DTA for studying the effect of strontium in the case of A 319 alloys. The results showed that it does not affect the solidification of primary (Al), however it modifies the kinetics of (Al)-Si eutectic. Opposite result is reported by Chen and Zhang [23] who described the effect of strontium and of cooling rate upon the liquidus temperature and eutectic depression of A 357 alloys.

The determination of the start of a phase change or thermal arrest is sometimes difficult, especially if the phase transformation starts with a slow heat release or absorption. Therefore, in some cases use has been made of intersection method between the baseline and curve slope to determine the temperature of the reaction start. However, this method sometimes offsets the actual value of the reaction due to the influence of alloy type especially with different scanning rates.

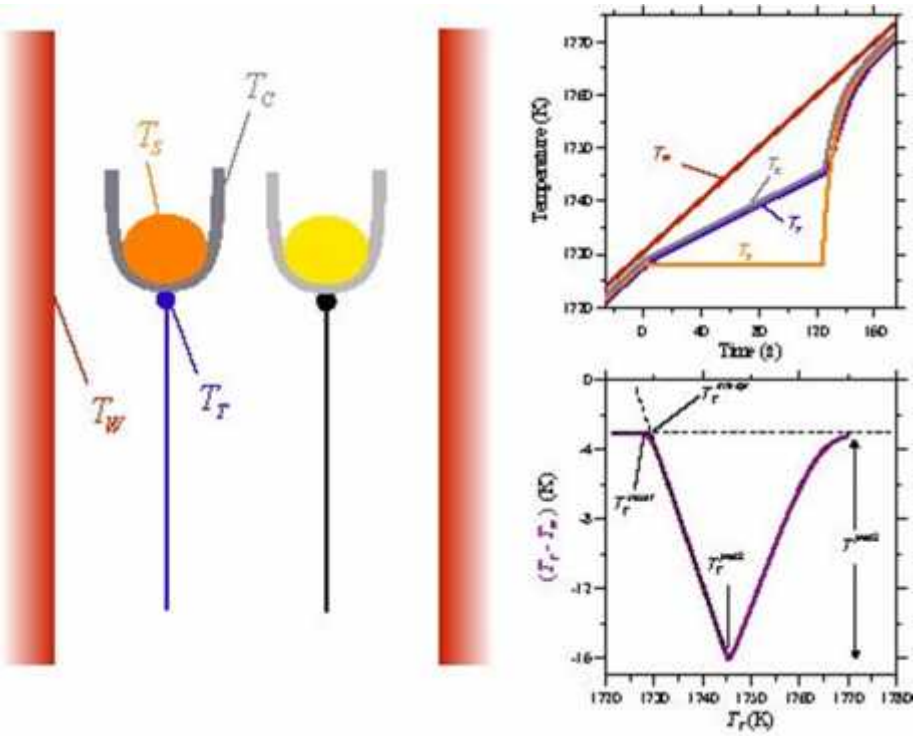

Figure 3.6. A typical DTA thermogram and schematic relation between sample and reference temperatures [19].

SETARAM-SETSYS 16/18 series illustrated in Figure 3.7 was used to study the morphology changes induced by cooling rate. The system can be used from ambient temperature to 1650°C and is also equipped with vacuum system for atmosphere control. In order to study the effect of cooling rate, the samples were machined into approximately 3.9 mm in diameter and 5 mm in height, then cleaned in a ultrasonic bath in acetone and finally

weighted before being subjected to DTA. The sample was put inside the alumina crucible and high purity alumina powder was used as reference. Prior to data acquisition, the furnace was purged with argon to minimize the atmosphere contamination and then, a steady low argon flux was used during the experiment.

Figure 3.7. DTA apparatus and tricouple type S sensor cell type used in the experiment

DTA experiments were performed with various heating and cooling rates for different experiments. From DTA thermogram, characteristic temperatures were extracted. These characteristic temperatures were associated with the phase transformations occurring during the heating and cooling processes and showed as peaks or thermal arrests. For the cooling curve, both the start or onset of thermal arrest and the peak temperature were utilized, and for the heating curve only the peak temperature was used due to difficulties in determining the onset of melting of beta phase and primary (Al) in ternary AlFeSi and commercial alloys. Figure 3.8 shows typical DTA thermogram of heating and cooling curve of Al6.5Si1Fe. The explanation for thermal arrest point associated with heating curve and cooling curve seen in Figure 3.8, as follow:

1. Cooling curve
    a. Primary (Al) start
    b. Primary (Al) peak
    c. Beta Phase start
    d. Beta Phase peak
    e. Eutectic (Al)-Si start
    f. Eutectic (Al)-Si peak

2. Heating curve
    x. Eutectic (Al)-Si melting peak
    y. Dissolution of beta phase
    z. End of fusion, (Al) liquidus

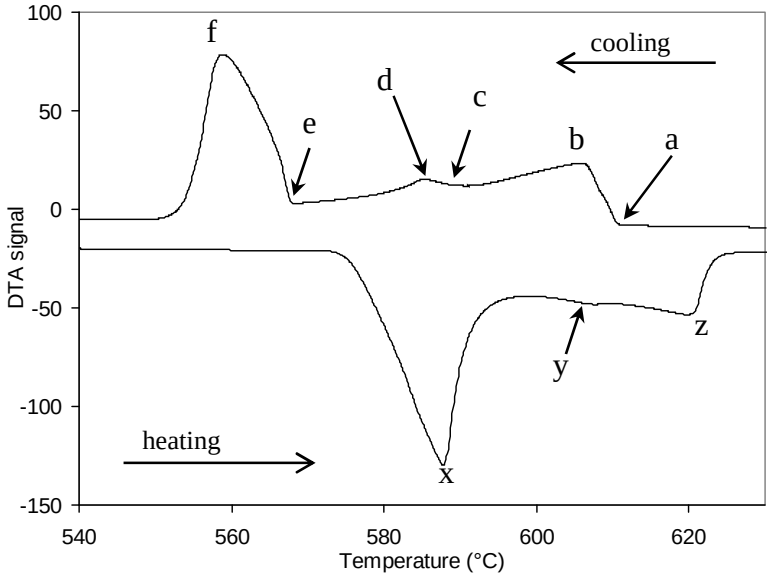

Figure 3.8 DTA thermograms recorded upon cooling and heating at 2°C/min scanning rate (the graphs were adjusted along the y axis to separate the curves)

3.3.1. DTA calibration

DTA calibration of the cell was performed by conducting series of heatings on a reference material with known melting temperature. The reference material should be a single element in high purity condition, to avoid any thermal arrest reading other than the liquidus melting point. The characteristic temperatures from the heating thermograms are then extrapolated to zero scanning rate for pin point the corresponding temperature. Therefore, the calibration method used is indirect where the temperature difference between the extrapolated temperature and the known temperature of the reference material is the value that should be used to correct to the actual experimental data.

We conducted the calibration by using Al of high purity grade. The sample was heated with the scanning rate of 1, 2 and 5^{o}C/min. The zero scanning rate extrapolation of heating rate square root showed the melting temperature at 655°C, thus the temperature was approximately 5°C lower than the melting point of pure Al at 660°C as seen in Figure 3.9.

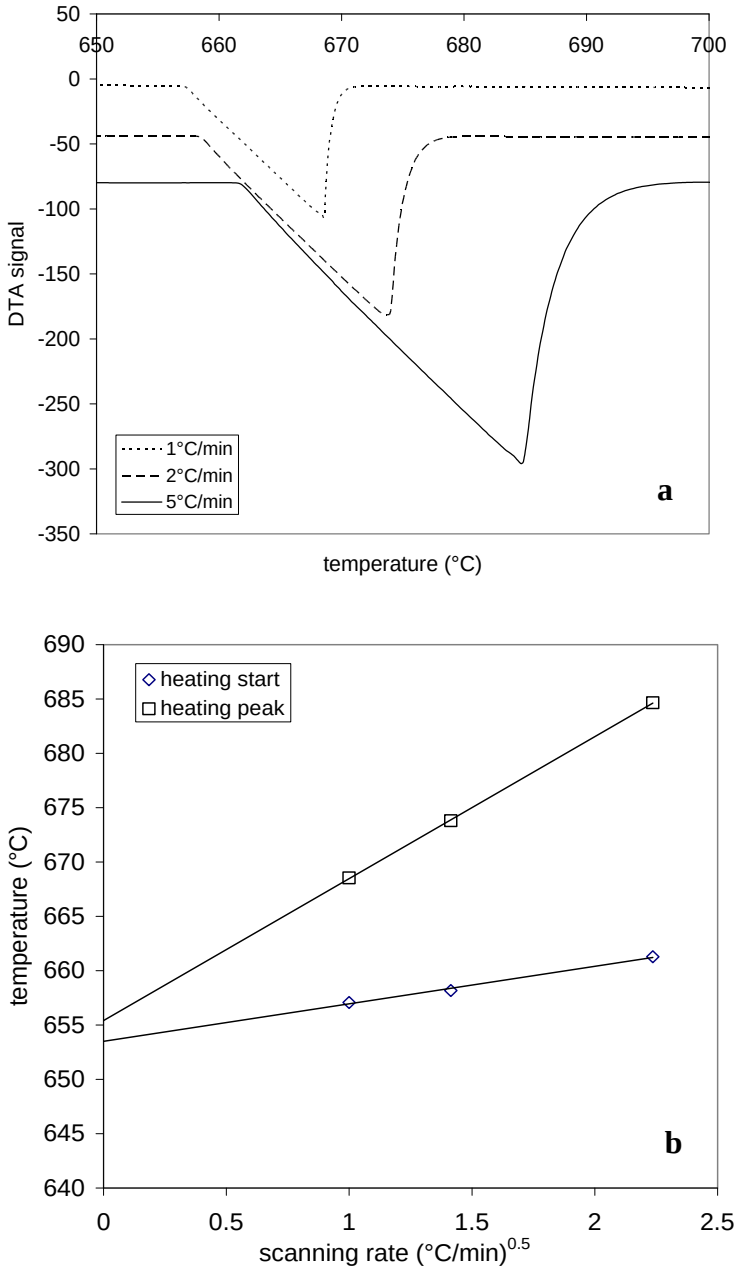

Figure. 3.9. DTA thermograms of high purity Al with the graphs adjusted along the y axis to separate the curves (a) and characteristic temperatures versus square root of the heating rate (b).

3.4. Microstructure characterization

3.4.1. Optical microscopy

Samples are prepared according to standard metallographic preparation after mounting in thermoset resin. Mechanical abrasion upon rotating grinding machine (Buehler Metaserv) with abrasive SiC paper started from size 180, 320, 600, 1000, 1200, 2400 and 4000 mesh. The samples are then polished with diamond paste of 3 µm and followed with 1 µm using Struers Tegra-Pol 21. The polishing step was finalized with OPS solution of 0.05 micron. Between each polishing step, the samples are rinsed with distilled water. Due to the corrosive

attack by OPS, the samples are rinsed with ethanol as soon as possible after the polishing to remove excess solution. The ultrasonic bath in ethanol for about 1 minute is used to remove any potential particle attached and is followed by drying with hot air before any observation under optical microscope. Enough contrast between the intermetallic phase and eutectic silicon makes no etching necessary for optical microscopy that is performed with a Nikon MA200 and a Olympus. The microscopes are connected to image capture software for digital image acquisition. Detail micrograph of some images can be seen in **Appendix 4.**

Deep etching is performed with a 10% HCl solution for 30 – 40 minutes. The acid dissolves most of the eutectic (Al) and leaves the eutectic silicon and intermetallic phase in the interdendritic region. Afterward, the sample was subjected to SEM for 3D morphology observation.

3.4.2. Scanning electron microscope (SEM)

The samples were prepared in the same way as for optical microscopy. For the examination, scanning electron microscope (SEM) LEO 435VP is utilized. The equipment is equipped with an energy dispersive spectrometer (EDS) detector for chemical composition micro-analysis. The sample stage has 5 axis motorized control with tilt angle of 0 to 90° and rotation of 360° (continuous). The VP extension stands for variable pressure which enables the SEM to vary the pressure inside the sample chamber and could accommodate for less conductive materials to be examined. The minimum working distance allowable is 10 mm, to be handled with care to avoid contact with the objective lens or electron back scattered detector. As for EDX detector, the optimum distance was 19 mm due to the distance and position of the detector. For more detail about micro-chemical analysis, a few additional tests were conducted using electron probe micro-analyzer (EPMA) which was performed at Observatoire Midi-Pyrénées.

3.4.3. Electron Back Scatter Diffraction (EBSD)

EBSD principle is based on the electron diffraction (Kikuchi band) pattern of secondary electron beam which allows characterizing the crystal structure and orientation of the observed sample region. For obtaining the pattern, the sample should be tilted at 70° from its horizontal axis. In preparation for EBSD, we should care regarding the effect of residual stresses on the sample surface. High stresses upon the surface would give difficulty for phase identification. Therefore, minimum force during sample preparation should be applied. The samples were prepared as follows:

1. Polishing using SiC paper 4000, 150 tr/min, under force of 10 N for 10 min.
2. Polishing with 3 micron diamond paste, 150 tr/min, under force of 10 N for 10 min.
3. Polishing cloth DP-Dur with OPS, 150 tr /min, under force of 10 N for 10 min.
4. Polishing cloth MD Nap with OPS, 150 tr /min, under force of 10 N for 5 min.

3.4.5. Image Analysis

Image analysis was performed using the ImageJ software (National Institute of Health –USA) and Aphelion^{TM} Dev software (ADCIS, France). The software programs were used to treat the SEM images and tomography images for beta phase characterization and analysis. Series of operations such as median filtering, thresholding were used to separate the beta phase from the Al matrix and calculate the average volume fraction and length of beta phase from various samples. The image software programs were also used to reconstruct 3D image from tomography experiment and perform calculation and image treatments.

3.4.6. Tomography

X-ray radiography imaging of material structure is widely used in industrial applications. Nevertheless, early utilization as a 3D image tool was carried out in medical imaging applications. X-ray tomographs utilize 2D slice radiographic image and generate 3D images which based on the work of Radon [24]. Tomographs in material science nowadays are used as a non-destructive method to visualize internal structure of an object and acquire information of their three dimensional geometries and properties [25-31]. In tomography, the sample is rotated around a single axis with small angle step while a series of 2D images is acquired, the images being then reconstructed numerically into a 3D image or series of slide image.

For the past 10 years the development of in situ tomograph for the study of solidification phenomena has increased significantly. This is due to the utilization of fast cameras to record the image which facilitates the observation of in situ solidification process [32]. The used of in situ method with X-ray can be seen in the work by Mathiesen et al. [33, 34] who studied the dendrite growth phenomena, growth dynamic and columnar – equiaxed transition. Kim et al. [35] studied the effect of iron on Al-Si-Cu alloy with radiography. Schenk et al. [36] also utilized the synchrotron to study direction solidification of aluminum alloy and analyze columnar to equiaxed transition. Furthermore, the in-situ experiment method developed at ESRF and SiMaP-Grenoble is allowing 3D imaging by rotating the sample during in-situ solidification process [37-41].

Early work on beta phase observation using in situ X-ray tomography and in situ synchrotron to study its growth morphology can be seen in the work by Wang et al. [42] and Terzi et al. [43]. Observation by Wang et al. [42] proposed several stages in beta growth: i). a rapid growth in early stage of beta phase precipitation which is later constrained by primary aluminum dendrite; ii) followed by attachment and diffusion growth where the plates thicken in later stage. Terzi et al. [43] study showed the beta phase nucleated at or near of the outer skin surface after primary aluminum nucleation, where the outer surface consists most probably in γ-Al_2O_3. The plates also display very rapid lateral growth and slow thickening. They also found that some eutectic silicon attached to a β-$Al_9Fe_2Si_2$ plate or outer oxide when they first appear. Both of this early works was performed to quaternary alloy Al-Si-Cu-Fe with a sample size of 1.5 mm in diameter and 3.2 mm long.

In the present work, two types of tomography, post-mortem and in-situ experiments were conducted for studying the microstructure and growth of beta phase. Post-mortem tomography experiments were carried out by using a GE Phoenix Nanotom equipped with a 180 kV/15W X-ray tube (Fermat – CIRIMAT). A monochromatic beam was transmitted and produced 1440 images as the specimen was rotated for 360° around its vertical axis (2.5 μm/voxel). An image stack of the volume was then constructed using Datos X (GE Sensing and Inspection GmbH) and VG Studio Max (Volume Graphic GmbH, Germany).

In-situ synchrotron tomography was conducted at European Synchrotron Radiation Facility (ESRF) line ID-19, with the holding furnace prepared by SiMaP, Grenoble. The sample was prepared as a cylinder with 1 mm in diameter and 3 mm in height. In the bottom, a 0.55 mm hole was drilled for inserting a thermocouple. A pink beam of 17.6 KeV with 700 projections was used with scan time of 0.75 sec resulting in a total of 36 tomographies (1.1 μm/voxel).

One of the basic differences between these methods is the X-ray source and beam characteristics, as seen in Figure 3.10. Laboratory tomography uses a single source which diverges into cone beam shape. In the case of post mortem, the energy emitted is also smaller, therefore to acquire a better resolution the sample should be located as close as possible to the beam source. While in synchrotron tomography, the beam is parallel and monochromatic which increase the spatial resolution without image magnification effect.

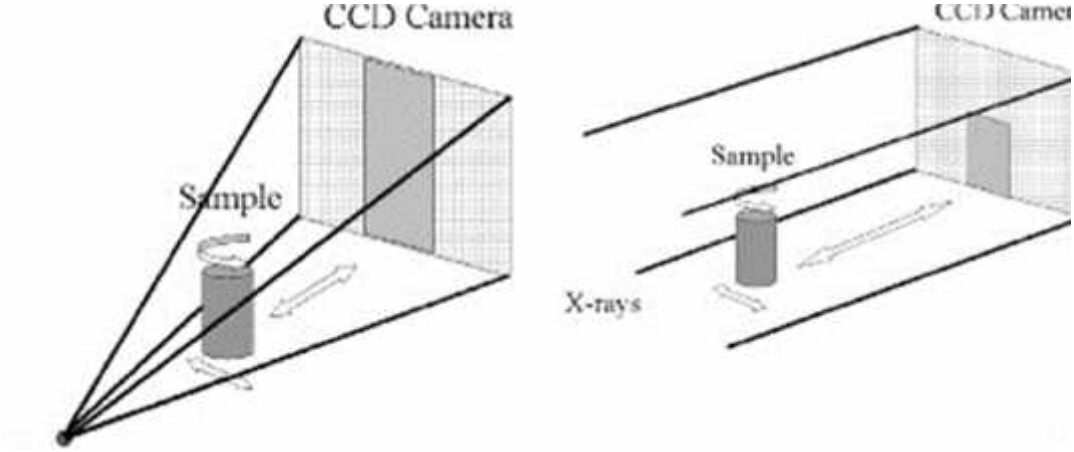

Figure 3.10. Schematic of the X-ray beams for tomography experiment s(a) post mortem, (b) synchrotron. [29]

In third generation synchrotron, based from the information provided by ESRF [44], the X-ray beam is emitted from the changing direction of high speed electrons which moves around in a storage ring circle. First, the electrons are produced in electron gun (Linac) and send to booster synchrotron which accelerates the electrons before injected into the storage ring. The beam is then directed to the beamline for the experiments, where each beamline have a specific ID number for different type of techniques and researches. For in-situ solidification experiments, the sample is mounted on alumina rod tip which rotates. The X-ray beam through the sample inside the furnace and CCD camera (FReLoN camera) record the transmitted X-ray beam. The apparatus set-up for the experiment used in this work can be seen in Figure 3.11.

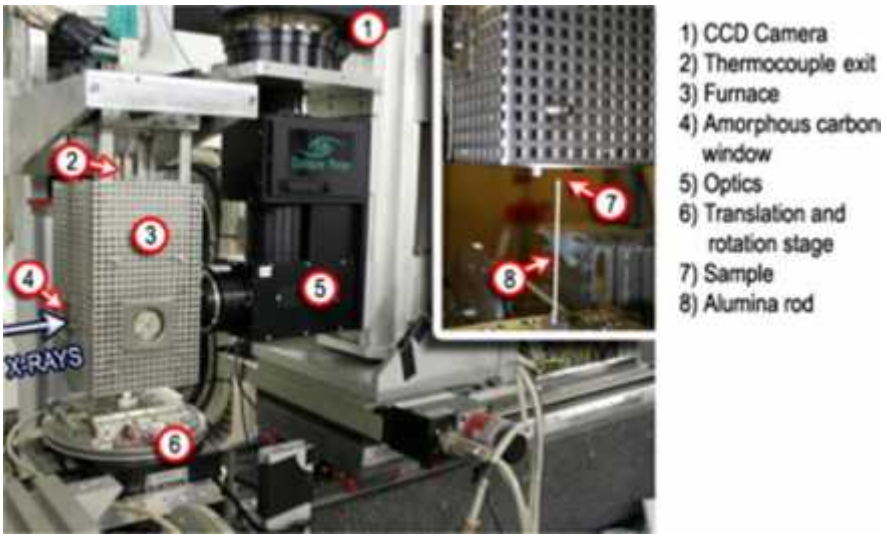

Figure. 3.11. Tomography experiment set up with holding furnace at ESRF ID-19 [37]

Reference.

1. B.L Tuttle: Proc. AFS/CMI Conf., Rosemont, IL, USA, December 1984, AFS, 1-37.
2. J. Morice and R. Portalier: Proc. AFS/CMI Conf., Rosemont, IL, USA, December 1984, AFS, 37-76.
3. L. Backerud, G. Chai and J. Tamminen: Solidification characteristics of Aluminum alloys, Vol.2, AFS/Skanaluminium, Des Plaines, Illinois, 1990.
4. S. Gowri, Comparison of thermal analysis Parameters of 356 and 359 alloy, AFS trans., 102, (1994), 503-508.
5. D. Apelian, G.K. Sigworth, K.R. Whaler, Assessment of grain refinement and modification of Al-Si foundry alloys by thermal analysis, AFS Trans., 92, (1984), 297-307.
6. G.K. Sigworth, Theoretical and practical aspects of the modification of Al-Si alloys, AFS Trans., 91, (1983), 7-16.
7. J.E. Gruzleski, B.M. Closset: The treatment of liquid aluminum-silicon alloys, AFS Inc., Des Plaines, Illinois, 1990.
8. J. Charbonnier, Microprocessor assisted thermal analysis testing of aluminum alloy structure, AFS Trans., 92, (1984), 907-921.
9. N. Tenekedjiev, H. Mulazimoglu, B. Closset, J.E. Gruzleski, Microstructural and thermal analysis of strontium treated aluminum silicon allous, AFS Inc., Des Plaines, Illinois, 1995.
10. L.F. Mondolfo, Aluminium alloys, structure and properties, Butterworths, London (1976).
11. R.Y. Wang, W. Lu, Spheroidization of eutectic silicon in direct-electrolytic Al-Si Alloy, Metall. Mater. Trans. A, 44A, (2013), 2799-2809.
12. A.T. Joenoes and J.E. Gruzleski, Magnesium effects on the microstructure of unmodified and modified Al-Si alloys, Cast met., 4, (1991), 62-72.
13. G. Stuhldreier, E. Mettingen, K.W. Stoffregen, Erfahrungen mit thermischen analyse von G-AlSi-legierungen, Giesserei, 68, (1981), 404-409.
14. F.C. Robles Hernandez, M.B. Djurdjevic, W.T. Kierkus, J.H. Sokolowski, Calculation of the liquidus temperature for hypo and hypereutectic aluminum silicon alloys, Mater. Sci. Eng., A. 396, (2005), 271–276.
15. M.B. Djurdjevic, Thermal description of hypoeutectic Al-Si-Cu alloys using silicon equivalency, Military Technical Courier, 60, (2012), 152-168.
16. H. Le Chatelier, De l'action de la chaleur sur les argiles, Bulletin de la Société Française de Minéralogie, 10, (1887), 204-211.
17. M.I. Pope, M.D. Jude, Differential thermal analysis, Heyden, London, 1980.
18. W.W. Wendlandt, Thermal Analysis, 3rd ed., John Wiley & Sons, Inc., New York, 1986.
19. W.J. Boettinger, U.R. Kattner; K.W. Moon, J. Perepezko, NIST recommended practice guide: DTA and Heat-Flux DSC measurements of alloy melting and Ffeezing, Special Publication 960-15, 2006.

20. S.W. Chen, C.C. Huang, J.C. Lin, The relationship between the peak shape of a DTA curve and the shape of a phase diagram, Chemical engineering science, 50, (1995), 417-431.

21. S.W. Chen, S. C. Jeng, Determination of solidification curve of commercial aluminum alloy, Metallurgical and Materials Transactions A, 27A (1996), 2722-2726.

22. E.J. Martinez. D, M.A. Cisneros G., D. Valtierra, J. Lacaze, Effect of strontium and cooling rate upon eutectic temperatures of A319 aluminum alloy, Scripta Materialia, 5 (2004), 439-443.

23. Z. Chen, R. Zhang, Effect of strontium on primary dendrite and eutectic temperature of A357 aluminum alloy, China Foundry, 7, (2010), 149.

24. J. Radon (1917) Translated as On determining functions from their integral values along certain manifolds by P.C. Parks in IEEE Transactions in Medical Imaging 5, (1986), 170-176.

25. L.Salvo, P. Cloetens, E. Maire, S. Zabler, J.J. Blandin, J.Y. Buffiere, W. Ludwig, E. Boller, D. Bellet, C. Josseron, X-ray micro-tomography an attractive characterisation technique in material science, Nuclear Instrument and Methods in Physical Research B, 200, (2003), 273-286.

26. E. Maire, J.Y. Buffiere, L. Salvo, J.J. Blandin, W. Ludwig, J.M. Letang, On the application of X-ray microtomography in the field of material science, Advance Engineering Materials, 3, (2001), 539-546.

27. C. Puncreobutr, P.D. Lee, R.W. Hamilton, B. Cai, T. Connolley, Synchrotron tomographic characterization of damage evolution during aluminum alloy solidification, Metallurgical and Materials Transactions A, 44, (2012), 5389-5395.

28. C. Puncreobutr, P.D. Lee, R.W. Hamilton, A.B. Phillion, Quantitative 3D characterization of solidification structure and defect evolution in Al alloys, JOM, 64, (2012), 89-95.

29. L. Salvo, P. Cloetens, E. Maire, S. Zabler, J.J. Blandin, J.Y. Buffiere, W. Ludwig, E. Boller, D. Bellet, C. Josseron, X-ray micro-tomography an attractive characterisation technique in material science, Nuclear Instrument and Methods in Physical Research B, 200, (2003), 273-286.

30. E. Maire, J.Y. Buffiere, L. Salvo, J.J. Blandin, W. Ludwig, J.M. Letang, On the application of X-ray microtomography in the field of material science, Advance Engineering Materials, 3, (2001), 539-546.

31. J. Kastner, B. Harrer, H.P. Degischer, High resolution cone beam x-ray computed tomography of 3D-microstructure of cast Al-alloys, Material Characterization, 2, (2011), 99-107.

32. O. Ludwig, M. Dimichiel, L. Salvo, M. Suéry, P. Falus, In-situ three-dimensional microstructure investigation of solidification of an Al-Cu alloy by ultrafast x-ray microtomography, Metallurgical and Materials Transactions A, 36A, (2005), 1515-1523.

33. R.H. Mathiesen, L. Arnberg, H. Nguyen-Thi, B. Billia, In situ X-ray video microscopy as a tool in solidification science, JOM, 64, (2012), 76-82.

34. R.H. Mathiesen, L. Arnberg, The real-time, high-resolution x-ray video microscopy of solidification in aluminum alloys, JOM, 59, (2007), 20-26.

35. B. Kim, S. Lee, S. Lee, H. Yasuda, Real-time radiographic observation of solidification behavior of Al-Si-Cu casting alloys with the variation of iron content, Material Transaction, 53, (2012), 374-379.

36. T. Schenk, H. Nguyen Thi, J. Gastaldi, G. Reinhart, V. Cristiglio, N. Mangelinck-Noel, H. Klein, J. Hartwig, B. Grushko, B. Billia, J. Barachel, Application of synchrotron x-ray imaging to the study of directional solidification of aluminium-based alloys, Journal of Crystal Growth, 275, (2005), 201-208.

37. S. Terzi, L. Salvo, M. Suéry, A.K. Dahle, E. Boller, Coarsening mechanisms in a dendritic Al–10% Cu alloy, Acta Materialia, 58, (2010), 20-30.

38. S. Terzi, E. Boller, L. Salvo, M. Suéry, In situ x-ray microtomography study of the solidification and remelted microstructures of Al-Cu alloys, International Journal of Cast Metals Research, 22, (2009), 275-278.

39. N. Limodin, L. Salvo, E. Boller, M. Suéry, M. Felberbaum, S. Gailliegue, K. Madi, In situ and real time 3-D microtomography investigation of dendrite solidification in an Al-10 wt.% Cu alloy, Acta Materialia, 57, (2009), 2300-2310.

40. S. Terzi, E. Boller, L. Salvo, M. Suéry, In situ x-ray microtomography study of the solidification and remelted microstructures of Al-Cu alloys, International Journal of Cast Metals Research, 22, (2009), 275-278.

41. D. Tolnai, P. Townsend, G. Requena, L. Salvo, J. Lendvai, H.P. Degischer, In situ synchrotron tomographic investigation of the solidification of an AlMg4.7Si8 alloy, Acta Materialia, 60 (2012), 2568-2577.

42. J. Wang, P.D Lee, R.W Hamilton, M. Li and J. Allison, The kinetics of Fe-rich intermetallic formation in Aluminum alloys / In situ observation, Scripta Materialia, 60, (2009), 516-519.

43. S. Terzi, J.A. Taylor, Y.H. Cho, L. Salvo, M. Suéry, E. Boller, A.K. Dahle, Insitu study of nucleation and growth of the irregular α-Al/β Al_5FeSi eutectic by 3D synchrotron X-ray microtomography, Acta Materialia , 58, (2010), 5370-5380.

44. ESRF website, available in http://www.esrf.eu/home.html, accessed in 24 March 2014.

4. Study of the effect of cooling rate on grain size and eutectic modification in A356 aluminum alloys

In this chapter, the effect of cooling rate on grain size and eutectic silicon modification is studied for industrial alloy A356. Temperature and time records are analyzed for characterizing and predicting refinement and modification effectiveness. An assessment was performed on a series of A356 samples with different grain refinement levels and casting moduli for achieving different cooling rates. The assessment is focused on the role of cooling rate (CR) and other parameters extracted from cooling curves related to grain nucleation regardless the level of grain refinement. The reference liquidus temperatures was obtained from calculation using TCAL2 database [1] which was used to evaluate the absolute nucleation undercooling. Furthermore, another assessment was performed on eutectic modification with strontium varying between 0.003-0.013 wt% and one sample modified with Na. The assessment focused on the eutectic depression and the role of cooling rate (CR) and other time or temperature parameters related to the eutectic modification phenomena regardless the level of the modifier element. In addition, DTA studies were also used to study the solidification reaction and the effect of strontium on the eutectic temperature depression.

4.1 Solidification reaction analysis: DTA

Typical solidification sequence for A356 alloy can be referred to previous work reported by Mackay et al. [2] and Bäkerud et al. [3]. Characteristic temperatures observed during solidification are listed in Table 4.1. Normally, the presence of iron is causing the formation of iron rich intermetallics. In alloy of A356, the iron content is usually quite small, therefore the formation of beta phase occurs with or after the (Al)-Si eutectic reaction as indicated in the solidification sequence reported by Bäkerud et al. [3]. Solidification ends with precipitation of Mg_2Si [2] or both Mg_2Si and π-phase [3].

Closset and Gruzleski [4] reported that the formation of π-phase occurs before that of Mg_2Si, this based on the volume fraction of the π-phase which is higher compared to Mg_2Si. Liu et al. [5] studied the formation of intermetallic in 6XXX alloy series and stated also the formation of π-phase occurs before the Mg_2Si reaction. They also reported the formation of Mg_2Si is through two-phase eutectic and three-phase eutectic reactions. However, Wang and Davidson [6] compared DSC records of as cast and heat treated Al-Si-Mg alloy and showed the disappearance of the lowest temperature peak corresponds to the dissolution of π-phase during heat treatment. Therefore, we assume the π-phase appears in the last reaction of the solidification sequence.

Table. 4.1. Solidification of A356 alloys

Solidification Reaction	Suggested start temperature (°C)		Association to cooling curve (Figure 4.1a)
	Mackay et al. [1]	Backerud et al. [2]	
$L \rightarrow (Al)$ dendrites	612	610-615	1
$L \rightarrow (Al) + Si$ or	577	577	2
$L \rightarrow (Al) + Si + \beta\text{-}Al_5FeSi$	-	575	-
$L \rightarrow (Al) + Si + Mg_2Si$	555	555	3a
$L \rightarrow (Al) + Si + Mg_2Si + \pi\text{-}Al_8FeMg_3Si_6$	-	550-554	3b

Figure 4.1. presents the DTA thermograms recorded upon heating and cooling of commercial aluminum-silicon alloys A356 which has been grain refined and modified with Sr. The thermograms show successive reactions upon solidification: precipitation of (Al) dendrites (1), (Al)-Si eutectic (2) and final eutectic precipitation (3), which can be linked to the reactions in Table 4.1. The same reactions also occur during heating with the opposite sequence. Observation of the thermal arrests for the final eutectic reaction (Mg_2Si and π-phase) shows two solidification reactions at low scanning rate; however, as the scanning rate increases, the two peaks merge into a single peak. This happens due to the small temperature difference in the phase precipitation of final eutectic reactions during solidification. The thermograms also show that the characteristic temperatures are shifted as the scanning rate changes. The temperature shift is mainly caused by the thermal resistance in thermocouple measurement of DTA apparatus [7].

From the thermogram of cooling rate 2°C/min seen in Figure 4.2, we could see the primary aluminum dendrites start growing at 613°C, followed by the (Al)-Si eutectic at 566°C. The final eutectic reactions are observed at 549°C and 545°C which correspond to Mg_2Si and π-phase respectively. All the characteristic temperatures were adjusted to account for DTA calibration (added 5°C). In comparison to the value shown in Table 4.1, DTA results show a shifting of the temperature related to the (Al)-Si eutectic reaction. The shift is related to the undercooling and the effect of strontium as eutectic silicon modifier which will be discussed in later part of this chapter.

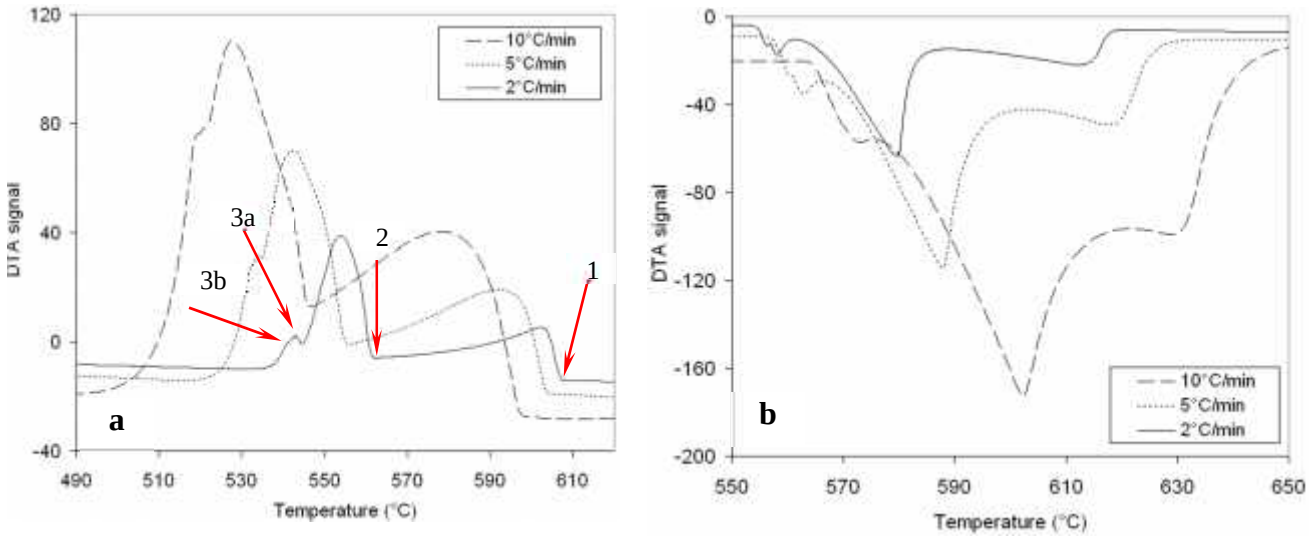

Figure 4.1. DTA thermograms recorded at different scanning rates (a) cooling, (b) heating (the graphs were adjusted along the y axis to separate the curves)

Observation of the thermograms did not show distinctive thermal arrest associated with beta phase precipitation even at low cooling rate. Due to low concentration of iron, the signal for precipitation of beta phase was hindered by the (Al)-Si eutectic reaction. Using first derivative of the DTA cooling curve, we could confirm that the beta phase precipitation takes place after the (Al)-Si eutectic has started as seen in Figure 4.2 (red circle mark).

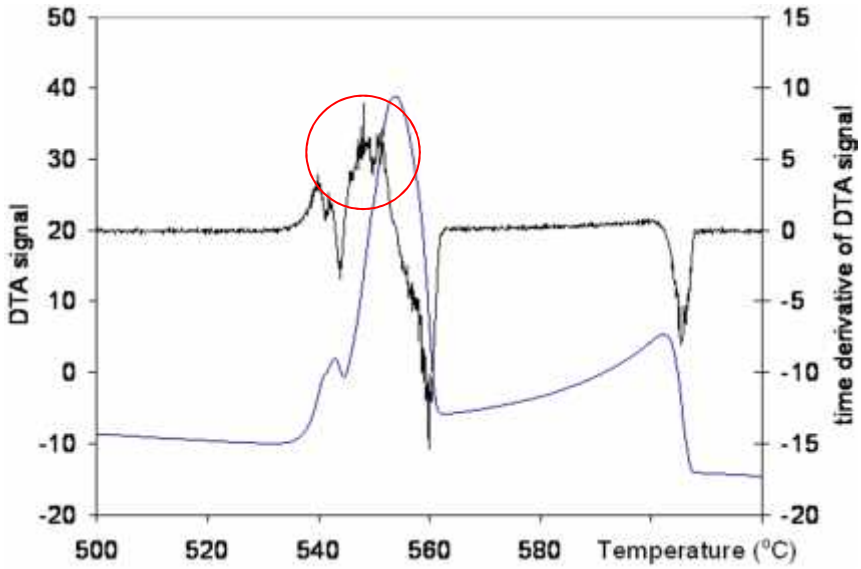

Figure 4.2. DTA thermogram recorded upon cooling at 2°C/min and its first derivative

4.2 Cooling curve analysis (various thermal modulus)

Cooling curve analysis was performed on a series of A356 alloys with chemical composition listed in **Chapter 3**. Figure 4.3 shows the typical cooling curves of the series

taken from various moduli of sand and metallic moulds, where the far right curve in each graph represents the largest and the left the smallest modulus.

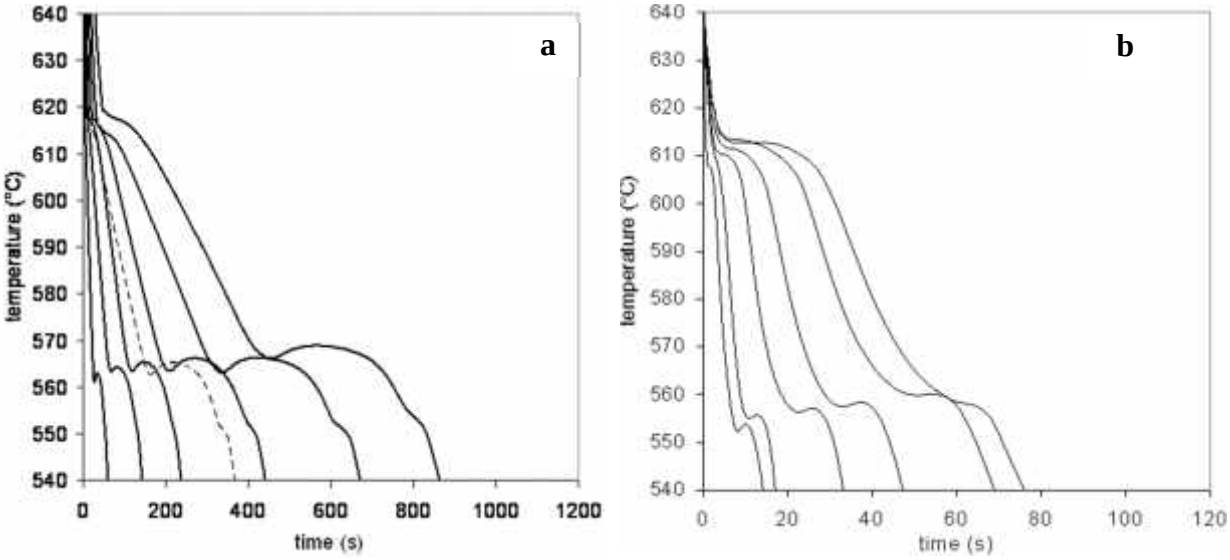

Figure 4.3. Typical cooling curves obtained for cylinder samples of different thermal moduli in sand (a) and metallic (b) moulds. (Dashed lines represent the standard thermal analysis cup)

The quick cup cooling curve is also drawn on the graph of sand mould, represented with dashed line. Even though the quick cup modulus is 0.605 cm, the cooling curve shows up between the curve for 0.8 and 1 TM (cm). This is influenced by the characteristic and properties of the material used for the quick cup which leads to a cooling rate which is smaller than for the sand mould with equal modulus. Observation also showed that the cooling rates varied among the alloys with the same modulus size. Several factors could be linked to this, such as material weight and temperature of the mould prior pouring which affects the heat extraction by the mould during the solidification process.

The graphs in Figure 4.4 and 4.5 plot the relationship between t_{coales} and t_f respectively and cooling rate. The graphs illustrate that using the liquid cooling rate (Figure 4.4) shows more scattering compared to the use of eutectic cooling rate (Figure 4.5). Less scattered values using the eutectic cooling rate may be due to the fact that heat release has achieved a steady-state at that time. The data in Figure 4.5 shows a slight shift (red circle in Figure 4.5) between the sand and metallic mould with more scattered data gathered from the metallic mould (largest modulus). This shift nearly disappears when using t_f (Figure 4.5b) and it may be concluded that all records are consistent between each other.

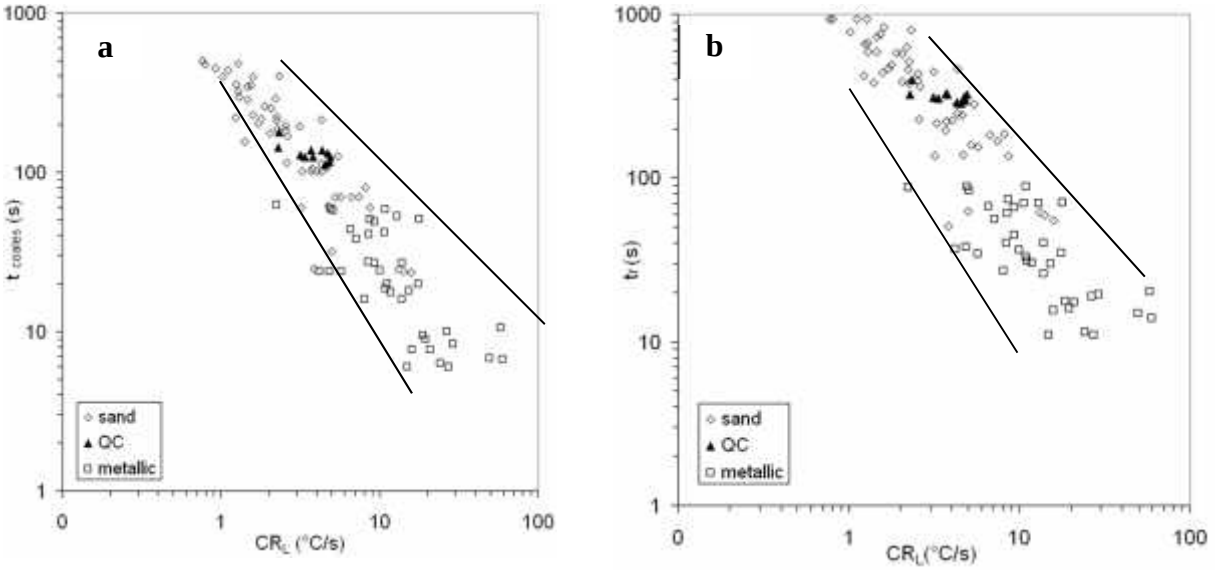

Figure 4.4. Comparison between liquid cooling rate vs. t_{coales} (a) and t_f (b)

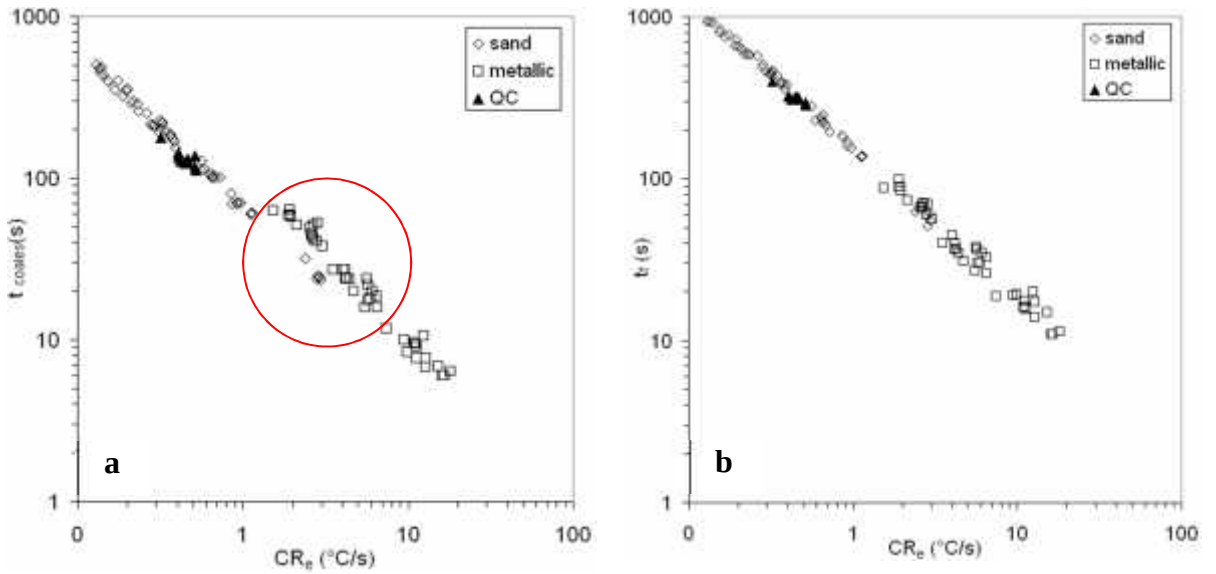

Figure 4.5. Comparison between eutectic cooling rate vs. t_{coales} (a) and t_f (b)

Observation of the alloys solidification range in Figure 4.6a shows a tendency of higher range when the cooling rate increases, especially in the case of metallic mould. The high cooling rates lowers the temperature formation of the final eutectic reactions (Mg_2Si and π-phase). This depression is related to the high undercooling necessary for the nucleation of these minor phases. Furthermore, the sensitivity of thermocouple reading also could add to the temperature depression. The correlation between t_f and solidification range in Figure 4.6b can be related to the cooling rate. The effect of cooling rate on the total solidification time has been already reported by Gowri [8] and Shabestari and Malaken [9].

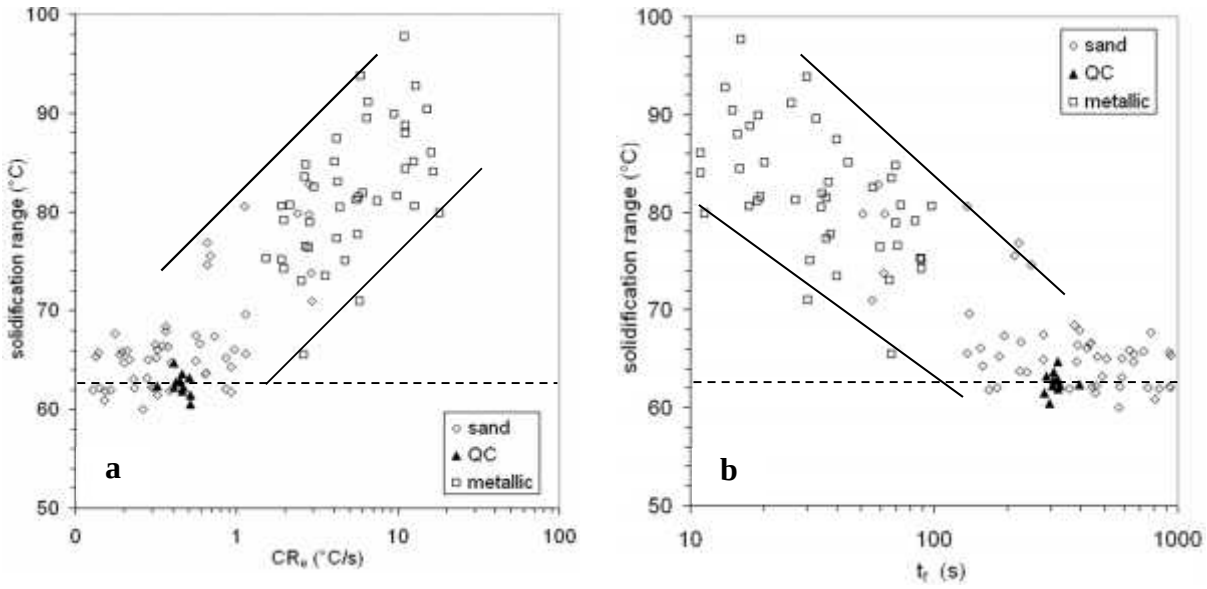

Figure 4.6. Comparison between solidification range vs. eutectic cooling rate (a) and t_f (b), (dashed line represents the mean value of the solidification range taken from quick cup data)

4.3. Discussion

4.3.1 Effectiveness of grain refining

Grain size prediction in cooling curve thermal analysis is usually linked with undercooling and recalescence during the nucleation phenomena, where no or lack of recalescence indicates a good nucleation which leads to fine grain size assessment [10]. Most of the grain size predictions in the cast house are made by using standard thermal analysis cup (quick cup), in which the cooling is controlled at low or moderate rate. However, in real casting condition, the geometry of the component varies and this could induce different cooling rates and degrees of undercooling across the part which affect the local grain size of the component.

As seen from Figure 4.7a, using the eutectic cooling rate gives an even distribution of scattered data between the lower and upper bounds. In the case for liquid cooling rate (Figure 4.7b) we could identify that some data were which originated from some of the smallest modulus metallic moulds (alloy code 1- M0.3, 4-M0.4 and 4-M0.3) could be outliers.

The correlation between nucleation recalescence and grain size is shown in Figure 4.8. In common practice, it is stated that nucleation recalescence can be used to estimate the final grain size by standard thermal analysis cup. i.e. at given cooling rate. The present results obtained with various cooling rates show that even though the curve shows no recalescence, the metallographic measurements show a wide range of observed grain size (0.2 - 0.7 mm). This evidences that nucleation recalescence alone cannot be used to determine the degree of grain refinement.

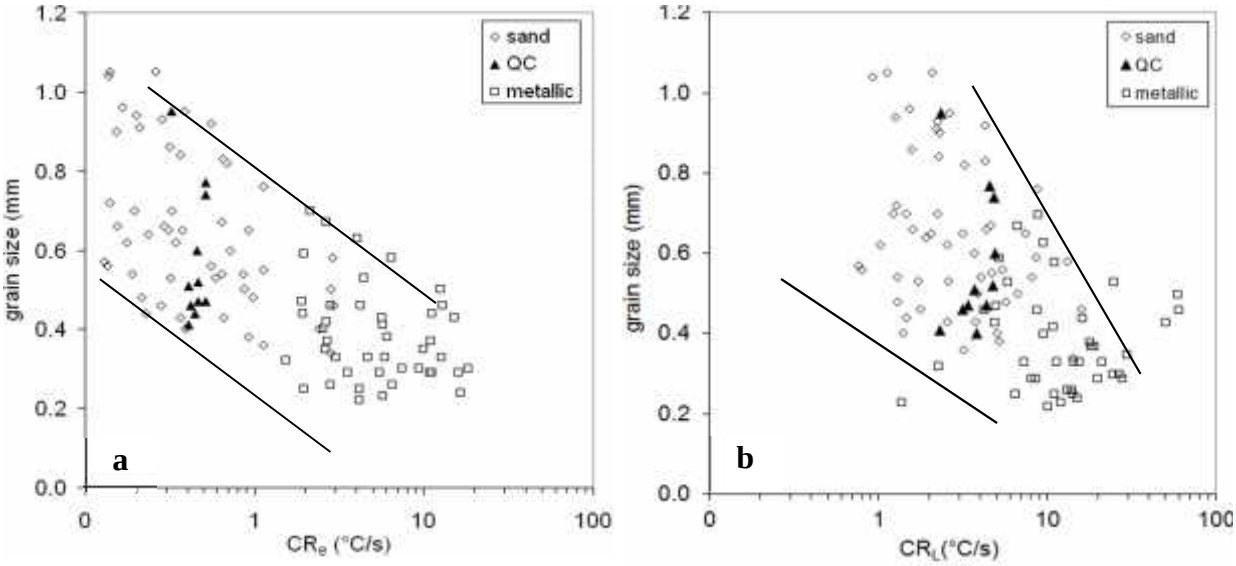

Figure 4.7. Comparison between grain size vs. eutectic cooling rate (a) and liquid cooling rate (b).

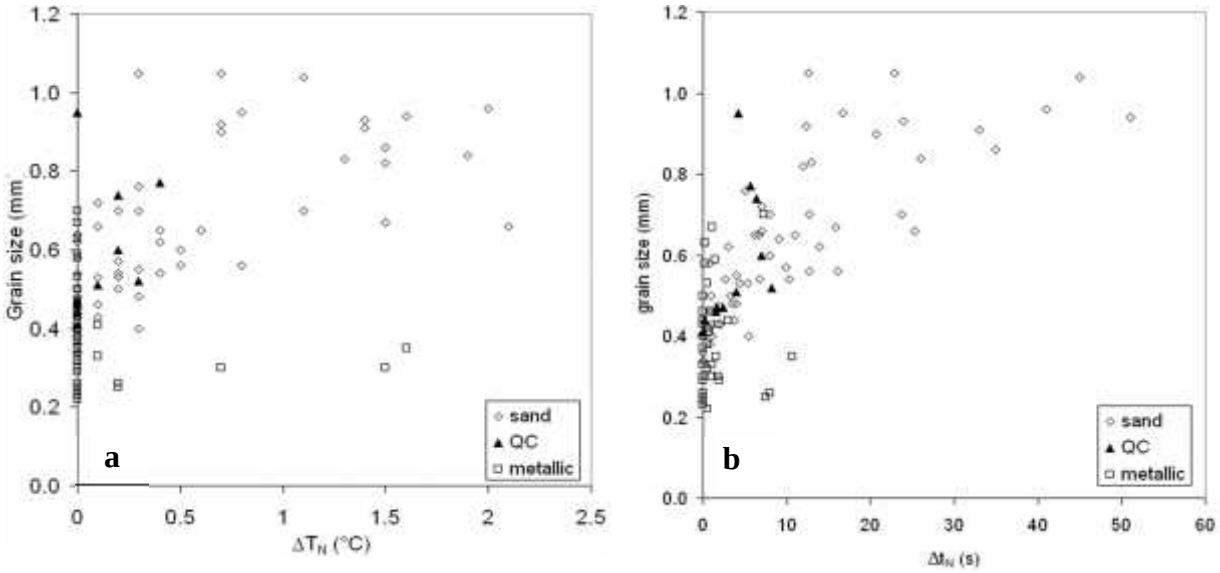

Figure 4.8. Comparison between grain size vs. nucleation recalescence (a), and nucleation time (b).

Other correlations have been looked for. For example, a comparison between grain size and nucleation time indicates that longer nucleation time related to larger grain size. This finding is in agreement with previous studies by Charbonnier [10] and Apelian et al. [11] using standard thermal analysis cup. Figure 4.9 illustrates the correlation between the parameter V_{max} with grain size (a) and nucleation recalescence (b). The graph shows most of the data being clustered to the center area (zero value regions), and no trend or correlation can be concluded from it.

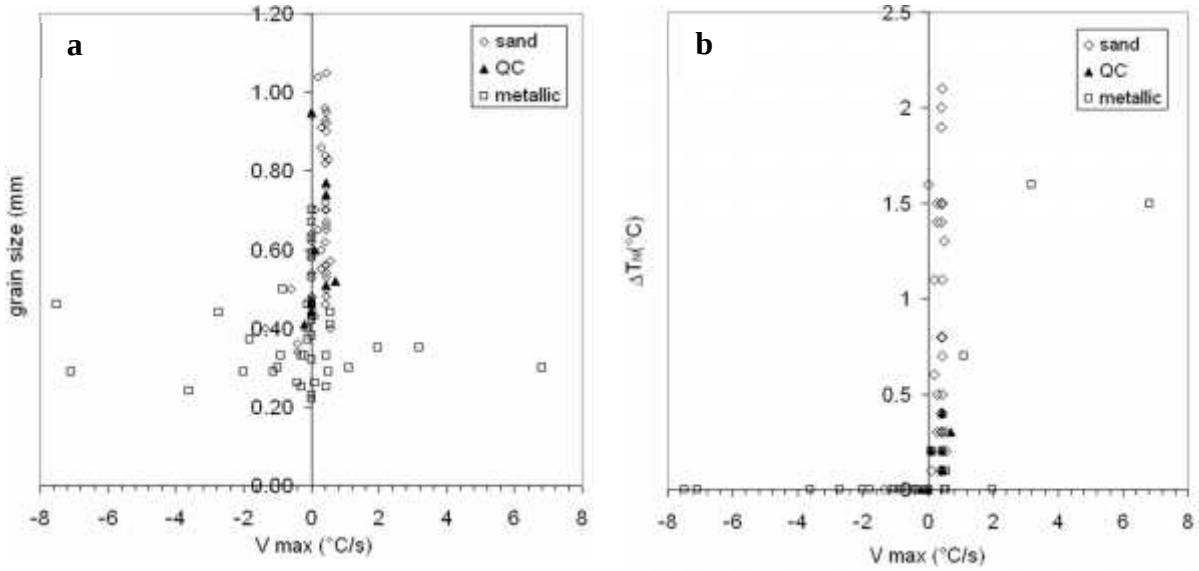

Figure 4.9. Plot of V_{max} vs. grain size (a) and nucleation recalescence (b).

Comparison between grain size and $T_{N,max}$ as seen in Figure 4.10 shows no direct correlation between these parameters. The graph shows that the data without recalescence is clustered in the low grain size range, where most of them were acquired from the metallic moulds. Figure 4.11 shows the comparison between the nucleation recalescence and nucleation time. The graph illustrates a correlation where the nucleation time increases with the increase of nucleation recalescence which also correlated with the cooling rate, even though some values from metallic mould sample are outliers (code : 3-M0.3, 6-M0.4 and 7-M0.3).

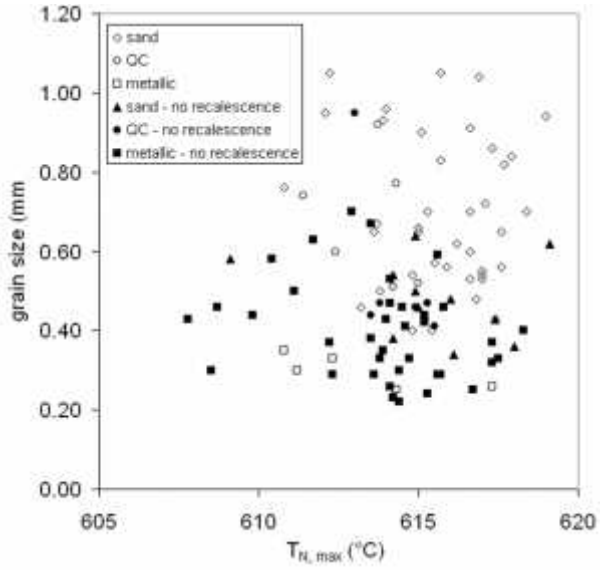

Figure 4.10. Comparison between grain size vs. $T_{N,\ max}$. Solid symbols represent data without recalescence.

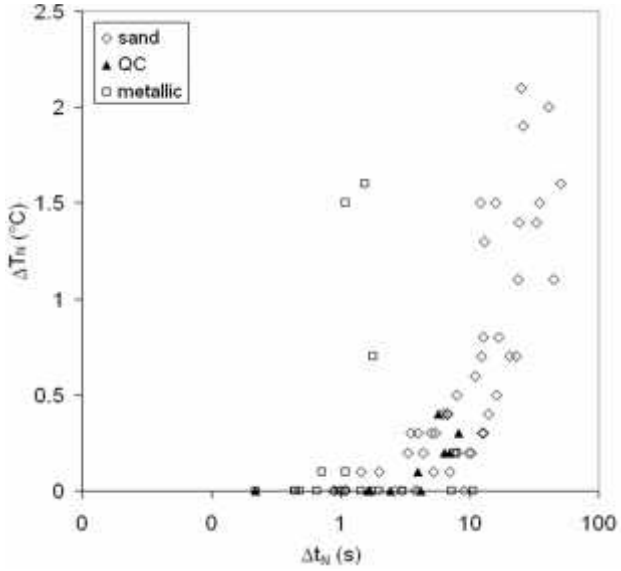

Figure 4.11. Comparison between nucleation time vs. nucleation recalescence.

Relation between the eutectic cooling rate and the absolute nucleation undercooling is shown in Figure 4.12. where it is seen that higher cooling rates lead to higher degree of undercooling. However, many negative undercoolings are predicted and this requires further investigation about thermocouple recording and the effect of composition on the liquidus temperature. This certainly has to do with the fact that absolute temperature values are not used for exploiting thermal records. Liquidus arrest is more sensitive to the changes in chemical composition and cooling rate compared to the eutectic arrest due to the data is taken in early solidification process when the heat release has not achieved a steady-state as already stated earlier.

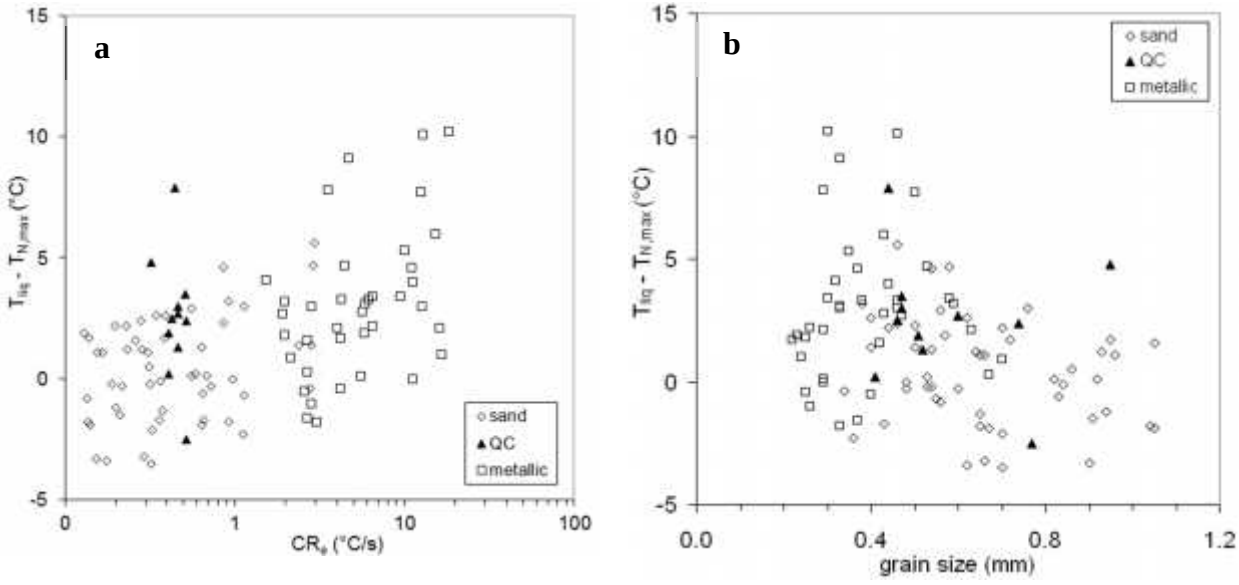

Figure 4.12. Comparison between absolute nucleation temperature vs. eutectic cooling rate (a) and grain size (b).

4.3.2. Statistical Analysis on grain refinement

A regression analysis was performed with several parameters with the purpose to establish a single correlation between the grain size and thermal analysis data. Parameters such as Modulus, nucleation time, liquid cooling rate, eutectic cooling rate and nucleation recalescence were considered as input variables with the measured grain size as output dependant variable. Prior to multiple linear regression analysis, a correlation test was performed on the sand and metallic sample series. The result is shown in Table 4.2. and parameters which have a correlation value in between -0.7 and 0.7 were excluded from further analysis.

Table 4.2. Correlation test for sand and metallic samples

	GS	*Modulus*	*CR_L*	*CR_e*	*Δt_N (s)*	*DAS*	*$(\Delta t_N * DAS)^{0.5}$*	*ΔT_N (°C)*	*Log CR_e*
GS	1								
Modulus	0.5162	1							
CR_L	-0.4095	-0.6152	1						
CR_e	-0.5466	-0.6879	0.8022	1					
Δt_N (s)	0.7623	0.5256	-0.3824	-0.4416	1				
DAS	0.7034	0.8340	-0.6650	-0.7625	0.6652	1			
$(\Delta t_N * DAS)^{0.5}$	0.8207	0.6485	-0.5112	-0.5920	0.9518	0.8245	1		
ΔT_N (°C)	0.5919	0.1873	-0.2120	-0.2220	0.7819	0.3925	0.7338	1	
Log CR_e	-0.7108	-0.7675	0.7259	0.8509	-0.6385	-0.9776	-0.8059	-0.3999	1

The multiple linear analysis was performed on both samples series, the result can be seen in Table 4.3.

Table 4.3. Multiple linear analysis result

Regression Statistics	
Multiple R	0.829627
R Square	0.688281
Adjusted R Square	0.675016
Standard Error	0.121027
Observations	99

	Coefficients
constant	0.614179
Δt_N (s)	-0.00124
DAS	-0.00467
$(\Delta t_N * DAS)^{0.5}$	0.011292
Log CR_e	-0.16882

The following expression was finally obtained:

$GS = 0.614 – 0.1688 \log CRe - 0.0046\ DAS + 0.0112(\Delta t_N * DAS)^{0.5} – 0.0012\ \Delta t_N$

The expression shows R^2 value of 0.68, and this low correlation value for the curve fitting indicated that not all the data have a simple linear correlation; further investigation would be needed to improve the expression. From the coefficients it can be seen that the grain size decreased with the increase of the cooling rate and increases with the square root of nucleation time x DAS. The comparison between calculated and measured value can be seen in Figure 4.13.

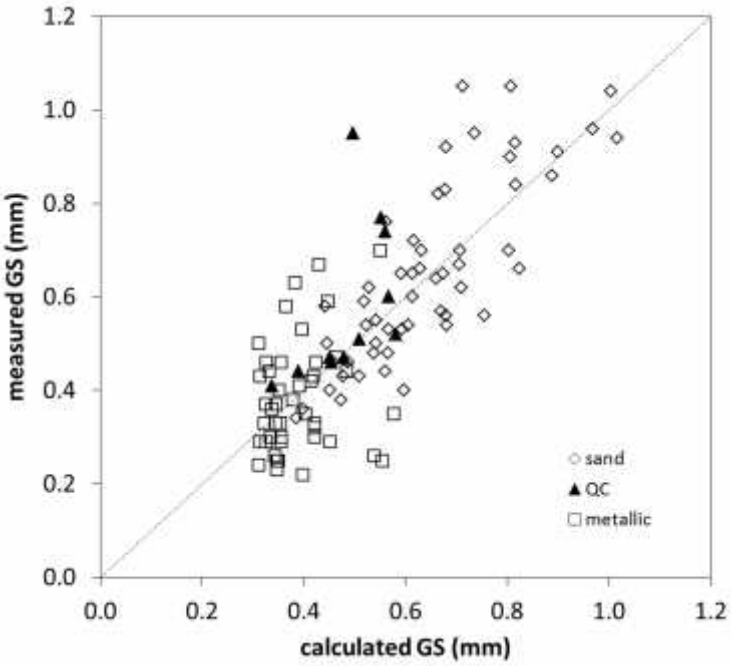

Figure 4.13. Plot of calculated GS vs. measured GS. The dashed line is bisector.

4.3.3 Eutectic silicon modification in Al-Si alloys

The method commonly used to measure the effectiveness of modification process is the change in the eutectic temperature undercooling also known as eutectic depression [10]. The depression has often been evaluated by comparing with the eutectic temperature of the unmodified alloy. However, in many cases, this latter cannot be obtained in a cast shop due the possibility of prior modification treatment to the alloys or the use of returns in the charge. In such conditions, the evaluation of the undercooling requires the knowledge of a reference eutectic temperature here denoted as T_R which should be given by the relevant phase diagram.

Figure 4.14 shows the as cast microstructure of silicon in both sand and metallic moulds from various thermal moduli. The microstructure also reveals other phases such as π ($Al_8FeMg_3Si_6$), Mg_2Si and beta (β-$Al_9Fe_2Si_2$). Observation in the case of metal mould reveals that all the eutectic silicon was well modified.

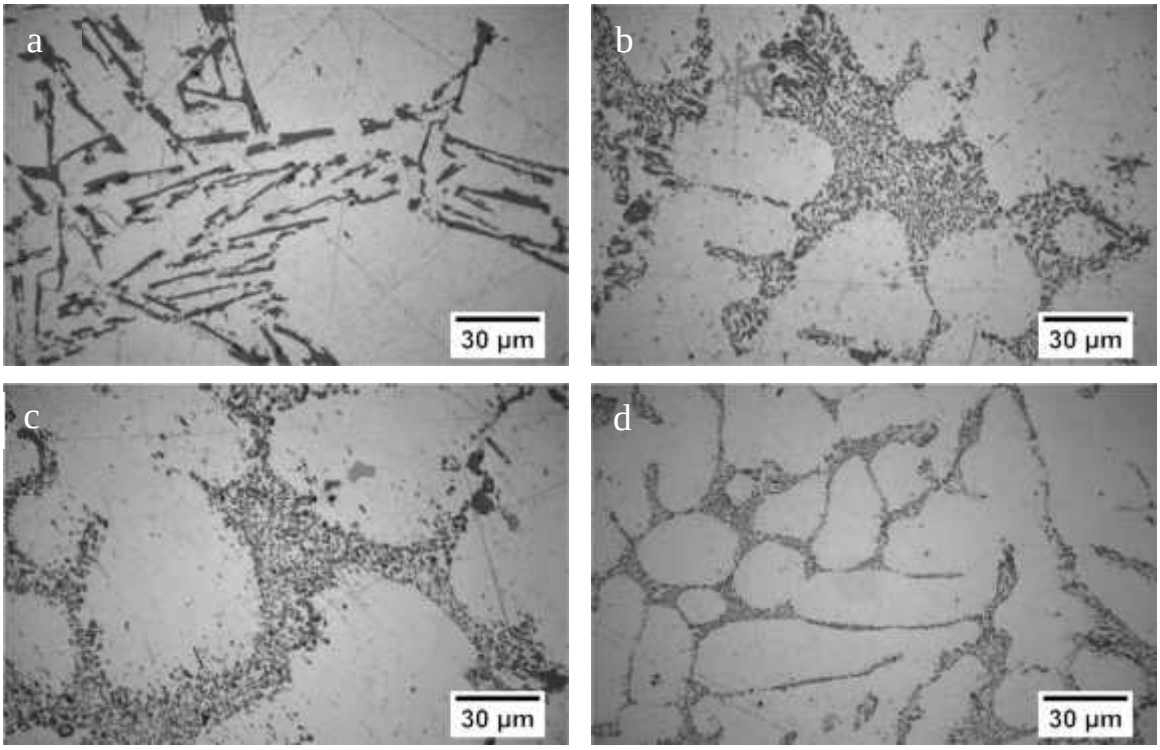

Fig. 4.14. Microstructure of alloy A356 samples, cast in sand (a, c) and metallic (b and d) moulds with maximum (a and b) and minimum (c and d) thermal modulus.

However, in the case of large thermal modulus in sand mould, the silicon modification appeared only partial. It is well known that the modification by strontium is less effective at low cooling rate. Previous work by Song et al. [12, 13] suggests that absorbed Sr fails to prevent the Si phase growth, in such a case, which then grows as in unmodified alloy. However, work by Wang and Davidson [6] on DSC samples suggests that the morphology changes because of premature Sr fading.

The correlation between the eutectic temperature and eutectic depression vs eutectic cooling rate is shown in Figure 4.15. It seen that the eutectic temperature decreases as the cooling rate increases and as a consequence the eutectic depression increases. In relation to the cooling curve analysis, the modification of eutectic silicon was related to the cooling rate and the eutectic depression (detail explanation regarding this nomenclature can be seen in **Chapter 3**). In general, if the eutectic temperature depression is over 5.5°C, the alloy is considered well modified with the microstructure having 90% fine fibrous structure [11].

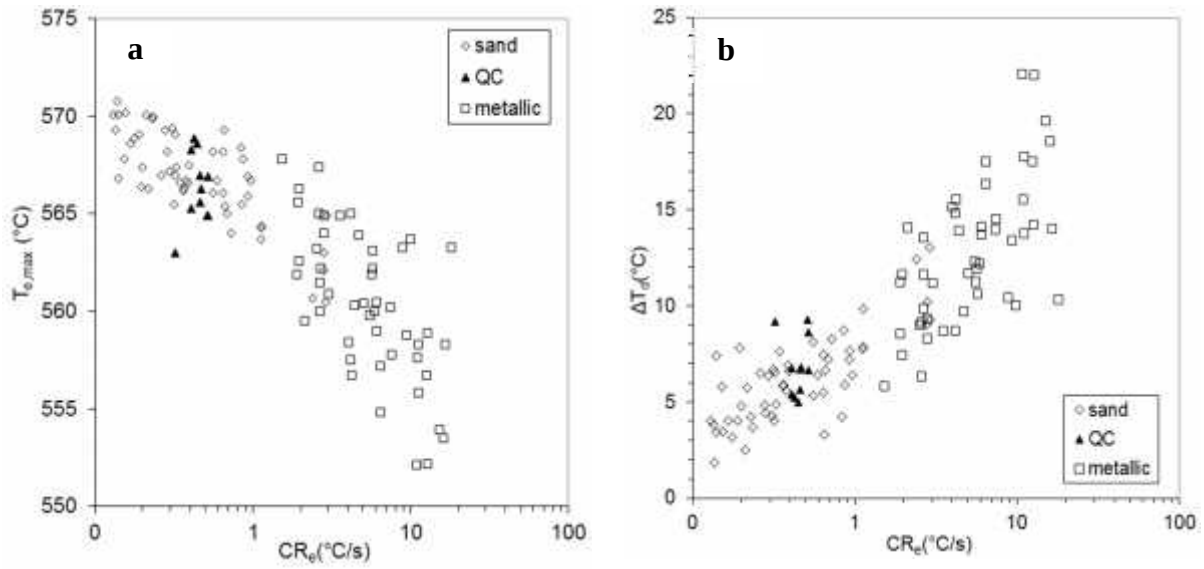

Figure 4.15. Comparison between eutectic cooling rate vs. $T_{e,max}$ (a) and eutectic depression (b).

From Figure 4.16, a comparison was made with observed modification level (ML) based on the AFS chart with the eutectic depression value and eutectic cooling rate. From the graph, a line can be drawn for the boundary of good modification level (ML value above 3). It showed that the necessary temperature depression needed for silicon modification is 7°C, which is slightly higher than previously reported and corresponds to a eutectic cooling rate higher than 1°C/s, with transition zone 0.5 – 1°C/s.

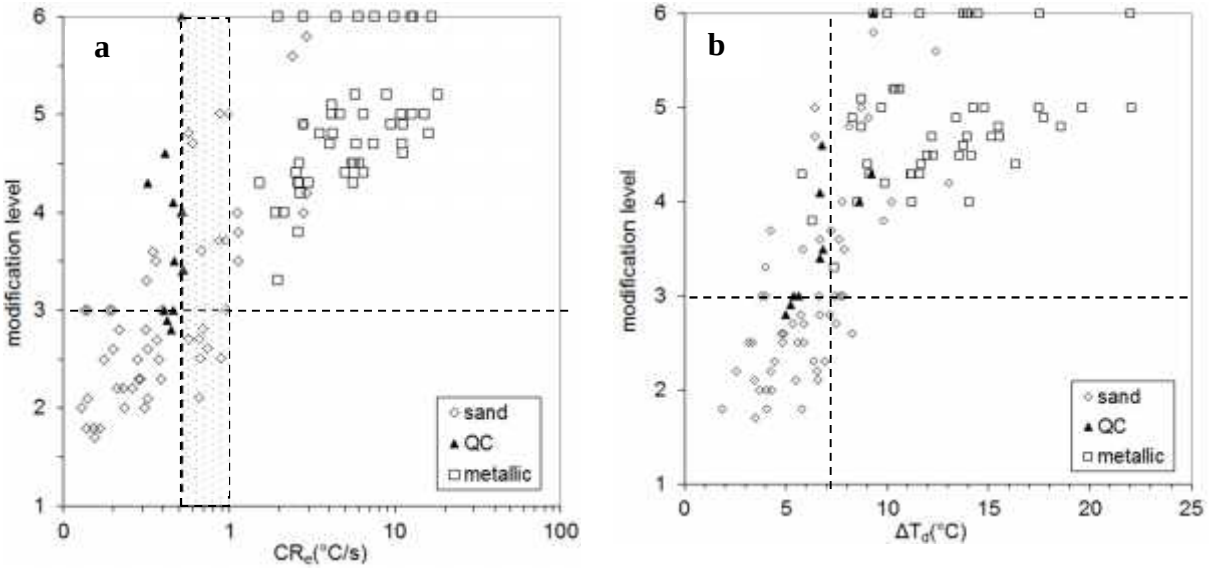

Figure 4.16. Comparison between modification level vs. eutectic cooling rate (a), eutectic depression (b).

Further analysis of correlation between the eutectic recalescence and eutectic cooling rate showed no clear trend, in contradiction with the work by Hosseini et al. [14]. The data appears highly scattered, this is also observed in the correlation with the eutectic depression, as seen in Figure 4.17 though here some trend could be noticed.

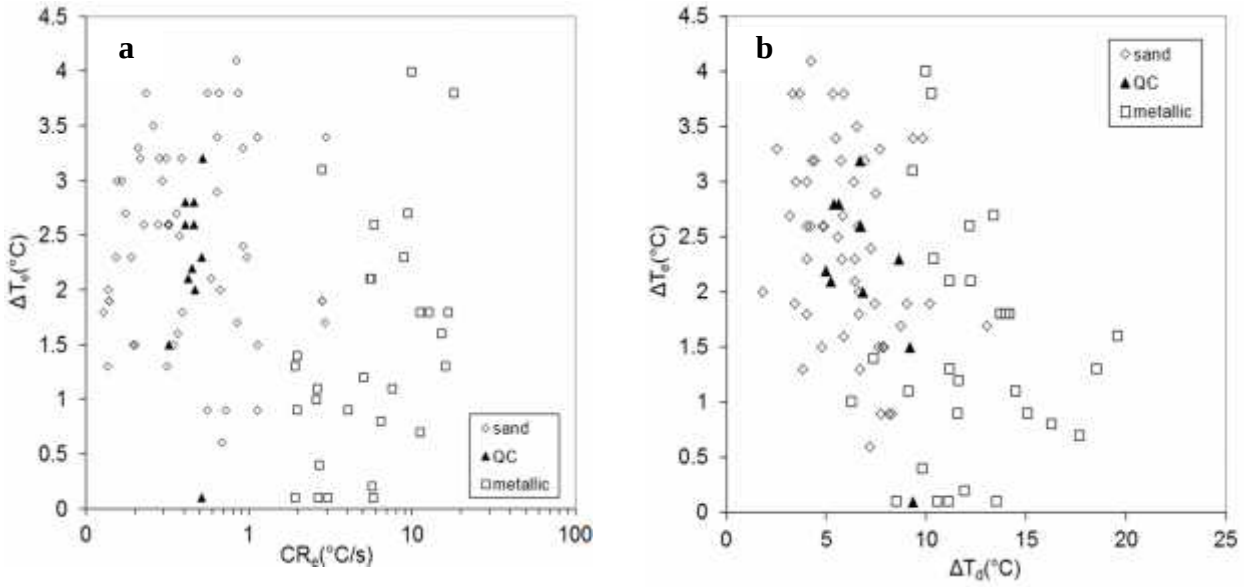

Figure 4.17. Comparison between eutectic recalescence with eutectic cooling rate (a) and eutectic depression (b).

Other correlations have been looked for e.g. a comparison between eutectic time with the depression and eutectic temperature as seen in Figure 4.18. As the temperature decreases, the eutectic time also decreases which correlates with the cooling rate effect. This relation is also observed in the relation between eutectic time and depression.

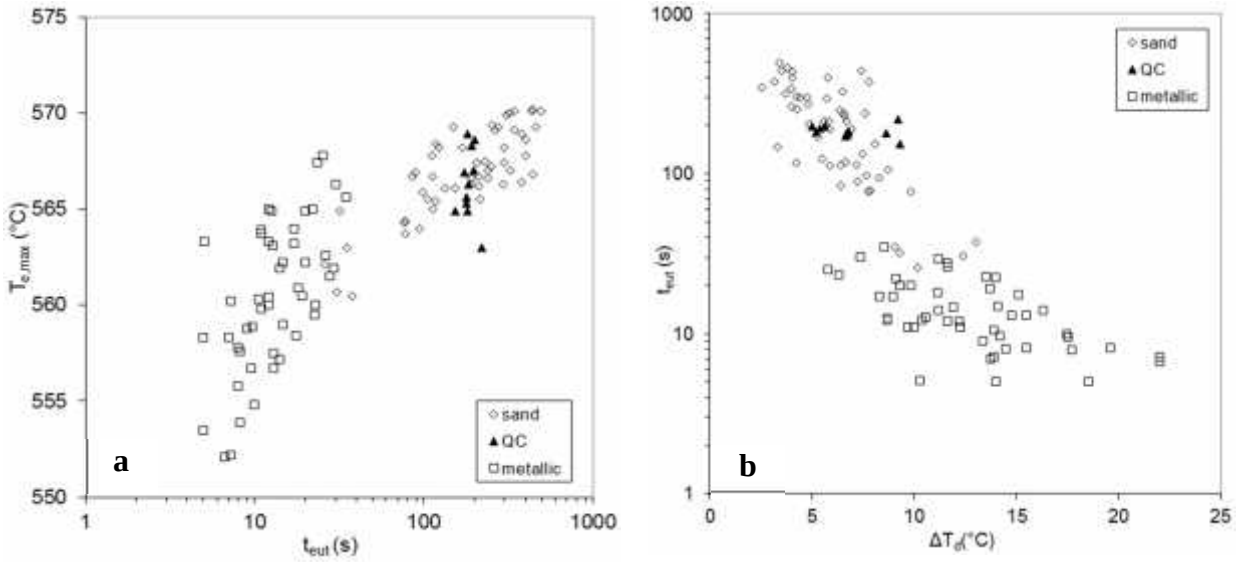

Figure 4.18. Plot of eutectic time vs. eutectic temperature (a) and eutectic depression (b).

The cooling rate not only has a relation with modification level but also with secondary dendrite arm spacing (SDAS). Measurement of SDAS is shown in Figure 4.19a as a function of eutectic cooling rate. It clearly shows that as the cooling rate increases, the SDAS becomes smaller. This result is in agreement with previous work by various authors on the relationship of solidification time or cooling rate with the dendrite arm spacing [15-17]. Furthermore, SDAS is also a function of t_{coales}, because it is subjected to coarsening or ripening, therefore it will increase over time. The relation can be written as follows:

$$SDAS = M*(t_f)^n$$

Where M is a constant that depends on the alloy's properties and n varies between 0.2-0.5 depending on the alloy system according Bouchard and Kirkaldy [18], even though most models consider n equal to 0.33 for ripening control. In the present case, the relation can be formulated as follows:

$$SDAS = 11.5*(t_{coales})^{0.33}$$

Niklas et al. [19] also study the relationship between solidification time and measured SDAS, and proposed an equation $SDAS = 9.3*(t_{coales})^{0.38}$. Comparison between measured SDAS and calculated SDAS using these two equations can be seen in Figure 4.19b.

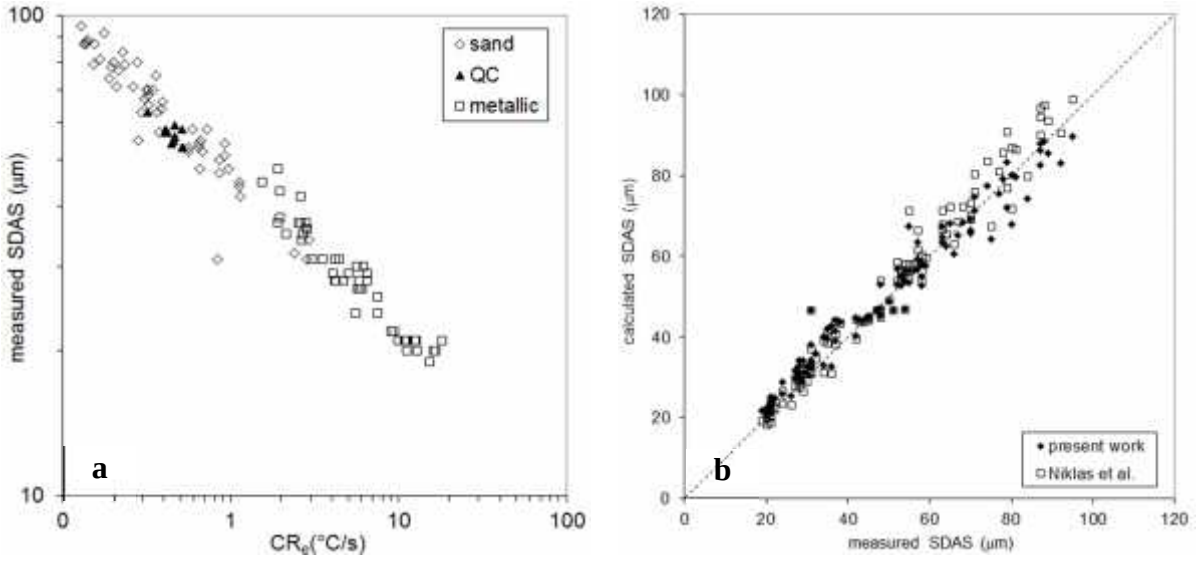

Figure 4.19. Comparison between measured SDAS vs. eutectic cooling rate (a) and calculated SDAS (b) (dash line is bisector).

4.3.4. Statistical Analysis on eutectic modification

A regression analysis was performed with several parameters with the purpose to establish a single correlation between the modification level and thermal analysis data. Parameters such as Modulus, eutectic cooling rate, eutectic depression, eutectic time, and eutectic recalescence were considered as input variables with the measured modification level as output variable. Such an attempt to quantify the relationship between eutectic depression and modification level can also be seen in the early work by Djurdjevic et al. [20] and Wang et al. [21]. Similar to the previous method used for grain refining, prior to multiple linear regression analysis, a correlation test was performed on the parameters as seen in Table 4.4. The analysis results appear in Table 4.4 and 4.5. Logarithm scale was used for simplification and improved the linear relationship with measured modification level. Parameters which have a correlation in between -0.8 and 0.8 were excluded from further analysis.

Table 4.4. Correlation test to sand and metallic samples

	ML	*Modulus*	log CR_e	$t_{eut}*\Delta T_e$ (°C)	ΔT_d	t_{eut}	ΔT_e (°C)
ML	1						
Modulus	-0.6747	1					
log CR_e	0.8993	-0.7647	1				
$t_{eut}*\Delta T_e$ (°C)	-0.8061	0.5630	-0.8192	1			
ΔT_d	0.767	-0.637	0.8762	-0.7081	1		
t_{eut}	-0.8033	0.6775	-0.8698	0.9327	-0.7572	1	
ΔT_e (°C)	-0.5315	0.0441	-0.4718	0.6529	-0.5678	0.4988	1

Table 4.5. Multiple linear analysis result

Regression Statistics	
Multiple R	0.911119
R Square	0.830137
Adjusted R Square	0.824071
Standard Error	0.500513
Observations	88

	Coefficients
constant	3.614834
log CR_e	1.508924
$t_{eut}*\Delta T_e$ (°C)	-0.00123
t_{eut}	0.0023

The following expression was finally obtained:

$ML = 3.615 + 1.5 \log CR_e + 0.0023\ t_{eut} - 0.0012\ (t_{eut}*\Delta T_e)$

In previous work [22] we have put emphasis on the eutectic depression effect; however multivariate analysis with larger samples showed the correlation with this parameter is less than 0.8, therefore it was excluded from current statistical analysis. The expression shows a satisfactory R^2 value of 0.83, and the comparison between calculated and measured values can be seen in Figure 4.20. It is seen however that the data appeared scattered for quick cup samples which could indicate that information from other unidentified parameters has an important effect to the modification level. The data also appeared more scattered for sand mould than for metallic moulds.

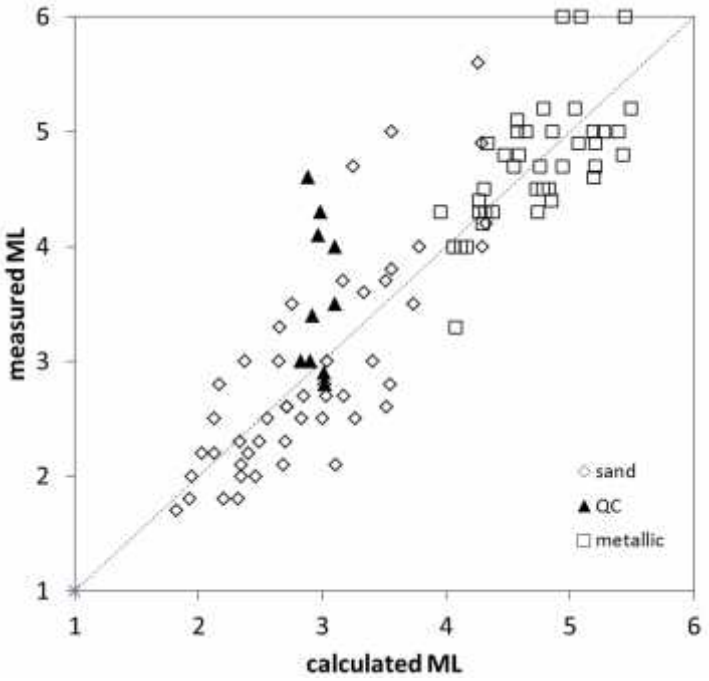

Figure 4.20. Plot of calculated ML vs. measured ML. The dashed line is bisector.

4.3.5. Eutectic modification at low cooling rate (Flake – Fibrous transition)

In a previous work [22], it has been seen that in samples with a eutectic cooling rate less than 0.7°C/s, the silicon is less modified compared to higher cooling rates. Song et al. [12] studied the critical cooling rate for eutectic modification on alloys with more than 10% Si. They suggested that the minimum critical value was 0.05°C/min for commercial alloys and a lower value at 0.025°C/min in high purity alloys. Zheng et al. [23] investigated several modifiers and proposed the critical cooling rate for strontium modifier at 0.66°C/s. To study these further, samples with low Sr were subjected to low cooling rates using DTA. Prior to scanning at slow cooling rate, the samples were run for one cycle of heating at 10°C/min and

cooling at 40°C/min to ensure a good contact between the crucible and the sample. The experiments were then performed at scanning rate 0.6°C/min to 30°C/min (0.01°C to 0.5°C/s).

Figures 4.21 and 4.22 show the microstructure of A-356 modified alloy for different cooling rates. As seen from the optical micrographs in Figure 4.21, the silicon (dark colour) appears unmodified in the sample with the 0.6°C/min, even though Sr was added to the alloy. As the cooling rate increases, the silicon gets slightly modified and the rating increases.

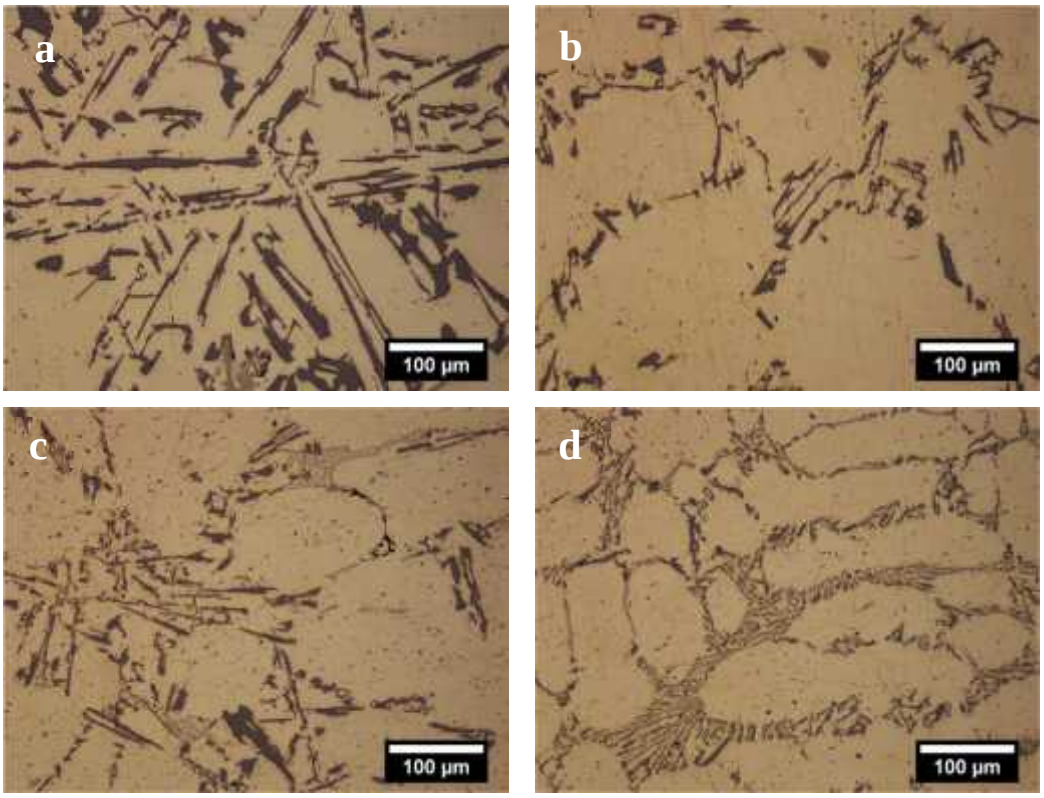

Figure 4.21. Microstructure of low strontium alloy A356 with different cooling rates (a) 0.6 °C/min, (b) 1 °C/min, (c) 6 °C/min and (d) 30 °C/min.

However, from the deep etched samples in Figure 4.22, the role of strontium in poisoning the nucleation site was not seen at low cooling rate. The eutectic silicon appeared plate like and the plate refined as the cooling rate increases. From these experiments, it can be concluded that a critical cooling rate higher than 30°C/min (0.5°C/s) is needed to ensure a good modification rating (above ML 3).

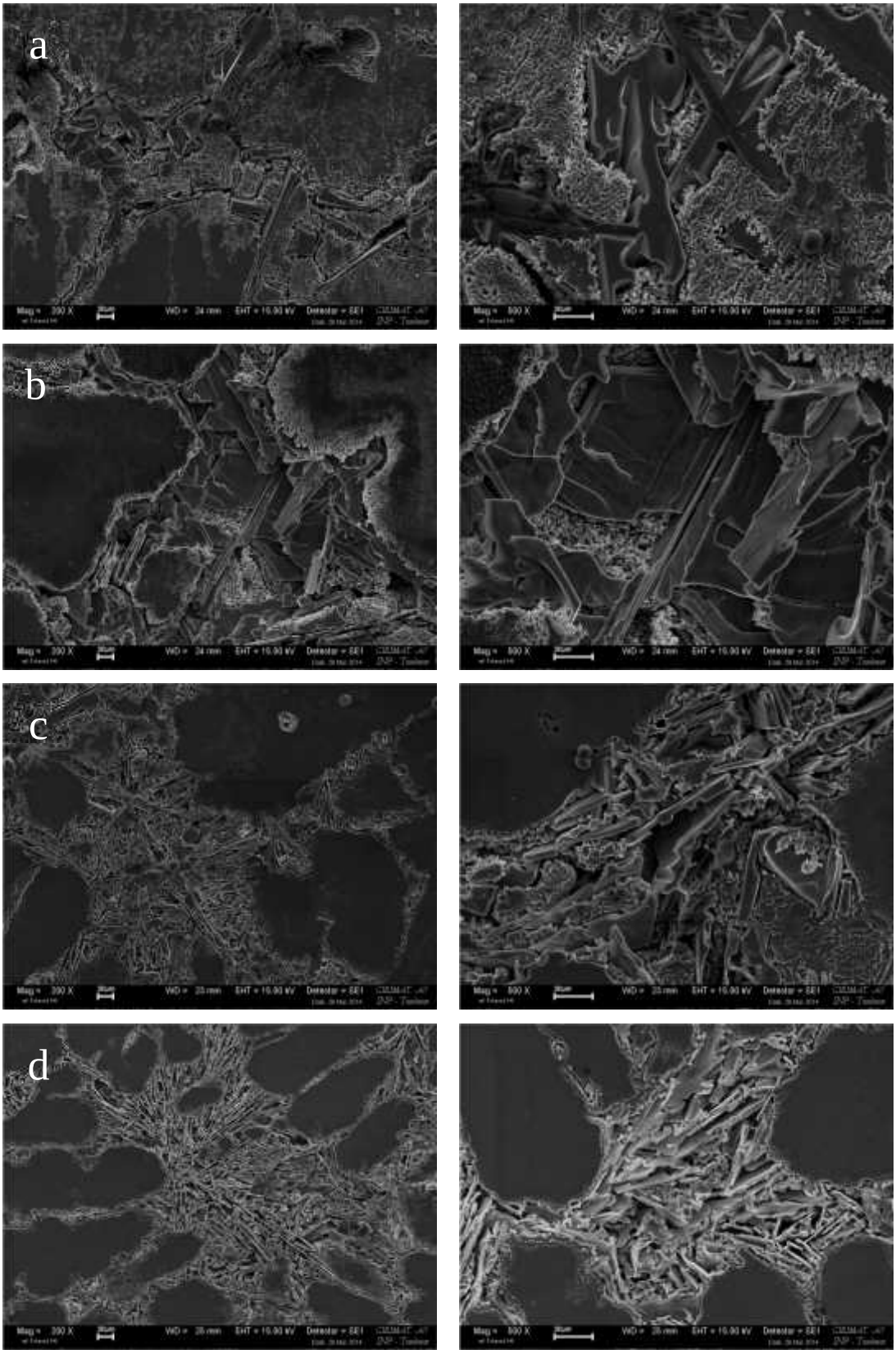

Figure 4.22. SEM micrograph from the same sample in Figure 4.21. (a) 0.6°C/min, (b) 1°C/min, (c) 6 °C/min and (d) 30°C/min.

The role of strontium in modification of silicon is a combination of two mechanisms, the nucleation poisoning and growth blocking which are also influenced by the solidification cooling rate. At very low cooling rate, strontium is unable to prevent silicon from growing, which means the poisoning of nucleation sites is not effective. This is the same as in the vanishing effect of blocking mechanism for silicon plate growth. However, in the case of isolated liquid pools (Figure 4.23 and Chapter 6), the eutectic silicon appeared with a very fine coral-like morphology. This structure has developed at high undercooling in the trapped liquid pools.

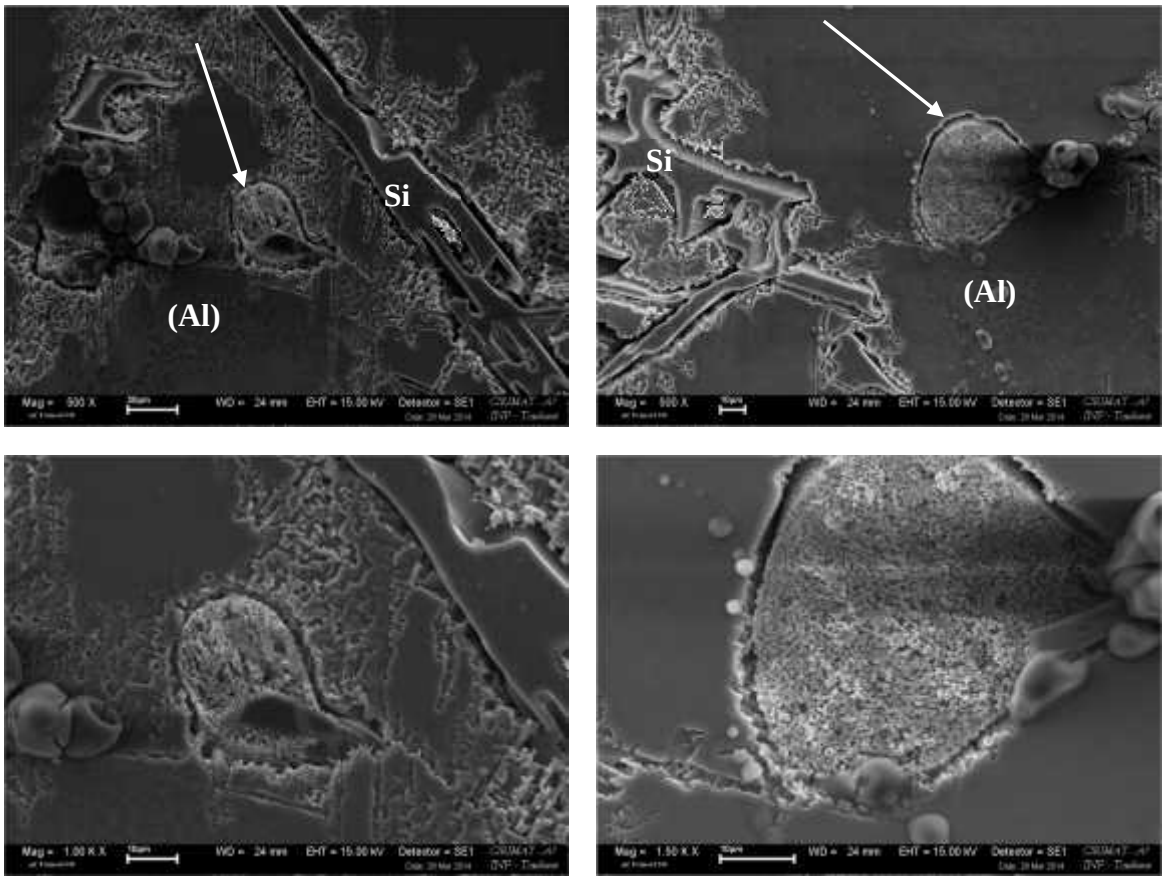

Figure 4.23. Isolated eutectic silicon showed coral like morphology of modified silicon taken from sample with cooling rate 0.6°C/min

Further analysis was conducted on the characteristic temperature of (Al)-Si eutectic upon heating and cooling DTA, by taking 3 samples from the alloys series (alloy code No.9, 10, 11 as A, B and C). These values are plotted versus the scanning rate in Figure 4.24. The values obtained by linear extrapolation to a zero scanning rate are thus expected to be the relevant temperatures of the reaction.

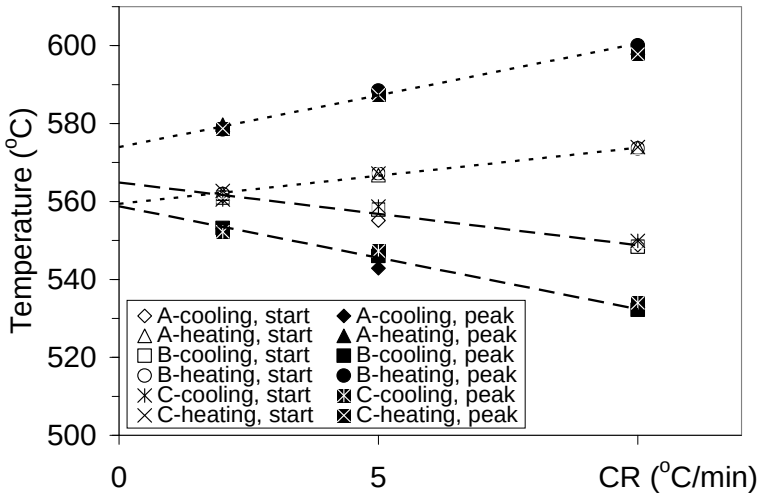

Figure 4.24. Correlation between characteristic temperature of (Al)-Si eutectic and scanning rate

Interesting result was noticed concerning the peak temperature on cooling which represents the end of the (Al)-Si eutectic reaction. Its characteristic temperature extrapolates to about the same temperature as the start temperature on heating. The start temperature upon heating extrapolates to 564°C (adjusted according to the DTA calibration), which shows 8°C below the calculated eutectic temperature at 572°C for the alloys investigated (evaluated as described in appendix 3). The extrapolation of start temperature upon cooling is at 569°C, which is again below the reference temperature at 572°C. The alloying elements have a prominent effect on the onset of melting of the eutectic (Al)-Si. The characteristic temperature during heating might be influenced by the partial dissolution of off-equilibrium phases, and this will affect the start temperature of melting. For cooling it appeared that alloying elements lead to a lower temperature for the start of the (Al)-Si eutectic than predicted. This could be due to increased undercooling for nucleation of silicon or to the effect of partial solid-state diffusion on the solidification path.

Summary

A study of the effect of cooling rate on the eutectic and grain size of Al alloy A356 was performed on sand and metallic mould castings having various moduli. Multiple regression analysis showed the influence of nucleation time, eutectic cooling rate and nucleation undercooling on the final grain size. Thermal analysis also showed that the (Al)-Si eutectic depression increases with the cooling rate as expected, though only values of cooling rate higher than 0.7°C/s relate to satisfactory modification of A356 alloy in either sand or metallic moulds. Multivariate statistical analysis of thermal analysis data showed the influence of cooling rate, coalescence time and DAS on the final grain size. In addition, thermal analysis experiments also indicated that the modification of eutectic silicon is not only a function of modifier element but also a function of cooling rate and eutectic time.

Further study on the flake-fibrous transition was performed by using DTA. Even though the record showed undercooling of the eutectic reaction at very low cooling rate (0.6°C/min), the micrograph showed the structure as unmodified eutectic. From this result we could conclude that the cooling rate has an effect to the modification of eutectic silicon morphology. In order to achieve modification level above 3, a critical cooling rate of at least above 30°C/min (0.5°C/s) should be ensured, in agreement with the value given above.

Reference

1. Thermocalc- TCAL2 database, available in http://www.thermocalc.com/media/11295/tcal2-1-1_extended_info.pdf, accessed in 5 April 2014.
2. R.I. Mackay, J.E. Gruzleski, Quantification of magnesium in 356 alloy via thermal analysis, Int. J. Cast Met. Res., 10, 5, (1998), 255-265.
3. L. Backerud, G. Chai and J. Tamminen: Solidification characteristics of aluminum alloys, Vol.2, AFS/Skanaluminium, Des Plaines, Illinois, 1990.
4. J.E. Gruzleski, B.M. Closset: The treatment of liquid aluminum-silicon alloys, AFS Inc., Des Plaines, Illinois, 1990.
5. Y.L. Liu, S.B. Kang, H.W. Kim, The complex microstructure in an as cast Al-Mg-Si alloy, Material letter, 41, (1999), 267-272.
6. Q.G. Wang, C.J. Davidson, Solidification and precipitation behaviour of Al-Si-Mg casting alloys, Journal of Material Science, 36, (2001), 739-750.
7. W.J. Boettinger, U.R. Kattner, On differential thermal analyzer curves for the melting and freezing of alloys, Metallurgical Transaction A, 33A, (2002), 1779-1794.
8. S. Gowri, Comparison of thermal analysis parameters of 356 and 359 alloys, AFS trans., 102, (1994), 503-508.
9. S.G. Shabestari and M. Malaken, Thermal analysis study of the effect of the cooling rate on the microstructure and solidification parameters of 319 aluminum alloy, Canadian Metallurgical Quarterly, 44, (2005), 305-312.
10. J. Charbonnier, Microprocessor assisted thermal analysis testing of aluminum alloy structure, AFS Trans., 92, (1984), 907-921.
11. D. Apelian, G.K. Sigworth, K.R. Whaler, Assessment of grain refinement and modification of Al-Si foundry alloys by thermal analysis, AFS trans., 92, (1984), 297-307.
12. K. Song, S. Park, H. Nakae, Effect of cooling rate on modification of Al-Si Alloy added by Sr , J.of the Japan Foundrymen's Society, 66, (1994), 822-826.
13. K. Song, H. Fuji, H. Nakae, H. Yamaura, A study on modification mechanism by Sr in Al-Si eutectic alloy, J. of Japan Institute of Light Metals, 43, (1993), 484-489.
14. V.A. Hosseini, S.G. Shabestari, R. Gholizadeh, Study on the effect of cooling rate on the solidification parameters, microstructure, and mechanical properties of LM13 alloy using cooling curve thermal analysis technique, Material and Design, 50, (2013), 7-14.
15. S. Gowri, F.H. Samuel, Effect of cooling rate on the solidification behavior of Al-7 Pct Si-SiCp metal-matrix composites, Metallurgical Transaction A, 23A, (1992), 3369-3376.
16. M.C. Fleming, T.Z. Kattamis, B.P. Bardes, Dendrite arm spacing in aluminium alloys, AFS trans., (1991) 501-506.
17. T. Okamoto, K. Kishitake, Dendritic structure in unidirectionally solidified aluminum, tin, and zinc base binary alloys, J. Crystal Growth, 29, (1975) 137-146.
18. D. Bouchard, J.S. Kirkaldy, Prediction of dendrite arm spacings in unsteady-and steady-state heat flow of unidirectionally solidified binary alloys, Metallurgical Material Transaction B, 28B, (1997), 651-663.

19. A. Niklas, U. Abaunza, A.I. Fernández-Calvo, J. Lacaze, R. Suárez., Thermal analysis as a microstructure prediction tool for A356 aluminium parts solidified under various cooling conditions, China Foundry, 8, (2011), 89-95

20. M. Djurdjevic, H. Jiang, J. Sokolowski, On-line prediction of aluminum–silicon eutectic modification level using thermal analysis, Material Characterization, 46, (2001), 31-28.

21. R. Wang, W. Lu, L.M. Hogan, Self-modification in direct electrolytic Al–Si alloys (DEASA) and its structural inheritance, Materials Science and Engineering A 348, (2003), 289-298.

22. D. Ferdian, J. Lacaze, I. Lizarralde, A. Niklas, A.I. Fernández-Calvo, Study of the effect of cooling rate on eutectic modification in A356 aluminium alloys, Material Science Forum, Vol 765- Light Metals Technology 2013, pp. 130-134

23. C. Zheng, L. Yao, Q. Zhang, Effect of cooling rate and modifier concentration on modification of Al-Si eutectic alloys, Acta Metallurgica Sinica, 18, (1982), 661-670.

5. Cooling rate effect on the precipitation of beta intermetallic phase: a DTA and Tomography study

Iron is considered as a detrimental element in Al-Si alloys due to the formation of iron-rich intermetallic phases during the solidification process as already mentioned in **Chapter 2**. The precipitation of iron rich intermetallic phase can be seen from the liquidus projection of the Al rich corner of Al-Fe-Si ternary phase diagram, as illustrated in Figure 5.1. Table 5.1. compares the temperature of the solidification reactions which occur in the Al rich corner of Al-Fe-Si system according to several studies. As we can see, the reaction in Table 5.1 associated to the invariant point in the Figure 5.1 is the eutectic giving the three solid phases (Al), Si and β.

Table 5.1. Reaction occurring during solidification at Al-Fe-Si system (Al rich corner)

Reaction	Temperature (°C)			
	Krendelberger et al.[1]	Philips [2]	Pontivichi et al. [3]	Takeda and Mutuzaki [4]
1. L + $\theta Al_{13}Fe_4$ → Al + α- Al_8Fe_2Si	636	629	630	-
2. L + α- Al_8Fe_2Si → Al + β-$Al_{4.5}FeSi$	609	611	613	615
3. L + δ-Al_3FeSi_2 → β-$Al_{4.5}FeSi$ +Si	596	596	595	600
4. L → Al + Si + β-$Al_{4.5}FeSi$	577	577	576	573

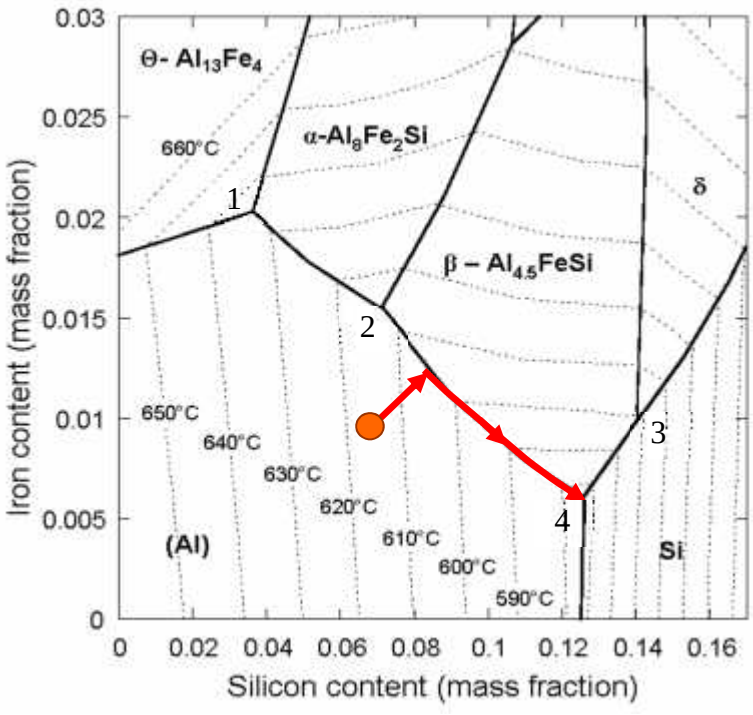

Figure 5.1. Liquidus projection of the Al corner of the Al-Fe-Si ternary system

From the ternary phase diagram, the precipitation of beta phase occurs along the line going from the reaction L + α → (Al) + β (2) to the ternary eutectic reaction of L → (Al) + (Si eutectic) + β.

In this work, a DTA analysis was performed to study and characterize the beta phase precipitation and growth for various cooling rates using high purity ternary alloy with chemical composition Al-6.5Si-1Fe (in mass%). Furthermore, analysis of DTA samples with 2D metallography was complemented to study the growth morphology and kinetics of beta phase by means of post mortem and in-situ synchrotron tomography.

5.1. DTA analysis and solidification path: Scheil and lever rule model

The DTA analysis was performed by recording the DTA signal with various scanning rates for heating of 0.2, 1, 2, 5, 10 and 17.5 °C/min, and for cooling of 0.2, 1, 2, 5, 10 and 40 °C/min. Prior to the cooling sequence, the samples were held at 650°C for 10 minutes to achieve homogenous melt condition. The recorded signal can be seen in Figures 5.2 and 5.3.

From each DTA thermogram, characteristic temperatures were extracted which are associated with the phase transformations occurring during the heating and cooling processes and showed as thermal arrest (onset and peak). Upon cooling, it is obvious that three solidification reactions occurred. The first thermal arrest corresponds to the nucleation of (Al) dendrites which then grow and form the matrix as the alloy is cooled into the L+(Al) region. The beta phase reaction $L \rightarrow$ (Al)+β follows when the interdendritic regions have been enriched in iron and sufficient driving force developed for the beta phase precipitation. The solidification ends with the invariant ternary eutectic $L \rightarrow$ α-(Al)+β +Si eutectic.

The same reactions occurred in reverse order for heating sequence. During heating, the first onset where the line changes from the baseline indicating that the eutectic (Al)-Si reaction temperature has been reached, followed by the dissolution of beta phase. The final arrest relates to the liquidus reaction and the signal returns to baseline indicating the alloy is fully liquid. Increasing the scanning rate leads to a shift of the thermal arrests to higher temperature upon heating and lower temperature upon cooling. The main reason for this is heat transfer resistance [5], although phase transformation kinetics may sometimes have an effect.

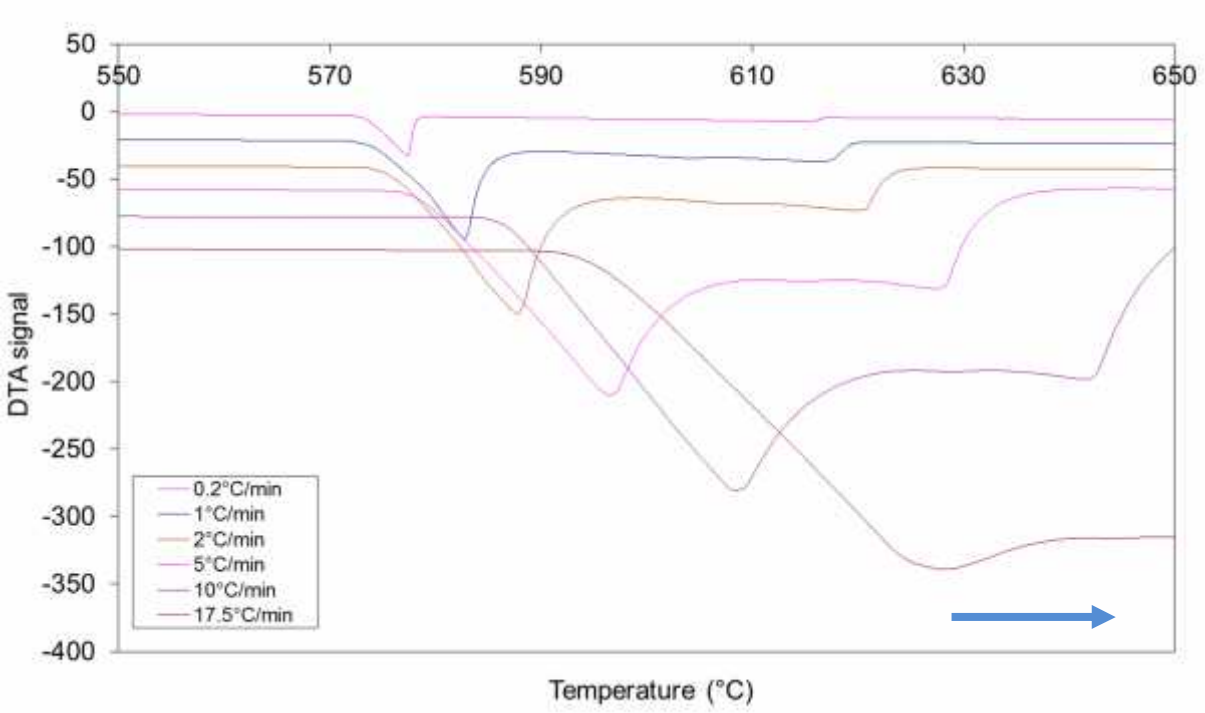

Figure 5.2. DTA thermograms recorded at different heating rates (the graphs were adjusted along the y axis to separate the curves)

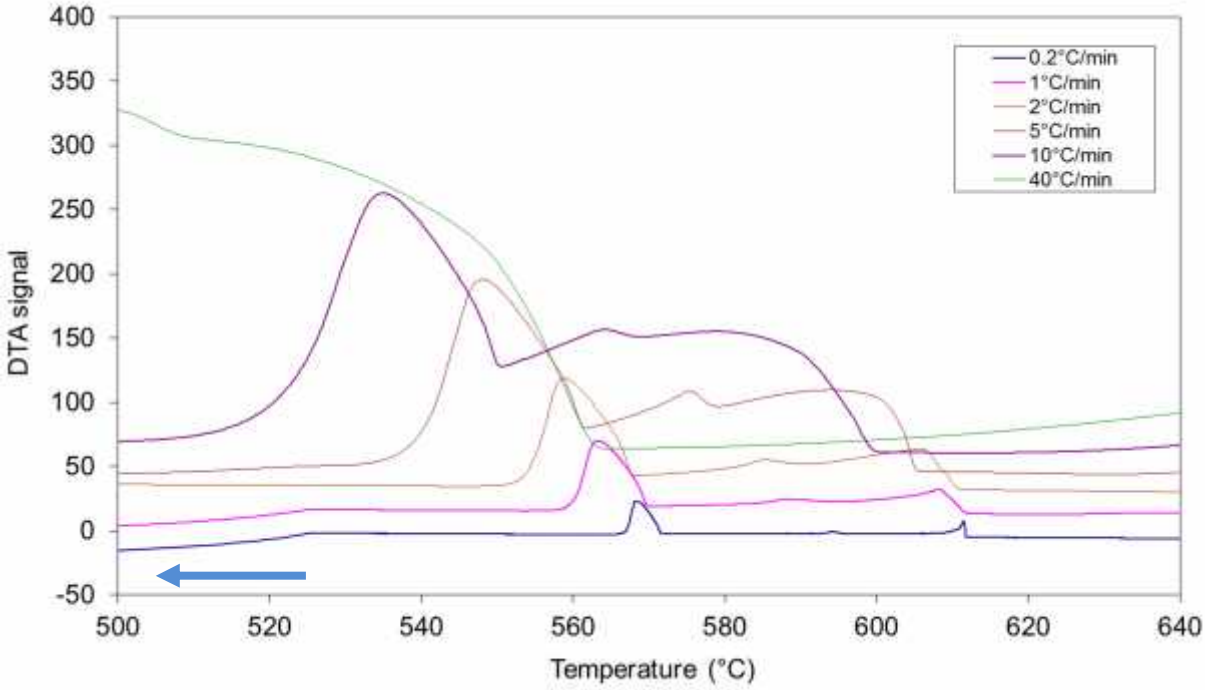

Figure 5.3. DTA thermograms recorded at different cooling rates (the graphs were adjusted along the y axis to separate the curves)

Focusing on the thermal arrest related to beta precipitation, it was observed that the onset and the peak temperatures differ by 2°C for a cooling rate of 0.2°C/min and by 4°C for a cooling rate of 10°C/min.

Further analysis was conducted on the characteristic temperatures extracted from DTA thermograms which are listed in Table 5.2 and 5.3 and plotted in Figure 5.4. The graphs show a linear relationship between the scanning rate and characteristic temperature.

Table 5.2. DTA characteristic temperatures when heating Al-6.5Si-1Fe alloy

	Scanning rate					
	0.2°C/min	1°C/min	2°C/min	5°C/min	10°C/min	17.5°C/min
Eutectic Silicon start	571.7	571.9	573.9	575.5	585.3	592
Eutectic Silicon peak	577.4	582.9	588	596.4	609.2	628.7
Dissolution beta phase peak	597.6	604.5	608.7	615.1	630.1	645.7
Primary Al start	609.2	609.6	611.5	620.5	634.4	650.2
Primary Al peak	615.1	616.7	620.3	627.5	642.4	657.5

Table 5.3. DTA characteristic temperatures when cooling Al-6.5Si-1Fe alloy

	Scanning rate					
	0.2°C/min	1°C/min	2°C/min	5°C/min	10°C/min	40°C/min
Primary Al start	611.7	611.7	610.5	605.2	599.1	562.6
Primary Al peak	611.3	607.6	605.4	594.4	578.9	542.2
Beta Phase start	595.2	593.5	590.2	578.1	567.9	508.4
Beta Phase peak	593.5	587.4	584.7	574.9	563.1	499.6
Eutectic Silicon start	571.6	569.8	567.7	561.1	549.9	492.2
Eutectic Silicon peak	568	562.8	558.3	547.6	534.1	462.9

Extrapolation to a zero scanning rate did not point to a single temperature. The liquidus of the studied alloy according to the experiments is found at 612.7°C, which is close to the value of 617.6°C calculated according to a previous assessment [6]. This difference is certainly due to the DTA cell calibration, and all temperature should be increased by 5°C. Extrapolation shows the value at 601.8°C for the beta phase reaction and 576°C for the (Al)-silicon eutectic after adjustement according to DTA calibration.

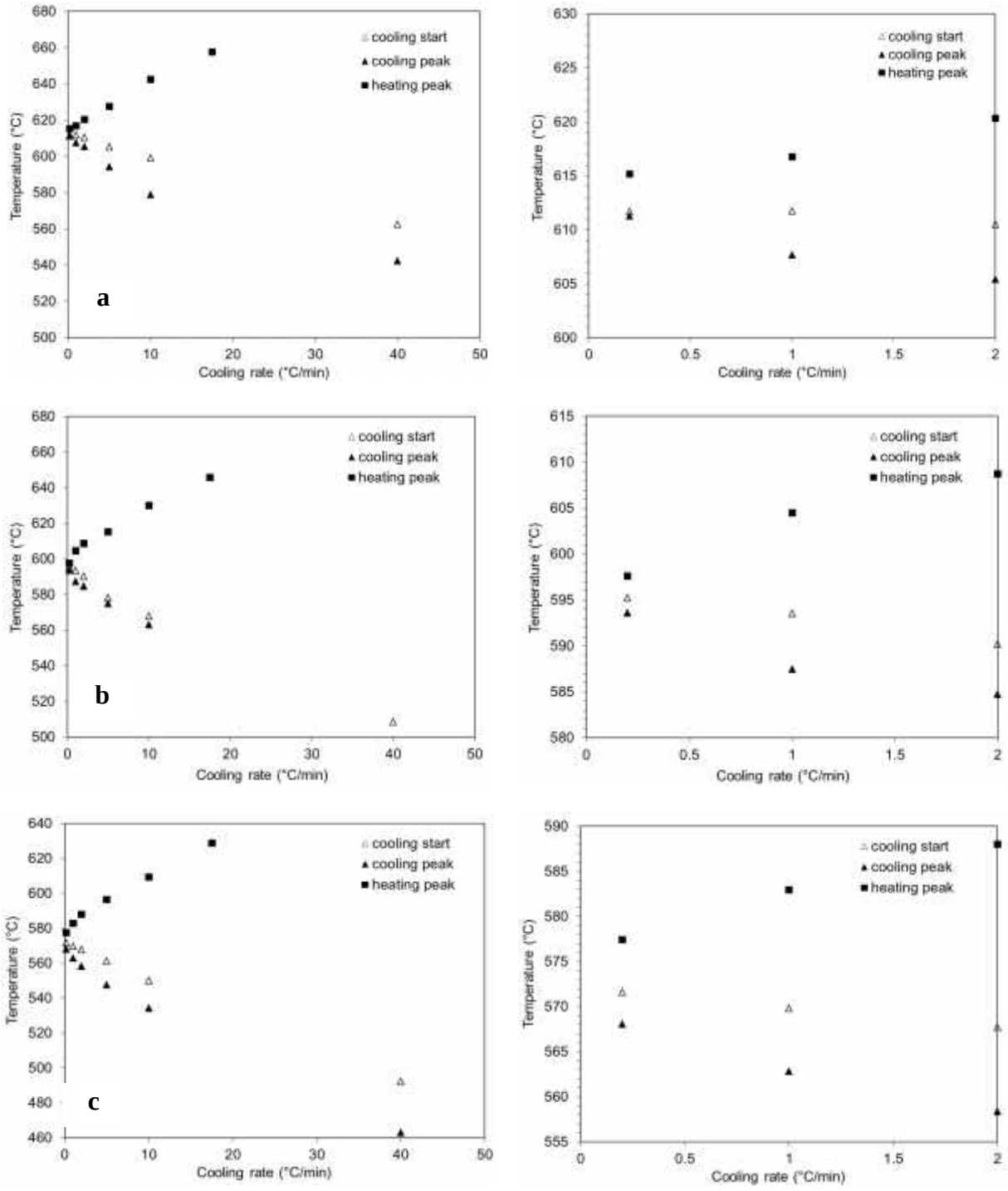

Figure 5.4. Effect of scanning rate on uncorrected characteristic temperatures (a). primary (Al), (b). beta phase formation, and (c). (Al)-Si eutectic reaction (right image is a zoom at low cooling rates)

5.2. DTA image analysis
5.2.1. 2D analysis

The DTA samples were prepared for metallographic observation under optical microscope and SEM for characterization of the beta phase. Micrographs showed the presence of beta phase, eutectic silicon and (Al) matrix. Figures 5.5, 5.6 and 5.7 illustrate the influence of cooling rate on the morphology of beta phase.

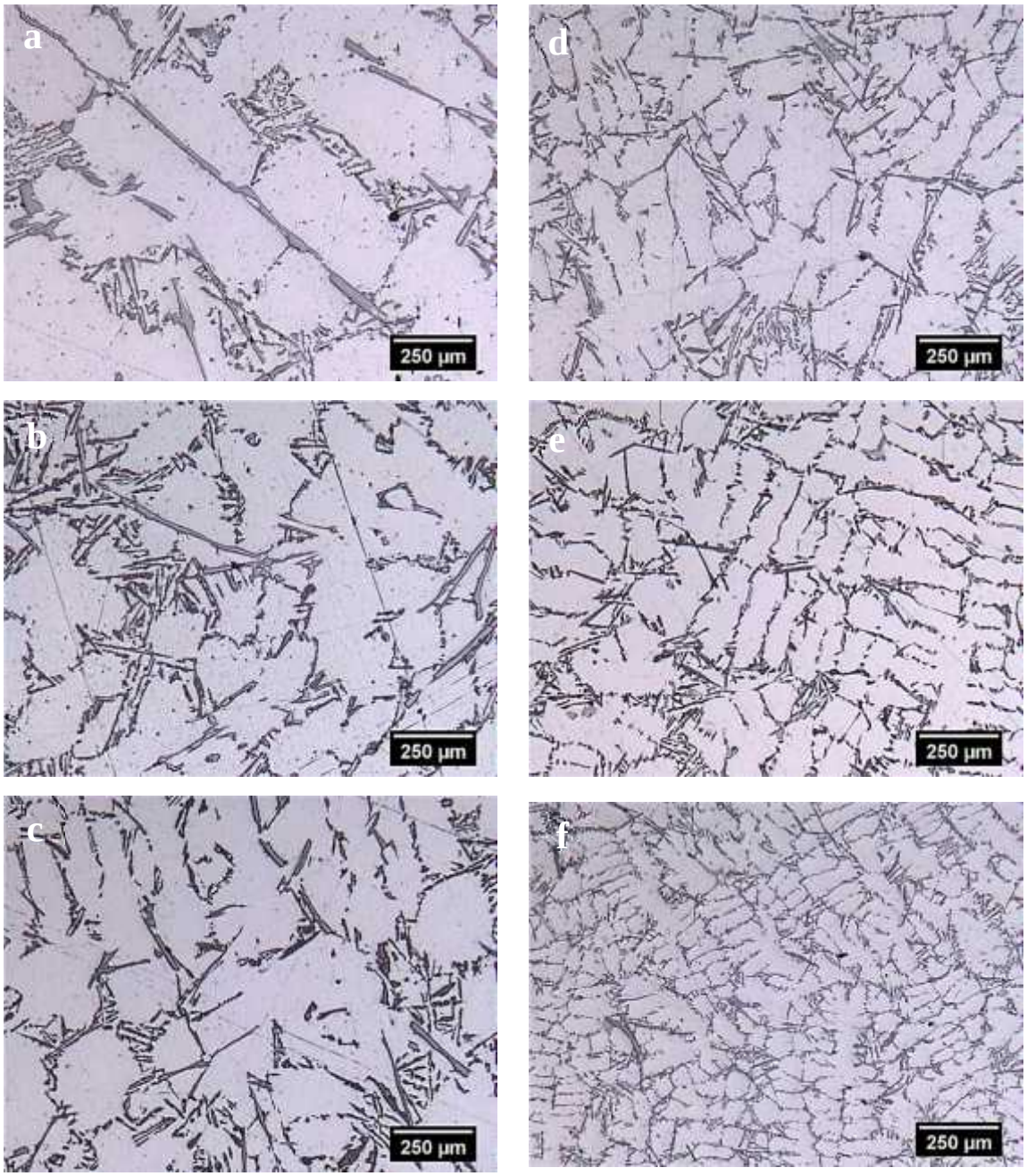

Figure 5.5. Micrographs of DTA samples cooled at various cooling rate (a) 0.2°C/min, (b) 1°C/min, (c) 2°C/min, (d) 5°C/min, (e) 10°C/min, (f) 40°C/min.

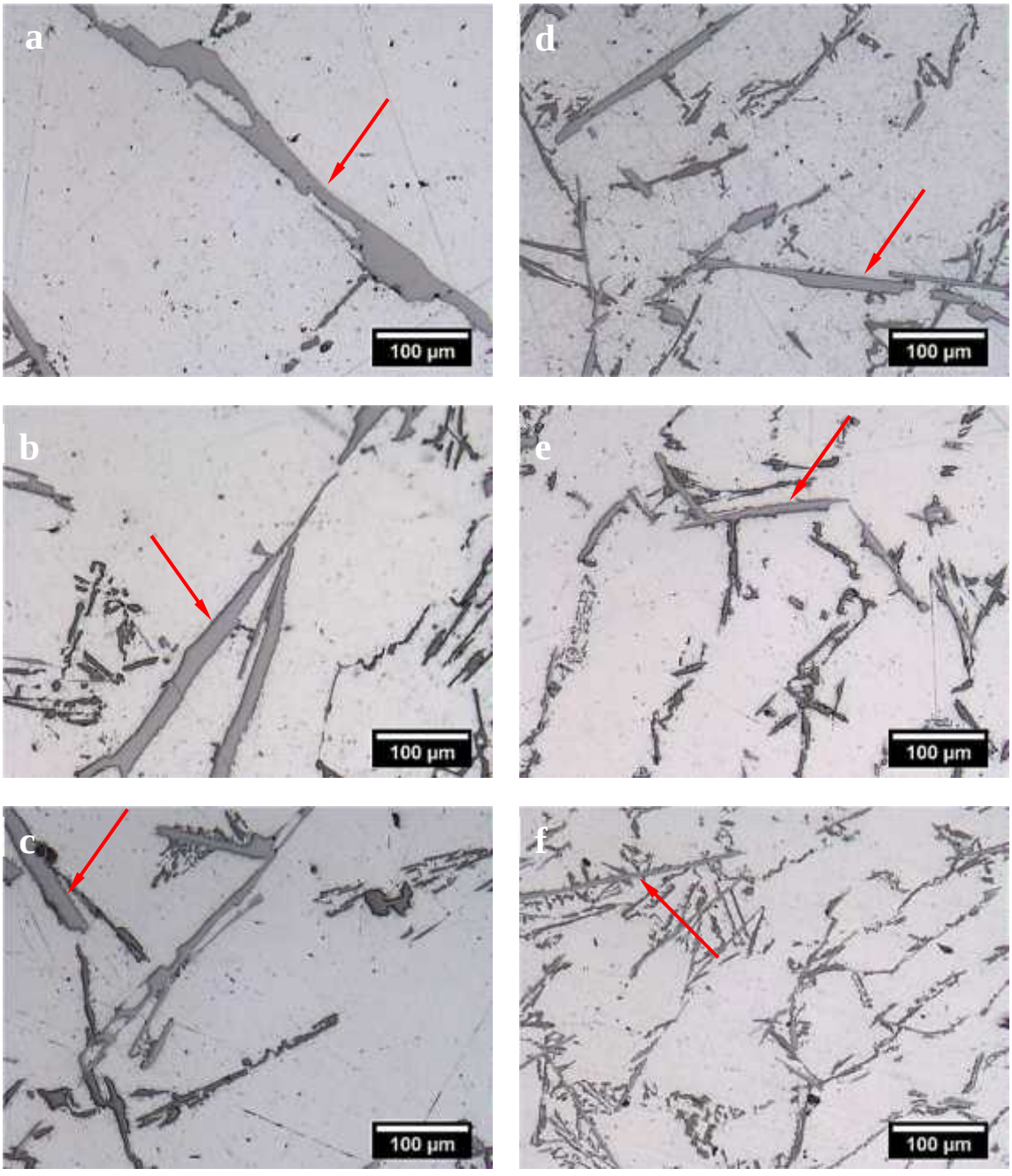

Figure 5.6. Micrographs of DTA samples cooled at various cooling rate at higher magnification (a) 0.2°C/min, (b) 1°C/min, (c) 2°C/min, (d) 5°C/min, (e) 10°C/min, (f) 40°C/min. Arrows indicate beta precipitates. The slightly darker precipitates are silicon lamellae.

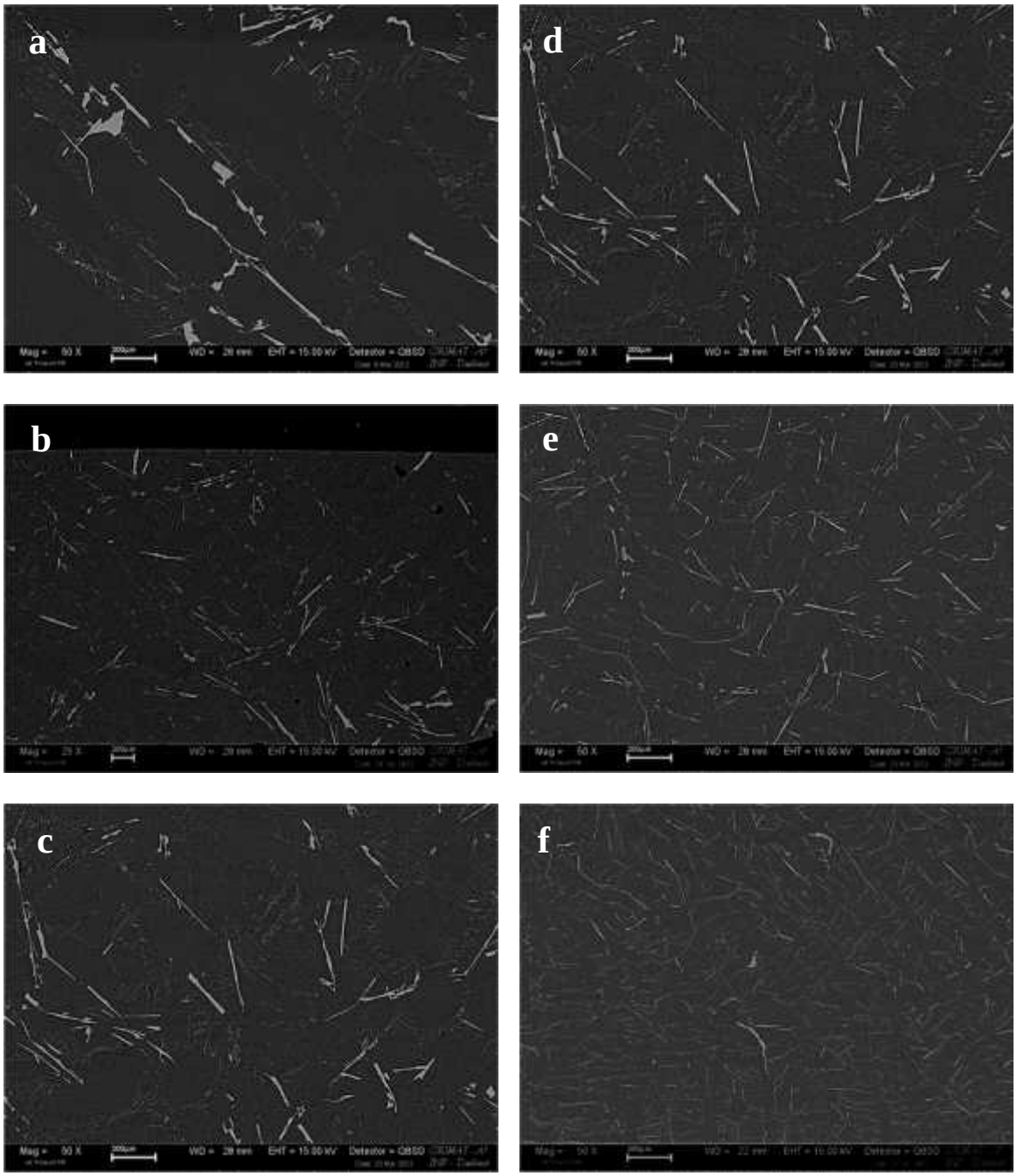

Figure 5.7. SEM micrographs of DTA samples cooled at various cooling rates (a) 0.2°C/min, (b) 1°C/min, (c) 2°C/min, (d) 5°C/min, (e) 10°C/min, (f) 40°C/min. Beta phase appear in light contrast.

In the sample with cooling rate of 0.2°C/min, the beta precipitates are seen to have long and thick needle-like morphology in 2D view. The beta phase size then reduced with the increase in cooling rate, as seen in the observation made in Figure.5.7 for sample with cooling rate of 40°C/min.

Beta phase volume fraction was evaluated from the SEM images and the analysis was carried out with Aphelion image analysis software. Series of operations such as threshold

segmentation and filtering were performed with the software to separate the beta phase from the matrix. The measurements were conducted by dividing the image cross section area into rows and columns, as seen in Figure 5.8, and labelled in numeric and alphabetic order. The total area observed was 3144 μm x 3072 μm (equal to 9.65 mm^2) for each sample. The volume fraction measurements for the two extreme cooling rates can be seen in Figure 5.9.

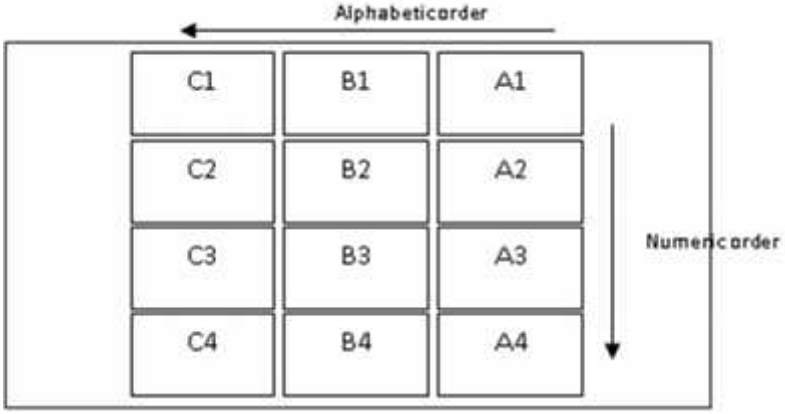

Figure 5.8. Illustration of measurement area within a sample cross section

Measurement of the volume fraction which was taken from cooling rate of 0.2°C/min showed a high fluctuation in the range from 1 to 4 pct. This scattering is also seen in samples at other low cooling rates. Apparently, the longer solidification time at low cooling rates allowed the beta phase to grow into large plates within the interdendritic regions. While the measurement taken at high cooling rate such as 40°C/min showed a more stable volume fraction with better distribution across the cross section, as indicated by low deviation value between the measured area, as seen in Figure 5.9b.

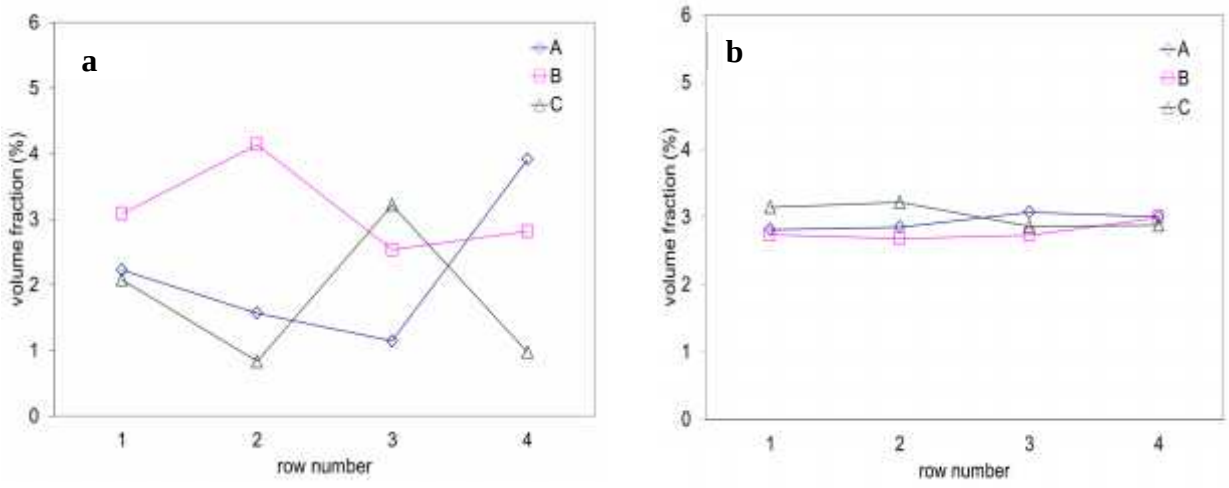

Figure 5.9. Volume fraction of beta phase for two cooling rates (a) 0.2 °C/min (b). 40 °C/min (x axis indicates the numeric order while the alphabetic order is represented by different symbols).

The total average volume fraction for all various cooling rates can be seen in Figure 5.10. The average value showed the range between 2.4 and 2.9 vol.%. The volume fraction appeared fluctuating with highest scatter at low cooling rates.

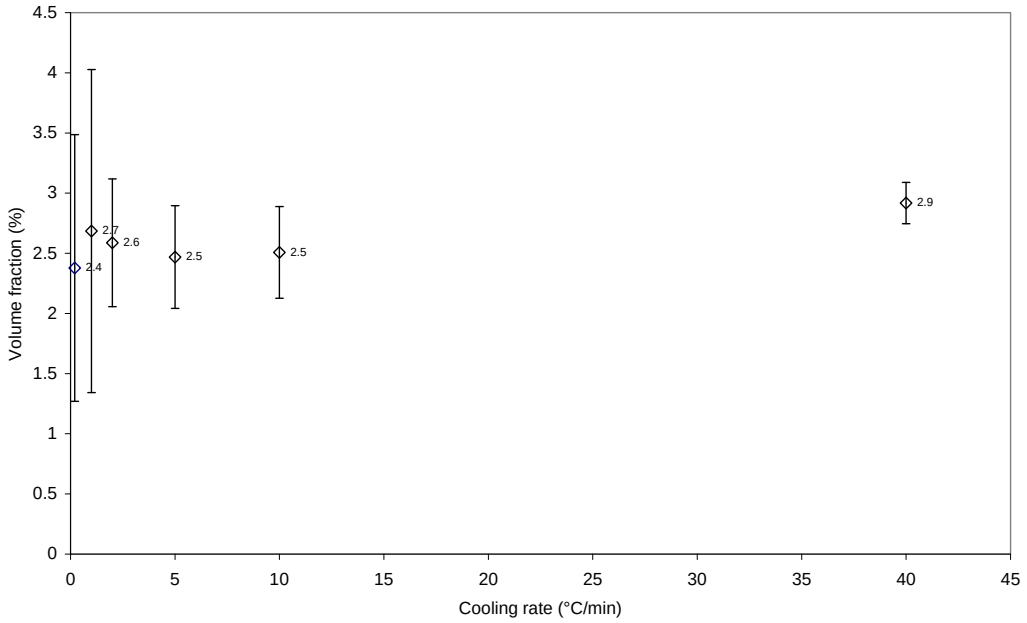

Figure 5.10. Comparison of average volume fraction in samples cooled at different cooling rates.

The beta phase length was evaluated from the same areas as for the volume fraction. The beta phase length was calculated from the data of maximum feret diameter acquired by the image analysis software. In the beta phase length evaluation, only the 5 longest beta phase particles from each sub-area were used. This method was selected to increase the differences between samples. Furthermore, this method could enhance the cooling rate effect on the beta phase morphology. Figure 5.11 shows the beta phase length decreases with increasing cooling rate from 1017 μm to 264 μm when the cooling rate changes from 0.2°C/min to 40°C/min.

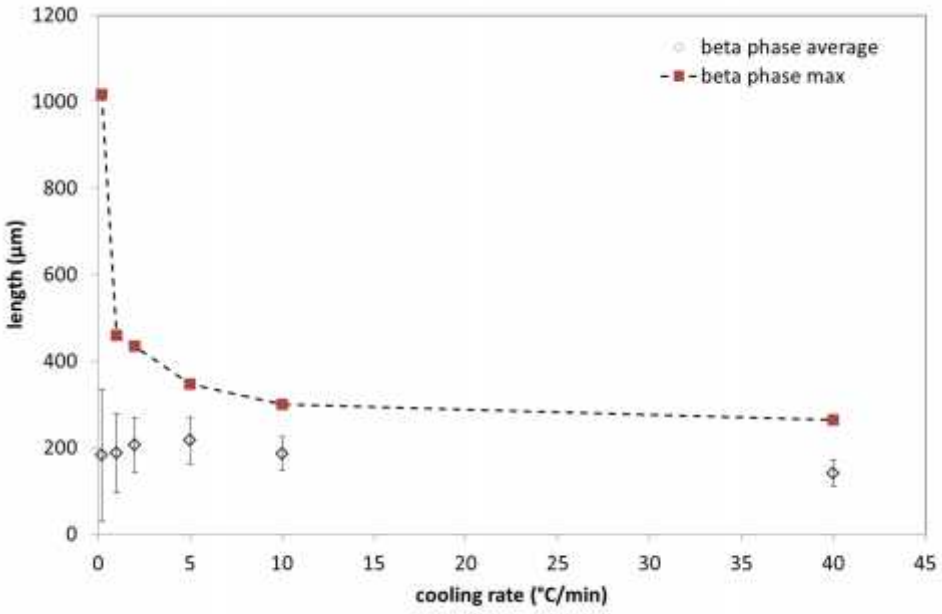

Figure 5.11. Evolution of the beta phase average length and maximum length in DTA samples cooled at various cooling rates.

5.2.2. 3D analysis – post mortem tomography.

Post mortem tomography was performed on the samples using a GE-Nanotom with the voxel size set at 2.5 µm, except for sample with cooling rate 40°C/min due to limitation in resolution of tomograph apparatus. Image treatment for beta phase morphology was performed by subtracting the beta phase through the use of sub volumes of size 1600x1600x800 voxels, with series of operations such as noise removal, median filtering and image stack which were performed with imageJ.

Further analysis was conducted by subjecting the 3D images to Aphelion software for further 3D measurement. Analysis for volume fraction was conducted by dividing the 3D volume into 8 parts, with 100 voxels in Z direction for each sub-volume. For visualization of beta phase morphology, we used the full image stack of 800 voxels in Z direction which gives a cylinder volume of approximately 25 mm^3. 3D rendering of volume reconstructed beta phase can be seen in Figure 5.12.

General view of the 3D images showed large plates for samples solidified at low cooling rate. Observation also showed that the beta phase appears to be surrounding the primary (Al) when blocked or restricted by the presence of (Al) dendrites. Impingement and branching was also observed between large beta plates. The results indicate that the beta phase plates grow in lateral direction is in agreement with the earlier finding by Dinnis et al. [7].

Cooling rate (°C/min)	Perspective view	Top view
0.2	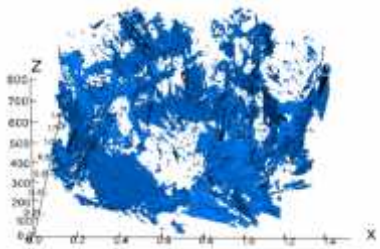	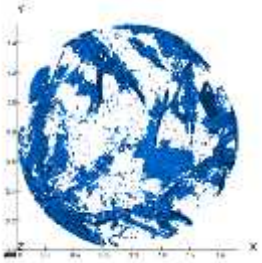
1	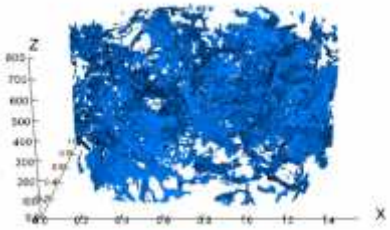	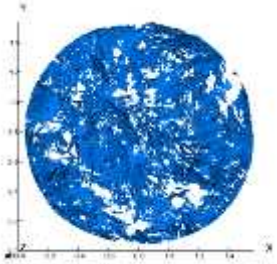
2	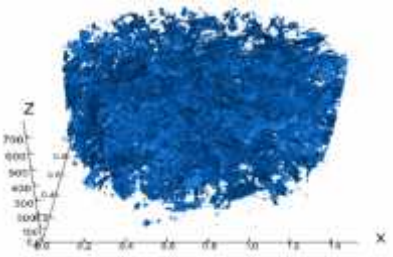	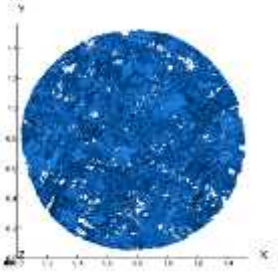
5	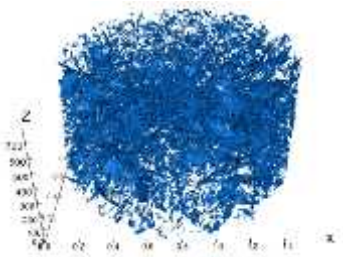	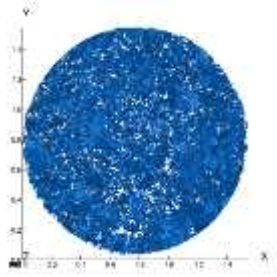
10	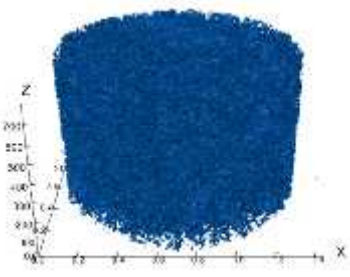	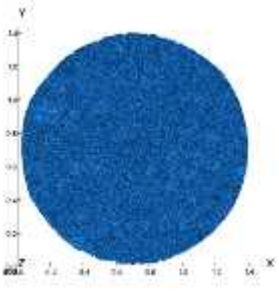

Figure 5.12. 3D rendering of beta phase for various cooling rates (voxel size in: 2.5 «m)

Figure 5.13 shows the volume fraction and surface area taken from 3D images. Volume fraction shows a consistent value for cooling rate of 0.2°C/min and 1°C/min, while the value increases for cooling rate 10°C/min. This is certainly related to the reduction in image quality of tomography images which causes the appearance of beta plates larger than their actual size. Beta phase morphology measurement was conducted for the 5 largest particles based on their surface area. The results showed the average beta phase surface area per plate decreases with the increase of cooling rate as expected. This is indicating that smaller beta particles are created as the cooling rate increases.

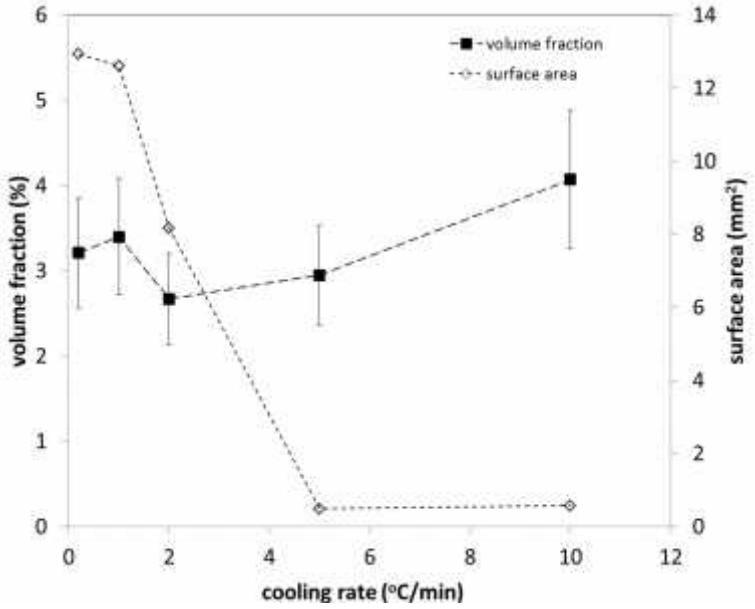

Figure 5.13. Overall beta phase volume fraction and surface area of the selected particles in 3D for different cooling rates.

5.3 In-situ Tomography

In this present work, the in-situ synchrotron tomography was recorded for a constant cooling rate of 10°C/min from the fully melt condition at 618°C to 575°C prior to the (Al)-Si eutectic reaction. The analysis will only focus on the precipitation and morphology of beta phase. Some original X-ray side view images can be seen in Figure 5.14. From these images, it was observed that the sample was bending and leant to one side due to volume shrinkage as the temperature cooled down. In these images, the beta phase can be seen as dark needles dispersed inside the sample.

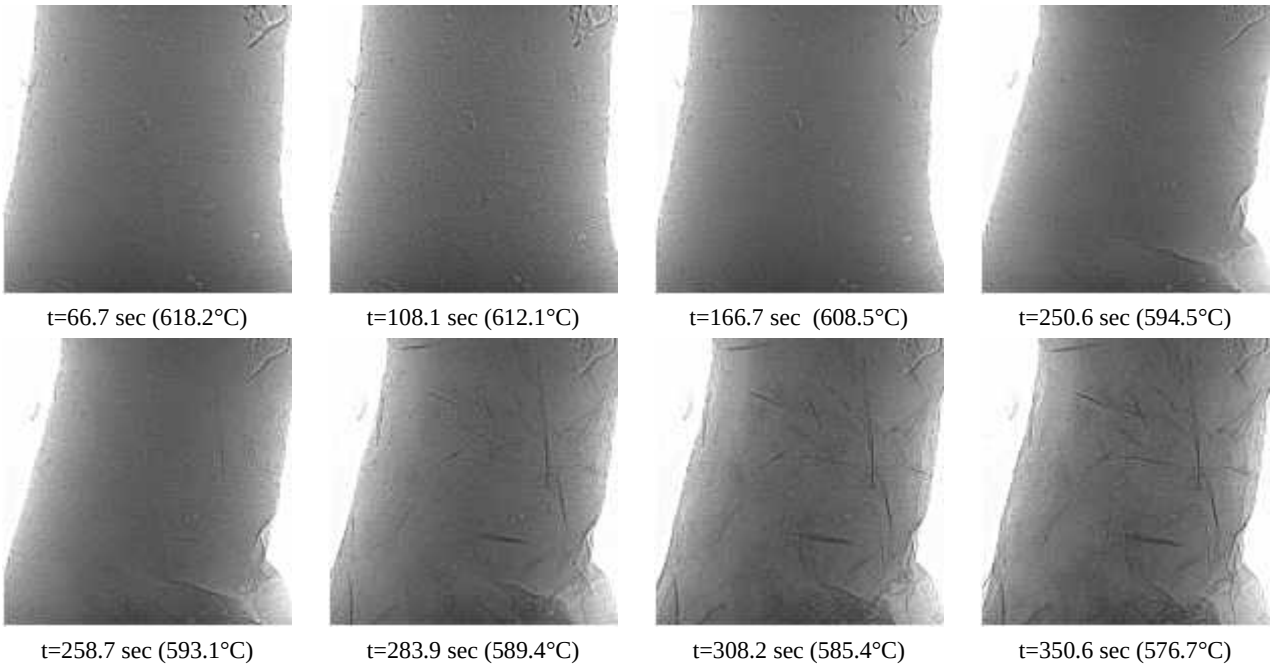

Figure 5.14. Original X ray 2D images from side view. Notice the shrinkage and bending of the sample during the solidification process.

The original X-ray images were then used for creating a reconstructed volume of 1008x1008x1008 voxels, with a voxel size of 1.1 μm. Analysis to the reconstructed volume tomograph showed the precipitation of primary (Al) dendrites at 608°C. The nucleation of beta phase occurred in several locations and started at 593°C. The beta phase growth occurred in interdendritic regions along with the continuing growth and coarsening of the primary (Al) dendrites. A single horizontal slice of the reconstructed volume selected from the middle of the sample can be seen in Figure 5.15.

In order to have more details about the beta phase growth, the data was treated with image analysis by extracting the beta precipitates through series of operation similar to the previous method using imageJ and Aphelion. Due to the similar white colour contrast of beta phase with the oxide skin, an additional masking operation consisting of a Gaussian-blur filtering, thresholding, iteration of erosion and dilation was added to remove the outer oxide layer. The analysis on the nucleation of beta phase was limited to a region of interest of 1008x1008x500 voxels. The volume was normalized to the solid sample cylinder shape; therefore the rendered volume is equal to 0.67 mm^3 taken in the middle region. This limitation was used to reduce the computational load for treating the images and calculation by image analysis. The 3D volume reconstructed rendering of in-situ tomograph can be seen in Figure 5.16.

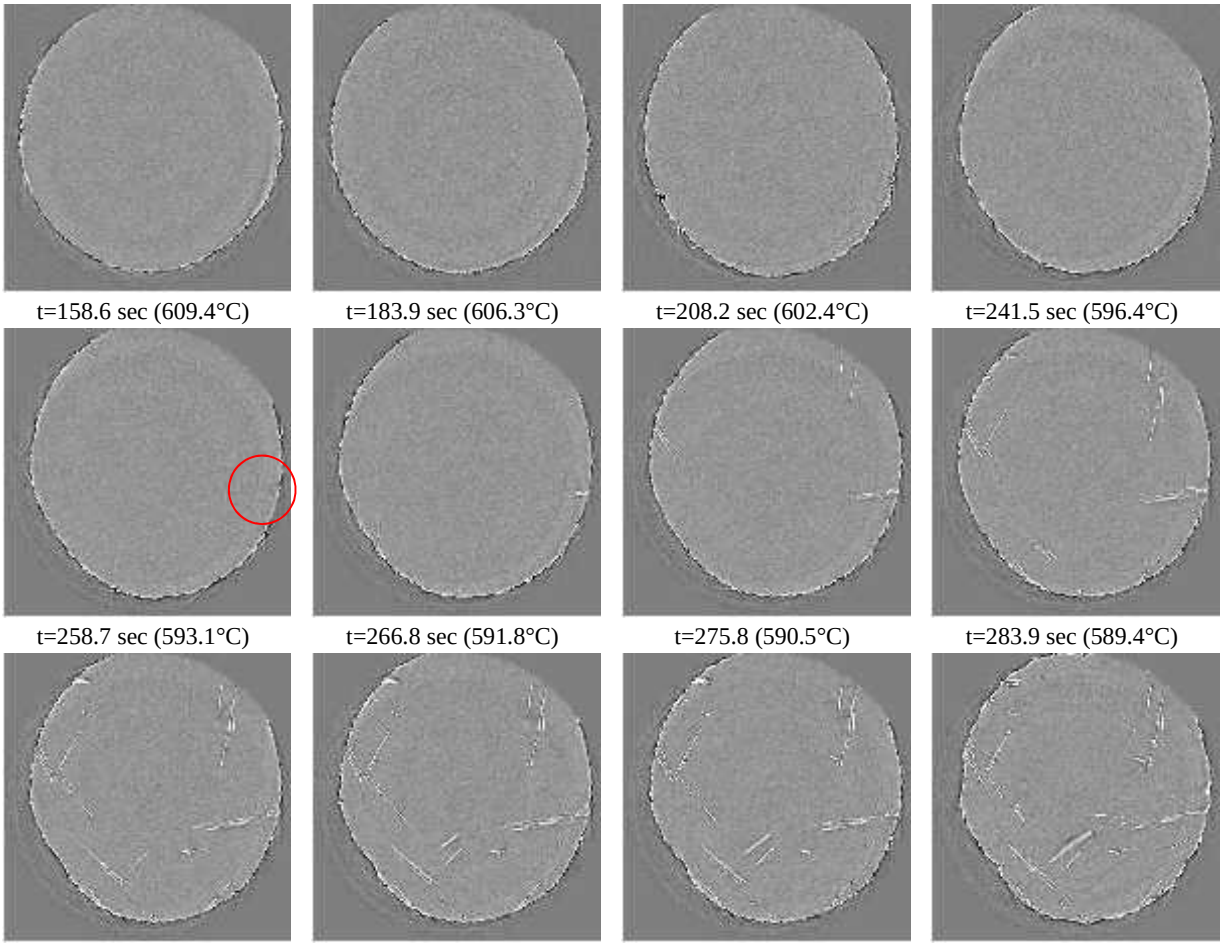

Figure 5.15. Image slices horizontally extracted from the middle of the reconstructed volume obtained during in situ solidification of Al6.5Si1Fe. The image corresponding to the first beta phase nucleation is marked with red circle.

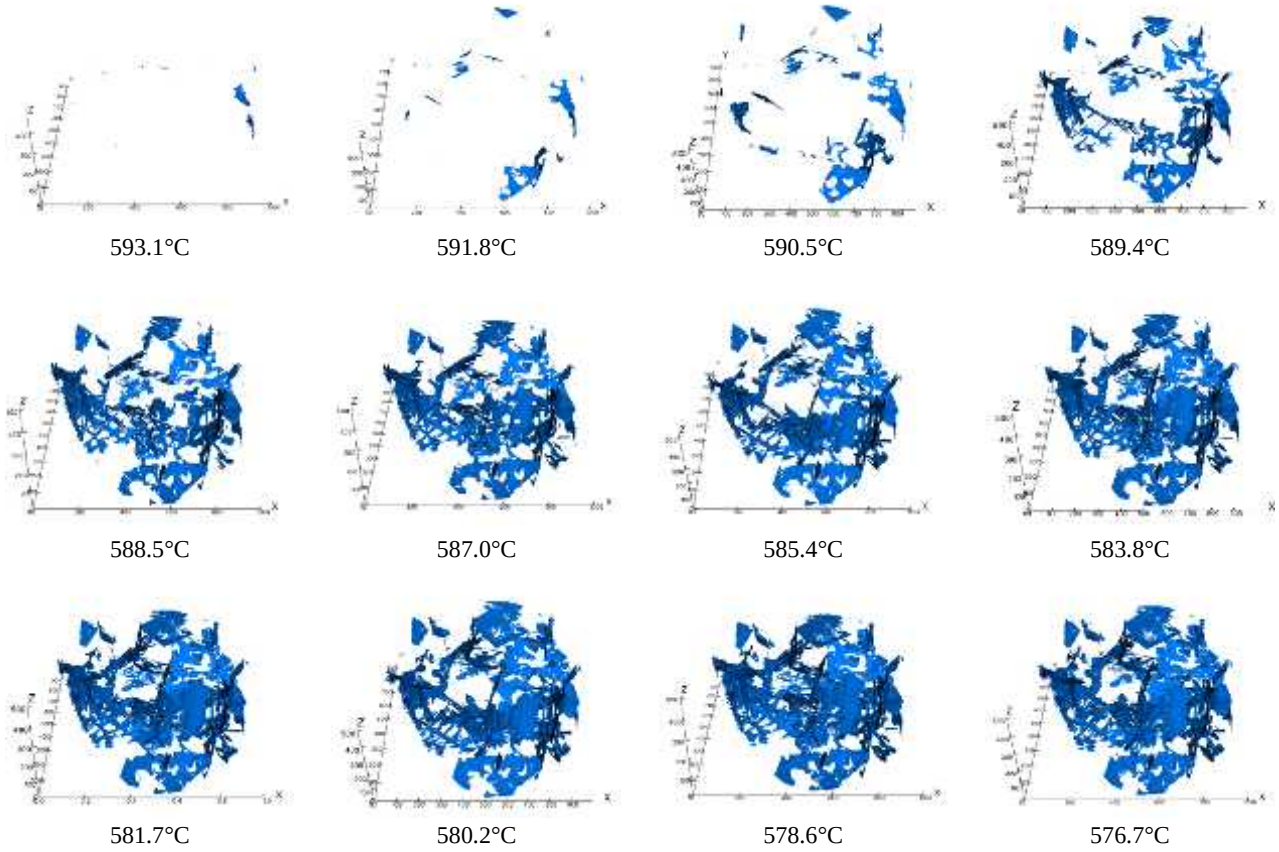

Figure 5.16. A series of 3D reconstructed of beta phase from the tomography image showing development of beta phase during solidification.

5.4. Discussion.

5.4.1. Cooling rate effect on beta phase.

All the DTA records have shown the same features regardless the scanning rate. Observation showed that the curves both upon heating and cooling become wider as the scanning rate increases. An interesting discovery related to the precipitation of beta phase is seen in the thermogram. The difference in temperature between onset and peak of the thermal arrest associated with beta precipitation appears small in comparison with primary (Al) or eutectic silicon reaction. This narrow temperature range for beta precipitation is related to the nature of beta growth morphology and volume fraction of the phase in the liquid bulk.

A comparison of solidification path as observed by DTA was made with thermodynamic calculation using Thermocalc. Both calculated and DTA experiment derived the same solidification sequence. The calculation following the equilibrium (Lever rule) and Scheil's equation using TCAl2 and COST 507 database are both shown in Figure 5.17.

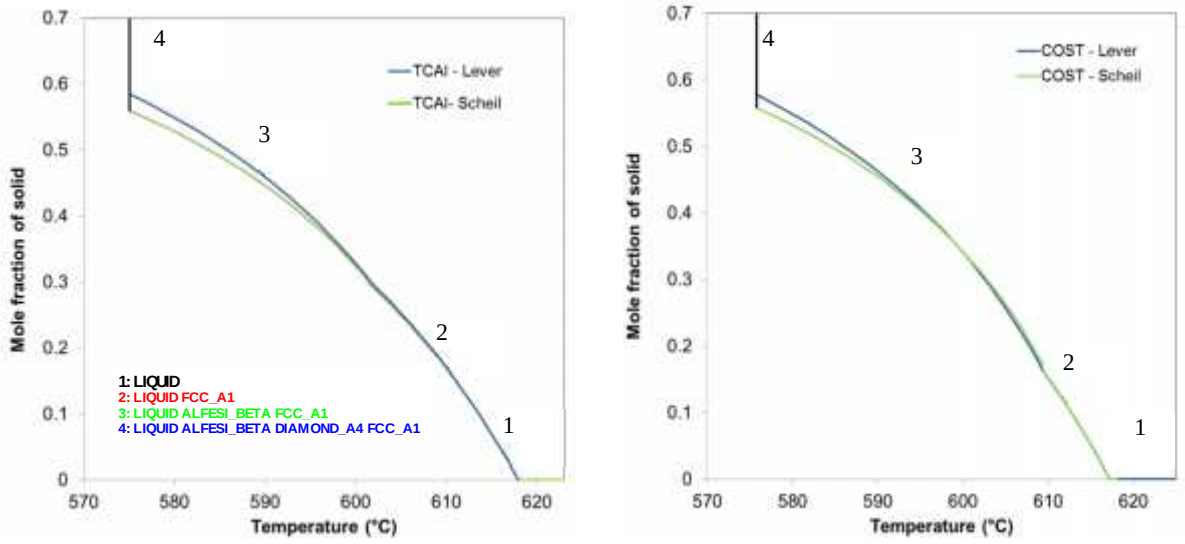

a. **b.**

Figure 5.17. Thermocalc calculation for beta phase precipitation for Al-6.5Si-1Fe (a) TCAl2 database, (b) COST 507 database.

Thermodynamic phase prediction based on solidification path with Scheil model and lever rule showed that both models follow the same path, as illustrated in Figure 5.17. The solidification path indicated that the beta phase precipitates prior to the eutectic (Al)-Si reaction. Lever rule calculation according to TCAl2 database shows that solidification starts with primary (Al) at 617.9°C and continues with beta phase formation starting at 601.7°C and at a solid fraction of ~0.29. With COST 507 database, the formation of beta phase starts is at 609.4°C which is 7 °C higher and at solid fraction of ~0.16. No other iron rich phase was predicted by the calculation for either solidification paths. DTA showed results very similar to prediction with the more recent database of TCAl2.

The effect of cooling rate on beta phase size is found similar to previous reports by Khalifa et al. [8] and Narayanan et al. [9]. In current experiments, the results revealed that, as the cooling rate increases, the beta phase appears shorter and more homogeneous in length and volume fraction, as illustrated in Figures 5.10 and 5.11. It is seen that as the cooling rate increases some nucleation sites for the beta phase appeared in the bulk that were distributed evenly within the sample away from the skin as seen in Figure 5.12. However at high cooling rate, it might be that part of the precipitated beta plates did not have enough time to get full extension. Then the excess of iron will participate to 3 phase eutectic precipitation during the (Al)-Si-β invariant reaction.

The nucleation site for the beta phase appears to be from the outer oxide surface (skin), followed by the beta phase expanding in radial direction toward the sample center, as

observed in sample with 0.2°C/min cooling rate. Accordingly, high volume fraction of beta phase was observed in the region adjacent to the skin oxide surface which is expected to have solidified first. Tomography observation at low cooling rate showed only a small fraction of independent beta precipitates not associated with the larger plates that nucleated from the outer skin. Interestingly, analysis to the growth path shows no direction preference of the beta precipitates, this could be due to the small space left in interdendritic regions which were already occupied by primary (Al) dendrites. Also in some cases, the beta phase appeared curved with changes in growth direction. Branching could often be related to the blocking of beta precipitates at the (Al) solid/liquid front. Observation also showed some small beta particles which did not develop into large plates in the interdendritic region in the sample cooled at 0.2°C/min.

At higher cooling rate, the initiation of beta precipitates seemed dispersed within the sample, between the (Al) dendrites. Unfortunately, the image quality generated by tomography is inadequate for detailed analysis of small beta precipitates because of the low spatial resolution capability of the tomograph (voxel size 2.5 μm).

Moreover, high cooling rate not only reduced the size of the beta phase precipitates, but also led to smaller dendrite arm spacing (DAS). Smaller DAS controlled the distribution of porosity and the dispersion of second phase particle [10]. Increasing the cooling rate in general will increase nucleation primary of (Al) and decrease the DAS. As a consequence, more finely distributed interdendritic regions would limit the beta phase growth due to less space within the interdendritic liquid between the (Al) dendrite.

5.4.6. Tomography cooling curve

Analysis to the cooling curve showed thermal arrests correlating to the nucleation and phase precipitation. In Figure 5.18 some undercooling is detected associated to the arrest that relates to nucleation of primary (Al) dendrites at 611°C. However the corresponding tomograph image did not show any primary (Al) precipitation. This could be related to the limited region of interest selected in the observed volume and the location of the inserted thermocouple. While for the cooling curve the data were recorded every second, the tomograph data was recorded within several seconds for each step. Therefore, the first nucleation event might have occurred earlier than the image capture in the tomography images. Precipitation of beta phase was recorded at 258 sec (593.1°C) in tomograph, while the curve showed the first nuclei for beta phase has appeared at 254.6 sec (593.8°C) (marked with red circle).

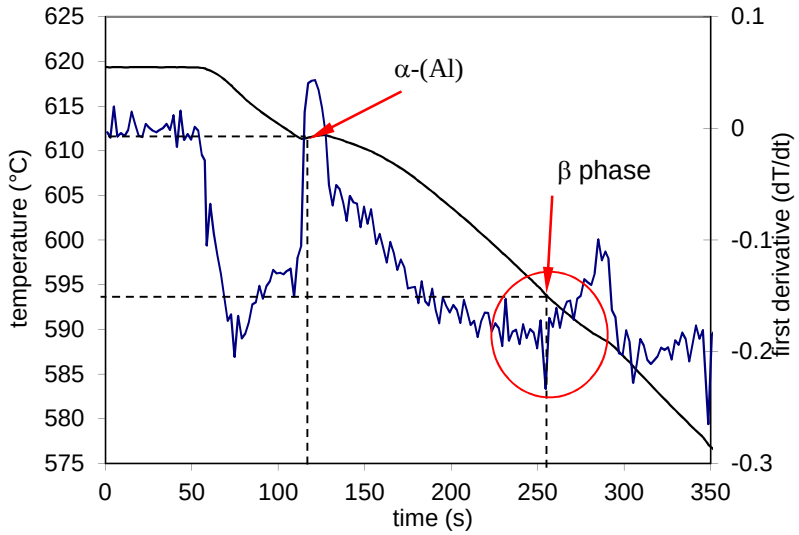

Figure 5.18. Tomograph cooling curve and first derivative of solidification Al-6.5Si-1Fe during the tomographic experiment.

The recorded temperature from the tomograph is lower compared to the data from thermodynamic software or DTA experiment, as seen in Table 5.4. This difference is due to the solidification undercooling phenomena where the experiment was performed at 10°C/min and the depression could be enhanced by the time lag in the thermocouple measurement. Nevertheless, it should be noted that the difference in liquidus temperature and beta precipitation is about the same.

Table 5.4. Comparison of the characteristic temperature of tomograph cooling curve with DTA experiment and thermodynamic calculation

Event	Time (s)	Temperature (°C)		
		In-situ tomography	DTA	TCAL-2
Start of scan	0.0	618.2	-	-
Observed α-Al dendrite	166.77	608.5	617.7	617.9
Observed β- $Al_9Fe_2Si_2$ nucleation	258.7	593.1	601.8	601.7
Saturated growth of β-$Al_9Fe_2Si_2$	300.3	587	-	-
End of scan	358.7	575.2		

5.4.2. Nucleation and growth of beta phase

Figure 5.19 shows the nucleation of beta phase from in-situ tomography, with each separate particle coloured differently. The first observed nucleation appeared in five sites at 593°C located on the outer oxide skin (due to oxide skin removing operation and weak phase contrast, some of the initiation sites were diminished during image analysis).

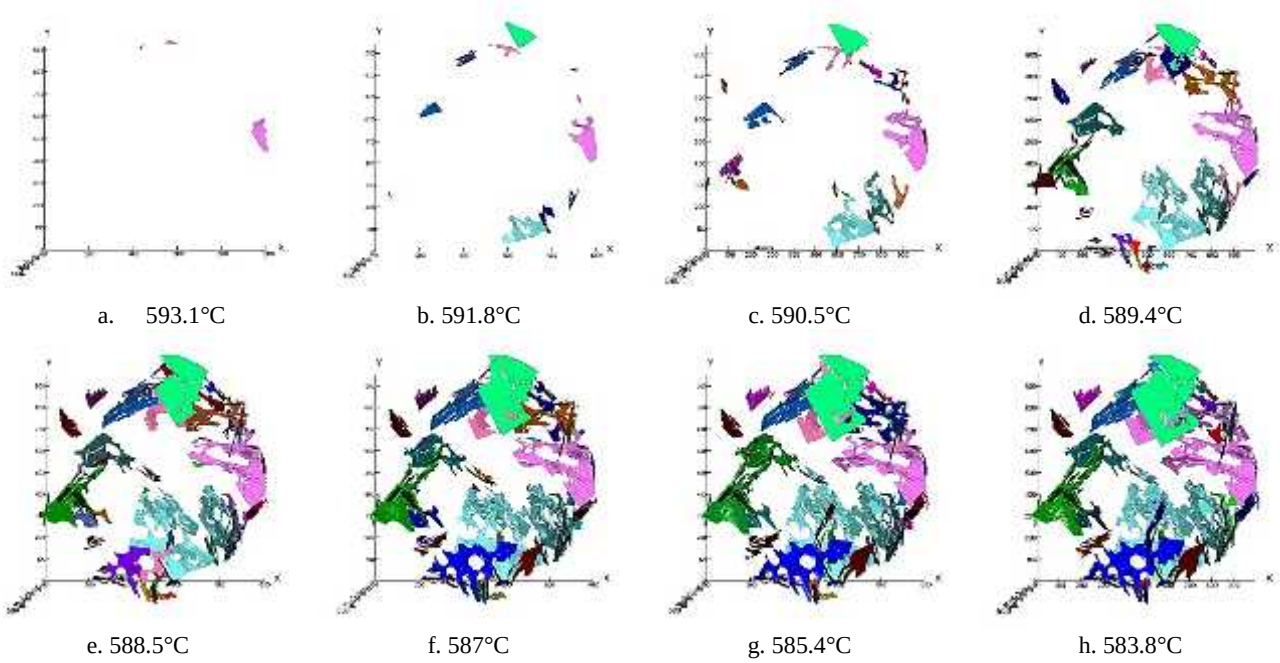

a. 593.1°C b. 591.8°C c. 590.5°C d. 589.4°C

e. 588.5°C f. 587°C g. 585.4°C h. 583.8°C

Figure 5.19. 3D visualization of beta phase nucleation where each colour represents single beta particle. Note that some particles impinged and connected in later stage.

As the solidification progresses, a rapid increase in the number of nucleation particles was detected and this continues until saturation. Observation showed no new nucleation below 587°C and notice was made of the rapid growth of beta phase. It is well known that the beta phase growth is characterized with high lateral growth rate. Analysis on the region of interest indicated that approximately 32 nucleation events of beta particles in total were observed during the solidification process as seen in Figure 5.20.

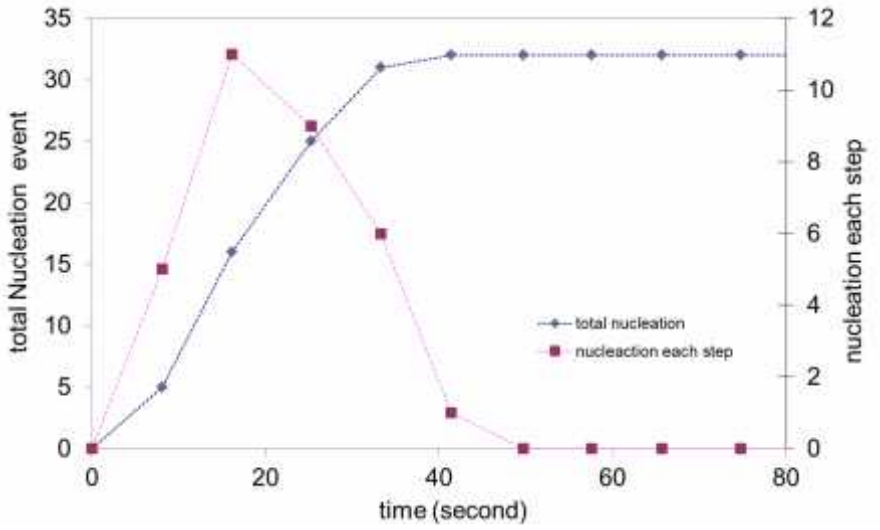

Figure 5.20. Nucleation event of beta in the sample region of interest.

A series of growth steps of a single beta phase are shown in Figure 5.21. The time scale was set from the first time the beta phase nucleation was observed, with zero value at the step before the observed beta precipitation. Examination of a single nucleation showed that a quick growth of beta phase occurred, where the phase length increases twice in one tomography step (approximately 2°C) as observed in early growth stage. The lateral growth begins to slow down as the temperature reaches 585°C.

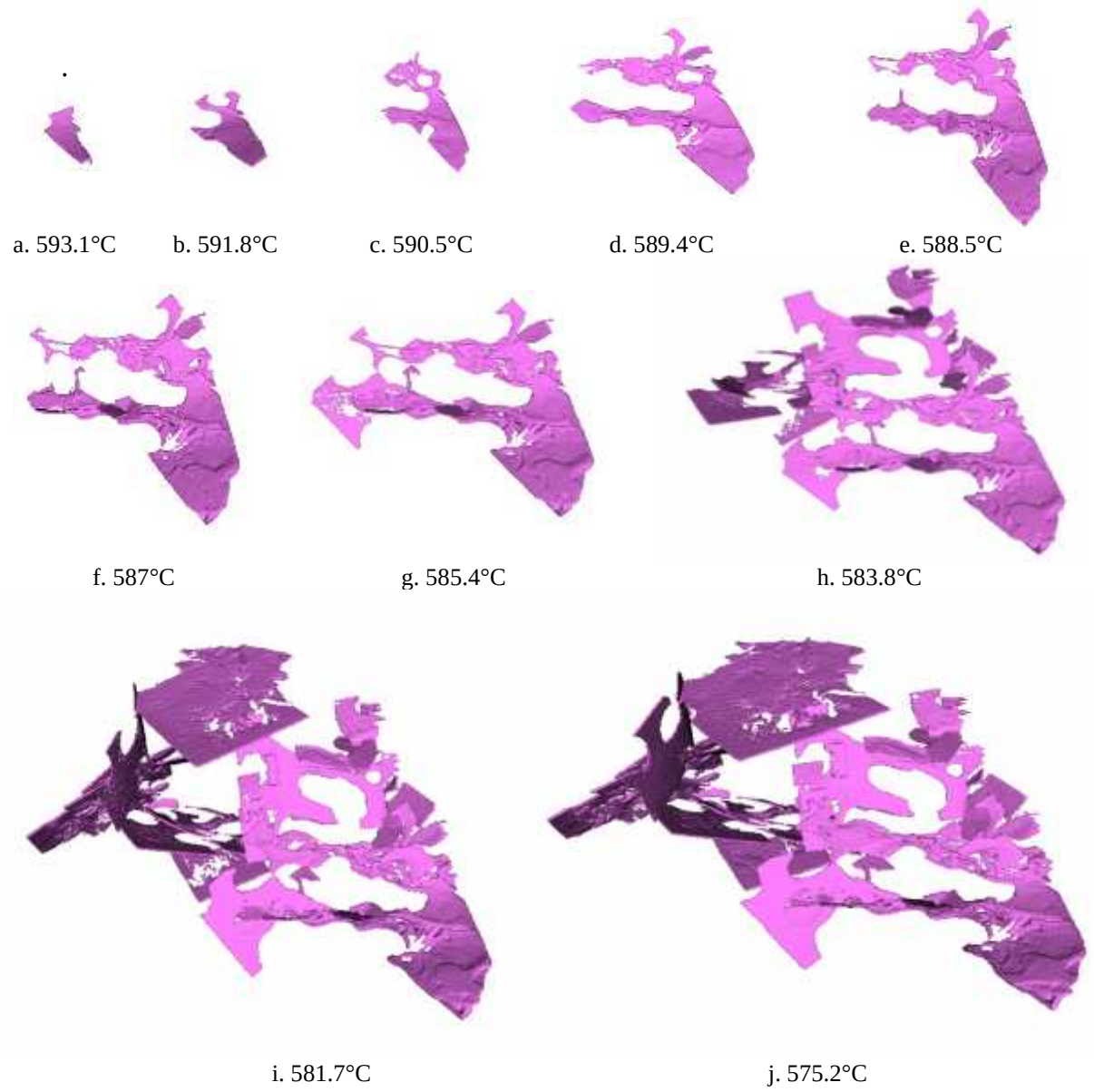

Figure 5.21. A series of reconstructed 3D images from a single nucleated beta precipitates taken at several steps during growth. As the solidification continues other precipitates got connected to the selected one. (Voxel size 1.1 «m)

As seen from the images, sometimes the dendrite arm of primary (Al) blocked their growth during the growth stage of the beta plate. However observation showed that the beta phase growth continues by surrounding the dendrite and some of the precipitates reconnected after passing the obstacle. During the course of the growth some branching and bending were also observed. Branching was noticed in intermediate stage growth and the interconnectivity was increased in later stage as the temperature dropped and the connection between precipitates created clusters of large beta precipitates.

In comparison to the tomography information from the post mortem analysis which used DTA samples, in-situ tomography data showed that the beta phase nucleated preferentially on the oxide skin surface, while in DTA some of the nucleation events occurred in the bulk. This could be explained by considering the volume of the sample used for in-situ tomography, where the sample diameter was only 1 mm, therefore the surface area to volume ratio of the sample is larger compared to DTA samples which reduces the possibility for the nucleation in the bulk of the sample. Furthermore, the beta appearance in the bulk could be related to three phase eutectic beta phase.

The lateral length measurements were taken from several beta precipitates at each tomograph step. From these length measurements, five beta particles labelled 1 to 5 were selected related to beta early nucleation for further analysis of their growth kinetics. The value acquired was in pixel and converted into μm. Three particles appeared at a same time step and the two others at the next time step. The complexity of beta phase morphology and growth orientation is causing difficulty for the correct measurement of the precipitates and for determining the exact location in the phase for maximum observed length. Other than that, during the course of solidification, some of the particles merged which made them unavailable for their complete length measurement. In general, we could classify the beta phase growth into three stages based on the length curve shape as: initial stage (I), peak stage (II) and decline or saturation stage (III), as seen in Figure 5.22.

The lateral growth of beta phase was highly influenced by the alloys chemical composition especially Fe content and the cooling rate during solidification. Data shows the beta phase grows first at high velocity. Other authors have reported similar finding regarding the beta phase growth behaviour in Al-Fe-Si-Cu alloy with a maximum growth rate up to 100 μm/s slowing down to 10 μm/s near the end of growth for a cooling rate of 20°C/min [11]. The measurements of beta phase growth during solidification step in tomography produce some bias because the acquisition corresponds to a 180° rotation. During the rotation, the beta continues to grow which makes some bias regarding the correct morphology and correlation

to the recorded time [12]. Therefore, the actual lateral growth of the beta might be higher than recorded. An error bar has accordingly been defined along the time axis in Figure 5.22. The error bar assumed that the beta phase grows occurred continuously during the image capturing in a single tomography step. The software then performed the reconstruction for 3D volume without information of the precise time corresponding to the recorded image.

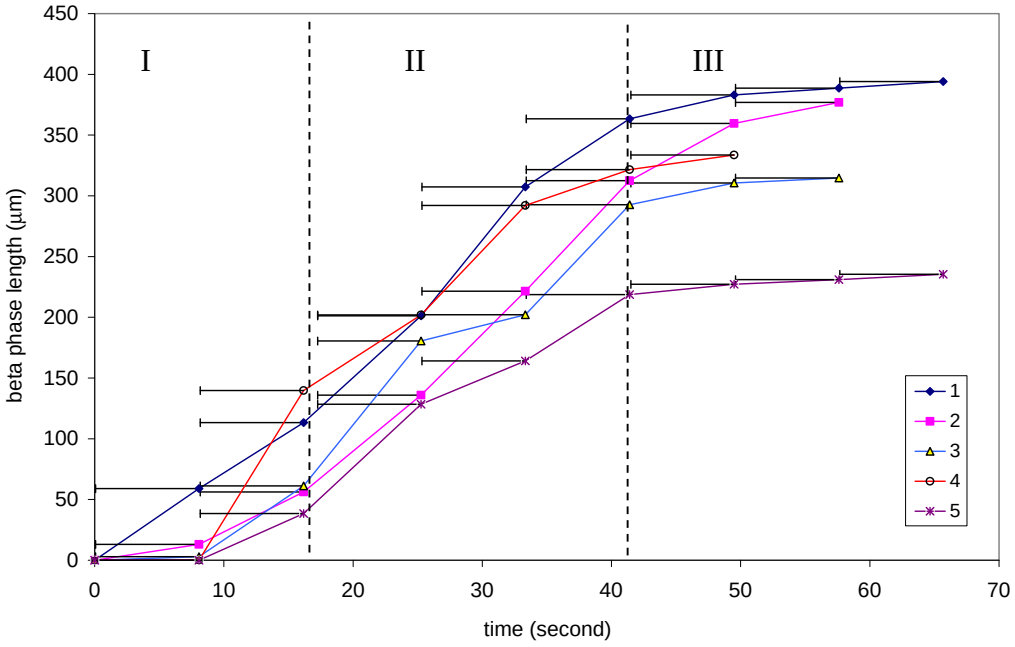

Figure 5.22. Evolution with time of the maximum length of selected beta precipitates

Figure 5.23 shows the growth rate value corresponding to data in Figure 5.22. Most of the precipitates reached saturation level after 40 second from the first observed growth of beta phase (587°C). After t = 40 second, all the precipitates have already reached saturation, this lack of driving force can be related to the high solid fraction in the liquid bulk. No new beta phase nucleation event occurred beyond that time as already illustrated in Figure 5.19. Individual analysis of 5 beta particle showed that the lateral growth rates varied among them and this variation was also seen between each step. The lateral growth was calculated with assumption that the recorded tomography image was taken in the middle of a single tomography step. The result showed the highest detected rate in stage I was at 34.5 µm/s (2070 µm/min). The rate then fluctuated in stage II within the range of 5-25 µm/s, and finally decreases at stage III. The variation between steps from a single precipitate could be caused by the blockage of (Al) dendrite and other obstacles in the interdendritic region that slowed down the growth rate.

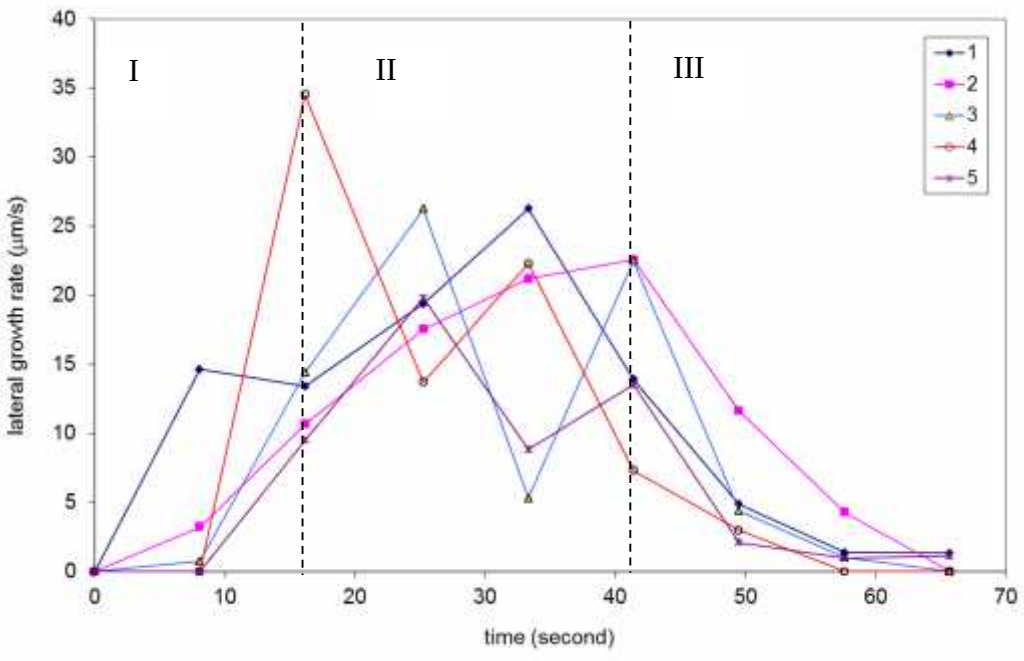

Figure 5.23. Lateral growth rate analysis of individual beta precipitates

5.4.3. Thickness features characteristic of beta phase

Beta phase thickening mechanism appeared to proceed by step growth, as illustrated in Figure 5.24. The step height indicated a certain thickness is required before the lateral growth progresses. For that purpose, the thickness of beta precipitates was measured on 3D images using imageJ with local thickness plug-in [13] developed based on the work of Hildebrand and Rüegsegger [14] and the data was rendered with volumeJ [15].

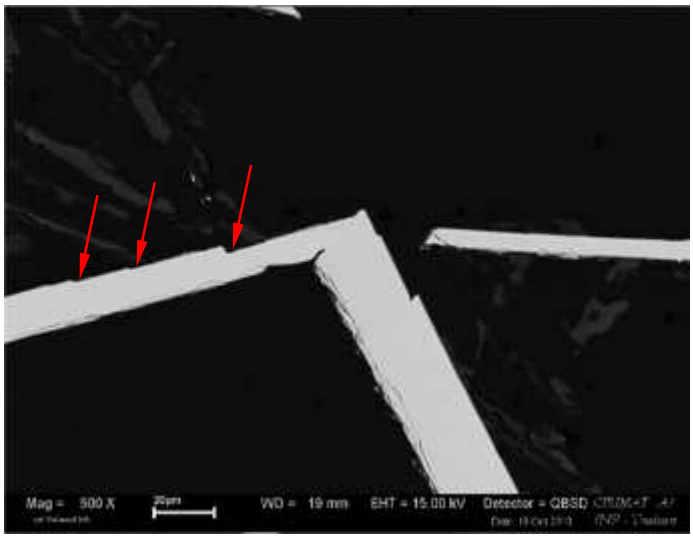

Figure 5.24. SEM micrograph showing growth step of beta precipitates (red arrows)

The analysis was performed on a sub-volume of 1008x1008x200 voxels. Prior to the analysis, imageJ noise reduction by removing individual pixels with the size of 1 in 2D was applied to the image. The thickness evaluation was limited by the resolution ability of the tomograph voxel size which is 1.1 μm for one voxel. The result for 3D thickness mapping can be seen in Figure 5.25.

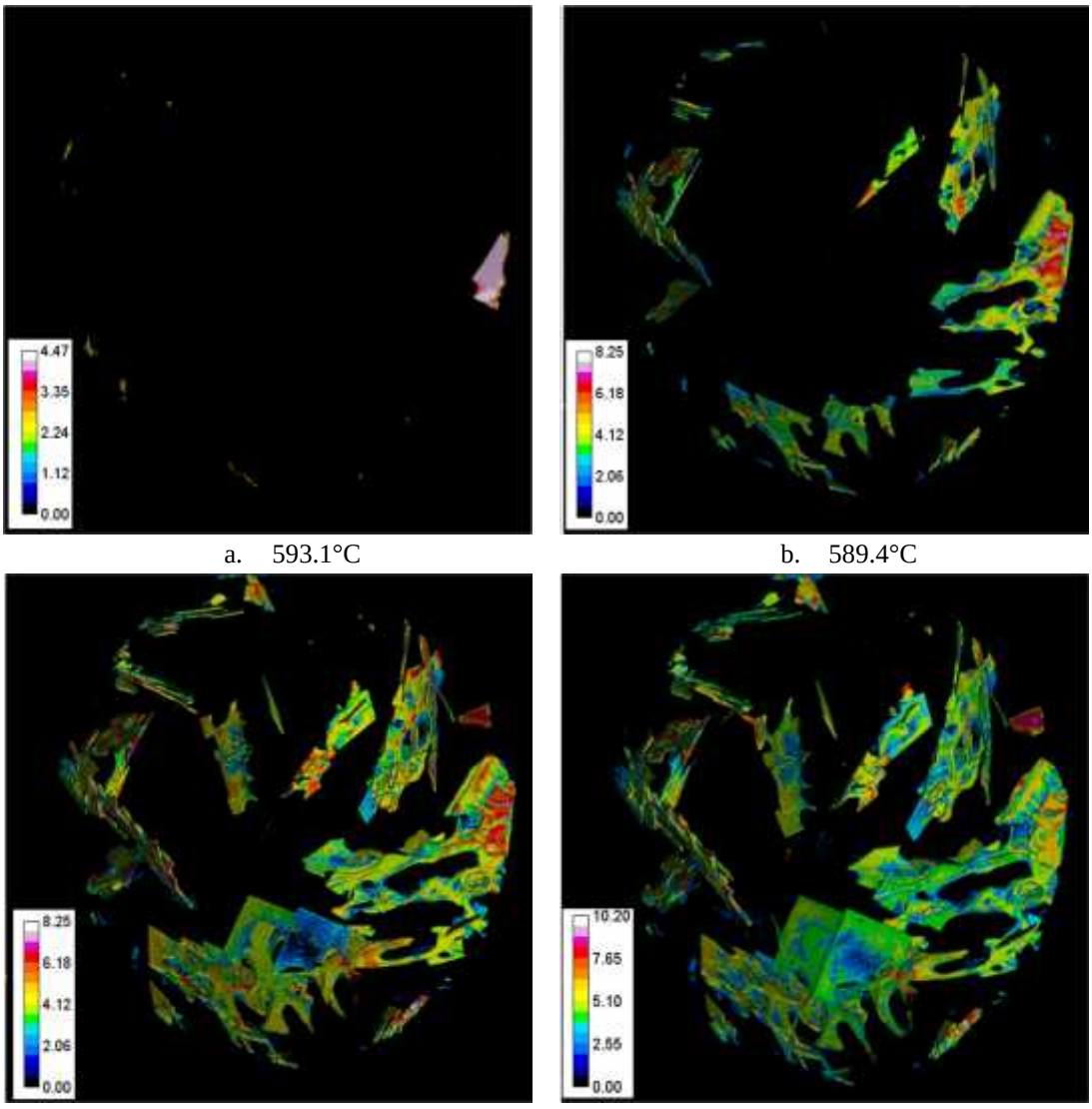

a. 593.1°C b. 589.4°C

c. 583.4°C d. 576.7°C

Figure 5.25. 3D rendering of thickness mapping of the beta phase taken at different growth steps. (the legend is in pixels)

Mapping of the thickness distribution from the histogram of local thickness from image in Figure 5.24 showed that three peaks corresponding to the thickness ranges of 4.5-4.99, 6.5-6.99 and 9.5-9.99 μm, as seen in Figure 5.26.

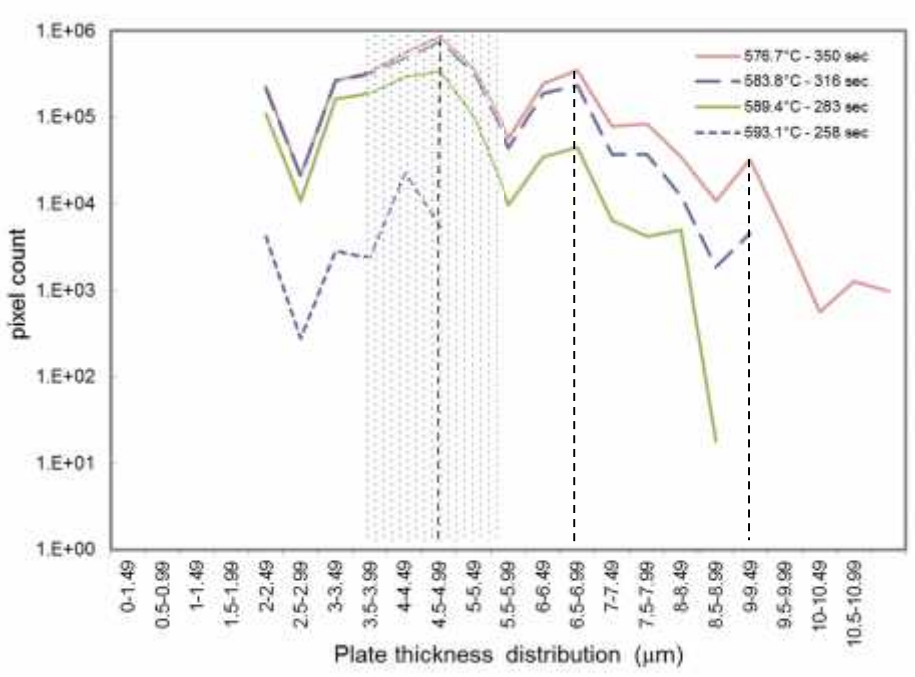

Figure 5.26. Thickness distribution of beta phase at different temperature stage.

The distribution range of 2-2.49 μm was the thinnest part of the plate which is the minimum measured value due to voxel limitation. From the graph it was noticed that the range of 3.5-5.99 μm is the largest area of thickness region which could be identified as the threshold for the beta thickening before further growth. As the temperature reaches near eutectic reaction some of the plates reach the thickness ranges of 9.5-9.99 μm and higher. Evolution of the beta phase shows no change in the characteristic and peak positions, this might indicate that certain critical thicknesses were required before any the phase lateral growth.

5.4.4 Kinetics and growth of beta phase.

Deep etching technique revealed 3D characteristics of beta phase. From SEM micrographs in Figure 5.27, we could see the beta phase branched without any preferential angle of branching. The eutectic silicon is seen attached to the beta phase, however it did not show the beta phase as the nucleation site for eutectic silicon. This can be seen from the images with a modified eutectic morphology, which indicates the eutectic silicon underwent a high undercooling due to liquid pool trapped between primary (Al) dendrites and beta plate where the plate did not nucleate silicon (see also page 82 and Chapter 6 for entrapped liquid).

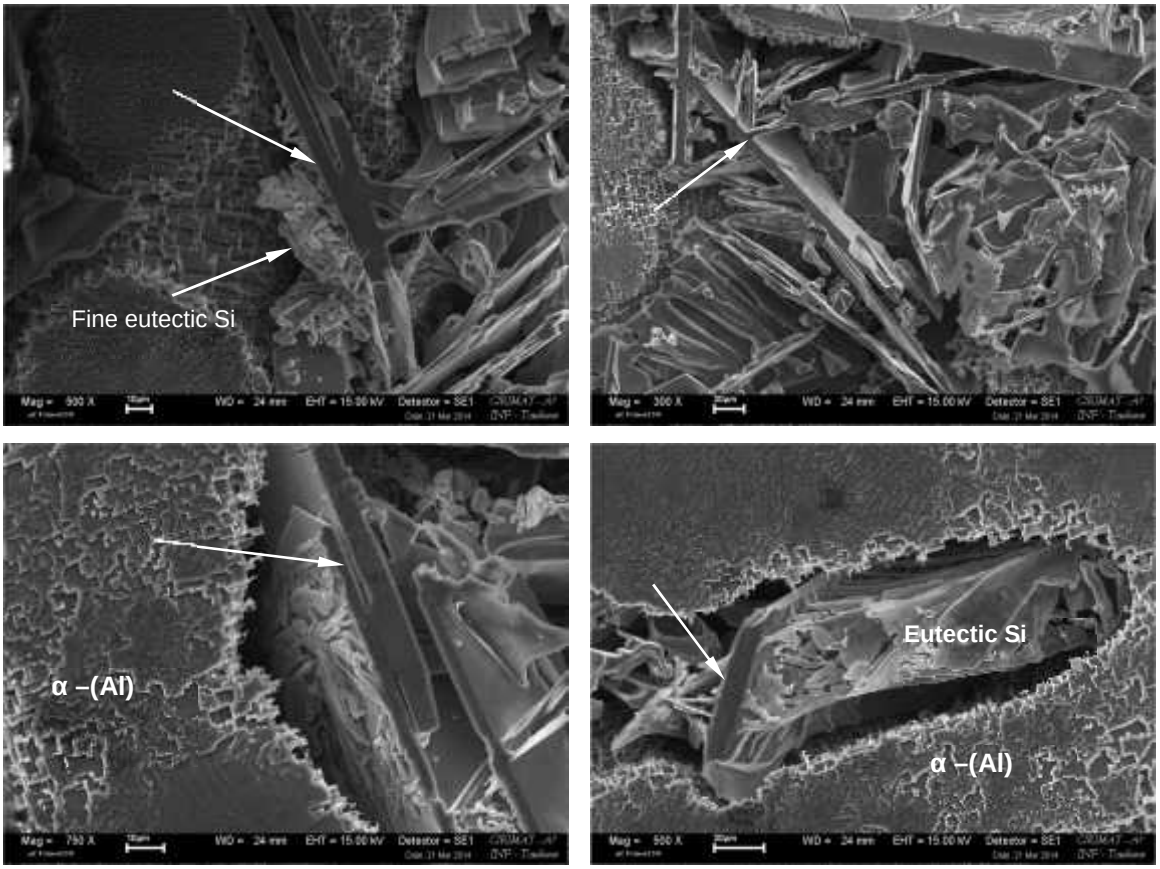

Figure.5.27 SEM micrographs of deeply etched sample showing the beta phase branching and surface attachment of eutectic silicon.

Further analysis from in-situ tomography image, we could notice the characteristic features of beta phase growth, as seen in Figure 5.28. The beta precipitates have the tendency to grow as rectangular thin plates which grow at a rapid lateral rate in the early stage of phase precipitation.

In summary, in-situ tomography shows that the growth of beta precipitates occurred rapidly by lateral expansion. Tomograph images show that the lateral growth is more dominant than the thickening mechanism during early stage of the growth. From the growth data of beta precipitates, we could see that their growth rate is influenced by the other phases formed during solidification. The presence of dendrite arms limits the lateral movement of the beta precipitates which forces them to encircle the dendrite arms, thus slowing the growth rate. The growth of beta is also controlled by the fraction of solid in the sample. As the solidification reaches the eutectic reaction, the solid fraction increases and limits the growth of beta phase.

Figure 5.28. 3D crystal characteristics of beta phase with rectangle appearance.

Figure 5.29 showed the surface contour of beta phase with faceted growth interface and steps as already mentioned earlier. Deep etch image showed the beta phase appeared as layers of plate which stop growing when blocked by the dendrite (Al).

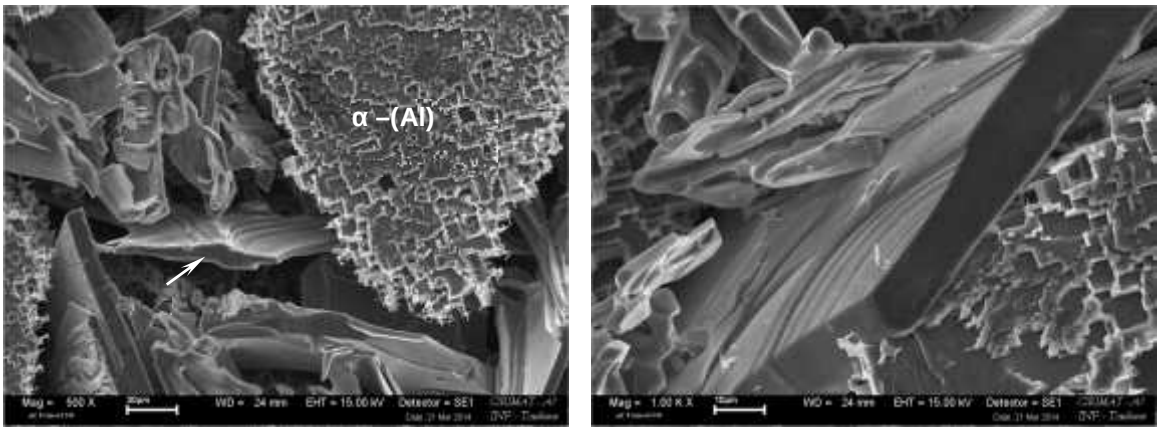

Figure 5.29. SEM micrographs of deeply etched sample showing step at the beta phase surface.

Analysis on the thickness of beta phase showed an interesting result where the thickness was distributed into 3 peaks (Figure 5.26). As time increases, the thickness of the plates increases especially in the regions close to the surface where the nucleation initiated. Thickness rate was measured from the highest plate thicknesses from each tomography step. The results showed that the beta precipitates thicken at a rate of 1.53 μm/s after nucleation and this slows down to 0.42 μm/s in the next stage. The thickening growth rate in the later stage can be evaluated to approximately 0.2 μm/s (12 μm/min). This result is much higher than reported by Terzi et al. [16] who estimated the rate to be ~2 μm/min with an experiment conducted at a cooling rate of 1.4°C/min, while for this work the experiment was at higher rate at 10°C/min.

The thickening mechanism was suppressed by the tendency of high lateral beta growth which is 10 times faster than thickening rate. As seen from the Figure 5.30 which compares these rates, the lateral growth rate is dominant in early stage, marked with very high value and slows down as the liquid fraction decreased leaving not enough room in the interdendritic regions for their growth. Nevertheless, the rate for thickening did not increase drastically after that point, probably due to the same reason where the liquid/solid interface limits their growth.

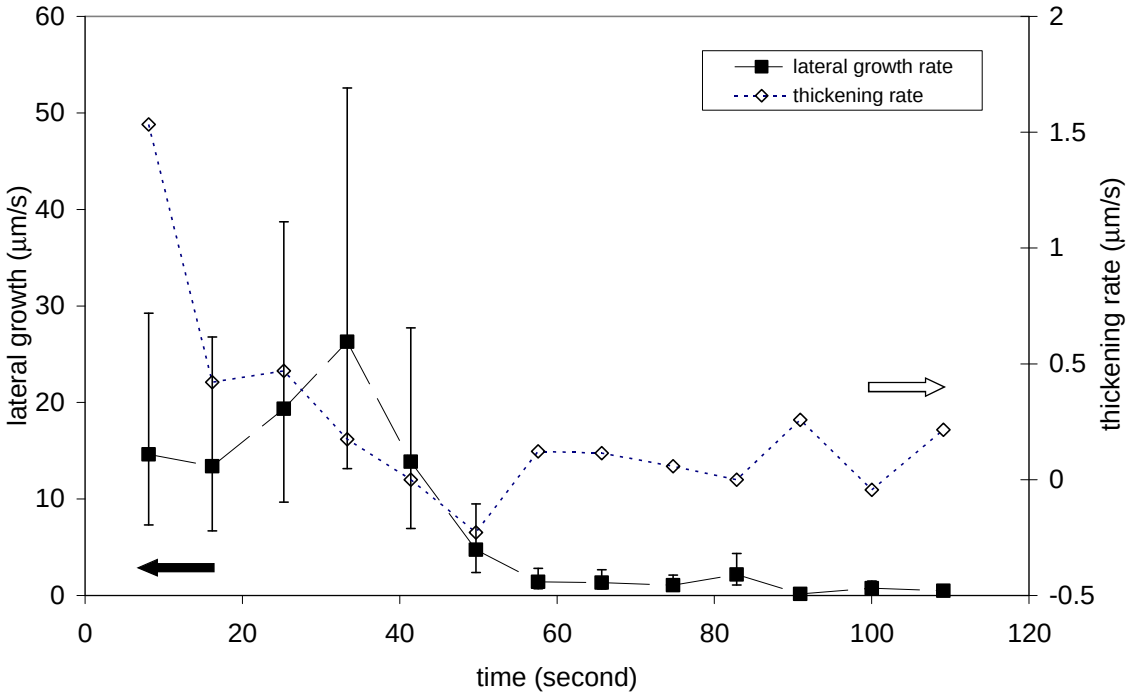

Figure 5.30. Comparison of lateral and thickening growth rates of beta phase (the lateral rate was taken from a single beta particle).

Further analysis was conducted on early and intermediate stage of thickening growth of a single beta plate as illustrated in Figure 5.31. Early stage of the beta phase growth shows a rapid increase in the thickness as seen from the thickness profile at 8, 16 and 25 sec. From the graph we could see that the number of pixels reduced between 16 and 25 sec for the thickness size of 6.5 µm, indicating that new layers developed which is noticed by the peak increase at 8.5 µm. From 25 sec to 33 sec, the plate expanded in lateral direction as noticed from the increase of thickness peak at 4.5 - 5 µm. Subsequently, at intermediate stage the plate areas widened as the temperature cooled down as seen in Figure 5.31b.

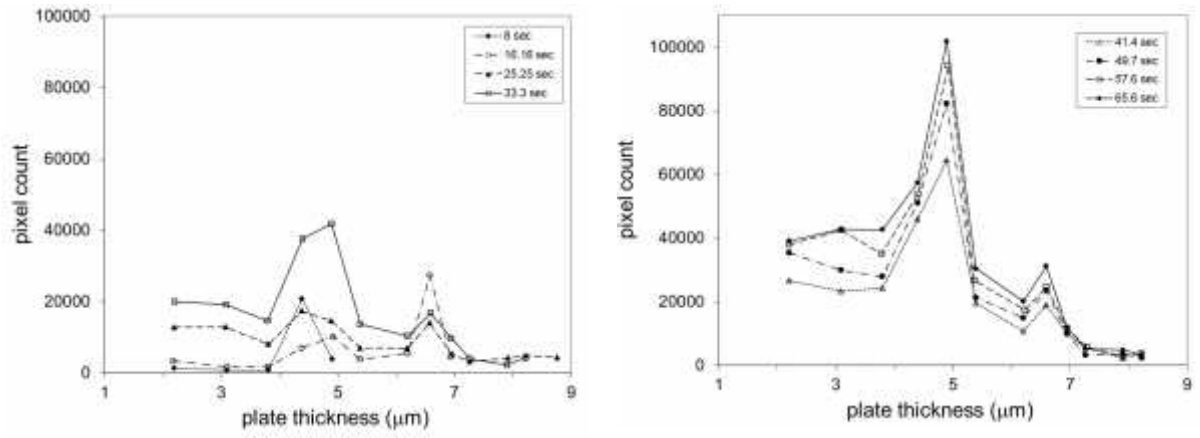

Figure 5.31. Thickness profile of beta phase during early growth (a) and at intermediate stage (b).

From the thickness mapping, we could see largest area of thickness at 5 μm and the difference to the next thickness peak approximately 1.5 - 2 μm. The growth at early stage to higher thickness could be triggered by the presence of obstacles such as dendrite arms. Therefore to compensate the disturbed lateral growth, thickening occurred. A growth model for beta precipitation based on the approach proposed by Amini and Abbaschian [17] for graphite flake growth is illustrated in Figure 5.32, with *V* as lateral growth and r* is the critical radius of the plate.

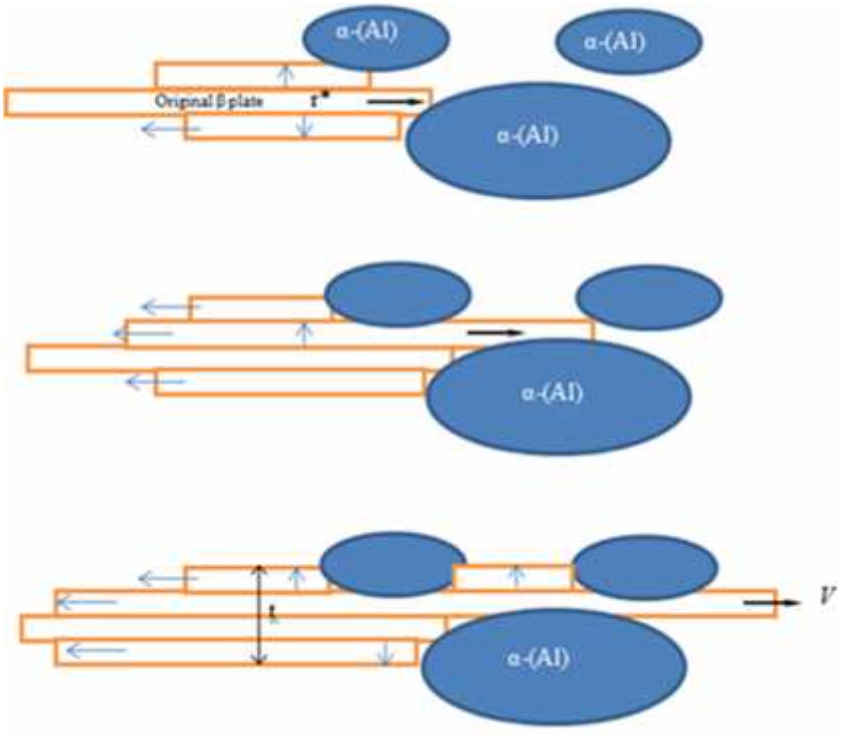

Figure 5.32. 2D lateral and thickening growth model for beta plate

The lateral growth of beta phase is controlled by the diffusion rate of elements at the tip interface of the plate. Since the diffusion coefficient for each element is different, we assumed that iron could determine the growth rate since it has the lowest value. For increase in the thickness of beta phase, we propose that new layers appear by twinning. However, the twinning mechanism related to the thickness growth remains unknown.

5.4.5. Volume fraction

The volume fraction of beta phase taken from in-situ tomography data increases rapidly in the beginning and saturates as the solidification continues as seen in Figure 5.32. This result is in agreement with the volume fraction prediction made by Thermocalc based following the Scheil model or lever rule. Slight differences compared with the Thermocalc calculation in the early step of tomograph could be influenced by the shrinkage which made the sample slightly bend and caused some of the surface to go out of the region of interest. In comparison to 2D volume fraction, the total volume fraction by in-situ tomograph is lower due to the final eutectic reaction have not been reached, when calculation by Thermocalc indicates a slight jump of the beta phase volume fraction at the three-phase (Al)-Si-β eutectic reaction.

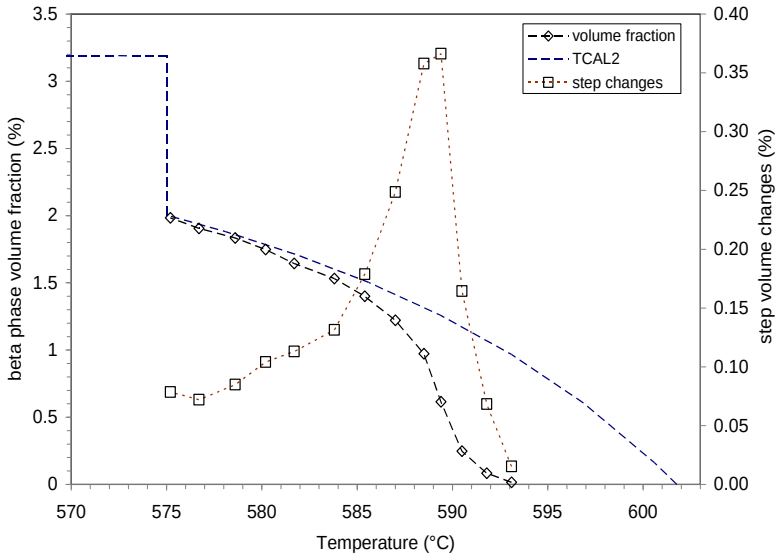

Figure 5.33. Overall volume fraction of beta phase evolution with temperature (TCAl2 calculation for beta phase volume fraction were superimposed).

The evolution of partial volume fraction of several beta phase particles showed that the particles merged at later stage during solidification. This can be seen in the Figure 5.33 for the case of particle no. 1 which merged with particle no.2 and 3 below 585°C.

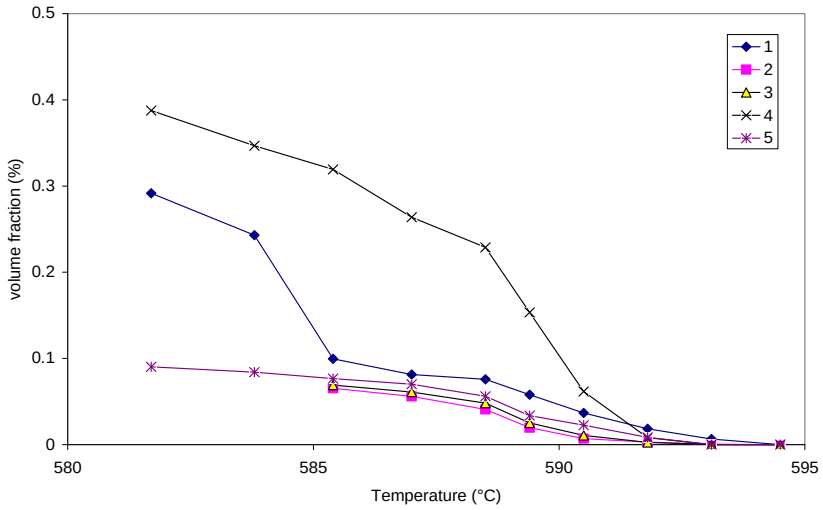

Figure 5.34. Evolution of partial volume fraction for some beta phase particles.

Summary

A study of the effect of cooling rate on the beta phase precipitation in Al-6.5Si-1Fe alloy by DTA was performed. DTA thermograms showed similar pattern for all scanning rates. The characteristic temperatures of the solidification reactions (liquidus, beta precipitation and final eutectic) shifted as the scanning rate changed due to thermal resistance. DTA analysis showed the beta phase precipitation as two-phase eutectic reaction.

The result showed that cooling rate has a significant effect on beta phase morphology. Low cooling rate produced long and thick beta precipitates. Most of beta precipitation occurs in a very narrow temperature window, which probably relates to the kinetics of their precipitation and the volume fraction of solid in the sample.

Analysis of 3D images showed how the beta precipitates grow laterally, particularly by surrounding the primary (Al) dendrite. The nucleation initiates from the outer skin surface of the samples and growth of beta plates proceeds toward the sample center for low cooling rate condition. However as the cooling rate increases, the initiation appears scattered in the bulk of the sample. Furthermore, the beta phase morphology appeared smaller at high cooling rate.

In situ tomography experiment revealed the nature of beta phase growth where the lateral growth dominated the growth mechanism. This lateral growth was marked by high growth rate which slowed down after a saturation level was reached. The slowing down of the lateral growth did not make the thickening rate to increase drastically, the high solid fraction might have limited the thickening growth.

Reference

1. N. Krendelsberger, F. Weitzer and J.C. Schuster, On the reaction scheme and liquidus surface in ternary system of Al-Fe-Si, Metallurgical and Materials Transactions A, 38, (2007),1681-1691.
2. H.W.L. Phillips: Annotated equilibrium diagrams of some aluminum systems, Institute of Metals, London, 1959.
3. S. Pontevichi, F. Bosselet, M. Peronnet, J.C. Viala, Stabilité thermique de la phase β-Al_5FeSi dans le système ternaire Al-Fe-Si, J. Phys IV France, 113, (2004), 81-84.
4. S. Takeda and K. Mutuzaki, The equilibrium diagram of the Fe–Al–Si system, Tetsu-to-Hagane, vol. 26 (1940), 335-361.
5. W.J Boettinger and U.R Kattner, On DTA curves for the melting and freezing of alloys, Metallurgical and Materials Transaction A, 33A (2002), 1779-1794
6. J. Lacaze, L. Eleno, B. Sundman, Thermodynamic assessment of the aluminum corner of the Al-Fe-Mn-Si system, Metallurgical and Materials Transaction A, 41, (2010), 2208-2215.
7. C.M Dinnis, J.A Taylor, A.K. Dahle, As cast morphology of iron intermetallic in Al-Si foundry alloys, Scripta Materialia, 53, (2005), 955-958.
8. W. Khalifa, F.H. Samuel, and J.E. Gruzleski, Iron intermetallic phases in the Al corner of the Al-Si-Fe system, Metallurgical and Materials Transactions A, 34, (2003), 807 – 825.
9. L.A. Narayanan, F.H. Samuel and J.E. Gruzleski, Crystallization behavior of iron-containing intermetallic compounds in 319 aluminum alloy, Metallurgical and Materials Transactions A, 25, (1994), 1761-1773.
10. M.O Shabani, A Mazahery, P. Davami, M. Razavi, Silicon morphology modelling during solidification process of A 356 Al alloy, Int. Journal of Cast Metals Research, 25, (2012), 53-58
11. J. Wang, P.D Lee, R.W Hamilton, M. Li, J. Allison, The kinetics of Fe-rich intermetallic formation in Aluminum alloys / In situ observation, Scripta Materialia, 60, (2009), 516-519
12. Private communication with Luc Salvo, March 2014.
13. R.P. Dougherty and K-H Kunzelmann, Computing local thickness of 3D structures with ImageJ, Microscopy & Microanalysis, 13, supplement S02, (2007), 1678-1679
14. T. Hildebrand and P. Rüegsegger, A new method for the model-independent assessment of thickness in three-dimensional images, Journal of Microscopy, 185, (1997), 67-75.
15. Michael Abramoff, VolumeJ plugin for ImageJ- v1.7a.
16. S. Terzi, J.A. Taylor, Y.H. Cho, L. Salvo, M. Suéry, E. Boller, A.K. Dahle, Insitu study of nucleation and growth of the irregular α-Al/β Al_5FeSi eutectic by 3D synchrotron X-ray microtomography, Acta Materialia, 58, (2010), 5370-5380.
17. S. Amini, R. Abbaschian, Nucleation and growth kinetics of grapheme layers from a molten phase, Carbon, 51, (2013), 110-123.

6. Variations in the solidification path of a high purity Al-Si-Fe alloy

The effect of very low cooling rate on the formation of intermetallic phase in a Al-6.5Si-1Fe alloy was investigated using DTA. Based on the thermodynamic calculation using Scheil and lever rule model, the only iron rich intermetallic phase predicted to precipitate for this chemical composition is β-$Al_9Fe_2Si_2$ phase. However, metallographic observation showed cluster of "chinese script" precipitates in the interdendritic region which was dispatched in various locations of the samples. This phase precipitation which is normally associated with the cubic alpha phase was not expected. In order to get a better understanding of script phase precipitation, further analysis with SEM equipped by EDS, EPMA, EBSD and μXRD was used in this study. Factors influencing the precipitation and nucleation of these "Chinese script" precipitates and the effect of cooling rate are also discussed.

Other than that, another solidification phenomenon known as rosette was also observed within the samples. Rosette can be characterized by the presence of a very fine eutectic structure within more ore less spherical areas. Analysis using EPMA and DTA were performed to study rosette precipitation. Detail image of DTA sample and quantitative analysis can be seen in **Appendix 4.**

6.1. Precipitation of Chinese script phase

6.1.1. DTA records

Earlier work [1] on the effect of cooling rate on the morphology of beta phase from Al-6.5Si-1Fe showed an anomaly in the precipitation of iron rich intermetallic phase. Metallographic examination of DTA sample with cooling rate of 0.2°C/min shows the appearance of a Chinese script precipitate; however this finding does not comply with the solidification path calculated for the studied alloy if it is assumed this morphology is associated to hexagonal alpha phase.

Based on that, further investigation was performed by using a near equilibrium condition to study the precipitation of this Chinese script phase. The DTA analysis was performed by recording the DTA signal with various low scanning rates for cooling of 0.02, 0.05 and 0.1°C/min from 620 to 590°C. The low scanning rate was applied from above the liquidus until beta phase precipitation was deemed to be finished based on previous experiments. After that, the DTA was cooled at 2°C/min. The sample was held at 620°C for 30 min before the cooling sequence was started.

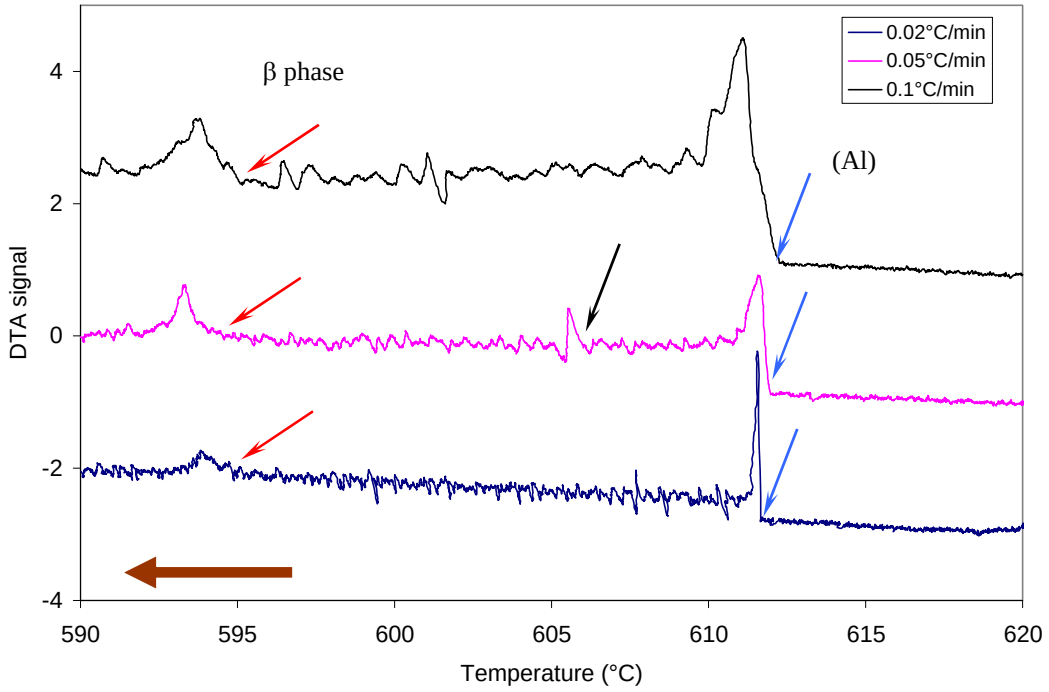

Figure 6.1. DTA thermograms recorded at very low cooling rates (the graphs are adjusted along the y axis to separate the curves with the lowest scanning rate at the bottom).

DTA thermograms in Figure 6.1 illustrate distinctive thermal arrests at the start of the cooling process which relate to the nucleation and growth of primary (Al) dendrites (blue arrows) and the beta phase precipitation reaction L → (Al) + β (red arrows). In between those two major peaks, a small peak (black arrow) was also detected in the sample with 0.05°C/min cooling rate which could be thought to be associated to the precipitation of Chinese script phase. However, that peak was not seen in other samples.

Moreover, the thermograms show a noise increase after the primary (Al) arrest. It is further seen that the noise amplitude is increased as the cooling rate increases. The likely explanation for this is related to the DTA principle which is based on measuring the signal difference between the sample and a reference being given the same heating or cooling rate. The change in thermal resistance at metal and crucible interface could cause this noise differences. Nevertheless, there also other possibility such as thermocouple characteristic in the DTA which used electric potential difference that could have been causing the noise.

6.1.2. Characterization: EDS analysis, EPMA, EBSD and «XRD study

The DTA samples were prepared for metallographic observation under optical microscope and SEM. Micrographs in Figure 6.2 and 6.3 clearly show the presence of Chinese script phase, plate-like beta phase and eutectic silicon.

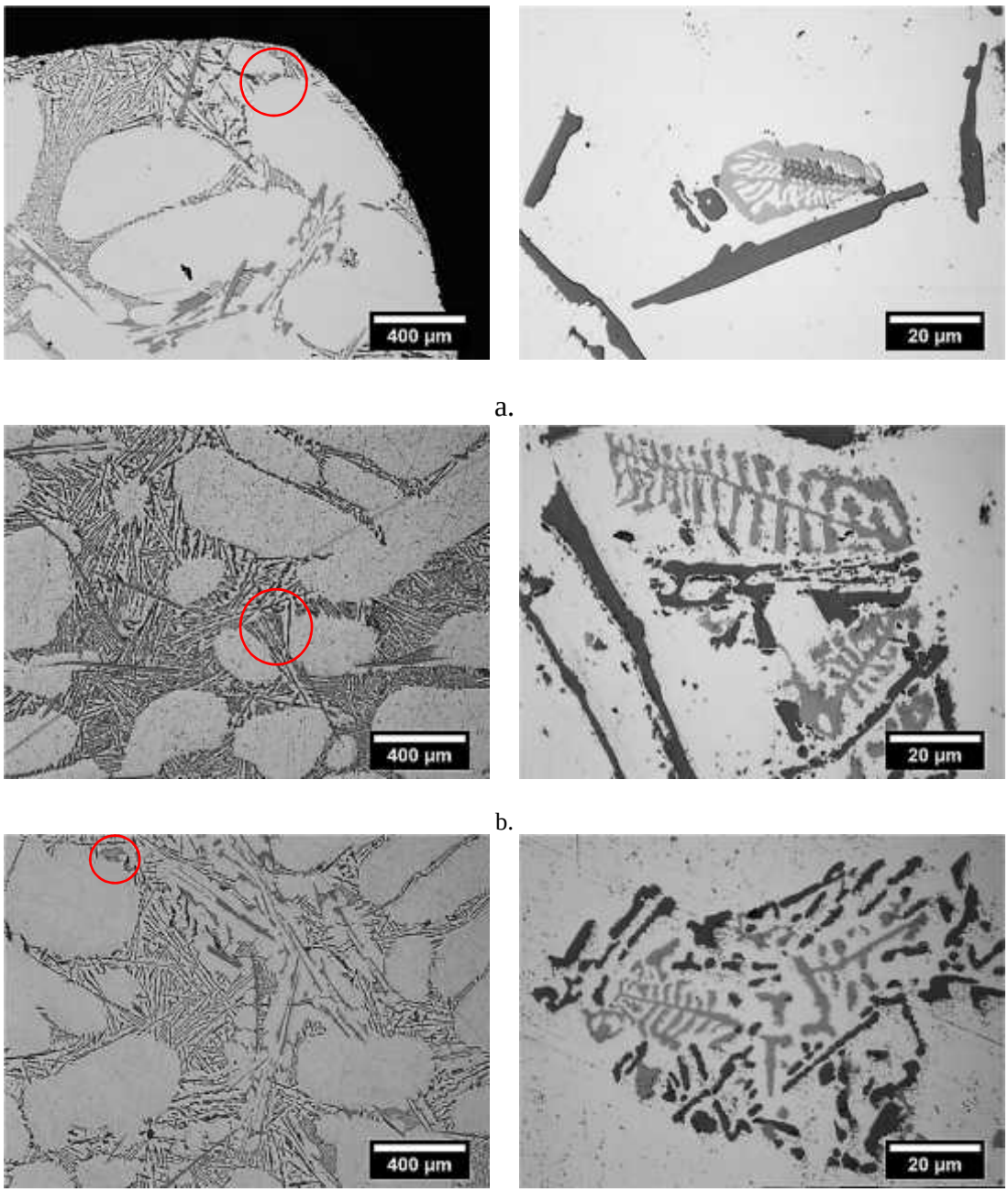

Figure 6.2. Micrographs of DTA samples for various cooling rates showing the presence of script phase in interdendritic regions (a) 0.02°C/min, (b) 0.05°C/min, and (c) 0.1°C/min (images to the right showed enlarged red circled areas).

The phase morphology which is characterized with fishbone or script shape appears in interdendritic regions, either in the middle or near to the surface of the sample. The size of the script precipitates varies but overall was less than 100 μm in length in 2D section. From the metallographic examination we could also notice that no or very few plate-like beta phase could be detected near script precipitates.

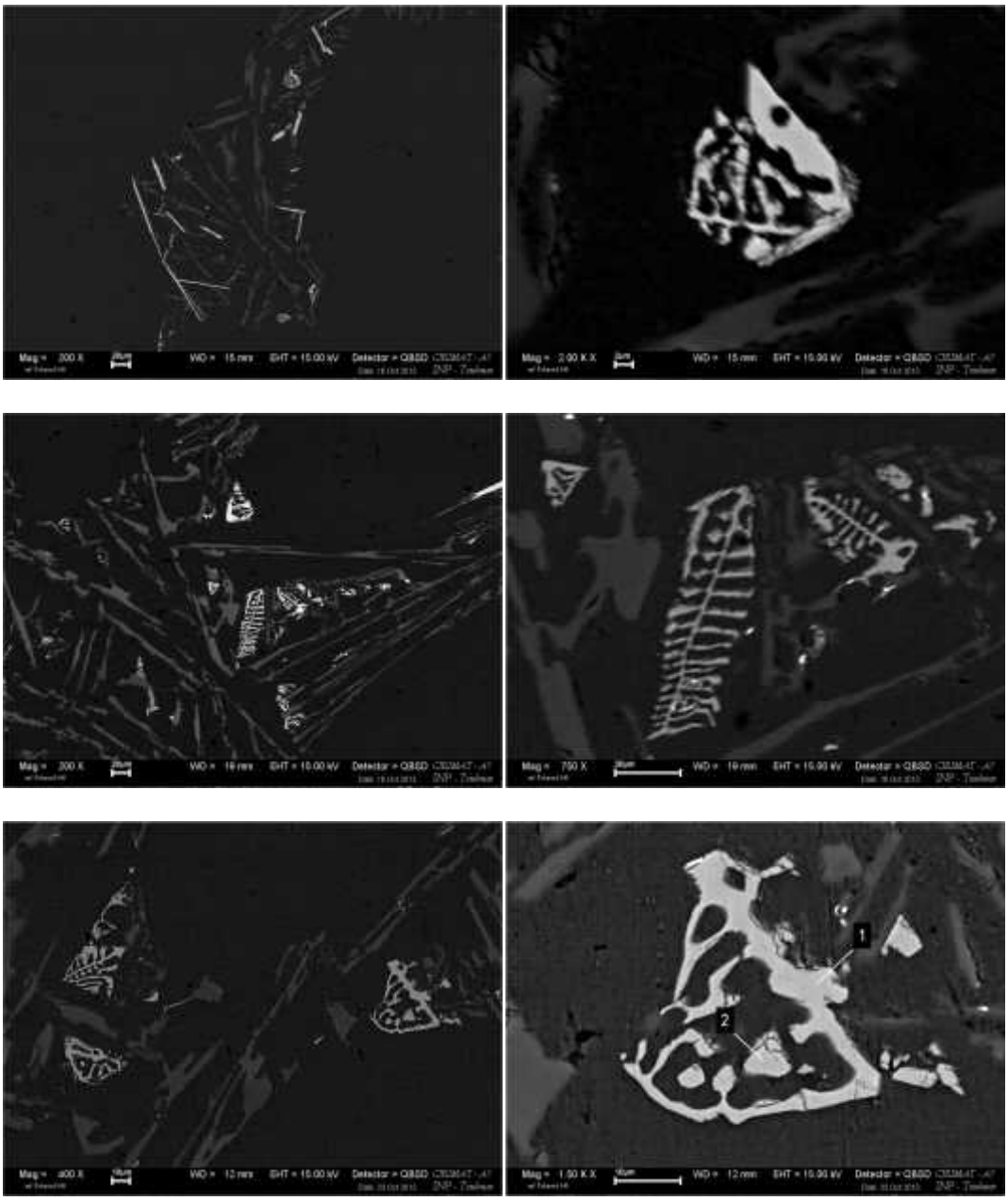

Figure 6.3. SEM micrographs showing clusters of script phase, taken from DTA sample with various cooling rate (a) 0.02°C/min (b) 0.05°C/min and (c) 0.1°C/min.

6.1.2.1 EDS and micro-probe analysis

EDS analysis of the chinese script phase was conducted on various locations as illustrated in Figure 6.4. The result revealed the presence of Al, Si and Fe and no minor element detected. The EDS quantitative analysis showed that script phase has a similar chemical composition to beta phase, as seen in Table 6.1.

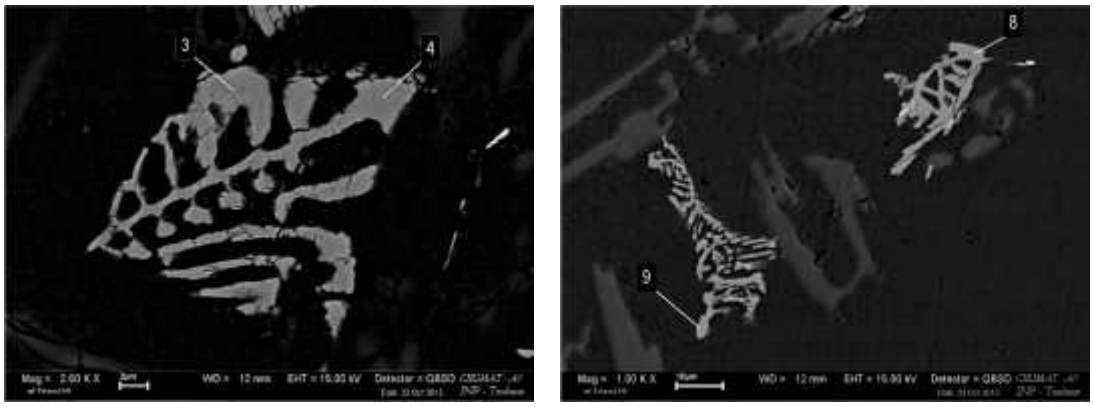

Figure 6.4 . SEM images showing script phase precipitates and the measurement locations taken from sample with cooling rate of 0.1°C/min.

Table 6.1. EDS results of script phase.

Test location No.	Chemical composition (wt%)		
	Al	Si	Fe
3	56.4	14.7	24.8
4	55.8	14.9	25
8	55.7	14.4	25
9	57.8	14.7	24.7
Average	**56.4**	**14.7**	**24.9**

Further analysis with electron micro probe analyzer (EPMA) was performed on the same sample and some locations corresponded to the previous EDS measurement, as seen in Figure 6.5. EPMA results as seen in Table 6.2 do not significantly differ from EDS results. The analysis reveals that the Si and Fe content in Chinese script phase was quite high with Fe/Si ratio around 1.8, thus the script phase could be classified into beta phase.

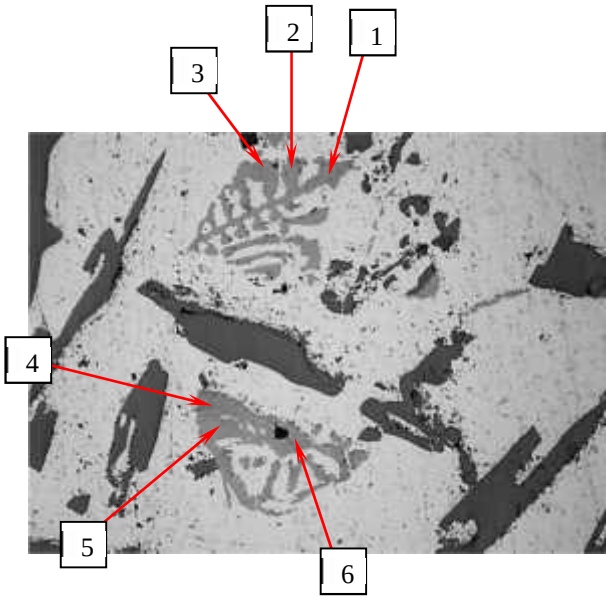

Figure 6.5. EPMA test point location of two script phase from the same sample as in Figure 4.

Table 6.2. EPMA result of script phase.

Phases	Test location No.	Chemical composition (wt%)		
		Al	Si	Fe
Script 1	1	52.64	14.66	27.13
	2	63.13	12.74	22.56
	3	57.82	13.83	25.05
	Average	**57.86**	**13.74**	**24.91**
Script 2	4	58.56	13.57	23.27
	5	53.91	14.82	26.6
	6	69.19	10.22	17.69
	Average	**60.55**	**12.87**	**22.52**

Analysis with EDS on the Chinese script phase also revealed the presence of cerium rich precipitates which appear in bright contrast in SEM as seen in the example of Figure 6.6.

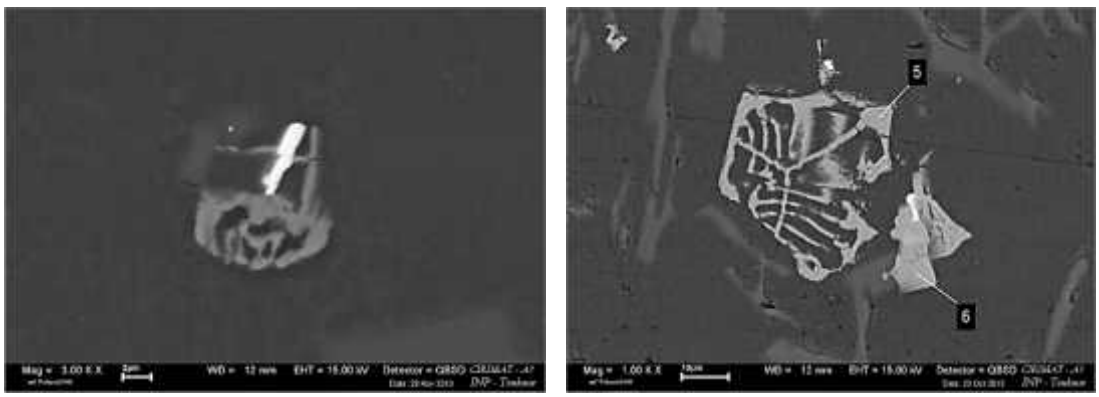

Figure 6.6. SEM micrographs showing cerium rich particles attached to script phase.

6.1.2.2. Micro XRD

X-ray analysis was performed using a micro XRD method (Bruker Advance D8 equipped with micro beam focus) on the area as seen in Figure 6.7. This method was used to confirm the previous metallographic result by crystal structure identification relating to JCPDS file. The XRD used a Cu-Kα radiation (λ = 1.54060 Å) with source parameters of 40 mA and 40 kV. Diffraction pattern was acquired between 15 and 80° in 2 theta with a step size of 0.03^{o} and exposure area (slit size) of 100x100 μm^{2}. Due to the use of micro-beam, the X-ray flux generated was very small, therefore the peak acquired was not quite high and required a longer and repeated acquisition to ensure sufficient recorded data.

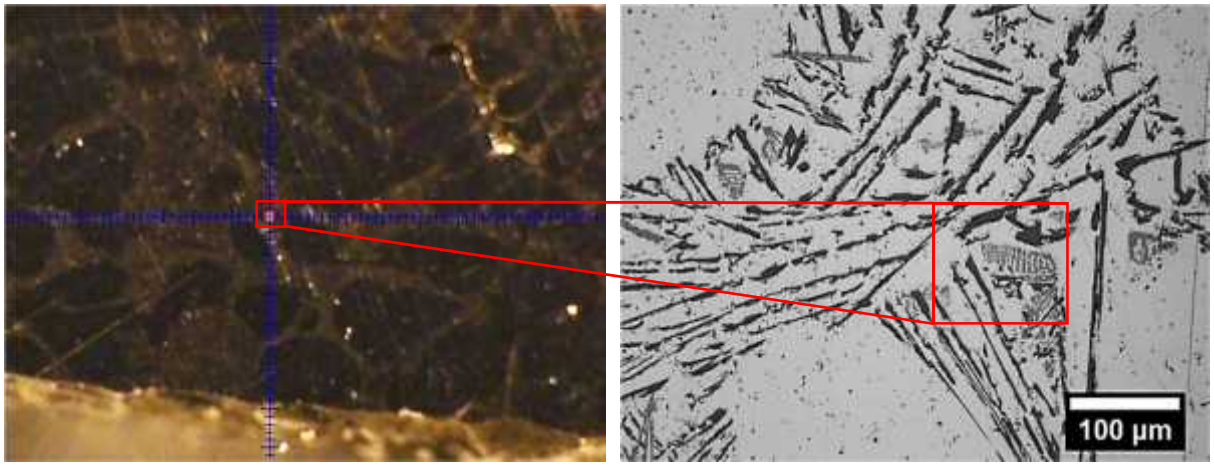

Figure 6.7. Location of the micro XRD beam.

Four major peaks were observed between 25 and 60° in 2 theta as seen in Figure 6.8. Based on a structural database search, those peaks appear to correspond to Al (111) and Si (111), (220), (311) as indexed with JCPDS cards no. 00-004-0787 and 00-027-1402 respectively. Very small additional peaks could be detected which are marked with solid symbols in Figure 6.8. The peaks could be indexed with JCPDS cards file no. 01-071-0238 which corresponds to $Al_{167.8}Fe_{44.9}Si_{23.9}$ phase and JCPDS card 00-054-0376 which corresponds to $Al_9Fe_2Si_2$. It was also verified that these peaks could not be indexed as alpha phase.

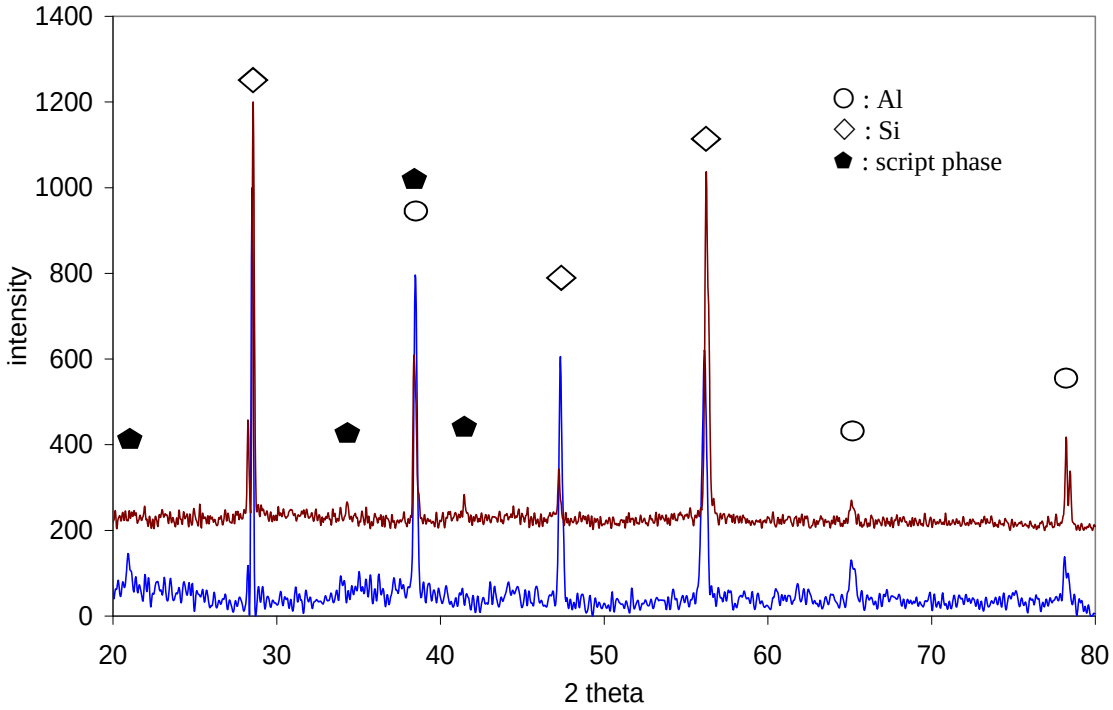

Figure 6.8. XRD patterns showing peaks of (Al), Si and script phase

6.1.2.3. EBSD analysis

In order to confirm the XRD result, further examination with EBSD was performed on Chinese script precipitates. Example of un-indexed and indexed Kikuchi pattern of the script phase can be seen in Figure 6.9. Its analysis indicates the script phase is monoclinic as β-$Al_9Fe_2Si_2$ while indexing could not match for hexagonal α-Al_8Fe_2Si. Median angular deviation (MAD) index method gives 0.76 with 10-band detected match for beta phase monoclinic structure.

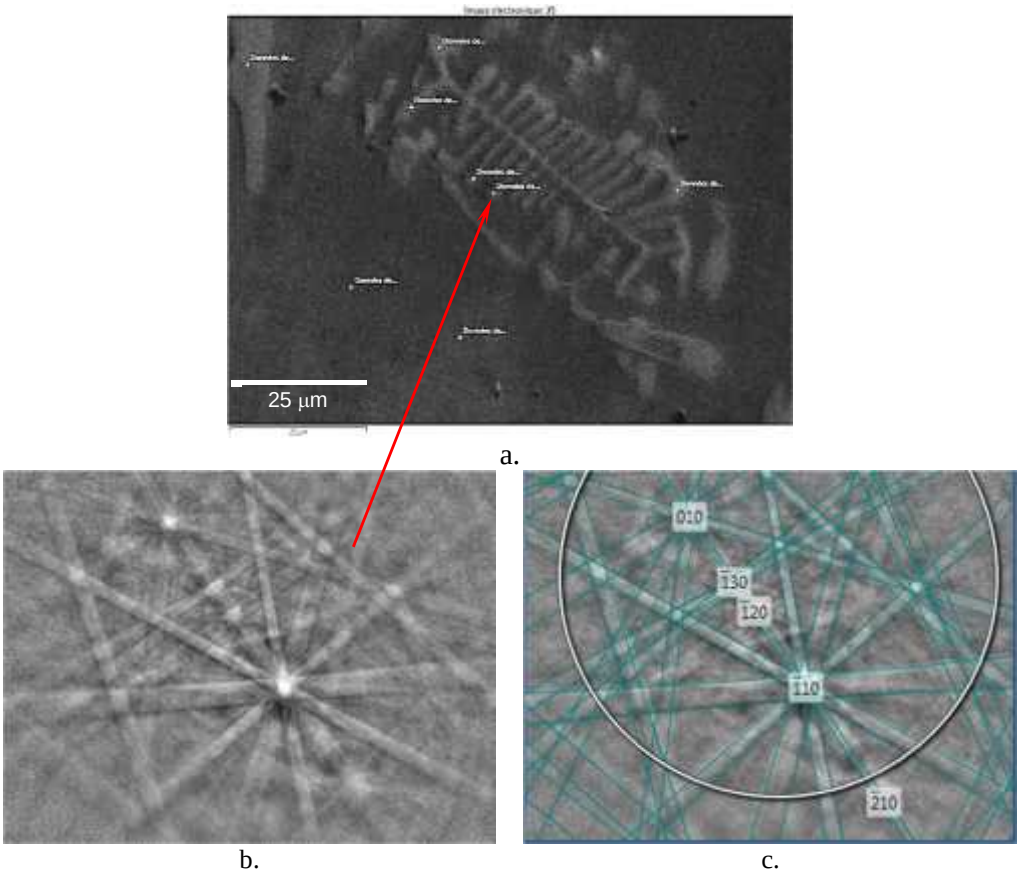

a.

b.

c.

Figure 6.9. EBSD pattern obtained from a script precipitates. (a) micrograph (b) unindexed pattern, (c) indexed pattern. The EBSD pattern is indexed according to the monoclinic β-$Al_9Fe_2Si_2$.

6.1.3. Discussion

Based on the experiment results, we would like to assess the formation of script phase by considering the solidification path and the effect of element to their formation. The solidification path of Al-6.5Si-1Fe was calculated assuming the solidification process follows lever rule or Scheil model as seen in previous chapter. Based on the solidification path, the only intermetallic phase appearing during solidification should be beta. However, as seen from the metallographic analysis, some Chinese script precipitates which are commonly associated to alpha phase with hexagonal (Al_8Fe_2Si) or cubic ($Al_{15}(Fe,Mn)_2Si_2$) structure.

According to the Al-Fe-Si ternary phase diagram one would expect any precipitate of hexagonal alpha should transform to monoclinic beta by a peritectic reaction during solidification. Such a transformation is illustrated in Figure 6.10 from Gorny et al. [2] in the case of sample cooled at 6°C/min. However, metallographic observation by SEM in the present work did not show any indication of phase transformation by peritectic reaction.

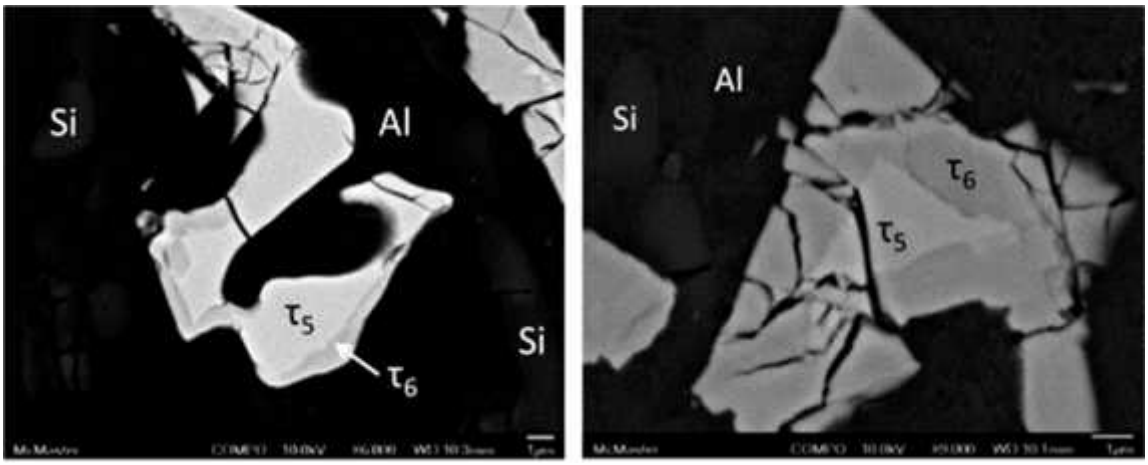

Figure 6.10. Peritectic reaction of alpha τ_5 to beta τ_6 phase, taken from Gorny et al. [2].

Though no sign of peritectic transformation could be observed in the present work, it could not be totally excluded that alpha transformed fully in beta due to slow cooling. An assumption could be made that it was thought possible that nucleation of alpha was favoured with respect to beta. Competitive nucleation of phases from the liquid is known to be influenced by the cooling rate condition, as noted by Langsurd [3] who reported the shift of phase boundaries to a higher iron content and lower silicon with increased cooling rate. The shift may be due either to delayed nucleation or to a change in solidification path. Therefore, in order for the alloy to have a hexagonal alpha precipitates, the solidification path should diverge to lower silicon and higher iron content. However, this condition more likely is not going to happen due to the homogeneity of element within the liquid.

Further analysis for the investigation of Chinese script phase nucleation was performed with DTA. The experiment was conducted at cooling rate of 0.05°C/min and reheating (2°C/min) the sample prior to the beta phase precipitation. If hexagonal alpha did precipitate because of more favourable nucleation kinetics than for beta, its precipitation should occurr first. The thermal arrest detected between the liquidus and beta precipitation (Figure 6.1) could then be associated with the script phase. However, the DTA thermogram of reheating sample did not show any thermal arrest that could be associated with dissolution of an iron rich phase, as seen in Figure 6.11. The small deviation observed before the liquidus peak prior returning to baseline (black arrow) is related to DTA apparatus characteristic. This result showed that the script-beta phase might have appeared together with the plate-like beta phase.

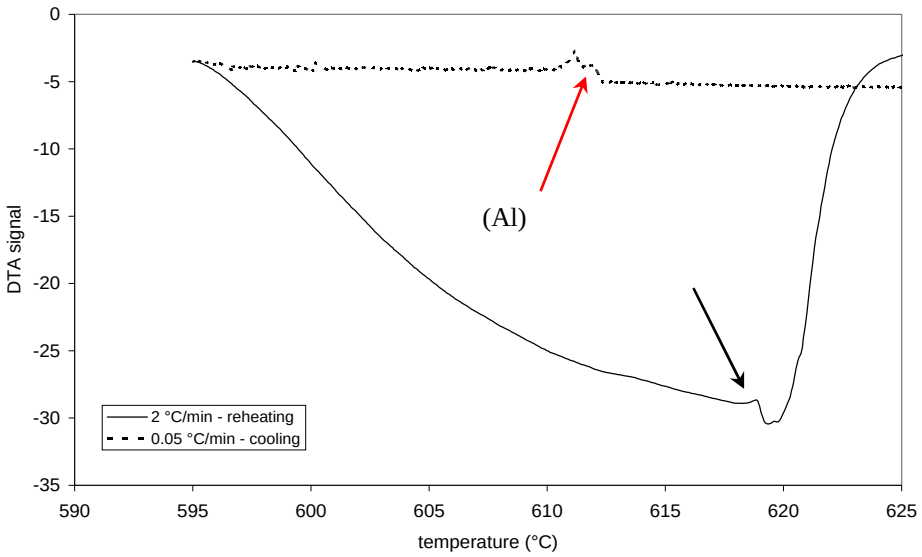

Figure 6.11. DTA thermogram during of cooling down to a temperature higher than for beta precipitation and then reheating to melting temperature.

Metallographic evaluation showed that there are no plate-like beta precipitates in the regions where the script-beta precipitates are observed. SEM micrograph of deep etched sample showed the script phase in the interdendritic region is surrounded by eutectic silicon as seen in Figure 6.12.

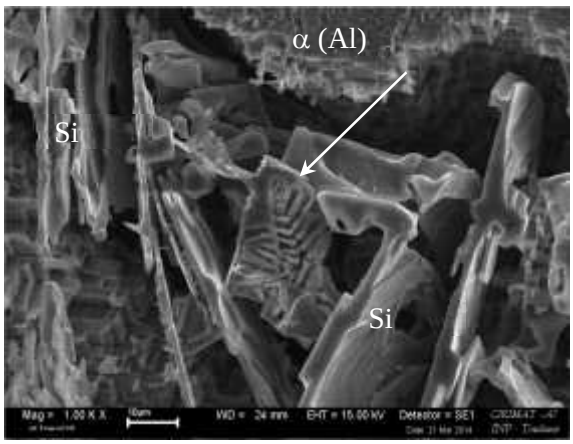

Figure 6.12. Script phase (white arrow) shown attached to eutectic silicon in the interdendritic region after deep etch.

Metallographic observation indicated the presence of another phase near or within the script precipitates, in the form of small plates attached or small particles dispersed within the script precipitates as illustrated in Figure 6.13. EDS analysis showed this phase to be a cerium rich phase, as seen in Figure 6.6. Cerium is known to improve the mechanical properties through modification of eutectic silicon [4-6]. Chen et al. [7] also reported that cerium

decreases the temperature for (Al) nucleation and might act as grain refiner, but no effect on iron-rich phases has been reported. If we exclude the script like precipitates have first formed as alpha, then this means they are a growth form of beta. Cerium should act on the growth, not necessarily on nucleation. Cerium precipitates thus indicate where this element was available.

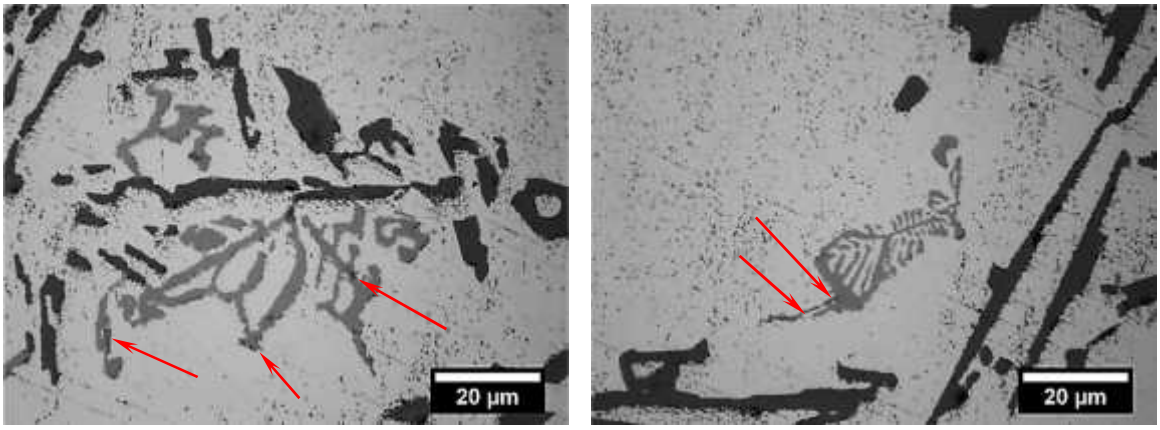

Figure 6.13. Optical micrographs showing the presence of Ce-rich phase attached and dispersed in the script phase (red arrow).

The mechanism for the morphology changes of beta phase could be related to the cooling rate. In low cooling condition, Chinese script beta precipitates were seen in interdendritic region. As the cooling rate increases, the phase becomes smaller and more difficult to distinguish in the matrix.

Ce-rich phase precipitation can be seen by following the liquidus projection of Al corner of the Al-Si-Ce phase diagram [8] as illustrated in Figure 6.14. For an alloy with low level of cerium, the most possible Ce-rich intermetallic to appear during solidification is τ_2 ($AlCeSi_2$) according to the tentative solidification path the eutectic line E_2 ($L \rightarrow \tau_2 + (Al) + Si$, 573 °C) reaction. At low cooling rate Ce-rich phase has enough time to precipitate while as the cooling rate increases the Ce-rich precipitates became difficult to detect and may have not had time to appear and grow.

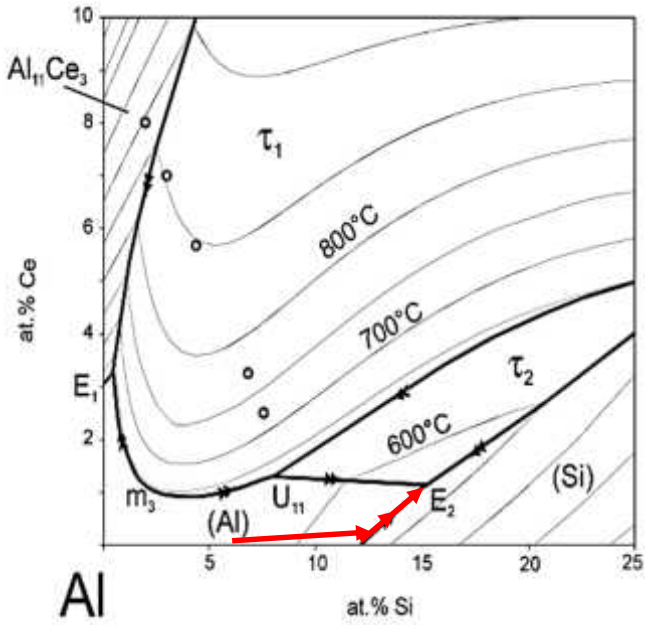

Figure 6.14. Liquidus projection of Al corner of Al-Si-Ce phase diagram [8].

6.2. Rosette microstructure

Another feature observed from the DTA samples was the appearance of rosettes, as seen in Figure 6.15. This morphology is recognized from the convex and smooth shape of pools, with fine multi-phase eutectic. Rosette also can be seen as ellipses or cabbages which indicate their formation is following the shape between dendrite arms.

Kim and Cantor [9] studied the formation of near perfect spherical rosette. They indicated that the rosettes formed under surface tensions which minimize the surface area and leads the formation of globular shape. Other researcher found the formation of the rosettes as isolated liquid pools entrapped between dendrite arms [10] or within the cellular columnar microstructure [11]. The appearance of rosette structure was also noticed in the case of overheating during solution heat treatment of Al alloys, where pocket of undissolved eutectic silicon appear entrapped within the (Al) matrix [12]. According to Lacaze et al. [10], the fine microstructure results from the fact that the liquid pools are isolated and greatly undercool before nucleation of new phases allow them to solidify.

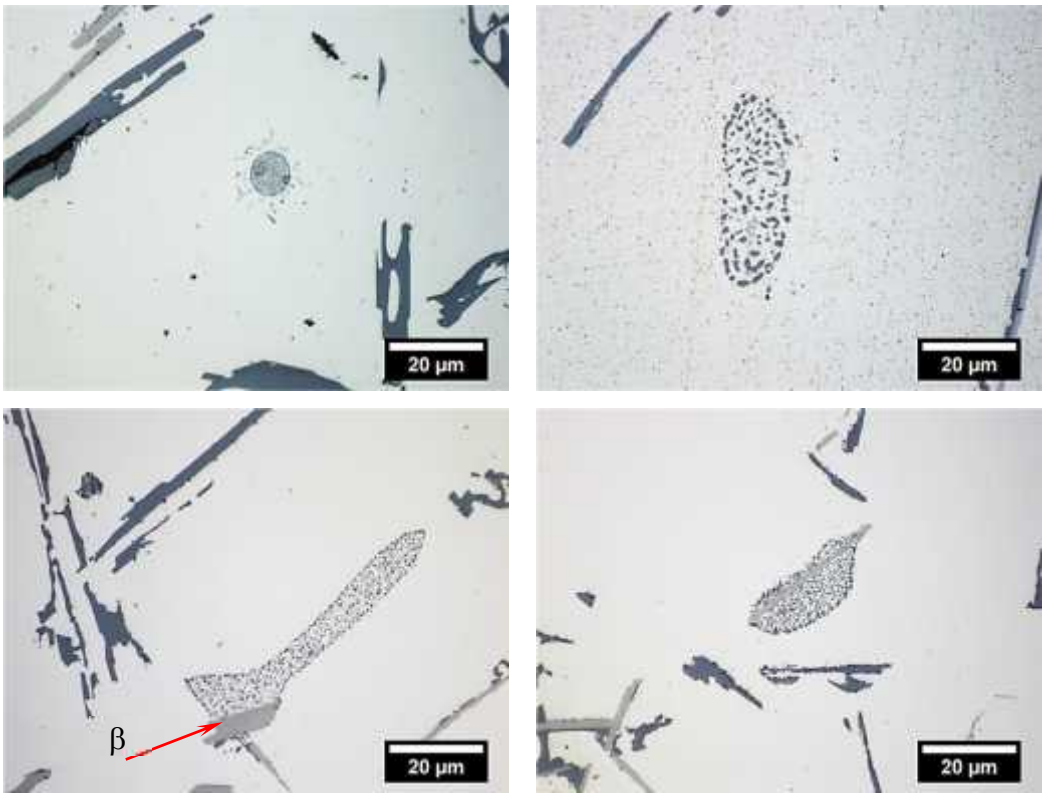

Figure 6.15. Micrograph of some rosettes seen by optical microscope from DTA samples cooled at 5°C/min and 40°C/min. (red arrow indicate beta phase).

6.2.1. Characterization : SEM, EPMA analysis

6.2.1.1. SEM morphology analysis.

Figure 6.16 presents different morphologies of rosette microstructure which were taken from a DTA sample cooled at 5°C/min. One observes fine particles of silicon and iron rich phase inside the cell. At the outer ring of the sphere, fine plates of solid state silicon precipitates formed which radiate from the rosette surface, as seen from optical micrograph image. In the third case, SEM shows the appearance of an iron rich phase which developed within the whole rosette by dendritic growth.

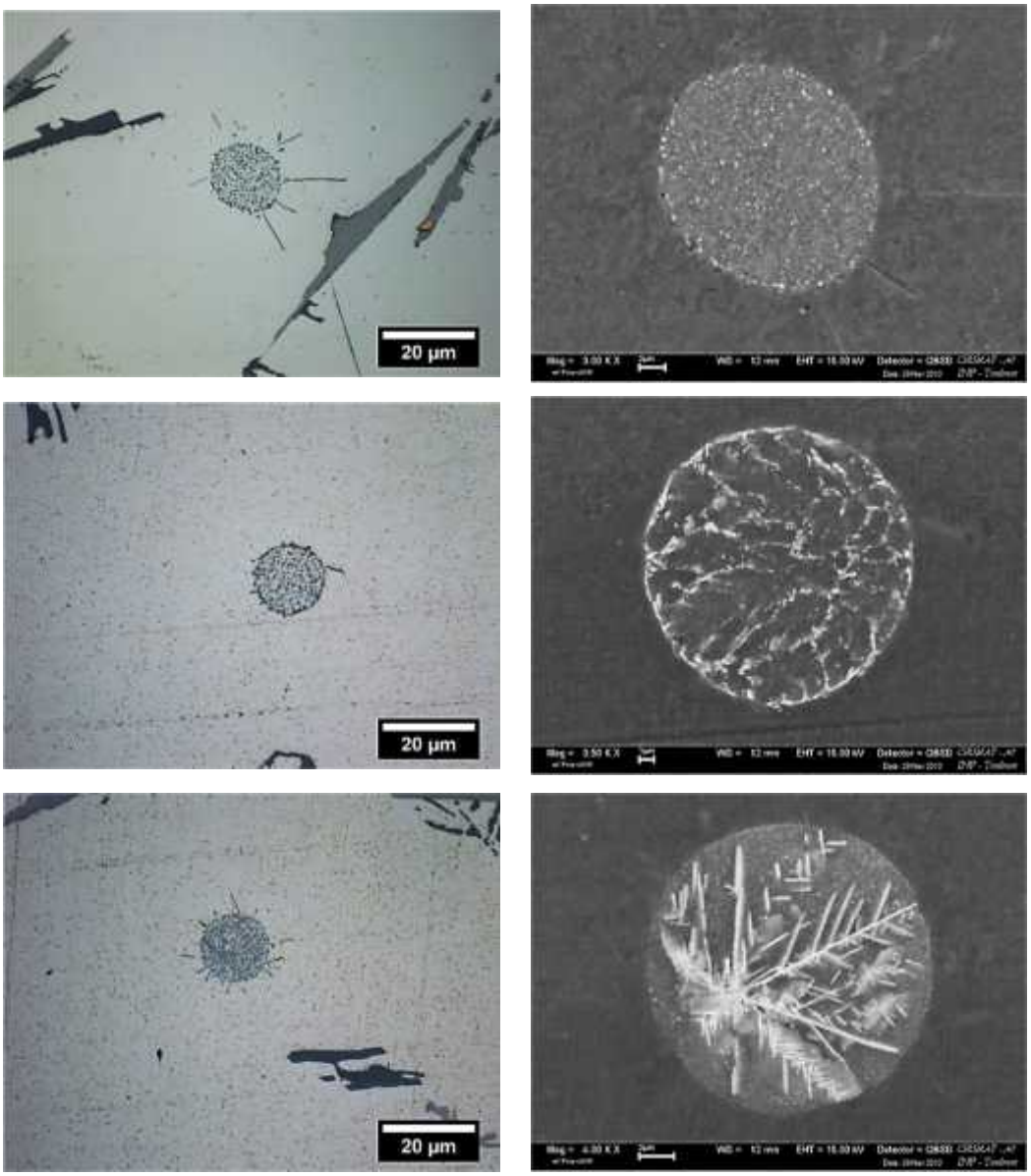

Figure 6.16. Micrograph of isolated rosettes from sample cooled at 5°C/min with different morphologies (optical micrograph to the left and SEM image to the left).

The cooling rates also have an impact on the morphology of the rosette phase. As seen from Figure 6.17, the rosette taken from cooling rate of 0.2°C/min have a larger eutectic particle size and sphere diameter compared to rosette from cooling rate of 10°C/min. This is probably due to coarsening of the microstructure after its formation.

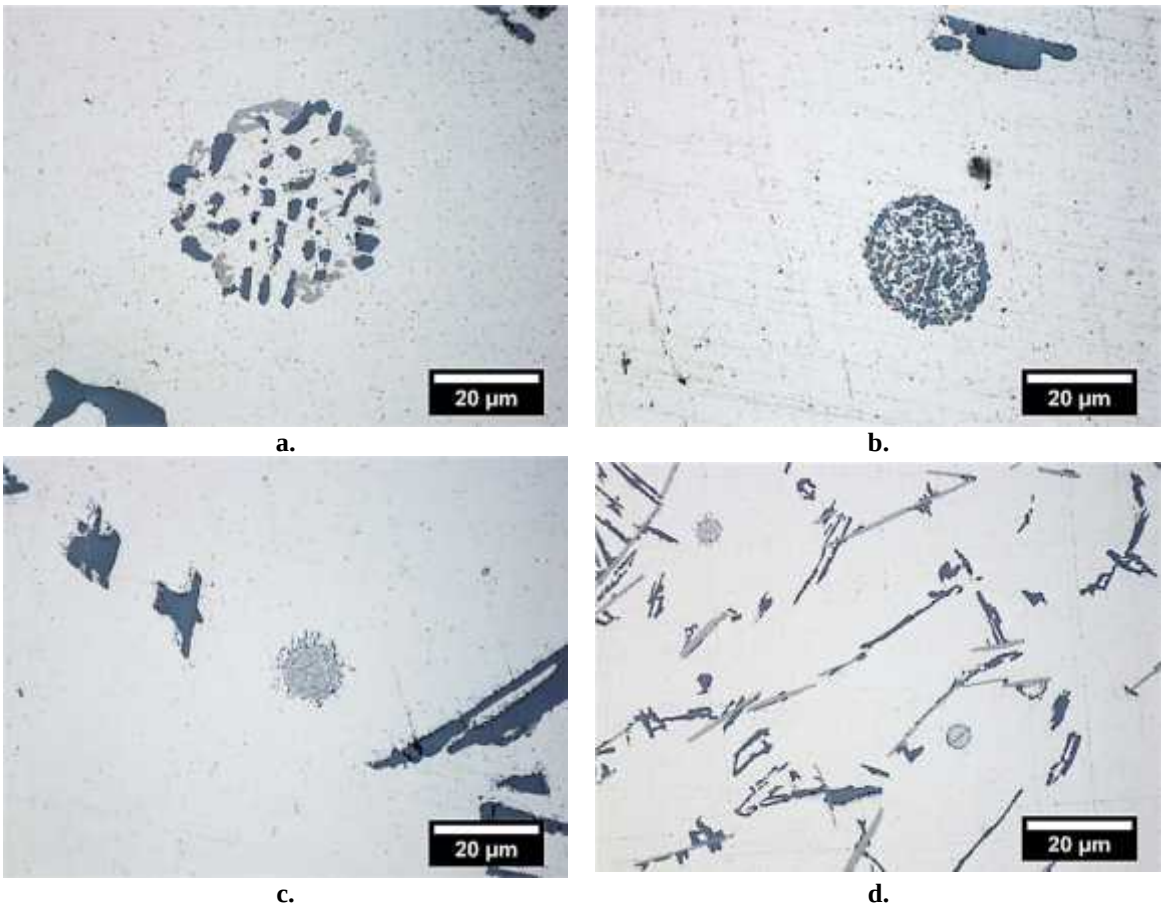

a. **b.**

c. **d.**

Figure 6.17. Micrographs of rosettes taken from sample cooled at different cooling rate (a) 0.2°C/min, (b) 1°C/min, (c) 10°C/min (d) 40°C/min.

6.2.1.2. Chemical analysis: EPMA

EPMA analysis was conducted on two samples with two types of measurement methods which were zone area and line scan across the rosettes. The zone area can be seen from the inset image in Figure 6.18. The line measurements were performed by acquiring data every 2-3 µm across the middle section of the rosettes.

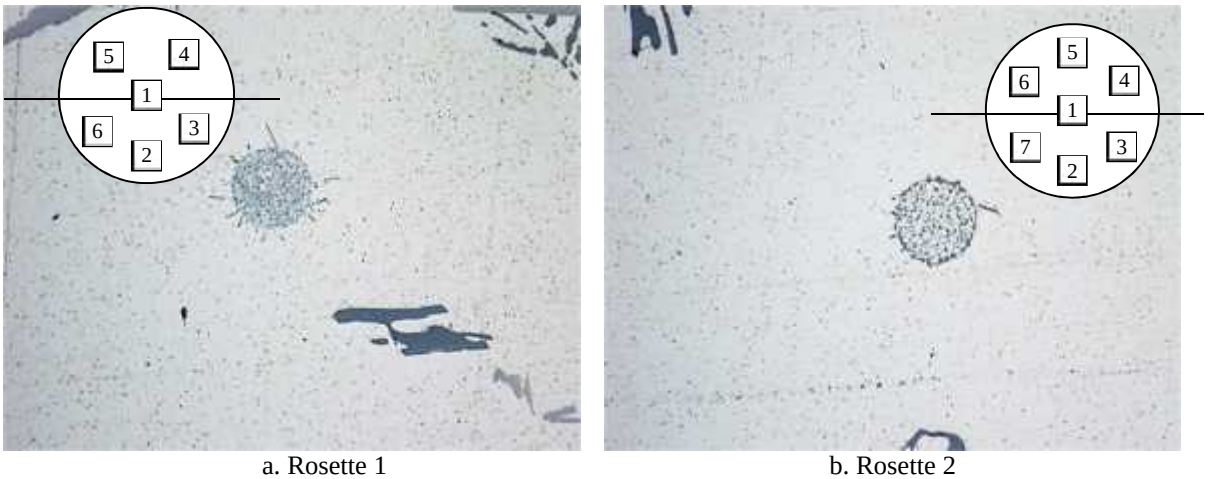

a. Rosette 1 b. Rosette 2

Figure 6.18. EPMA test locations of the rosette taken from DTA sample with cooling rate of 5 °C/min.

EPMA spot analysis showed the total of element contents to range between 89 to 96%. That this is less than 100% is probably related to the fact that rosettes are multi-phase [13,14]. Table 6.3 list the area values with very small trace element of Ca, Ti and Mn appearing.

Table 6.3. The EPMA result.

Rosette 1	Chemical composition (wt%)						sum (%)
	Al	Si	Fe	Ca	Ti	Mn	
1	56.93	27.09	7.38	0.01	-	-	91.41
2	54.85	27.25	9.73	-	-	0.01	91.84
3	58.31	29.79	4.15	-	-	-	92.25
4	57.79	29.35	4.59	-	-	-	91.73
5	57.85	25.51	6.42	-	0.02	-	89.8
6	57.95	28.32	4.97	-	-	-	91.24
average	57.28	27.89	6.21	-	-	-	91.38

Rosette 2	Chemical composition (wt%)						sum (%)
	Al	Si	Fe	Ca	Ti	Mn	
1	68.06	22.27	3.14	0.01	-	-	93.48
2	67.4	24.94	2.8	0.01	-	-	95.15
3	68.47	24.42	1.96	-	0.03	0.02	94.9
4	67.11	25.83	3.11	-	-	0.01	96.06
5	68.02	24.05	1.75	-	-	0.02	93.84
6	64.17	26.54	1.73	0.01	-	-	92.45
7	67.41	24.19	2.51	-	-	0.02	94.13
average	67.23	24.61	2.43				94.27

Analysis to the line scan illustrated in Figure 6.19 showed small fluctuations of silicon for rosette 1 and high content of silicon at the outer surface of rosette 2. Different phases with complex morphology of iron rich particle within the rosette are thought to have caused the fluctuations.

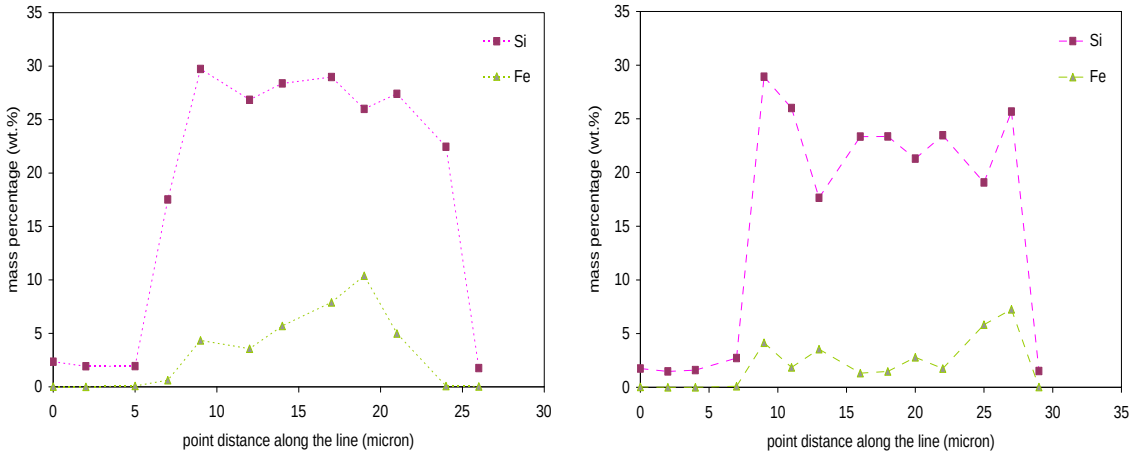

a. Rosette 1 b. Rosette 2

Figure 6.19. Fe and Si profiles from the line scan from each rosette.

6.2.2. DTA analysis

Further study on rosette precipitation was performed using DTA. Early studies by Lacaze et al. [10] on Al-Cu-Mg-Si alloy showed thermal arrests associated to rosette formation at the end of solidification. The formation of rosette has a similarity with the solidification condition of entrapped liquid pool. For this study, to create the entrapped liquid pool phenomena, the experiments were conducted by holding the alloy at a temperature below the (Al) liquidus temperature. The experiment was conducted by holding the sample in mushy zone at 595°C and then cooling them at 5°C/min. However, analysis to the DTA thermogram showed there was no obvious thermal arrest associated with rosettes formation. The small fraction of rosettes within the alloys is the reason for that as not enough of heat evolved during their solidification. Metallographic examination of the holding samples showed the presence of rosette between dendrite arms spacing as seen Figure 6.20. Small particles of silicon are also seen dispersed within the (Al) matrix which results certainly from solid-state precipitation.

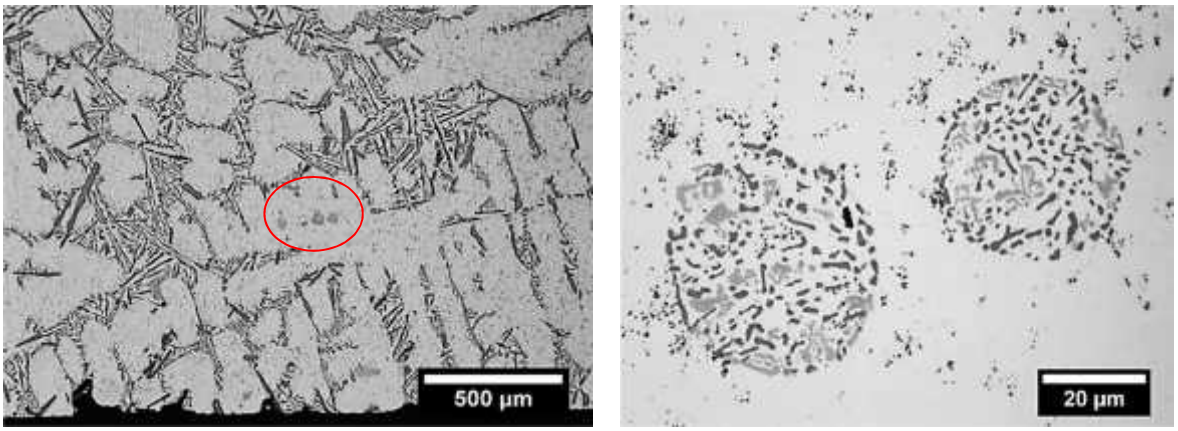

Figure 6.20. Micrograph of rosette from DTA sample with cooling rate at 5°C/min after holding at 595°C for 30 minutes.

6.2.3. Discussion

From the morphology analysis of several samples, very fine eutectic silicon was observed within the rosette. In some of the rosettes, silicon plates also appeared encircling the rosette as seen in Figure 6.16. As stated earlier, the formation of rosettes in this case is more likely due to the liquid entrapment between dendrite arms. This finding is also in agreement with Terzi et al. [15] investigation on the dendrite coarsening mechanism and showed the liquid entrapment between dendrite arms in their in-situ tomography result. Attempts to see the 3D morphology of rosette from figure 6.20 was performed by deep etch technique. SEM micrograph showed the rosette not only as a small sphere, but deep etch sample indicated a form of cylinder shape with fine eutectic. Micrograph also revealed the presence of intermetallic phase within the rosette which is noticed from its plate shape (red arrow in Figure 6.21).

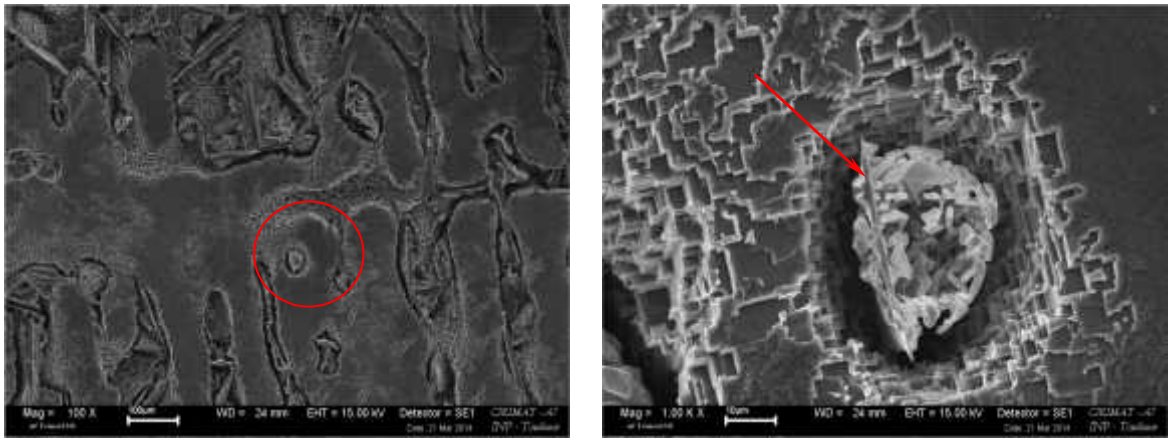

Figure 6.21. Deep etch of rosette showed cylinder shape appearance of fine eutectic silicon and intermetallic plate.

The fine structure of rosette is associated with large undercooling for its solidification. Therefore, in order to illustrate the undercooling effect, EPMA results of the rosette corrected to 100% were then superimposed on the Al-Fe-Si liquidus projection, as illustrated in Figure 6.22. In the condition where no nucleation event of iron rich phases occurs, the solidification path of (Al) primary phase proceeds with continuous increase in Fe and Si. By taking into account the Si and Fe composition on the rosettes temperature precipitation with the equation of T = 660 – (6.64*wt%Si) – (2.77*wt%Fe), the amount of undercooling for rosettes solidification can be calculated. The results showed an undercooling of 119 °C and 87 °C respectively for two rosettes after the (Al)-Si eutectic reaction.

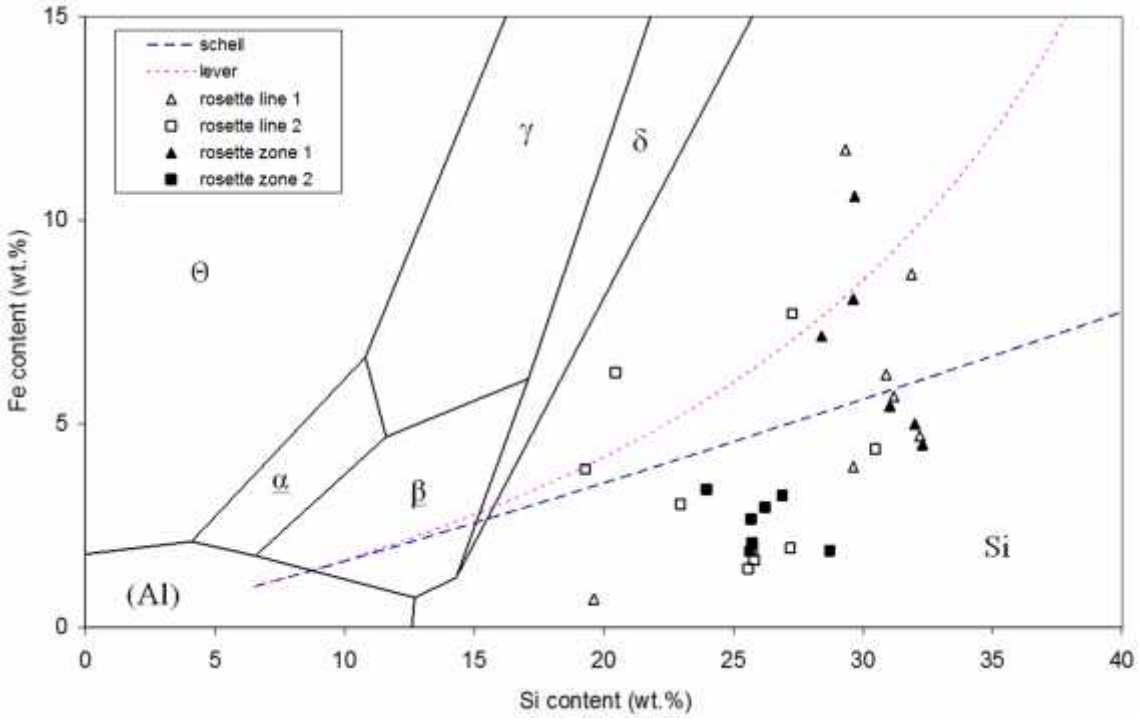

Figure 6.22. EPMA results of rosette superimposed on the Al corner of Al-Fe-Si liquidus projection. (Θ-$Al_{13}Fe_4$, α-Al_8Fe_2Si, β-$Al_9Fe_2Si_2$, ¥-Al_3FeSi, ¢-Al_3FeSi_2).

Interesting finding is related to the nucleation of eutectic silicon. Some researchers believe that beta phase precipitates could act as nucleation site for silicon [16, 17]. This assumption was probably made due to the presence of silicon attached to the beta phase in metallographic examination. However, evidence is provided here that beta phase did not act as nucleation site for silicon as can be seen by considering the micrograph in Figure 6.15. The image clearly shows a large beta plate attached to a fine eutectic in a rosette. If the beta phase acted as nucleation site, the plate like silicon would have precipitated instead of a fine eutectic structure. This result is in agreement with previous studies by Lu and Dahle [18].

EDS analysis from another sample showed an interesting finding about an iron rich intermetallic phase as seen in Figure 6.23. The rosette phase with delta phase composition has been detected with cerium content within the sphere, without any precipitation of Ce-rich phase. Cerium inside the lattice crystal of iron rich phase has certainly substituted to Fe. Cerium would be dissolved in the liquid until late in solidification, and the small precipitates mentioned previously (page 136) should thus have appeared after beta precipitation, possibly also in solid-state.

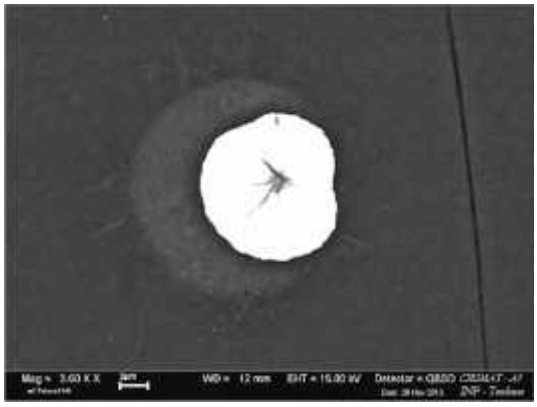

Figure 6.23. Rosette intermetallic phase with cerium entrapped with the iron rich phase.

The different morphologies of rosettes with different cooling rate related to the undercooling induced by cooling rate. At higher cooling rate, the undercooling is expected to be higher than at lower rate. From the observation, in general it was seen that the rosettes at higher cooling rate have a finer eutectic structure, indicating a very high undercooling of rosette precipitation. DTA experiment by holding below the liquidus temperature also lead to rosettes, however the structure within the rosettes was coarse. In this case, it seems the maximum undercooling probably has not been reached and the cooling rate is not high enough when the rosettes precipitate. This morphology changes established that the undercooling mechanism plays an important role for the morphology formation and growth of phases within the rosette.

Summary

A study on deviation of the solidification path in Al6.5Si1Fe alloy was performed. DTA samples cooled in near equilibrium condition by applying very low cooling rate revealed script phase precipitates in interdendritic regions. The characterization of the script phase shows it corresponds to beta phase based on the monoclinic crystal structure and chemical analysis. This finding shows that differentiation of second phase based on morphology can be ambiguous.

Different analyzes were conducted on rosettes which is another anomaly of the solidification path. It appeared that the formation is highly related to large undercoolings and isolation of the liquid pool from the bulk liquid. Characterization of the rosettes revealed multi-phase precipitates within the rosette. Cooling rate and chemical composition inside the pool determined the resulting precipitates.

Reference

1. D. Ferdian, B. Suharno, B. Duployer, C. Tenailleau, L. Salvo, J. Lacaze, Differential thermal analysis assessment of beta phase precipitation in Al-6.5Si-1Fe alloy, Transactions of the Indian Institute of Metals, 65, (2012), 821-825.
2. Gorny, J. Manickaraj, Z. Cai, S. Shankar, Evolution of Fe based intermetallic phases in Al–Si hypoeutectic casting alloys: Influence of the Si and Fe concentrations, and solidification rate, Journal of Alloys and Compounds, 577, 15, (2013), 103-124.
3. Y. Langsrud, Silicon in commercial aluminium alloys-what becomes of it during DC-casting, Key Eng. Mat, 44-45, (1990), 95-116.
4. B.J. Ye, C.R. Looper, D.Y. Lu, C.S. Kang, An assessment of the role of rare earth in the eutectic modification of cast aluminum-silicon alloys, AFS trans., 92,(1984), 533–544.
5. M. Ravi, U.T.S. Pillai, B.C. Pai, A D. Damodaran, E.S. Dwarakadasa, A study of the influence of mischmetal additions to Al-7Si-0.3Mg (LM 25/356) alloy, Metallurgical and Materials Transactions A, 27, (1996), 1283-1292.
6. Y.C. Tsai, S.L. Lee and C.K. Lin, Effect of trace Ce addition on the microstructures and mechanical properties of A356 (AL–7Si–0.35 Mg) aluminum alloys, Journal of the Chinese Institute of Engineers, 34, (2011), 609–616.
7. Z. Chen, X. Hao, J. Zhao, C. Ma, Kinetic nucleation of primary α(Al) dendrites in Al–7%Si–Mg cast alloys with Ce and Sr additions, Transactions of Nonferrous Metals Society of China, 23, (2013)3561–3567.
8. J. Grobner, D. Mirkovic, R. Schmid-Fetzer, Thermodynamic aspects of the constitution. grain refining, and solidification enthalpies of Al-Ce-Si Alloys., Metall. Mater. Trans. A., 35, (2004), 3349-3362.
9. W.T. Kim and B.Cantor, Heterogeneous nucleation of Al_2Cu in Al-Cu eutectic liquid droplets embedded in an Al matrix, Acta Metall. Mat., 42, 9 (1994), 3045-3053.
10. J. Lacaze, G. Lesoult, I. Ansara, Rosettes in Al-Cu-Mg-Si aluminium alloys, Materials Science Forum, 217-222, (1996), 171-176.
11. D.T.L. Alexander and A.L Greer, Formation of eutectic intermetallic rosettes by entrapment of liquid droplets during cellular columnar growth, Acta Materialia, 52, (2004), 5853-5861.
12. J.R. Davis, Aluminum and aluminum alloys, ASM international, 1993
13. S. Ahrweiler, L. Ratke, J. Lacaze, Microsegregation and microstructural features of directionally solidified AlSi and AlSiMg alloys, Advanced Engineering Materials, 5, (2003) 17-23.
14. J. Lacaze, P. Benigni, A. Howe, Some issues concerning experiment and models for alloy microsegregation, Advanced Engineering Materials, 5, (2003) 37-46.
15. S. Terzi, L. Salvo, M. Suéry, A.K. Dahle, E. Boller, Coarsening mechanisms in a dendritic Al–10% Cu alloy, Acta Materialia, 58, (2010), 20-30.
16. J.A. Taylor, G.B. Schaffer, D.H. StJohn, The role of iron in the formation of porosity in Al-Si-Cu-based casting alloys: Part III. A microstructural model, Metallurgical and Materials Transactions A, 30, (1999), 1657-1662.

17. L. Liu, A.M. Samuel, F.H. Samuel, H.W. Doty, and S. Valtierra, Role of iron in relation to silicon modification in Sr-treated 319 and 356 alloys, Int. J. Cast Met. Res, 16, (2003), 397–408.

18. L. Lu, A.K. Dahle, Iron-rich intermetallic phases and their role in casting defect formation in hypoeutectic Al−Si alloys, Metallurgical and Materials Transactions A, 36, (2005), 819-835.

7. Conclusion and perspectives

The objective of this study was to investigate some features of casting and solidification of Al-Si alloys which are extensively used, in particular in automotive industry. Control of melt preparation before casting is routinely made by thermal analysis with standard cups and dedicated to ensuring appropriate microstructure in terms of grain size and eutectic modification. The analysis of the characteristic features of cooling curves obtained from thermal cup was here extended to solidification of castings with various cooling rates. Multivariate statistical analysis provided insight in the correlation between the various possible parameters and their significance. Thermal analysis showed the influence of nucleation time, eutectic cooling rate and DAS on the final grain size. In addition, thermal analysis experiments also indicated that the modification of eutectic silicon is not only a function of modifier element but also a function of cooling rates, eutectic time and combination of eutectic recalescence x eutectic time.

Further study with DTA for various cooling rates established the relation of cooling rate with eutectic modification level. Extrapolation data from DTA analysis of commercial alloys (A356) showed the presence of eutectic temperature depression, which usually relates to the effectiveness of eutectic modification as the effect of strontium addition. However, observation showed that eutectic depression is not necessarily accompanied with modified eutectic silicon. This result shows that the eutectic modification might be combination of growth blocking and hindering nucleation by modifier element.

While added in Al-Si die cast alloys, iron appears in mould cast alloys because of recycling. Emphasis has been put here on the most detrimental iron-rich intermetallic, i.e the so-called beta $Al_9Fe_2Si_2$ monoclinic phase. Cooling rate effect on beta precipitation in Al-6.5Si-1Fe alloy was performed with DTA. The result showed that cooling rate has a significant effect on beta phase morphology. Low cooling rate produced long and thick beta precipitates. 3D analysis showed the beta precipitates grow in lateral direction in plate-like appearance. Most of the plates were nucleated on the skin surface and grow toward the center. In situ tomography experiment revealed the nature of beta phase growth where the lateral growth dominated the growth mechanism. The growth was marked by high growth rate which slowed down after a saturation level was reached. The slowing down does not lead to a sudden increase of the thickening rate, the high solid fraction might have limited the thickening growth.

At very low cooling rates, it has been observed that Fe-rich precipitates appear both as plates and as Chinese-script precipitates. These two forms were not intermixed but occupied

different areas in the samples. Chemical analysis, μ-XRD and EBSD all showed the Chinese-script precipitates to be β-phase as are the plates. This finding stresses the need not to differentiate microstructure analysis of Al-Si alloys on only shape recognition microscopic observations.

Finally, microstructure analysis of DTA samples showed the formation of some rosettes especially at high cooling rates which correspond to liquid that becomes isolated within the (Al) matrix during the solidification process. Because being separated from the interdendritic areas, solidification of these pools needs independent nucleation phenomena of Si and Fe-rich intermetallics. This means for most of them a significant undercooling which leads to a very fine multi-phase solidification microstructure. EPMA evaluation of rosette's composition clearly illustrated the high undercooling mentioned above. Two original observations were made:

1. δ-phase precipitation.
2. Blocky β-precipitates were found in several rosettes which completed their solidification with very fine (Al)-Si eutectic. This shows that β does not nucleate Si as it has been previously reported.

Thermal analysis has shown itself as a tool that can be used to predict grain size and eutectic modification. It also showed the capability to identify phase reaction during solidification process. For future work, it would be of interest to study further the capability and sensitivity of thermal analysis with different chemical compositions, grain refiners and modifiers.

A model for beta phase growth has been proposed which still requires detailed calculation and could be developed further with numerical simulation. Furthermore, it would be of interest to utilize in-situ tomography for studying modification of eutectic silicon, adding a heavier element such as Zn to the (Al) solid solution to enhance the phase contrast between Al and Si.

Appendix

Appendix 1

Chemical Composition

Hydro Aluminium

Hydro Aluminium Deutschland GmbH
Forschung und Entwicklung Bonn
Servicezentrum Chemie und Oberflächen
Labor für chemische Untersuchungen
Georg-von-Boeselager-Str. 21
53117 Bonn

Hydro Aluminium Deutschland GmbH · Postfach 2468 · 53014 Bonn

Herrn Schofer
RDB

Kopie: Herrn Winterscheid

Fax:

Prüfbericht-Nr.: **CA06546**
(Seiten: 1)

Sachbearbeiter Fr. Maschke
Telefon 0228 -552-2272
Telefax 0228 -552-2452

Datei : W:\ANORGANF\BERICH06\Ca06546.Doc

Datum 21-06-2006

Stoffbezeichnung :	AlSi7Fe1
Probenbezeichnung :	Ch41882
Probeneingang :	13.06.06
Prüfauftrag :	Si, Fe
Prüfverfahren :	CA4683
Stoffbeschreibung :	Pilzprobe

Bestellnummer :	B06XS022
Probenahme :	Kunde
Probenanzahl :	1
Rückstellmuster :	Anorganik, 6 Wo.

Prüfergebnis

[Gew.-%]	Ch41882
Si	6,51
Fe	0,93

Masche

Appendix 2

Thermal Analysis Data

Sand mould

REF	Modulus	TN min	TN max	Vmax	ΔTN	t1	t2	Δ_{tn}	Te min	Te max	Te2	range	t3	t4	t coales	t eutectic	tf	Td	CRL	CRe	ML	GS	DAS
1	1.5	615.4	615.7	0.45	0.3	23.98	36.52	12.54	568.2	570.1	553.5	62.2	459.14	951.06	435.16	491.92	927.08	3.42	1.11	0.14	2.1	1.05	89
	1.15	611.5	612.2	0.45	0.7	18.92	41.8	22.88	563.5	567	552.2	60	269.94	594.34	251.02	324.4	575.42	6.52	2.07	0.26	2.2	1.05	71
	1	611.3	612.1	0.45	0.8	12.32	29.04	16.72	563.4	566.6	550.2	61.9	181.5	372.46	169.18	190.96	360.14	6.92	2.63	0.39	2.3	0.95	64
	0.8	613	613.7	0.45	0.7	7.7	20.02	12.32	564.4	568.2	548.8	64.9	120.34	289.78	112.64	169.44	282.08	5.32	4.27	0.56	2.7	0.92	53
	0.6	610.5	610.8	0.45	0.3	5.5	10.56	5.06	560.3	563.7	545.2	65.6	65.34	142.78	59.84	77.44	137.28	9.82	8.64	1.13	3.8	0.76	44
	0.4		609.1	0	0	3.52	4.4	0.88	558.8	560.5	535.3	73.8	27.94	65.56	24.42	37.62	62.04	13.02	13.18	2.91	4.2	0.58	34
2	1.5	615.8	616.9	0.2	1.1	62	107	45.00	568.8	570.8			510		448			1.83	0.92	0.14	1.8	1.04	87
	1.15	612	614	0.4	2	43	84	41.00	565.6	568.6	552	62	396	797	353	401	754	4.03	1.53	0.17	1.8	0.96	81
	1	615.2	616.6	0.3	1.4	28	61	33.00	566.8	570.1	550.7	65.9	319	663	291	344	635	2.53	2.20	0.21	2.2	0.91	71
	0.8	612.5	613.9	0.4	1.4	27	51	24.00	565	568.2	548.9	65	239	539	212	300	512	4.43	2.25	0.28	2.3	0.93	55
	0.6	614.4	615.7	0.5	1.3	16	29	13.00	565.5	569.3	541.1	74.6	118	266	102	148	250	3.33	4.30	0.65	2.5	0.83	48
	0.4	615.6	615.7	0.1	0.1	6	8	2.00	564.3	568.4	540.2	75.5	76	193	70	117	187	4.23	8.60	0.84	3.7	0.59	31
3	1.5	614.9	615	0.45	0.1	43.12	50.16	7.04	567.2	570.2	553.1	61.9	437.58	879.56	394.46	441.98	836.44	3.49	1.59	0.15	1.7	0.66	87
	1.15		614.9	0	0	28.38	37.4	9.02	566.2	570	552.7	62.2	288.86	608.3	260.48	319.44	579.92	3.69	1.89	0.23	2	0.64	79
	1	614.6	615	0.45	0.4	20.68	26.84	6.16	566.2	569.4	552.8	62.2	213.4	466.84	192.72	253.44	446.16	4.29	3.13	0.31	2	0.65	67
	0.8	614.4	614.8	0.45	0.4	12.98	19.8	6.82	564.8	568.2	551.1	63.7	114.18	237.6	101.2	123.42	224.62	5.49	4.02	0.64	2.1	0.54	53
	0.6	613.6	613.8	0.45	0.2	6.16	9.46	3.30	564	567.8	551.7	62.1	76.12	188.1	69.96	111.98	181.94	5.89	6.67	0.86	2.5	0.50	47
4	1.5	617	617.1	0.41	0.1	34.56	41.52	6.96	564.9	566.8	551.4	65.7	518.64	960.96	484.08	442.32	926.4	7.41	1.27	0.14	3	0.72	88
	1.15	616.3	616.6	0.41	0.3	22.56	35.28	12.72	564.9	566.4	550.8	65.8	368.68	745.2	346.12	376.52	722.64	7.81	1.46	0.20	3	0.70	78
	1	615.8	616.2	0.41	0.4	18.72	32.64	13.92	565.1	566.6	549.7	66.5	214.56	453.84	195.84	239.28	435.12	7.61	2.55	0.34	3.6	0.62	70
	0.8	615.1	615.9	0.41	0.8	12	24.72	12.72	565.2	566.1	548.4	67.5	139.2	292.32	127.2	153.12	280.32	8.11	5.42	0.56	4.8	0.56	52
	0.6		614.2	0	0	5.28	7.92	2.64	563.8	565.5	549	65.2	85.2	190.8	79.92	105.6	185.52	8.71	8.12	0.85	5	0.54	50
	0.4	613.1	613.2	0.41	0.1	2.4	3.84	1.44	561.5	564.9	542.2	71	25.92	57.84	23.52	31.92	55.44	9.31	15.83	2.95	5.8	0.46	
5	1.5	617.1	617.6	0.45	0.5	46.64	62.7	16.06	568	569.3	552.3	65.3	522.94	983.18	476.3	460.24	936.54	3.81	0.80	0.13	3	0.56	87
	1.15	616.8	617	0.45	0.2	32.56	42.9	10.34	566.8	569.1	551.5	65.5	355.74	698.06	323.18	342.32	665.5	4.01	1.29	0.19	3	0.54	74
	1	616.9	617	0.45	0.1	22.22	27.5	5.28	566.5	569.1	551.8	65.2	225.06	487.74	202.84	262.68	465.52	4.01	1.71	0.32	3.3	0.53	70
	0.8	616.4	616.6	0.45	0.2	14.74	19.14	4.40	564.6	566.7	549.9	66.7	129.14	242.44	114.4	113.3	227.7	6.41	2.58	0.59	4.7	0.53	58
	0.6	616.5	616.8	0.45	0.3	8.14	11.66	3.52	564.4	566.7	550.7	66.1	78.32	163.24	70.18	84.92	155.1	6.41	5.68	0.97	5	0.48	48
	0.4		615.4	-1.36	0	7.04	8.14	1.10		560.7	535.5	79.9	38.72	69.52	31.68	30.8	62.48	12.41	5.00	2.40	5.6	0.40	32
6	1.5	615.3	615.5	0.55	0.2	90.54	100.44	9.90	568.3	570.1	553.5	62	594.36	1026	503.82	431.64	935.46	4.02	0.77	0.13	2	0.57	95
	1.15		615.2	0	0	54.9	58.68	3.78	567.3	569.9	552.1	63.1	341.1	647.1	286.2	306	592.2	4.22	1.46	0.23	2.2	0.44	84
	1		615	0	0	39.6	40.68	1.08	566.7	569.3	551.8	63.2	255.78	528.84	216.18	273.06	489.24	4.82	1.78	0.28	2.5	0.46	80
	0.8	614.5	614.8	0.55	0.3	46.08	51.48	5.40	565.7	567.5	550.1	64.7	200.5	430.02	154.42	229.52	383.94	6.62	1.40	0.39	3	0.40	66
	0.6		614.2		0	15.12	16.02	0.90	564.5	566.9	549.9	64.3	85.32	174.06	70.2	88.74	158.94	7.22	5.22	0.92	3.7	0.38	54
8	1.5	614.4	615.1	0.45	0.7	23.76	44.44	20.68	565.5	567.8	554.2	60.9	426.8	828.08	403.04	401.28	804.32	5.77	2.32	0.15	1.8	0.90	79
	1.15	614.2	615.3	0.45	1.1	14.74	38.5	23.76	564.4	567	553.8	61.5	236.06	474.76	221.32	238.7	460.02	6.57	2.23	0.32	2.1	0.70	68
	1	612.9	615	0.45	2.1	11.44	36.74	25.30	564.2	567.2	552.7	62.3	224.4	473.44	212.96	249.04	462	6.37	4.32	0.29	2.3	0.66	63
	0.8	612.2	613.7	0.45	1.5	7.48	23.32	15.84	563.2	566.1	550.1	63.6	113.96	247.5	106.48	133.54	240.02	7.47	4.64	0.64	2.7	0.67	54
	0.6	613.2	613.6	0.45	0.4	4.84	11.44	6.60	562.6	565.9	551.8	61.8	74.8	172.48	69.96	97.68	167.64	7.67	7.42	0.93	3	0.65	51
9	1.5		619.1	0	0	49	52.00	3.00	566.2	568.9	551.4	67.7	448	825	399	377	776	3.15	1.02	0.18	2.5	0.62	92
	1.15		616	0	0	37	41.00	4.00	563.1	566.3	551	65	336	630	299	294	593	5.75	1.30	0.22	2.8	0.48	77
	1		617.4	0	0	24	25.00	1.00	563.5	566.2	549.5	67.9	208	420	184	212	396	5.85	2.55	0.36	3.5	0.43	75
	0.8	617.3	617.4	0.1	0.1	14	16.00	2.00	563.4	565.4	540.5	76.9	119	237	105	118	223	6.65	3.75	0.66	3.6	0.43	55
	0.6		618	-0.4	0	8	8.00	0.00	563.4	564.3	537.4	80.6	68	145	60	77	137	7.75	3.20	1.12	4	0.36	45
	0.4		616.1	-0.4	0	3	3.00	0.00	561.1	563	533.3	82.8	27	62	24	35	59	9.05	14.10	2.80	4.9	0.34	36
10	1.5	617.4	619	0	0	56	107	51.00	565.9	567.4	554.3	64.7	414	713	358	299	657	4.79	1.25	0.20	2.6	0.94	80
	1.15	615.8	617.3	0.3	1.5	39	74	35.00	564.2	565.5	550.7	66.6	268	481	229	213	442	6.69	1.57	0.32	2.8	0.86	70
	1	616	617.9	0.4	1.9	25	51	26.00	564.7	566.3	549.5	68.4	212	401	187	189	376	5.89	2.27	0.37	2.7	0.84	63
	0.8	616.2	617.7	0.4	1.5	14	26	12.00	564.4	565	542.1	75.6	116	229	102	113	215	7.19	3.25	0.69	2.8	0.82	52
11	1.15	618.2	618.4	0.1	0.2	31	39	8.00	564.8	567.4	552.3	66.1	251	455	220	204	424	4.88	1.22	0.32	2.6	0.70	65
	1	617	617.6	0.2	0.6	21	32	11.00	564.2	566.7	551.2	66.4	198	410	177	212	389	5.58	2.05	0.38	2.5	0.65	57
	0.8	616.1	616.6	0.3	0.5	12	20	8.00	563.1	564	549.2	67.4	113	207	101	94	195	8.28	3.70	0.72	2.6	0.60	58
	0.6	616.7	617	0.3	0.3	6	10	4.00	562.9	564.4	547.4	69.6	67	145	61	78	139	7.88	4.70	1.14	3.5	0.55	42
	0.4		614.9	-0.6	0	2	3	1.00	560.2	562.1	535.1	79.8	27	53	25	26	51	10.18	0.00	2.83	4	0.50	31

Quick cup

REF	Modulus	TN min	TN max	Vmax	ΔTN	t1	t2	Δ_{tn}	Te min	Te max	Te2	range	t3	t4	t. coales	t eutectic	tf	Td	CRL	Cre	ML	GS	DAS
1	0.605	611.2	611.4	0.45	0.2	10.56	16.5	5.94	562.6	564.9	550.9	60.5	126.88	307.56	116.32	180.68	297	8.62	4.82	0.52	4	0.74	53
2	0.605	612.2	612.4	0.1	0.2	12	19	7.00	564.2	567	550.5	61.9	136	334	124	198	322	5.63	4.90	0.46	3	0.6	55
3	0.605	614.1	614.2	0.45	0.1	15.4	19.36	3.96	565.5	568.3	551.9	62.3	151.8	343.2	136.4	191.4	327.8	5.39	3.71	0.41	3	0.51	58
4	0.605		615.4	0	0	12.48	13.44	0.96	564.8	564.9	552.1	63.3	150.24	304.32	137.76	154.08	291.84	9.31	4.33	0.51	6	0.47	58
5	0.605		613.8	0	0	22.22	24.64	2.42	564.3	566.3	551.5	62.3	146.52	330.44	124.3	183.92	308.22	6.81	3.38	0.47	3.5	0.47	56
6	0.605		615	0	0	24.46	25.02	0.56	566.8	568.9	552.1	62.9	152.64	334.08	128.18	181.44	309.62	5.22	3.15	0.42	2.9	0.46	57
7	0.605		613.2	0	0	13.2	13.42	0.22	566.4	568.6	550.6	62.6	137.28	335.94	124.08	198.66	322.74	5.00	3.79	0.45	2.8	0.4	54
8	0.605	613.9	614.3	0.45	0.4	11.44	18.26	6.82	563.7	566.9	552.8	61.5	124.96	297.88	113.52	172.92	286.44	6.67	4.55	0.52	3.4	0.77	53
9	0.605		615.5	-0.2	0	20	20	0.00	562.7	565.3	550.8	64.7	164	342	144	178	322	6.75	2.30	0.41	4.6	0.41	57
10	0.605		613	0	0	17.5	21.7	4.20	561.5	563	550.6	62.4	195.3	413.7	177.8	218.4	396.2	9.19	2.33	0.32	4.3	0.95	63
11	0.605	614.7	615	0.71	0.3	13.16	21.42	8.26	563	565.6	551.4	63.6	145.32	323.96	132.16	178.64	310.8	6.68	4.73	0.46	4.1	0.52	59

Metallic mould

REF	Modulus	TN min	TN max	Vmax	ΔTN	t1	t2	Δ_{tn}	Te min	Te max	Te2	range	t3	t4	t coales	t eutectic	tf	Td	CRL	Cre	ML	GS	DAS
1	1.15		612.9	0	0	6.6	13.86	7.26		559.5	532.2	80.7	57.64	80.08	51.04	22.44	73.48	14.02	8.64	2.14	4	0.70	35
	1		613.5	0	0	6.16	7.26	1.10	559.9	560	530	83.5	50.16	73.04	44	22.88	66.88	13.52	6.59	2.66	4.5	0.67	34
	0.8		611.7	0	0	5.5	5.72	0.22	557.5	558.4	526.6	85.1	32.56	50.16	27.06	17.6	44.66	15.12	9.32	4.04	4.7	0.63	29
	0.6		610.4	0	0	3.96	4.18	0.22	556.4	557.2	520.9	89.5	22.66	36.74	18.7	14.08	32.78	16.32	10.91	6.46	4.4	0.58	28
	0.4		609.8	-2.72	0	2.86	2.86	0.00	555.1	555.8	521.9	87.9	10.56	18.48	7.7	7.92	15.62	17.72	15.91	11.23	4.9	0.44	20
	0.3		607.8	0	0	1.32	1.32	0.00	552.3	553.9	517.4	90.4	8.14	16.28	6.82	8.14	14.96	19.62	49.55	15.17	5	0.43	19
3	1.15	614.1	614.3	0.45	0.2	4.4	11.88	7.48	564.9	566.3	540.1	74.2	63.14	93.28	58.74	30.14	88.88	7.39	10.91	1.97	3.3	0.25	43
	1		616.2	0	0	3.08	6.38	3.30	566.4	567.4	538.8	77.4	44.44	67.98	41.36	23.54	64.9	6.29		2.60	3.8	0.23	37
	0.8		614.4	0	0	5.28	5.72	0.44		565	537.1	77.3	29.48	41.58	24.2	12.1	36.3	8.69	10.00	4.19	5.1	0.22	31
	0.6		614.2	0	0	5.06	5.06	0.00	563	563.1	543.2	71	22.66	35.42	17.6	12.76	30.36	10.59	11.82	5.77	5.2	0.23	28
	0.4		612.7	0	0	1.54	1.54	0.00	561	563.3	529	83.7	11.88	23.98	10.34	12.1	22.44	10.39		8.95	5.2	0.36	22
	0.3	609.2	610.8	3.18	1.6	1.32	2.86	1.54	559.7	563.7	529.2	81.6	9.68	20.68	8.36	11	19.36	9.99	29.09	9.96	6	0.35	21
4	1.15		615.6	0	0	7.2	8.64	1.44	561.7	562.6	536.5	79.1	64.8	91.2	57.6	26.4	84	11.61	5.08	1.96	6	0.59	38
	1		615.8	0	0	5.28	6.24	0.96	561.8	564.9	539.4	76.4	45.84	65.76	40.56	19.92	60.48	9.31	8.54	2.82	6	0.46	37
	0.8		614.1	0	0	4.08	4.56	0.48		560.3	533.6	80.5	28.08	38.64	24	10.56	34.56	13.91	5.73	4.41	6	0.53	31
	0.6		612.4	-1.66	0	2.16	2.16	0.00		560.5	507.5	104.9	15.84	35.04	13.68	19.2	32.88	13.71	24.58	6.05	6	0.53	27
	0.4		611.1	-0.83	0	2.4	2.4	0.00		556.7	526	85.1	12.96	22.56	10.56	9.6	20.16	17.51	58.33	12.55	6	0.50	21
	0.3		608.7	-7.5	0	1.2	1.2	0.00		552.2	516	92.7	7.92	15.12	6.72	7.2	13.92	22.01	59.58	12.86	6	0.46	20
5	1.15		614.1	0	0	16.94	18.92	1.98	560.6	561.9	538.9	75.2	76.12	105.46	59.18	29.34	88.52	11.21	4.91	1.91	4	0.47	37
	1		615.2	0	0	9.9	10.56	0.66		561.5	530.4	84.8	52.14	79.86	42.24	27.72	69.96	11.61	10.67	2.67	4.3	0.42	35
	0.8		614	0	0	10.78	12.54	1.76	559.8	561.9	536.3	77.7	34.54	48.62	23.76	14.08	37.84	11.21	4.85	5.64	4.3	0.43	30
	0.6		613.5	0	0	7.03	7.48	0.45		559	531.6	81.9	27.06	41.8	20.03	14.74	34.77	14.11	17.56	6.10	4.5	0.38	30
	0.4		612.2	-1.81	0	3.08	3.08	0.00		557.6	523.4	88.8	12.54	20.68	9.46	8.14	17.6	15.51	18.64	11.07	4.7	0.37	21
	0.3		613.8	-0.9	0	2.19	2.19	0.00	557.1	558.9	533.2	80.6	9.9	19.58	7.71	9.68	17.39	14.21	20.91	12.78	5	0.33	21
6	1.15		615.2	0.55	0	1.98	5.04	3.06	565.5	565.6	534.6	80.6	65.52	100.44	63.54	34.92	98.46	8.52		1.92	4	0.44	48
	1		613.9	1.98	0	1.44	12.06	10.62	563.9	565	548.4	65.5	46.26	68.22	44.82	21.96	66.78	9.12		2.61	4.3	0.35	42
	0.6	614.5	614.6	0.55	0.1	1.08	1.8	0.72	562	562.2	533.1	81.5	22.86	37.44	21.78	14.58	36.36	11.92		5.71	4.5	0.41	27
	0.4	607.8	608.5	1.1	0.7	0.9	2.7	1.80		560.2	527.4	81.1	12.6	19.8	11.7	7.2	18.9	13.92		7.44	4.7	0.30	24
	0.3		612.3	-1.1	0	1.08	1.08	0.00		552.1	514.6	97.7	10.6	17.28	9.52	6.68	16.2	22.02		10.93	5	0.29	21
7	1.15		617.3	0	0	8.58	9.02	0.44		567.8	542	75.3	71.5	96.58	62.92	25.08	88	5.8	2.23	1.54	4.3	0.32	45
	0.8		613.6		0	5.28	7.26	1.98		564.9	540.1	73.5	32.56	45.1	27.28	12.54	39.82	8.7	8.41	3.54	4.8	0.29	31
	0.6	612.2	612.3	0.45	0.1	4.18	5.28	1.10		563.9	537.2	75.1	24.2	35.2	20.02	11	31.02	9.7	11.14	4.70	5	0.33	28
	0.4																						
	0.3	609.7	611.2	6.81	1.5	3.74	4.84	1.10	559.5	563.3	531.3	79.9	10.12	15.18	6.38	5.06	11.44	10.3	24.09	18.19	5.2	0.30	21
9	1.15		617.3	-0.1	0	7	7	0.00	561.8	562.2	540.8	76.5	58	78	51	20	71	9.85	17.80	2.68	4.2	0.37	35
	1		617.5	-0.2	0	6	6	0.00	560.8	560.9	535	82.5	44	62	38	18	56	11.15	7.15	3.04	4.3	0.33	31
	0.8		615.9	-0.3	0	5	5	0.00	559.2	560.4	543.5	72.4	30	42	25	12	37	11.65	14.10	5.02	4.4	0.33	29
	0.6		615.6	0.5	0	5	5	0.00	557.7	559.8	534.4	81.2	21	32	16	11	27	12.25	8.00	5.53	4.5	0.29	24
	0.4		615.7	-2	0	2	2	0.00	556.5	558.3	531.3	84.4	11	18	9	7	16	13.75	19.50	11.20	4.6	0.29	21
	0.3		613.6	-7.1	0	1	1	0.00	552.2	553.5	527.6	86	7	12	6	5	11	18.55	27.30	16.10	4.8	0.29	20
10	1.15		618.3	-0.1	0	5	5	0.00		563.2	545.3	73	54	71	49	17	66	8.99	9.30	2.55	4.4	0.40	37
	0.8		614.5	-0.1	0	6	6	0.00		556.7	531.5	83	30	43	24	13	37	15.49	4.18	4.24	4.8	0.46	28
	0.6		614.7	-0.3	0	4	4	0.00	557.4	560	520.9	93.8	22	34	18	12	30	12.19	15.30	5.88	4.7	0.33	27
	0.4		614.4	-1	0	2	2	0.00	556.1	558.8	524.5	89.9	12	21	10	9	19	13.39	26.40	9.45	4.9	0.30	22
11	1.15	617.1	617.3	0.1	0.2	6	14	8.00		564	538.4	78.9	59	76	53	17	70	8.28	12.90	2.83	4.9	0.26	36
	0.8		616.7	-0.3	0	3	3	0.00		557.5	529.3	87.4	30	43	27	13	40	14.78	13.90	4.17	5	0.25	28
	0.6		614.1	-0.4	0	4	4	0.00		554.8	523	91.1	20	30	16	10	26	17.48	13.80	6.50	5	0.26	29
	0.4		614.9	-2.6	0	1	1	0.00	556.7	557.8	527.2	87.7	12	20	11	8	19	14.48		7.53	6	0.25	26
	0.3		615.3	-3.6	0	1	1	0.00	556.5	558.3	531.3	84	7	12	6	5	11	13.98	14.90	16.60	6	0.24	20

Appendix 3

Assessment on Mondolfo's eutectic temperature of A3xx alloys

One of the most used methods to evaluate the reference temperature of the (Al)-Si eutectic was proposed by Apelian et al. [1] who derived an equation expressing the eutectic temperature as a function of alloy's composition from the phase diagram compiled by Mondolfo [2]. The so-called "*Mondolfo's equation*" is still widely accepted as seen in the recent work by Wang and Lu [3].

Mondolfo's **equation**

In his work, Mondolfo equation evaluated the effect of six elements (Cu, Fe, Mg, Mn, Ni and Zn) on the (Al)-Si binary eutectic set at $w_{e,Si}$ =12.5 wt.% Si and $T_{e,Si}$ =577°C. The equation considered that the effect of these elements should be additive, so that the effect of each one could be evaluated based on the related ternary phase diagram. As an example, Figure 1 shows schematically the projection of the liquidus surface of the Al-Fe-Si system (right part of the diagram) and the evolution of the (Al)-Si eutectic temperature (left part of the diagram), i.e. along the line e_{si}-E_{Fe}, where E_{Fe} is the three phase invariant eutectic point.

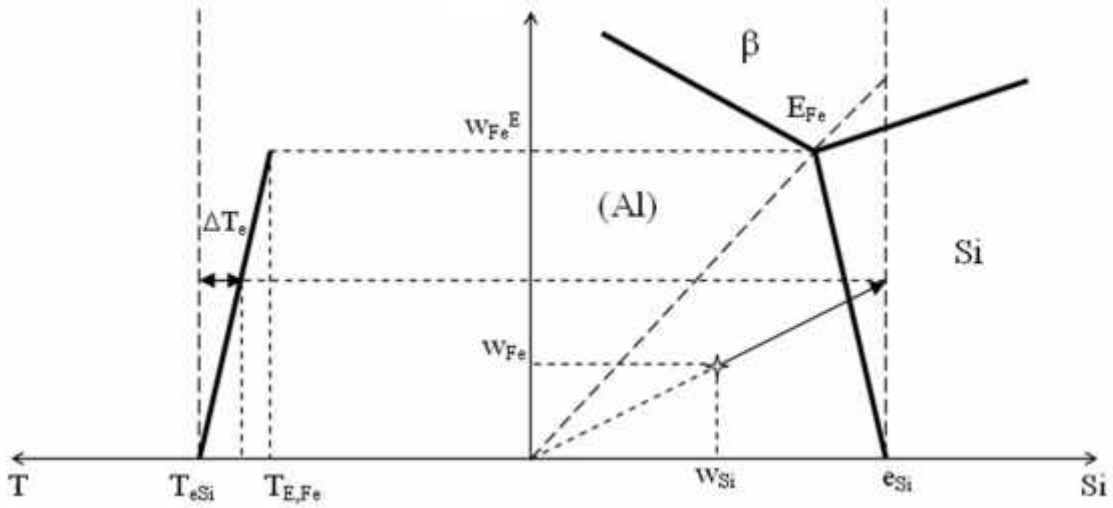

Figure 1. Schematic Al corner of the ternary Al-Si-Fe system

Assuming linearity of the temperature change (ΔT_e) along the two-fold eutectic-line, one has:

$$\Delta T_e = \frac{T_{e,Si} - T_{E,Fe}}{w_{Fe}^{E}} \cdot w_{Fe}^{(Al)-Si} = a_i \cdot w_{Fe}^{(Al)-Si} \qquad (1)$$

where $w_{Fe}^{(Al)-Si}$ is the iron weight content along the (Al)-Si eutectic line.

For any alloy with composition (w_{Si}, w_{Fe}) such as the one represented with the cross in the right side of figure 1, Mondolfo assumes that solidification of the (Al) primary phase leads to a liquid enrichment in Fe in proportion of $\frac{w_{e,Si}}{w_{Si}}$. This corresponds to the arrow in the graph.

Accordingly, the (Al)-Si eutectic temperature for this alloy is decreased with respect to $T_{e,Si}$ by:

$$\Delta T_e = a_i \cdot w_{Fe} \cdot \frac{w_{e,Si}}{w_{Si}} \qquad (2)$$

Mondolfo further assumed that the effect of alloying elements is additive, so that the reference temperature for the start of the (Al)-Si eutectic reaction of an alloy is given as:

$$T_e = T_{e,Si} - \frac{w_{e,Si}}{w_{Si}} \cdot \sum_X (a_X \cdot w_X) \qquad (3)$$

where the sum is extended to all X alloying elements.

Ternary Al-Si-X phase diagrams where X is Fe, Mg, Mn and Ni, are very similar, i.e with a e_{si}-E_X line that is at nearly constant Si. Data relative to these diagrams and relevant to the present work are listed in Table 1, where $w_{Si}^{E,X}$ and $w_X^{E,X}$ are the Si and X content of the ternary invariant eutectic, $w_X^{E,S}$ is the X content in solid (Al) in equilibrium with the ternary eutectic liquid and $T_{E,X}$ is the ternary eutectic temperature. The partition coefficients between (Al) and the liquid, k_X, have been evaluated with the ternary eutectic data and are also listed in the table. Mondolfo used ternary phase diagrams mostly according to the extensive work by Philips [4]. Updated data were presently selected for the systems with Cu [5], Mn [6], and Zn [7], with Mondolfo's original data then listed between brackets in Table 1. The last two columns list the a_X values according to Mondolfo and to the present work respectively.

Using the partition coefficients in table 1, one can calculate the solidification path of Al-Si-X ternary alloys according to lever rule and Scheil's model. This is illustrated in Figure 2 in the case of Ni where is seen that Scheil and lever rule solidification paths are nearly superimposed. Interestingly enough, it is also noted that Mondolfo's evaluation of the solidification path which is illustrated with the arrow lies close to these calculations. These observations apply to the other three elements, Mg, Fe and Mn. However, it is also clear from the graph in Figure 2 that the method applies only to alloy having their composition in the triangle Al-e_{Si}-E_X. Thus, Modolfo's method should be used only for alloys with a maximum content in X such that they precipitate the (Al)-Si eutectic before any other eutectic phase. This maximum, w_X^{max}, depends on the alloy's Si content and is given as:

$$w_X^{max} = \frac{w_{Si}}{w_{Si}^{E,X}} \cdot w_X^{E,X} \qquad (4)$$

Table 1. Ternary eutectic points data of selected Al-Si-X ternary systems. See the text for definitions; compositions in wt.% and temperature in Celsius. Mondolfo's values are between brackets when they have been updated.

Element	$w_{Si}^{E,X}$	$w_X^{E,S}$	$w_X^{E,X}$	k_X	$T_{E,X}$	Mondolfo's factor a_x	$\frac{Te-T_{E,X}}{w_X^{E,X}}$	$\frac{w_{Si}^{E,X}}{w_{Si}^{(Al)-Si}}$	Proposed factor a_x
Mg	12.95	0.85	4.96	0.171	555	4.43	4.43	1.036	4.59
Fe	12	0.05	0.7	0.071	576	1.43	1.43	0.96	1.37
Cu	6 (5)	4.5	25.6 (27)	0.175	521 (525)	1.93	2.187	0.48 0.75*	1.65
Zn	4.2 (3)		40 (80)	0.46	535 (440)	1.71	1.05	0.336	0.35
Mn	12. 7 (12)	0.03	0.4 (1)	0.075	576 (574)	3	2.5	1.016	2.54
Ni	11	0.05	5	0.01	557	4	4	0.88	3.52

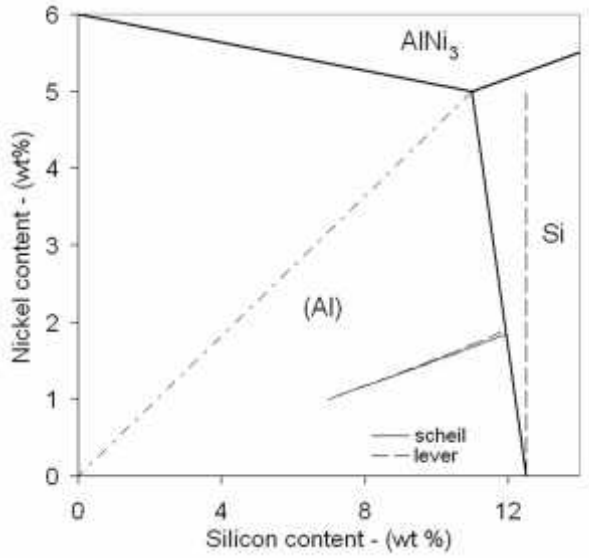

Figure 2. Solidification path in the ternary Al-Si-Ni phase system.

For alloys with low level in alloying elements such as A356 where the total content in elements other than Al and Si is less than 1%, the accuracy of Mondolfo's equation is quite good in predicting the (Al)-Si eutectic temperature [8]. However, the equation fails to predict correctly in aluminum-silicon alloys with high Cu alloying content such as A319.]. The reason for this is evidenced when considering the Al-Si-Cu phase diagram in Fig. 2b drawn according to He et al. [5]. It is seen that the (Al)-Si eutectic line moves far away to the left of the line at 12.5 wt. %Si along with increasing copper content. This leads to copper contents as estimated by the method much higher than the one when the solidification path reaches the (Al)-Si eutectic line. The maximum overestimation of the copper content is obtained for the ternary eutectic point when the method would give 2.5 (i.e. 12.5/5.0) times too high copper content. This means that the a_{Cu} coefficient as listed in Table 1 as “original factor” should be multiplied by 0.4. Because the actual copper contents in the Al-Si alloys are much lower than

the value at the ternary eutectic point, the correction cannot be that dramatic in all practicality. With the experimental data analyzed below, it has been found that a multiplication factor of 0.75 gives appropriate results, i.e. a_{Cu} was set to 1.65 after accounting for the effect of Si ternary eutectic content, see Table 1. The Al-Si-Zn phase diagram is somehow similar to the Al-Si-Cu one in that the ternary invariant eutectic is located far away from the binary (Al)-Si eutectic, and in fact is very close to the Zn-rich corner of the phase diagram. For this system and owing to the low Zn levels in A3xx alloys, it seemed wiser to use the reported isopleth section at 5.3 at.%Si [7,9] to estimate the effect of Zn on the two-fold (Al)-Si saturation line. The corresponding data is shown in Table 1 where it is seen that the final estimate of a_{Zn} differs greatly from the one assessed with the Apelian's method.

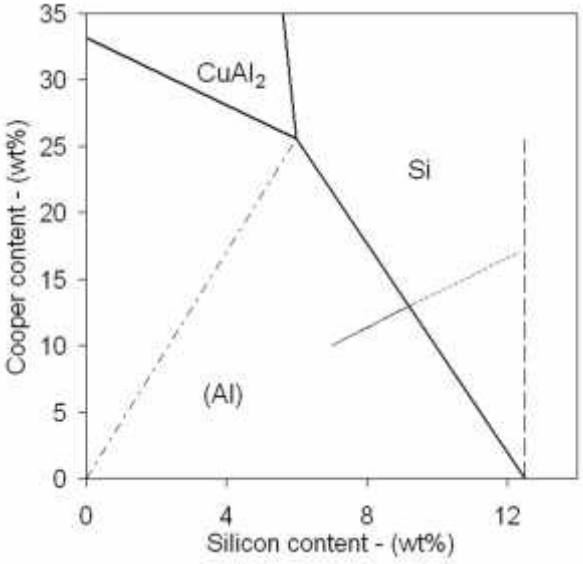

Figure 3. Solidification path in the ternary Al-Si-Cu phase diagram.

As a result, to accommodate the line changes, the updated equation are incorporated the changes of silicon content along the eutectic line and writes as follow:

$$T_e\left(^oC\right)=577-\frac{12.5}{w_{Si}}\cdot\left(4.59\cdot w_{Mg}+1.37\cdot w_{Fe}+1.65\cdot w_{Cu}+0.35\cdot w_{Zn}+2.54\cdot w_{Mn}+3.52\cdot w_{Ni}\right) \quad (5)$$

The equation itself also restricted by the level of silicon. In the case of very low silicon content such as less than 1 wt%, the calculated result would be much lower than the actual measurement. Therefore, the equation should be limited to chemical composition as follow: Si : 1-12.5, , Mg ≤ 4.9, Fe ≤ 0.7, Cu ≤ 5, Zn ≤ 5, Mn ≤ 0.4 and Ni ≤ 5.

Other equations

There are several approach proposed to calculate the eutectic temperature. A different point of view was made by Morinaka [10] who introduced an equation for magnesium content calculation in aluminium alloy. Nevertheless, this work is appeared as another simplified Mondolfo approach which only considered the magnesium effect to the ternary eutectic temperature. A simple approach has been used by Vijayaraghavan et al. [11] that only considered the copper content in the A319 alloys obtained from the ternary Al-Si-Cu phase diagram.

$$T_e=577.8-1.6\cdot w_{Cu} \quad (6)$$

Studies by Joenoes and Gruzleski [12] which focused on the magnesium effect are proposed a series of empiric calculation with a coefficient depending on Si content in the alloys

Alloy	Equation	Max. wt% Mg	
Al-7Si	T_e= 579 –17.6 Mg	1.01	(7)
Al-13Si	T_e= 576 – 6.9Mg	0.98	(8)
A 413.2	T_e= 574.6 – 8.7Mg	1.25	(9)

Hausler and Schneider [13] also proposed a polynomial equation for Al-11Si base alloy made from the experiment with Mg content up to 1 %

$$T_e = 577 - 5.8 \cdot w_{Mg^2} - 4.7 \cdot w_{Mg} \quad (9)$$

While those previous proposed equation only consider one element to the calculation and limited to one type of alloy chemical composition, Sthuldreier et al. [14] already considered 3 major elements in Al-Si-X ternary systems, which are Mg, Cu and Fe to the equation.

$$T_e = 577 - \left(11 \cdot w_{Mg} + 1.8 \cdot w_{Fe} + 2.5 \cdot w_{Cu}\right) \quad (10)$$

Similar approach also proposed by Drossel [15] which create the equation using regression analysis from their experiment data.

$$\begin{aligned} T_e &= 577 - \left(12.9 \cdot w_{Cu} + 32.3 \cdot w_{Fe} + 72.9 \cdot w_{Mg} + 22.4 \cdot w_{Mn}\right) \\ &+ \left(33.05 \cdot w_{Zn} + 0.6 \cdot w_{Si,Cu} + 59 \cdot w_{Fe,Mn} + 11.6 \cdot w_{Cu,Mg} + 2.8 \cdot w_{Si,Mg}\right) \end{aligned} \quad (11)$$

However, Drossel limits the equation application to the following chemical composition:

Si ≤ 9.3	Cu ≤2.5	Mg ≤ 0.6	Fe ≤ 1.15
Mn ≤ 0.4	Zn ≤ 0.63	Ni ≤ 0.43	Ti ≤ 0.05

Such an approach, that does not consider the enrichment in *i* of the liquid during primary (Al) precipitation.

A different approach was used derived by Djurdjevic, Sokolowski and collaborator [16,17]. They described the (Al) liquidus line with second order polynomial for Al-x systems of eutectic and then define a silicon equivalent (Si_{eq}) for each element x. They considered that other element as part of the Al-Si binary phase which increases the total silicon content.

$$Si_{eq} = w_{Si} + \sum_i (a_i + b_i w_i + c_i w_i^2) \quad (12)$$

which is used to calculate the liquidus of an alloy.

$$T_L = 660.452 - \left(6.11 Si_{eq} + 0.057 Si_{eq}^2\right) \quad (13)$$

The author limits the equation application to the following chemical composition for liquidus calculation as follow Si ≤ 12.6, Cu ≤10, Mg ≤ 10 and Zn ≤ 10 [18]. Then the enrichment of the liquid is described as did Mondolfo to calculate the eutectic temperature which writes:

$$T_e = 660.452 - \left(6.11 Si_{eq} + 0.057 Si_{eq}^2\right) \cdot \left(\frac{12.3}{w_{Si}}\right) \quad (14)$$

where $w_{e,si}$ has been set to 12.3.

Comparison

One of the difficulties with treating thermal analysis data is the influence of cooling rate upon the eutectic depression. Experiment have showed that higher cooling rate causing a higher undercooling, therefore at higher cooling rate a lower eutectic temperature is detected by the apparatus. Other than that, there were two method normally used to extract the eutectic temperature from the cooling curve, which is $T_{E,G}^{Al\text{-}Si}$ and $T_{E,Nuc}^{Al\text{-}Si}$. Unfortunately, the common practice of using $T_{E,Nuc}^{Al\text{-}Si}$ is appeared inappropriate for determining the eutectic temperature. The method has the tendency to record the eutectic temperature at higher value than the actual eutectic temperature, as can be seen from a comparison to the CALPHAD calculation in Table 2. This phenomenon also clearly showed on thermal analysis cooling curve data with high cooling rate and high undercooling.

A comparison with other equation on calculated eutectic temperature, thermal analysis data acquired from several literature [1,16,19,20-28] and CALPHAD (thermocalc – TCAL1 database) with scheil calculation [27] is shown in Table 2.

Table 2. Comparison of several empiric calculations with experiment data and thermocalc database (Al)-Si (TCAL1)

Si	Cu	Fe	Mg	Mn	Zn	Ni	Calculated (°C)				Thermal Analysis (°C)	Calphad -TCAl1 (°C)	Method	Ref
							Proposed	[10]	[20]	[23]				
6.85	0.02	0.19	0.39	0.00	0.00	0.00	573.2	573.3	572.3	578.8	573.5	573.4	$T_{E,G}^{Al-Si}$	1
9.18	3.22	1.01	0.06	0.06	2.28	0.04	566.0	560.5	566.5	560.8	564.4	565.0	$T_{E,G}^{Al-Si}$	**19**
7.13	0.96	0.14	0.28	0.01	0.01	0.00	571.6	571.1	571.3	575.3	573.1	571.6	$T_{E,Nuc}^{Al-Si}$	16
7.05	1.98	0.13	0.28	0.01	0.01	0.00	568.6	567.6	568.7	572.0	569.1	568.5	$T_{E,Nuc}^{Al-Si}$	16
9.16	1.05	0.14	0.27	0.01	0.01	0.00	572.6	572.3	571.2	574.6	572.4	572.6	$T_{E,Nuc}^{Al-Si}$	16
9.02	2.44	0.12	0.27	0.01	0.01	0.00	569.4	568.5	567.7	571.3	570.2	569.3	$T_{E,Nuc}^{Al-Si}$	16
9.45	4.38	0.14	0.27	0.01	0.01	0.00	565.5	563.9	562.8	568.1	566.4	565.3	$T_{E,Nuc}^{Al-Si}$	16
10.84	0.94	0.14	0.27	0.01	0.01	0.00	573.5	573.2	571.4	574.3	574.5	573.5	$T_{E,Nuc}^{Al-Si}$	16
10.92	1.95	0.14	0.26	0.01	0.01	0.00	571.7	571.1	569.0	571.9	573.2	571.5	$T_{E,Nuc}^{Al-Si}$	16
7.00	0.24	0.17	0.40	0.03	0.00	0.17	571.4	571.2	571.7	576.5	569.8	572.1	$T_{E,G}^{Al-Si}$	20
6.90	0.24	0.18	0.39	0.03	0.00	0.15	571.5	571.3	571.8	576.6	571.8	572.1	$T_{E,G}^{Al-Si}$	20
5.20	3.00	0.31	0.30	0.05	0.00	0.04	560.1	558.1	565.6	564.4	558.8	560.7	$T_{E,G}^{Al-Si}$	**20**
5.10	2.91	0.30	0.27	0.05	0.00	0.03	560.6	558.6	566.2	564.6	562.1	561.0	$T_{E,G}^{Al-Si}$	**20**
5.00	2.91	0.30	0.26	0.05	0.00	0.04	560.3	558.2	566.3	564.3	561.9	560.8	$T_{E,G}^{Al-Si}$	**20**
11.30	2.02	0.40	0.27	0.00	0.00	0.00	571.3	570.7	568.3	570.4	572.3	571.0	$T_{E,G}^{Al-Si}$	21
6.91	3.31	0.16	0.00	0.00	0.00	0.05	566.4	564.6	568.4	568.1	567.6	565.8	$T_{E,G}^{Al-Si}$	22
7.28	0.00	0.14	0.30	0.00	0.00	0.01	574.2	574.3	573.4	579.0	575.0	574.4	$T_{E,G}^{Al-Si}$	23
9.98	0.01	0.12	0.01	0.01	0.00	0.00	576.7	576.7	576.6	577.5	575.5	576.6	-	24
8.03	1.09	0.14	0.00	0.00	0.00	0.00	573.9	573.4	574.0	574.9	575.0	573.5	$T_{E,Nuc}^{Al-Si}$	25
8.14	1.93	0.12	0.00	0.00	0.00	0.00	571.8	571.0	571.9	572.5	572.0	571.4	$T_{E,Nuc}^{Al-Si}$	25
8.03	2.96	0.14	0.00	0.00	0.00	0.00	569.1	567.7	569.3	569.9	569.3	568.5	$T_{E,Nuc}^{Al-Si}$	25
7.84	4.30	0.14	0.00	0.00	0.00	0.00	565.3	563.4	566.0	567.6	565.9	564.8	$T_{E,Nuc}^{Al-Si}$	25
4.85	1.03	0.09	0.14	0.01	0.01	0.00	570.6	569.8	572.7	575.1	572.4	570.4	$T_{E,Nuc}^{Al-Si}$	26
5.01	2.06	0.10	0.26	0.01	0.01	0.00	565.1	563.7	568.8	570.5	567.2	565.2	$T_{E,Nuc}^{Al-Si}$	26
7.55	3.45	0.39	0.33	0.24	0.01	0.01	563.1	561.4	564.1	564.5	563.5	563.7	$T_{E,G}^{Al-Si}$	**27**

*bold at ref column indicated that intermetallic phase is form prior the eutectic silicon reaction

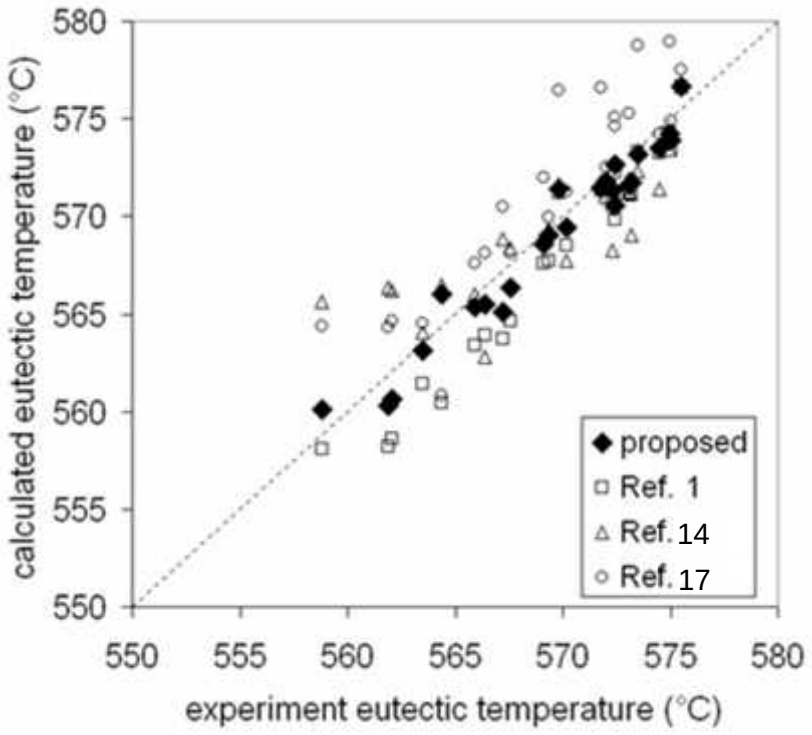

Figure 4. Graph showing the correlation between experiment data and calculated eutectic temperature (the dotted line is the bisector)

Figure 4 plotted the result between the empiric calculated and experiment eutectic temperature. The graph showed that the equation 1 (Mondolfo's equation) is not suitable to calculate an Al-Si alloy with higher alloying element, where the deviation becoming larger as the eutectic temperature drop due to the effect of high cooper content. While the equation from ref 14 (Stuhldreier equation) although have a low average, yet the data appears highly scattered and predict the eutectic temperature above the measured data for high Cu content. Equation from ref 17 (Silicon equivalent) shows a good consistency, however their calculation is shows above the correlation line for most of the calculated temperature. Furthermore, the equation also appeared fail to predict for an alloy with low addition element (the calculation showed their prediction value is above the eutectic silicon temperature). As for the proposed equation, it is showed a good agreement to the experiment, with deviation approximately ±1°C.

Reference

1. D. Apelian, G.K. Sigworth, K.R. Whaler: AFS trans., 1984, vol.92, pp. 297-307.
2. L.F. Mondolfo, Aluminum alloys: structure and properties, Butterworth, London, 1976.
3. R.Y. Wang, W. Lu, Spheroidization of eutectic silicon in direct-electrolytic Al-Si Alloy, Metall. Mater. Trans. A, 44 (2013) 2799-2809.
4. H.W.L. Phillips, Annotated equilibrium diagrams of some aluminium alloy systems, Monograph No. 25, Inst. Met., London, 1959
5. C.Y. He, Y. Du, H.L. Chen, and H. Xu, Experimental investigation and thermodynamic modeling of the Al–Cu–Si system, CALPHAD 33 (2009) 200-210.
6. Y. Du, Z. Jin, B. Huang, W. Gong, H. Xu, Z. Yuan, J.C. Schuster, F. Weitzer and N. Krendelsberger, A thermodynamic description of the Al-Mn-Si system over the entire composition and temperature ranges, Metall. Mater. Trans. A. 35 (2004) 1613-1628.

7. K. Suzuki, M. Kagayama, Y. Takeuchi, Eutectic phase equilibrium of Al-Si-Zn system and its applicability for lower temperature brazing, J. Jpn. Inst. Light Met. 43 (1993) 533-538. (in Japanese)
8. G.K. Sigworth: AFS trans., 1983, vol.93, pp. 7-16
9. M.H.G. Jacob and P.J. Spencer, A critical thermodynamic evaluation of the systems Si-Zn and Al-Si-Zn, CALPHAD 20 (1996) 307-320.
10. M. Morinaka: US Patent No.6,345,910, 12 February 2002
11. R. Vijayaraghavan, N.Palle, J.Boileau, J.Zindel, R.Beals, F.Bradley: Scr. Mater., 1996, vol.35,7 , pp. 861-867.
12. A.T. Joenoes, J.E. Gruzzleski,: Cast Met., 1991, 4,2, pp. 62-72.
13. L. Hausler, W.Schneider: J.of Light Metals, 2002, 2, pp. 17-26.
14. G. Stuhldreier, E. Mettingen, K.W. Stoffregen: Giesserei, 1981, vol.68 pp.404-409
15. G. Drossel, Der einfluss von schmelzebehandlungen auf die dichtheit von gusskoerpon aus Al-Si Gusslegierungen. Giessereitechnik, 27,1 (1981) 7-12
16. M.B. Djurjevic: Military technical courier, 2012, vol.60,1, pp. 152-168.
17. M.B. Djurdjevic, W. T. Kierkus, G. E. Byczynski and J. H. Sokolowski: AFS Trans., 1998, vol.47, pp. 143-147.
18. F.C. Robles Hernandez, M.B. Djurdjevic, W.T. Kierkus, J.H. Sokolowski: Mater. Sci. Eng., A, 2005, vol.396, pp. 271–276.
19. S.Gowri, F.H.Samuel, Effect of alloying elements on the solidification characteristics and microstructure of Al-Si-Cu-Mg-Fe 380 alloy, Metallurgical and Material Transactions A, Vol.25A, 1994, p.437-448
20. J. Charbonnier: AFS Trans., 1984, vol.92, pp. 907-921
21. S. Farahany, A. Ourdjini, M.H. Idrsi, S.G. Shabestari: Thermochim. Acta, 2013, 553, pp. 59-68
22. Y.M. Han, A.M. Samuel, F.H. Samuel, H.W. Doty: Int. J. Cast Met. Res, 2008, vol.21, 5, pp. 371-380.
23. S. Thompson, S.L. Cockroft, M.A. Wells: Mater. Sci. Technol., 20, 2004, p.194-200
24. S.D. McDonald, A.K. Dahle, J.A. Taylor, D.H. StJohn: Metall. Trans. A, 2004, Vol.35A, pp. 1829-1873.
25. M.B. Djurdjevic, G. Huber, Z. Odanovic: J. Therm. Anal. Calorim., 2013, vol.111, 5, pp. 1365-1373
26. M.B. Djurdevic, Z. Odanovic, N. Talijan: JOM, 2011, vol.63, 11, pp. 1-7
27. M.B. Djurdjevic, H. Jiang, J. Sokolowski: Mater. Charact., 2001, vol.46,1, pp. 31-38
28. Thermo-Calc Software TCAL1 database version 1.0, http://www.thermocalc.com (Accessed 28 March 2013)

Appendix 4

Optical Microstructure

A356 – sand and metal mould series

Sample code No. 9

Sand mould

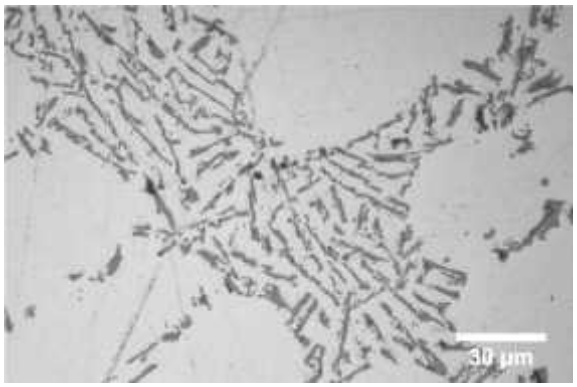

M 1.5

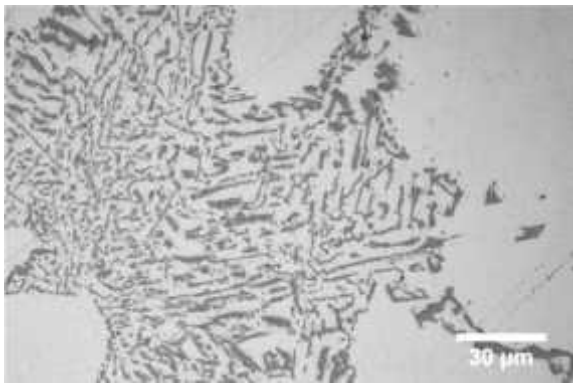

Metallic mould

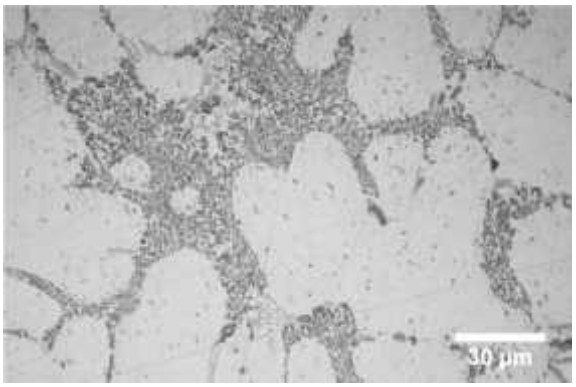

M 1.15

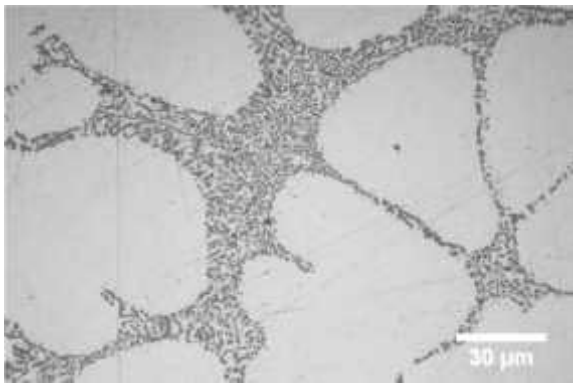

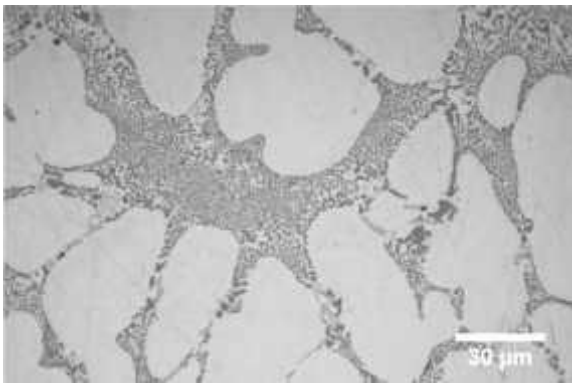

M 1

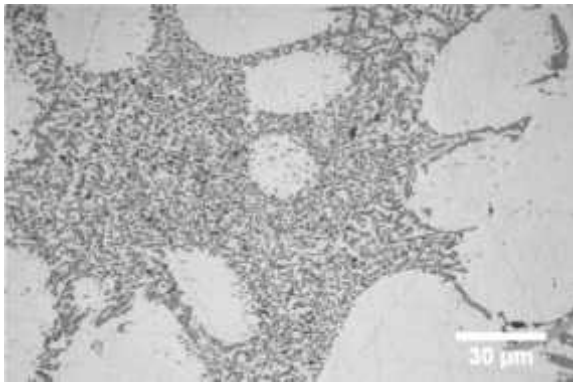

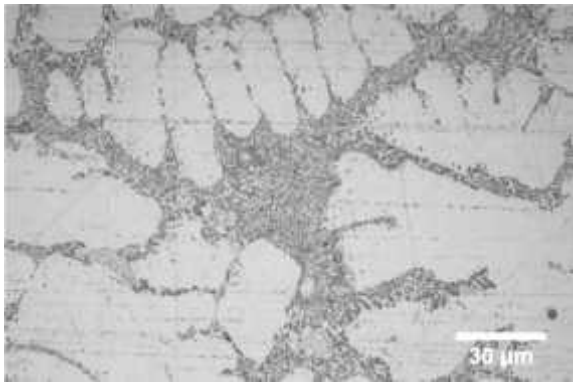

M 0.8

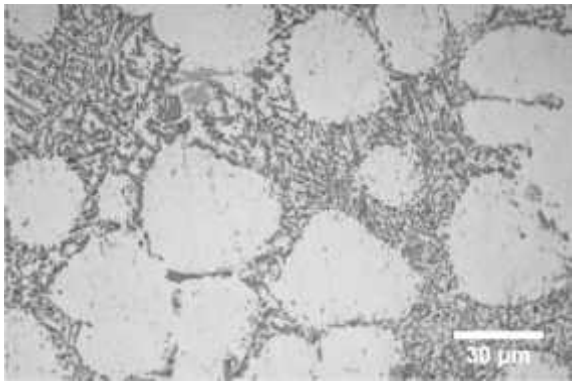

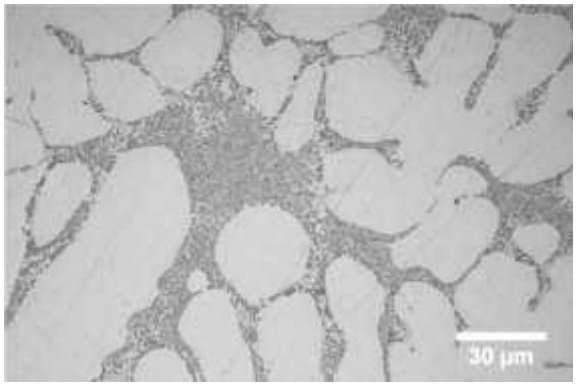

M 0.6

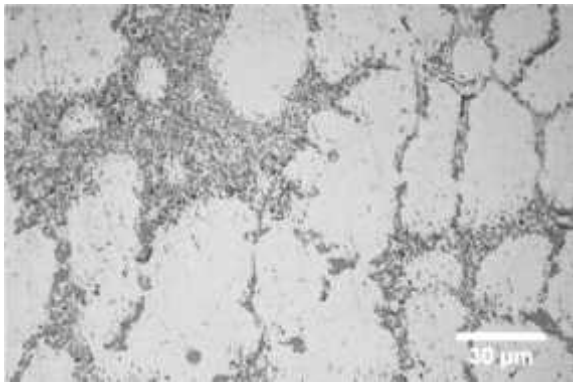

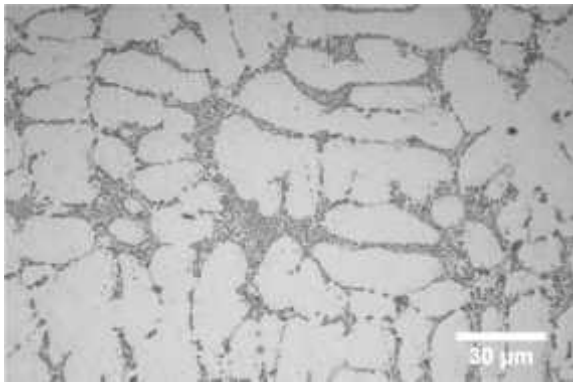

M 0.4

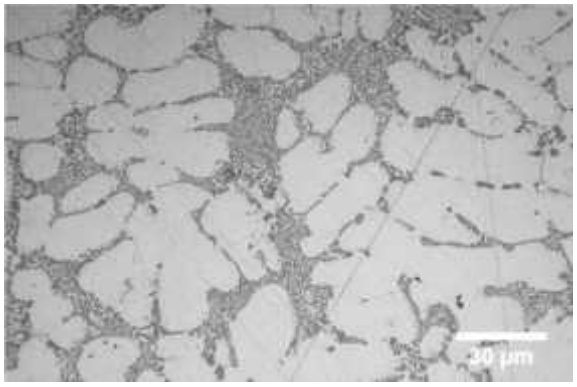

M 0.3

Sample code no. 10

Sand mould

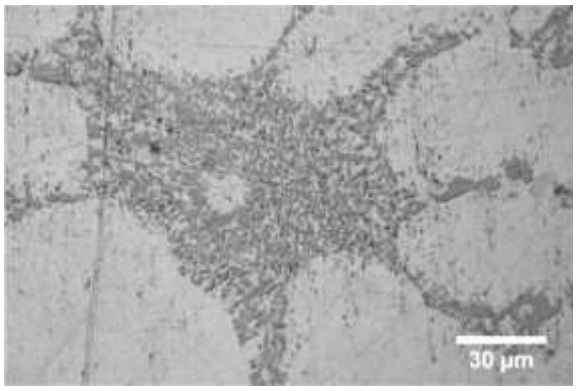

M 1.5

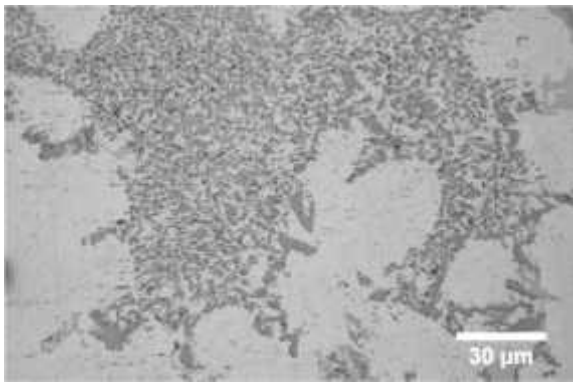

M 1.15

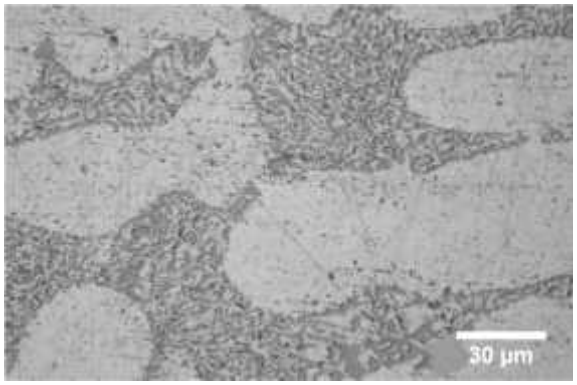

M 1

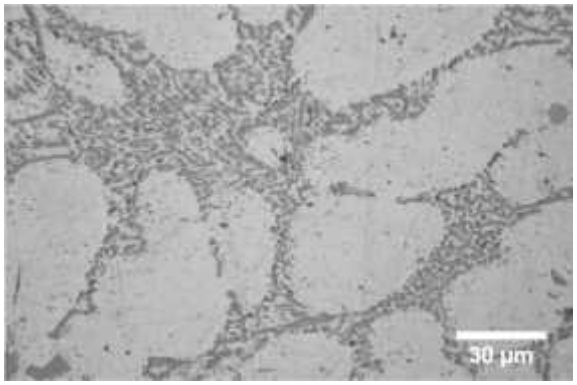

M 0.8

Metallic mould

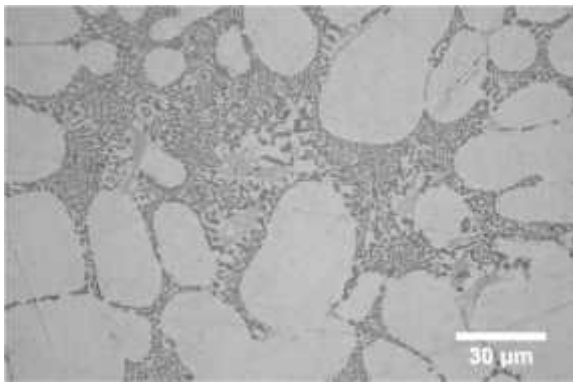

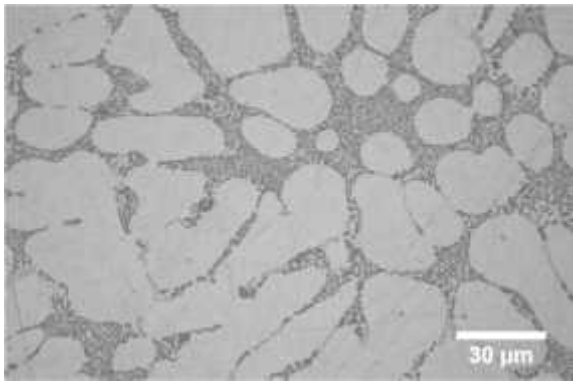

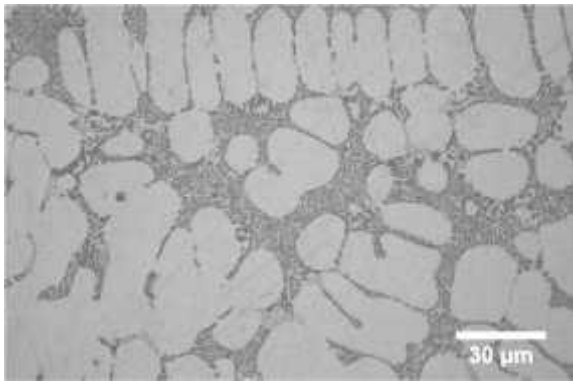

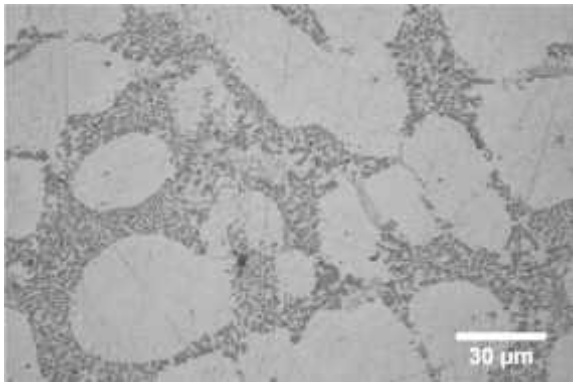

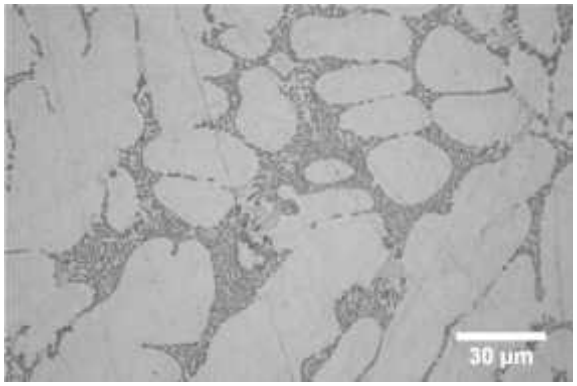

M 0.6

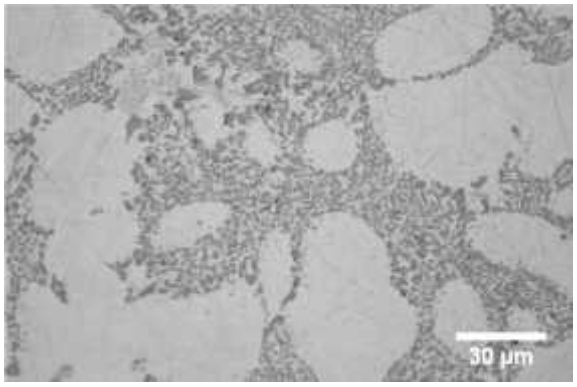

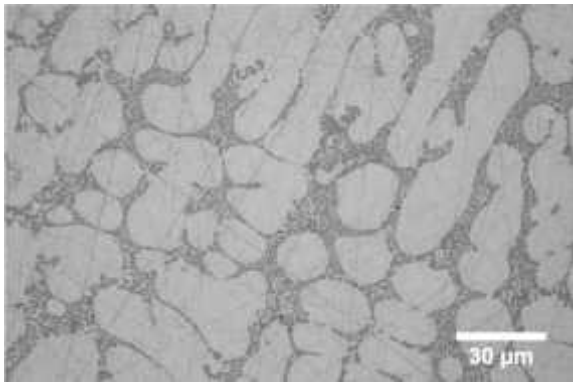

M 0.4

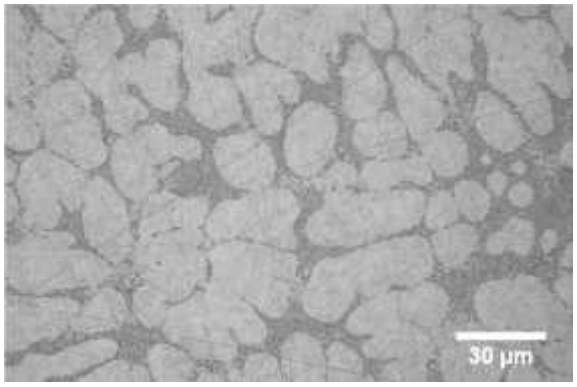

M 0.3

Sample code no.11

Sand mould

Metallic mould

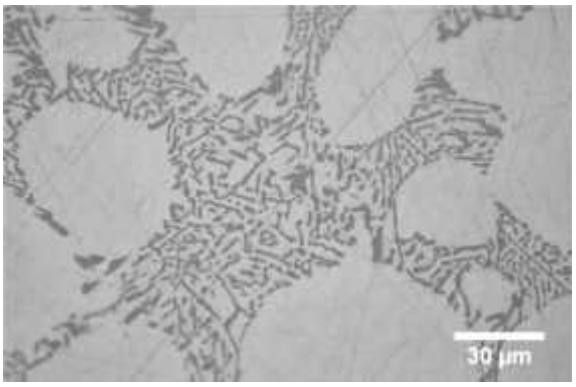

M 1.5

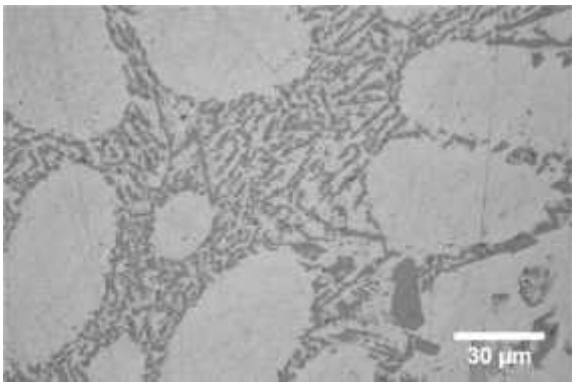

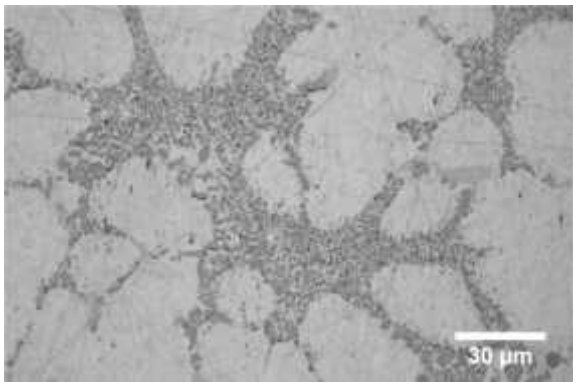

M 1.15

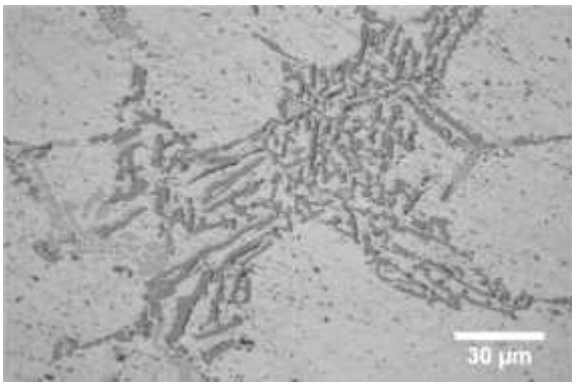

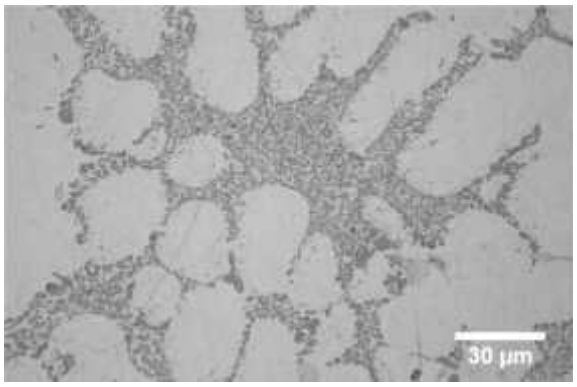

M 1

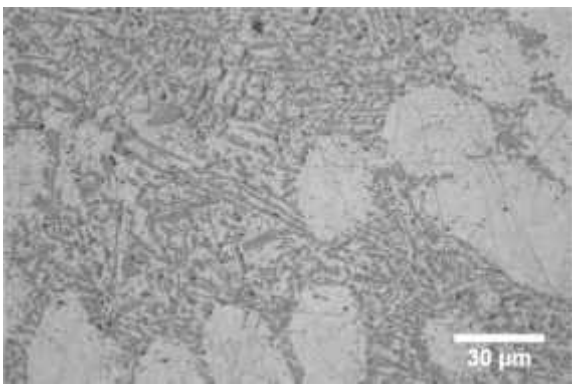

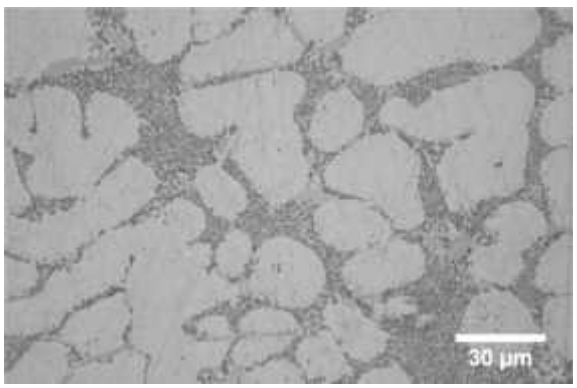

M 0.8

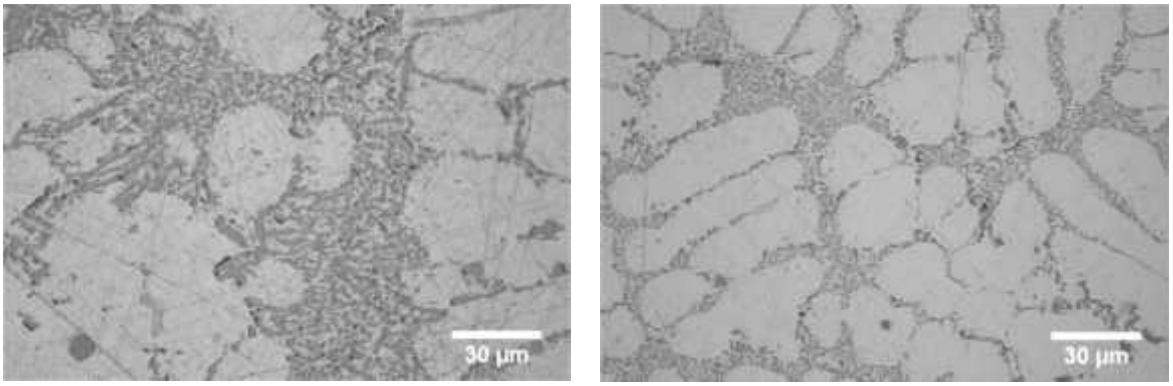

M 0.6

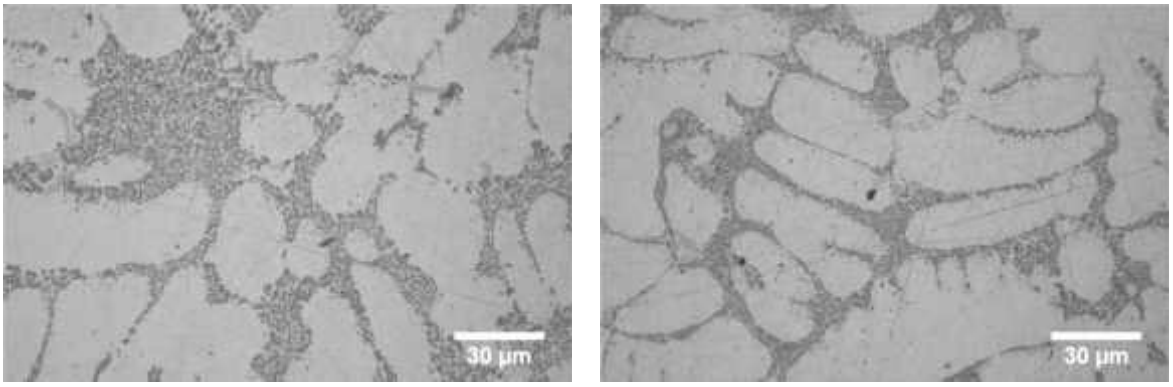

M 0.4

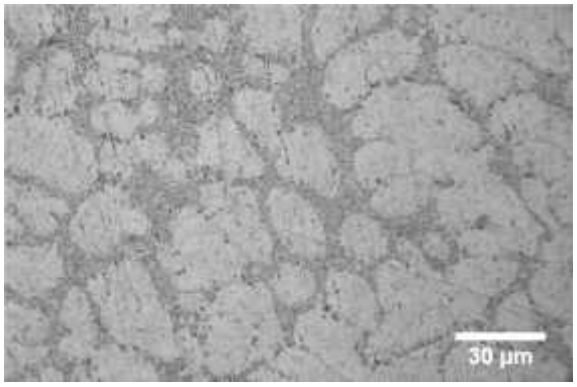

M 0.3

DTA- flake to fibrous transition

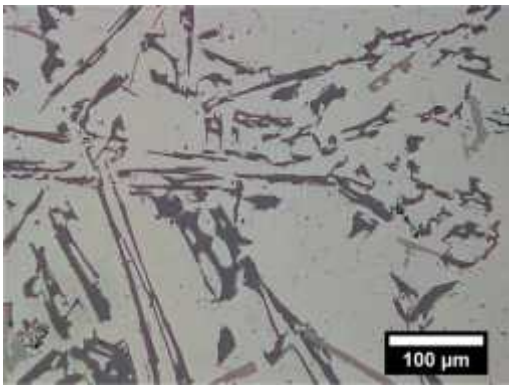

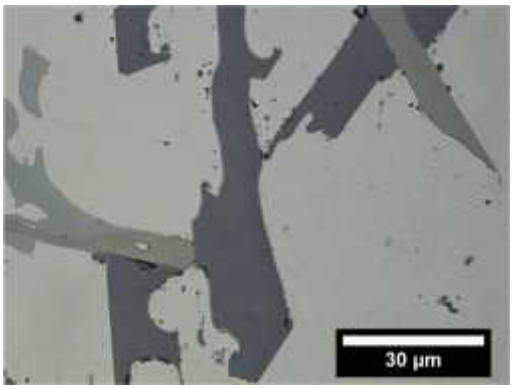

0.6°C/min

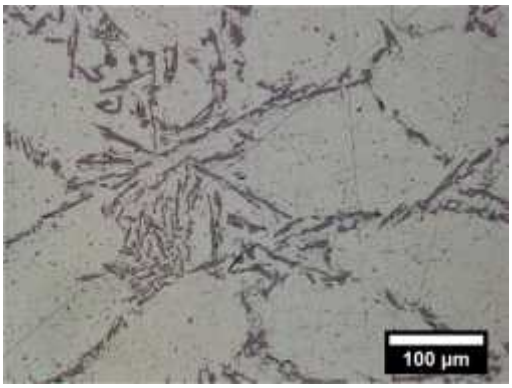

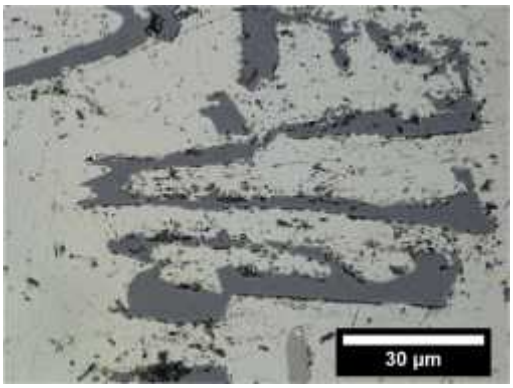

1°C/min

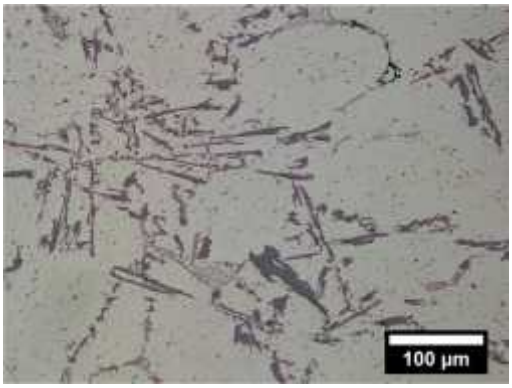

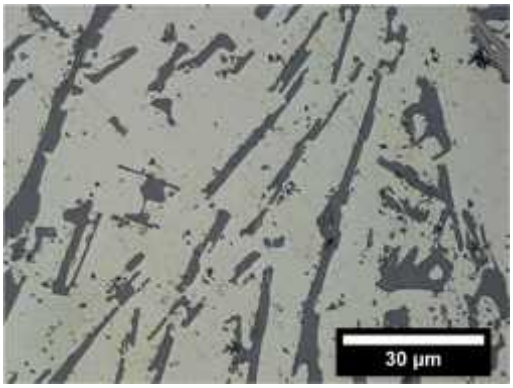

6°C/min

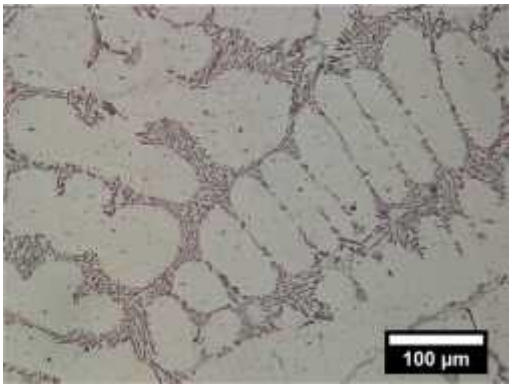

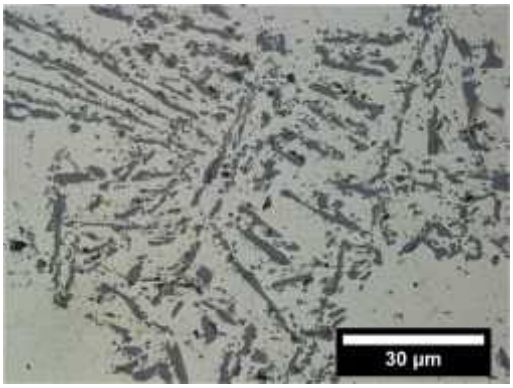

30°C/min

D**TA – various cooling rates**

DTA – Cooling rate 0.02°C/min

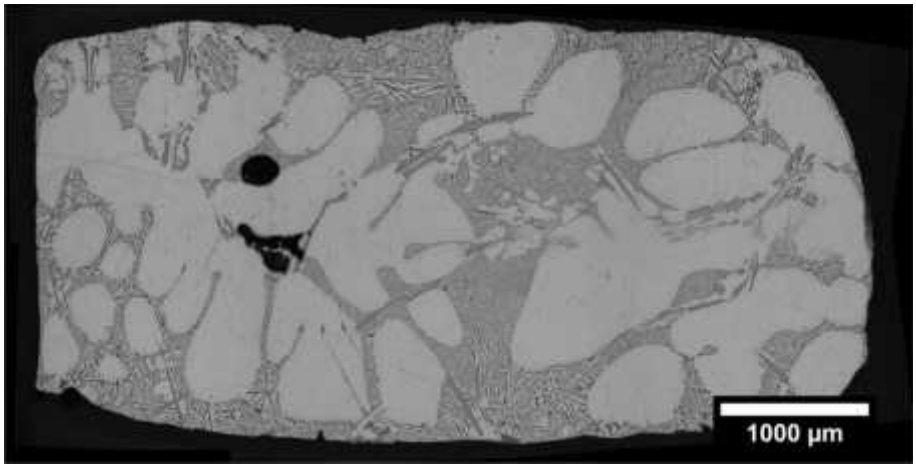

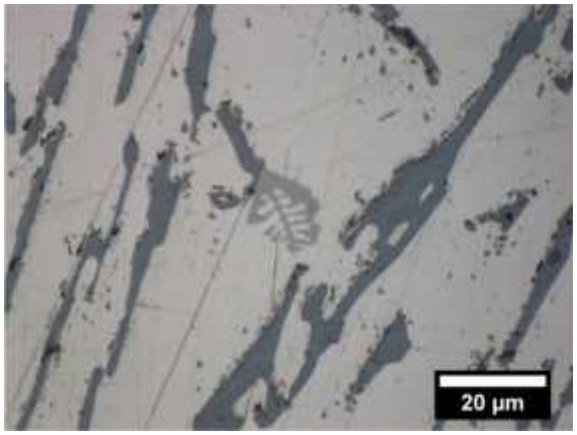

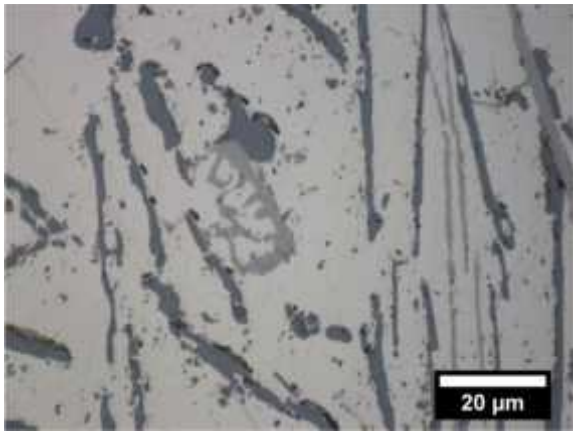

DTA – Cooling rate 0.05°C/min

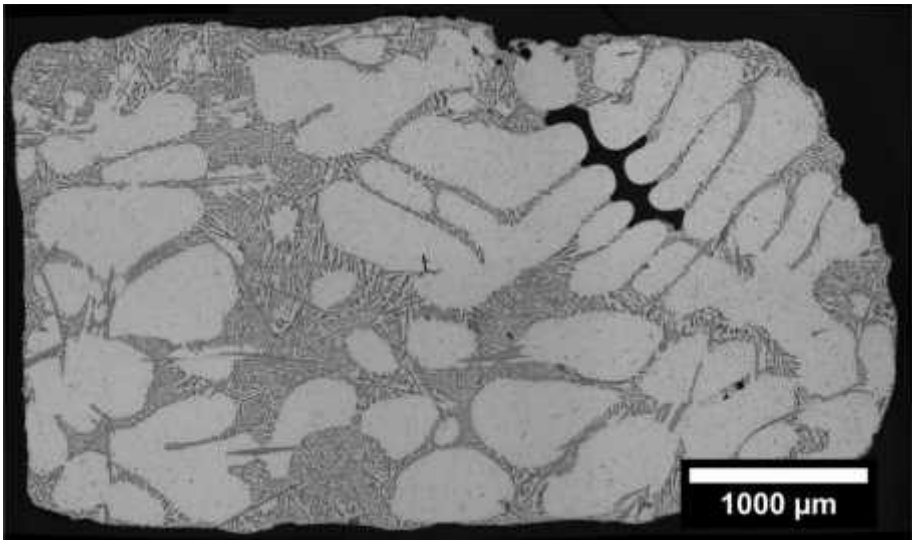

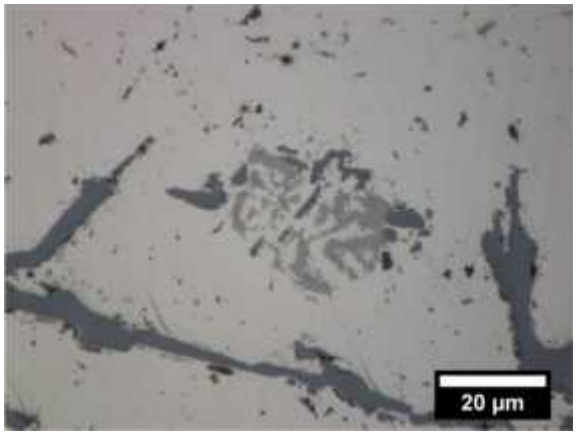

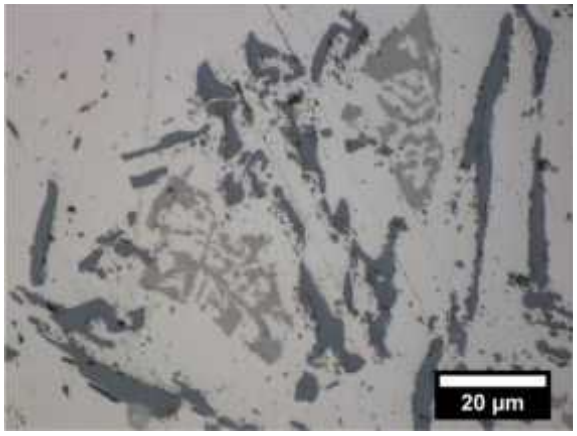

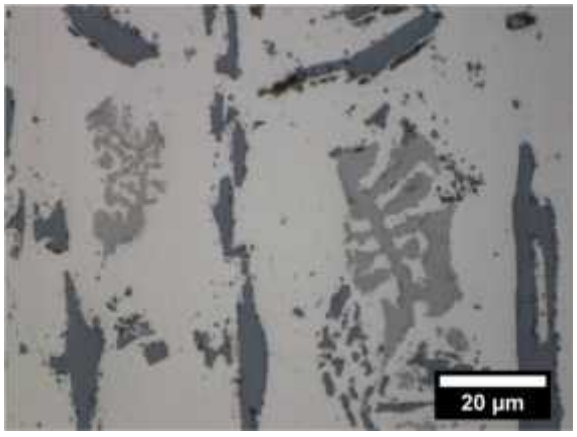

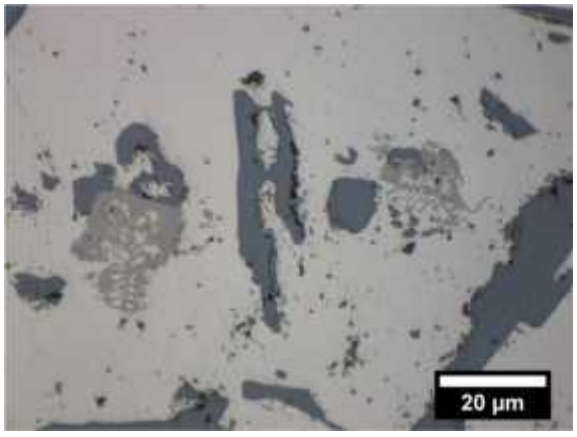

DTA – Cooling rate 0.1°C/min

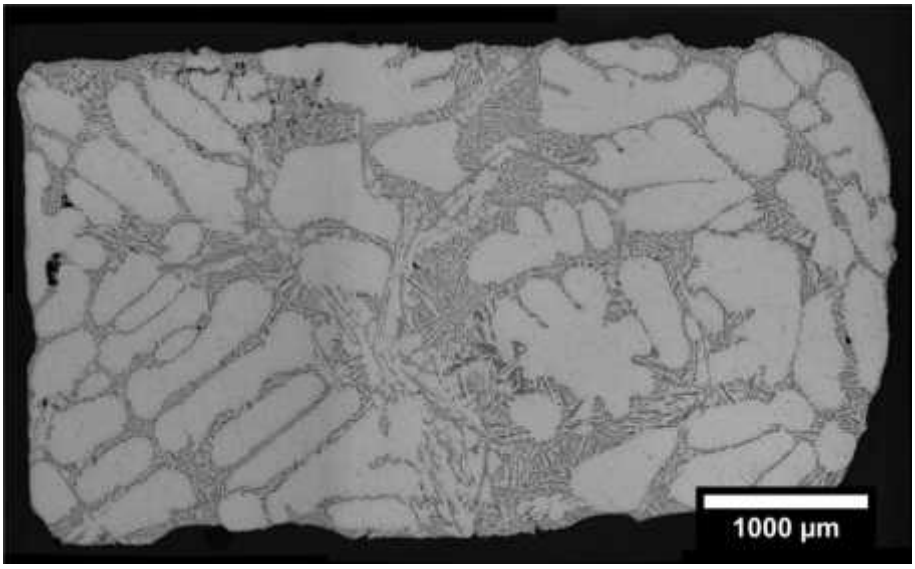

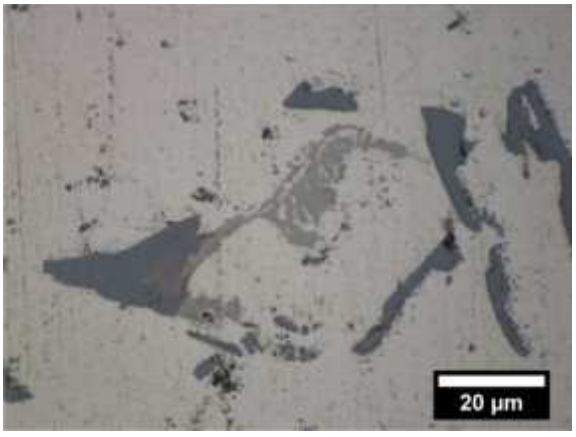

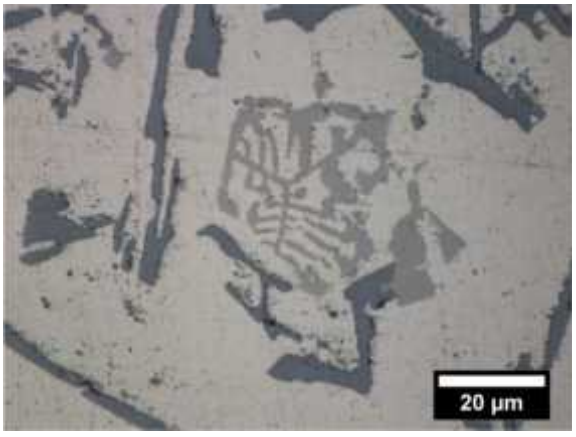

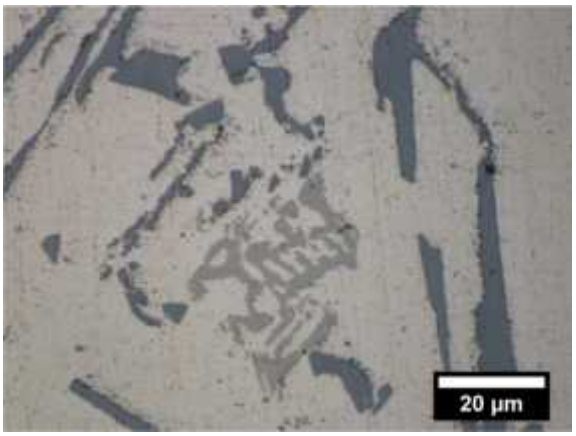

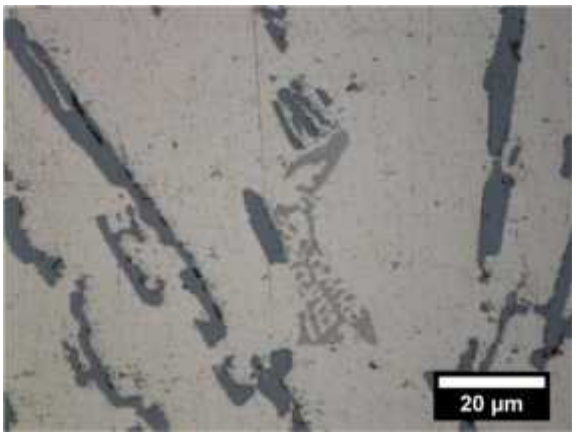

DTA – Cooling rate 0.2°C/min

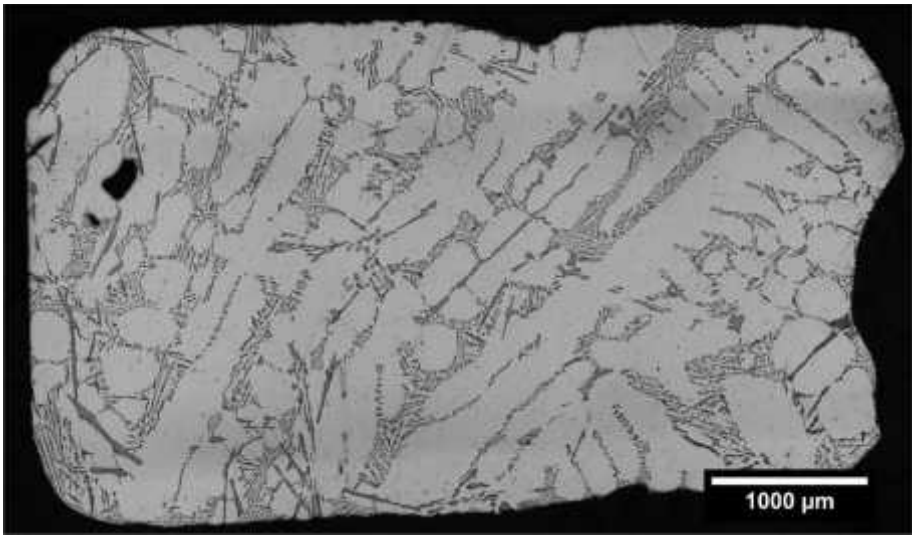

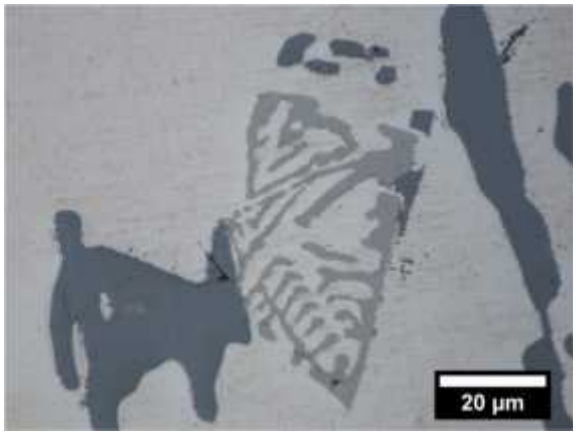

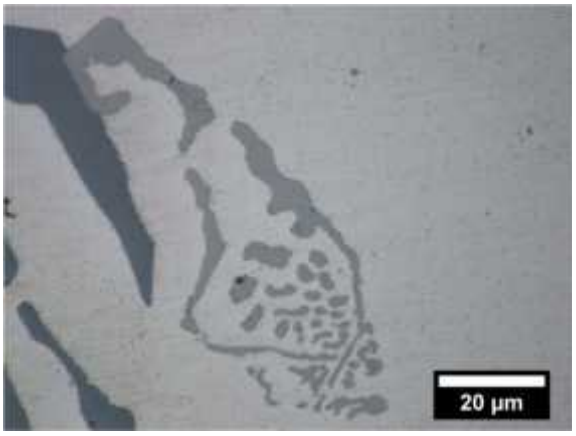

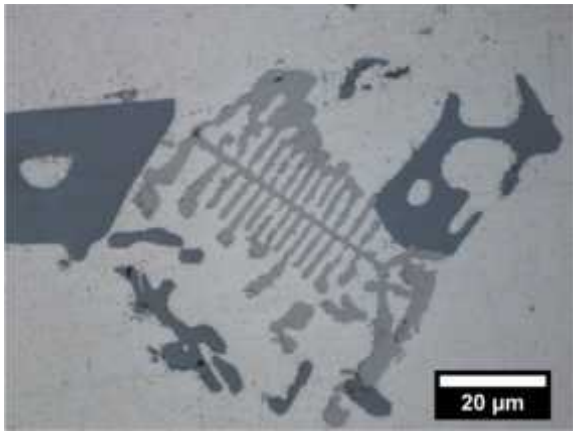

DTA – Cooling rate 1°C/min

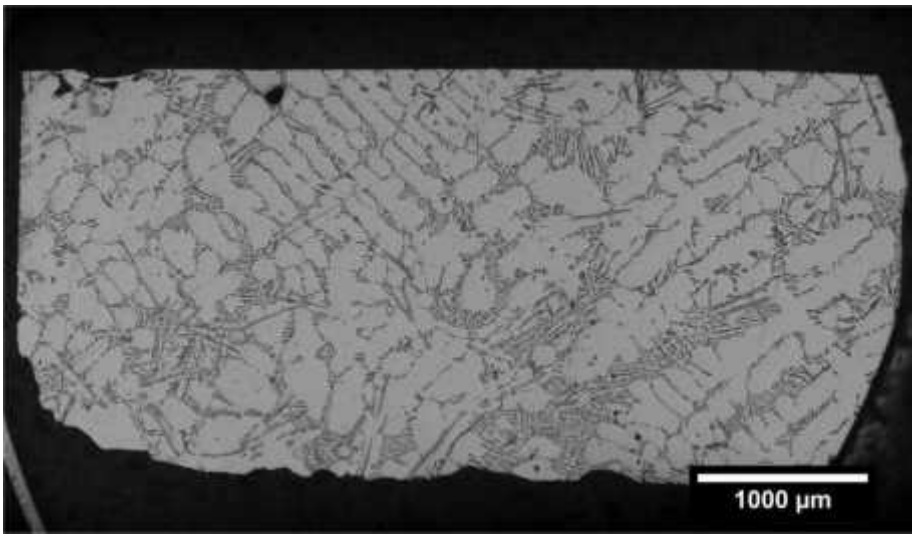

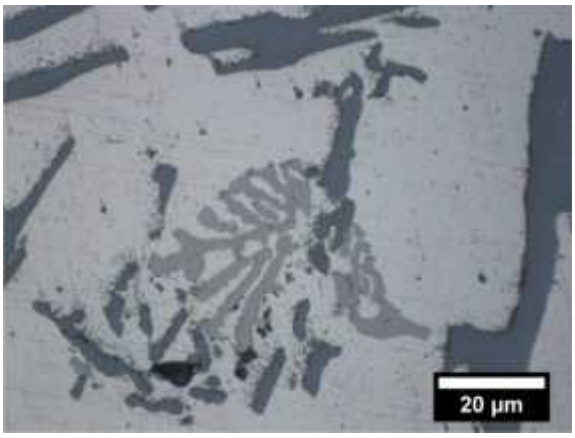

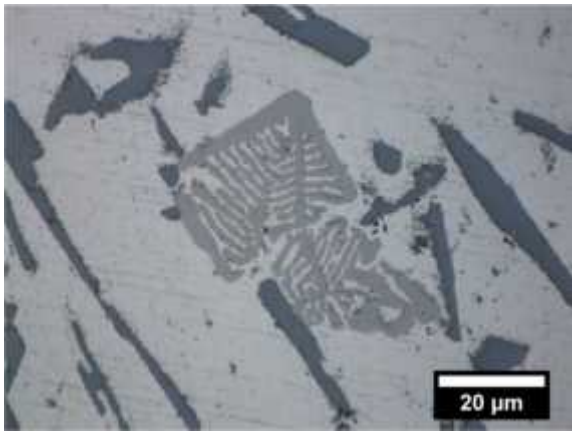

DTA – Cooling rate 2°C/min

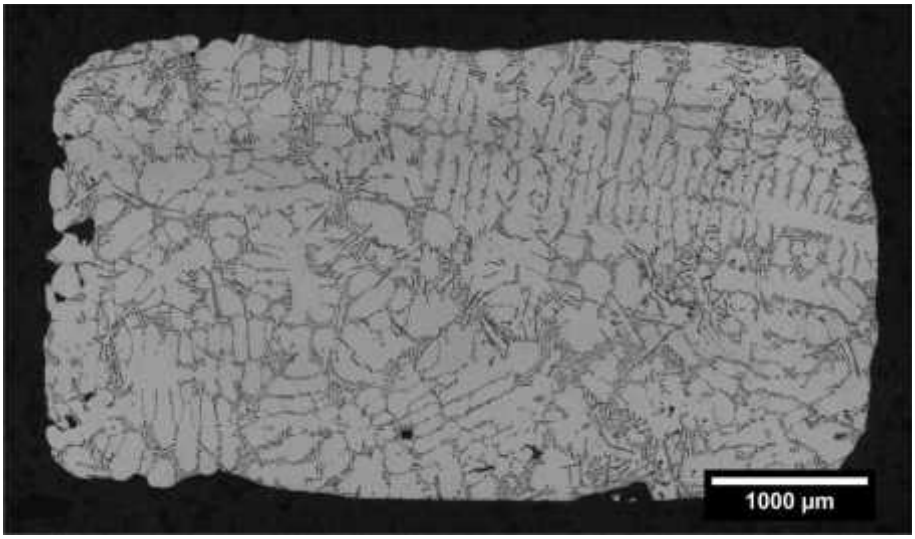

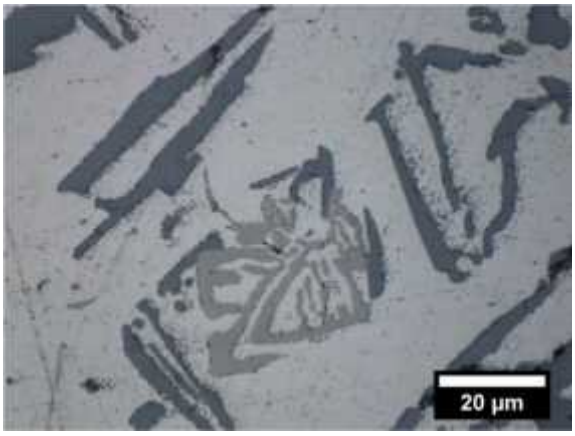

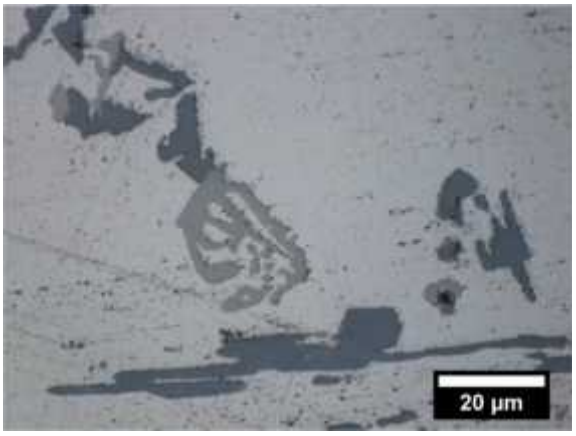

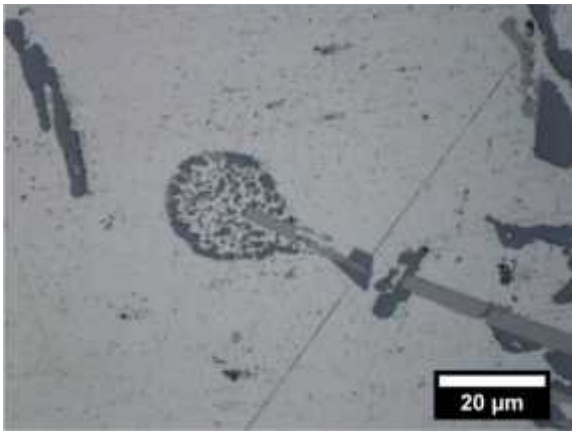

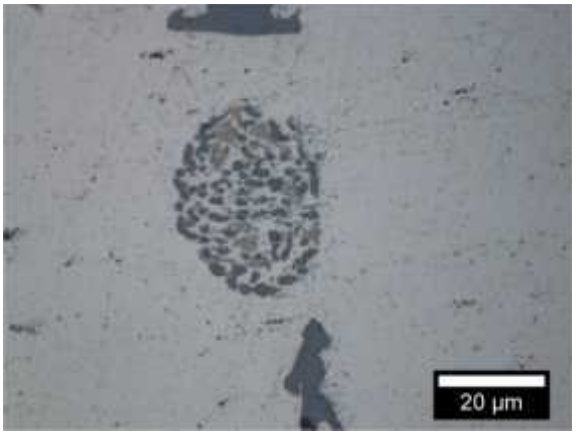

DTA – Cooling rate 5°C/min

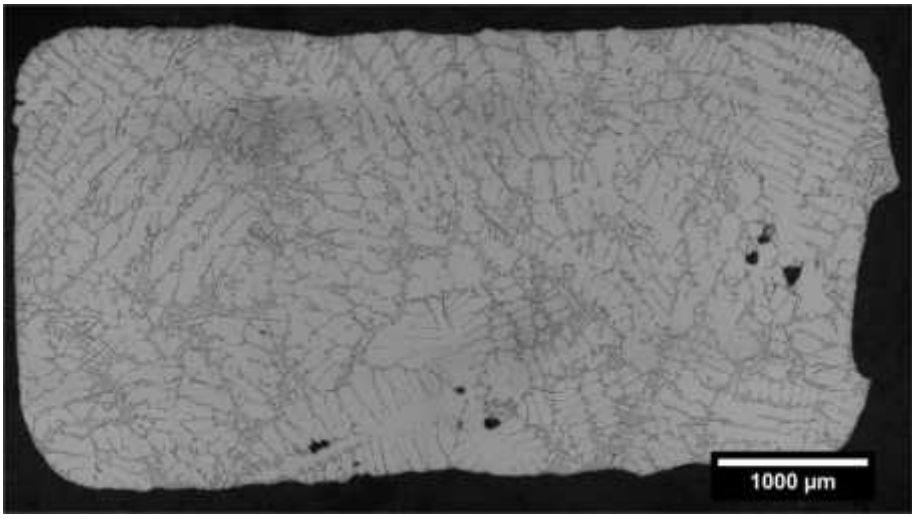

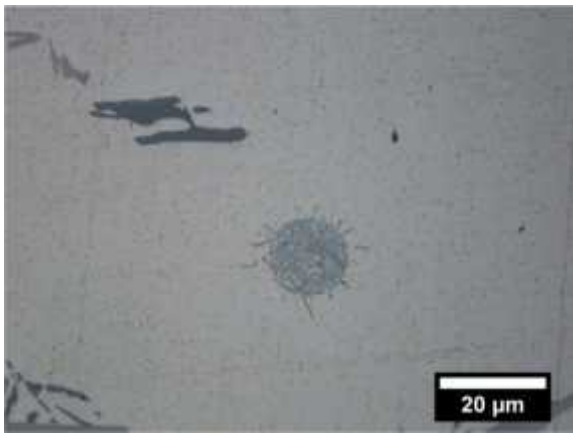

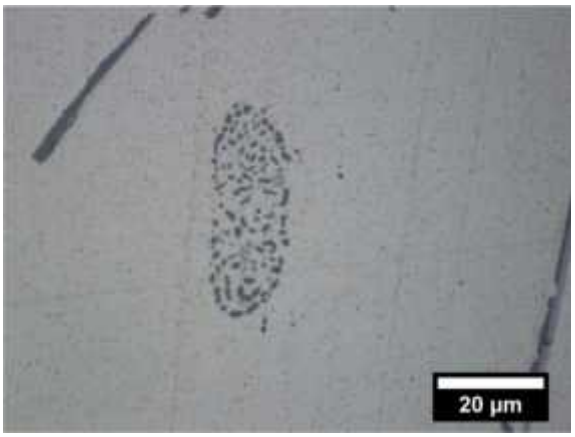

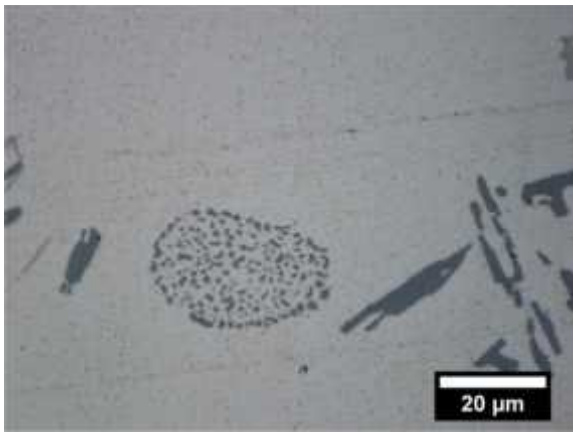

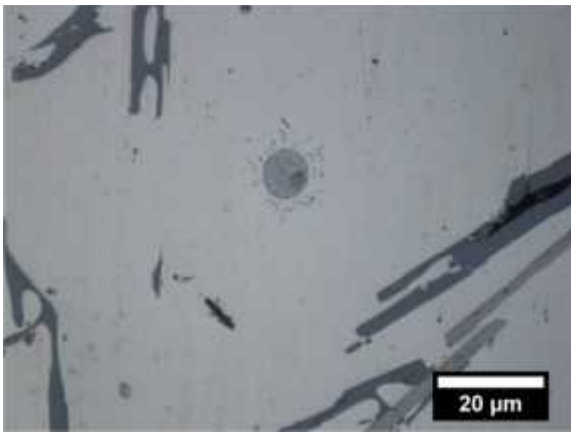

DTA – Cooling rate 10°C/min

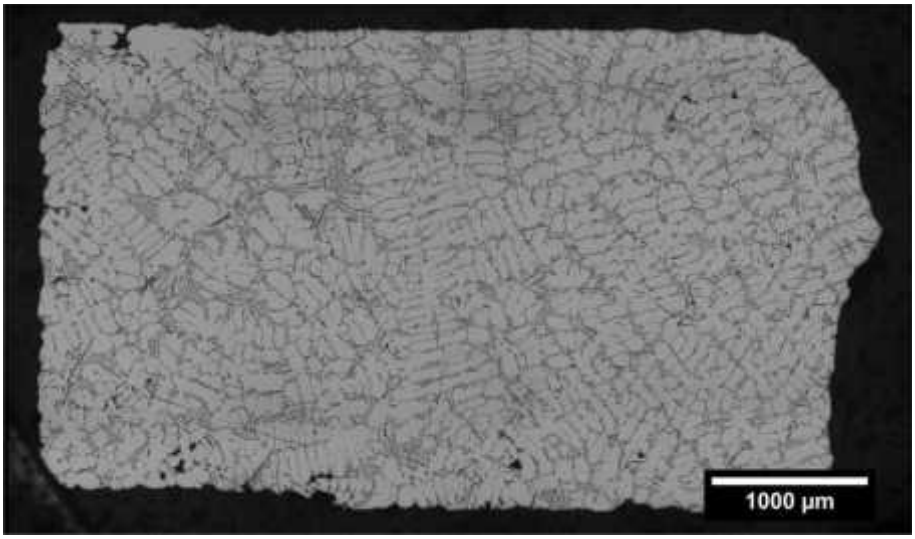

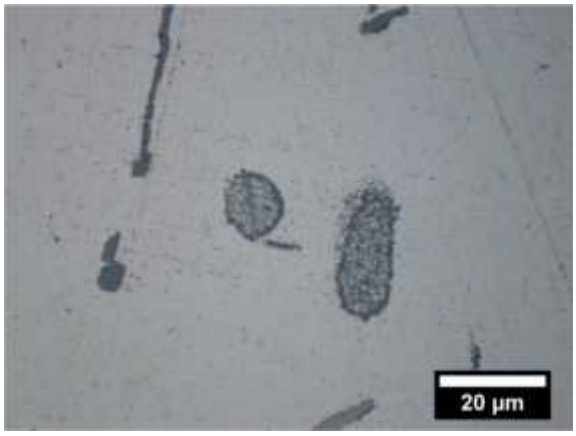

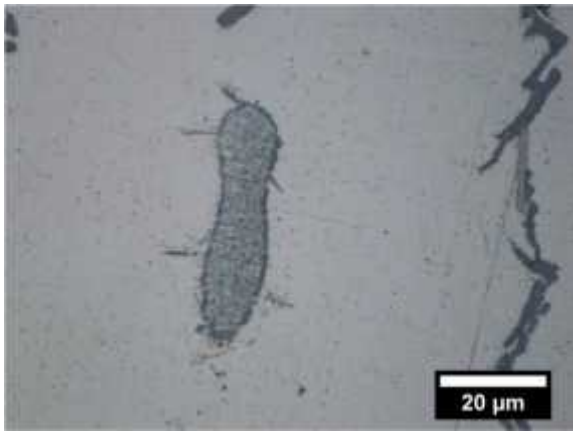

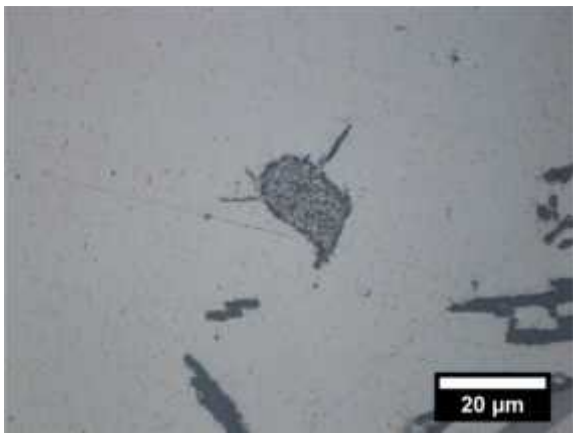

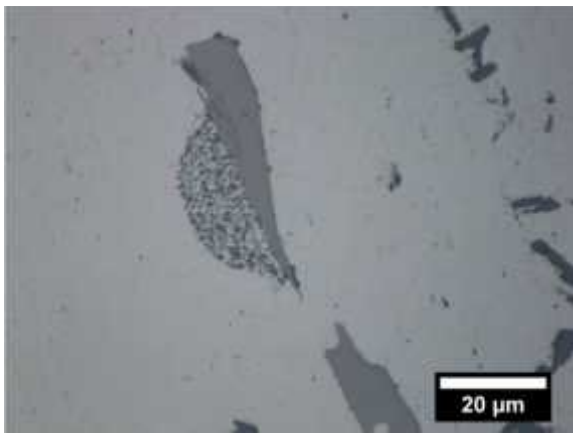

DTA – Cooling rate 40°C/min

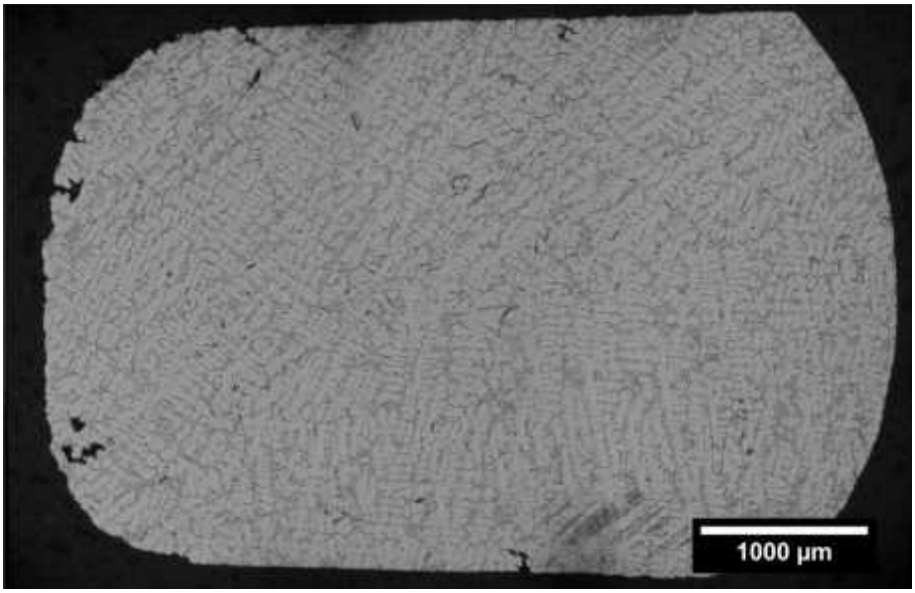

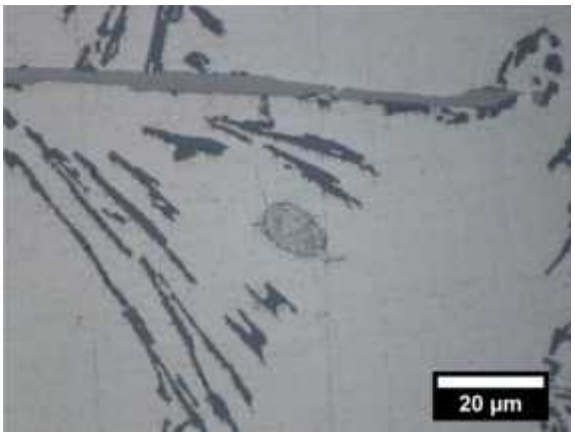

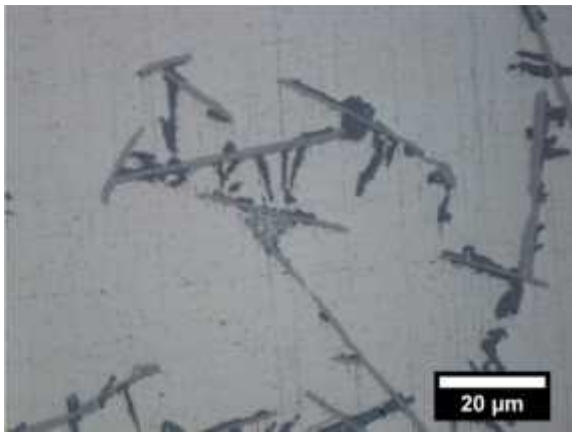

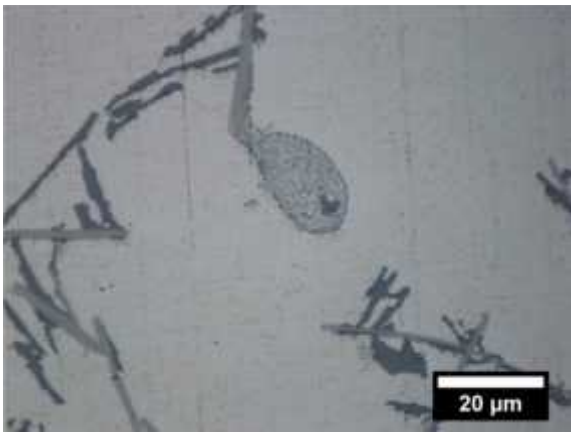

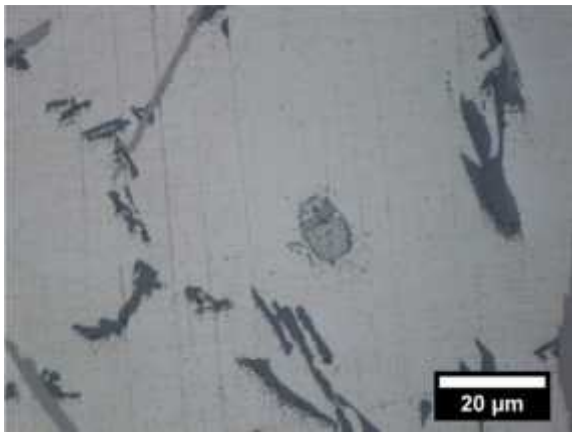

Quantitative analysis

Observed Microstructure Features	Cooling rates (°C/min)								
	0.02	0.05	0.1	0.2	1	2	5	10	40
Script phase	4	14	9	6	8	4	-	-	-
Rosettes	-	-	1	2	1	3	6	7	24

Appendix 5.

List of publications

1. D. Ferdian, B. Suharno, B. Duployer, C. Tenailleau, L. Salvo, J. Lacaze, Differential thermal analysis assessment of beta phase precipitation in Al-6.5Si-1Fe Alloy, Transactions of the Indian Institute of Metals, Volume 65, Issue 6, December 2012, pp 821-825.

2. D. Ferdian, J. Lacaze, I. Lizarralde, A. Niklas, A.I. Fernández-Calvo, Study of the effect of cooling rate on eutectic modification in A356 aluminium alloys, Material Science Forum, Vol. 765- Light Metals Technology 2013, pp. 130-134

3. D. Ferdian, J. Lacaze, Evaluation of (Al)-Si Eutectic Reference Temperature of A3XX alloys, Material Science Forum, Vol. 790-791 (2014) - Solidification and Gravity VI, pp. 367 - 372

4. J. Lacaze, D. Ferdian, I. Lizarralde, A. Niklas, S. Eguskiza, A.I. Fernández-Calvo, Improved grain size prediction in aluminium-silicon alloys by thermal analysis, 71st World Foundry Congress, 19-21 May 2014, Bilbao – Spain.

Trans Indian Inst Met
DOI 10.1007/s12666-012-0182-1

TECHNICAL PAPER

TP 2634

Differential Thermal Analysis Assessment of Beta Phase Precipitation in Al-6.5Si-1Fe Alloy

D. Ferdian · B. Suharno · B. Duployer · C. Tenailleau · L. Salvo · J. Lacaze

Received: 29 June 2012 / Accepted: 11 September 2012

Abstract Iron-bearing intermetallic phases formed during solidification of Al–Si casting alloys are known for having detrimental effect on their mechanical properties. This is particularly the case of the β-Al_5FeSi phase which precipitates as thin and extended plates. Many researchers already studied the factors that could influence the formation of this phase and in most cases it has been concluded that low-level additives (e.g. manganese) may lead to the replacement of the beta phase with other intermetallics that are less harmful because of being more compact.In this preliminary work, differential thermal analysis (DTA) was used to study the effect of cooling rate (0.2–40 °C/min) on beta phase formation in Al-6.5Si-1Fe alloy. The effect of cooling rate on the characteristic temperature for phase changes was described and compared to literature information. The beta phase was then characterized using scanning electron microscopy and X-ray tomography. Metallographic analysis showed the phase morphology was heavily affected by the cooling rate, and parameters to quantify this have been selected and measured. Moreover, observation also revealed that some alpha phase precipitates at low cooling rate.

Keywords Beta intermetallic phase · DTA · Cooling rate · X-ray tomography

1 Introduction

Aluminum–silicon alloys are widely used as foundry alloys due to their fluidity characteristic and mechanical properties. Alloying elements such as magnesium and copper are usually added to enhance their mechanical properties. However, other elements such as iron are detrimental due to the formation of iron-rich intermetallic phases in interdendritic regions of Al–Si alloys during the solidification process. This is particularly the case of the beta Al_5FeSi phase. Depending on the iron level in the alloy, Dinnis et al. [1] summarized that the precipitation of beta phase occurs before the (α-Al)-Si eutectic, after it or else together in a ternary eutectic. Work by Franek et al. [2] showed that when the iron level is above 0.7 pct, the beta phase tends to crystallize as large platelets. Lu and Dahle [3] also observed that over 0.7 pct iron, the beta phase forms prior to the eutectic (Al)-Si reaction. Other than the iron content, the morphology of beta phase is influenced by the cooling rate [4, 5], with its size decreasing when the cooling rate is increased [5].

Thermal analysis has been applied to understand changes during solidification. The temperature change recorded during the solidification process is plotted against time thus creating a cooling curve. Thermal analysis can be used to evaluate and quantify grain size, level of Si modification, phase transformation temperature and solid fraction [6]. Differential thermal analysis (DTA) has more sensitivity

D. Ferdian (✉) · J. Lacaze
CIRIMAT, UMR CNRS 5085, ENSIACET, BP 44362,
31030 Toulouse Cedex 4, France
e-mail: deni.ferdian@ensiacet.fr

D. Ferdian · B. Suharno
Department Metallurgy and Material, Universitas Indonesia,
Kampus Baru UI, Depok 16424, Indonesia

B. Duployer · C. Tenailleau
CIRIMAT, UMR CNRS 5085, Université Paul Sabatier,
31062 Toulouse Cedex 9, France

L. Salvo
SIMAP, Grenoble INP, ENSE3, BP 46, 38402,
St Martin d Heres Cedex, France

Published online: 09 October 2012

and reliability compared to conventional thermal analysis in particular concerning the scanning rate control. DTA can be used in the same way as thermal analysis, e.g. for solid fraction evaluation [7].

In the present work, DTA analysis and metallographic observation of Al-6.5Si-1Fe alloy are described. The objective of this study is to characterize the effect of cooling rate on the growth of beta phase.

2 Experimental

A synthetic hypoeutectic Al-6.5Si-1Fe alloy was prepared into 8 mm in diameter rods by hot extrusion. Samples were then machined into rods of approximately 3.9 mm in diameter and 6 mm in height, and then subjected to DTA using SETARAM –SETSYS apparatus. All experiments were carried out under a low argon flux. The DTA signals were recorded with scanning rates for heating of 0.2, 1, 2, 5, 10 and 17.5 °C/min (not presented in this work), and for cooling of 0.2, 1, 2, 5, 10 and 40 °C/min. At the end of heating, the samples were held at a upper temperature of 650 °C for 10 min, except for sample with cooling rate of 40 °C/min when the upper holding temperature was 670 °C. Each run was made twice for having samples for metallographic and for tomographic investigation.

The DTA samples were prepared for metallographic observation under SEM and characterization of the beta phase was achieved with a magnification of 100. Images were recorded by dividing the sample cross section into rows and columns. The 2D image analysis was carried out with Aphelion software (ADCIS). The analysis was performed for 2D volume fraction and beta phase length analysis.

Furthermore, X-ray tomograms were obtained using a GE Phoenix Nanotom 180. A monochromatic beam with energy of 80 KeV was transmitted and produced 1,440 images as the specimen underwent a 360° rotation (2.5 µm/voxel). An image stack of volume was constructed using Datos X (Pheonix X-ray system) and VG Studio Max (Volume Graphic GmbH, Germany). ImageJ (National Institute of Health, USA) was further used to reconstruct and visualize the 3D image with region of interest of 1,600 × 1,600 × 800 voxels. For 3D volume fraction, the volume was divided into 8 parts, with 100 voxels in Z direction for each sub volume. Median filter, threshold and dilation were used to separate the beta phase from the Al matrix.

3 Result and Discussion

All DTA records showed the same pattern regardless the scanning rate, although the thermal arrests become wider as the scanning rate increases. Figure 1 shows the DTA thermogram upon cooling for a scanning rate of 2 °C/min.

Three solidification reactions occur successively at decreasing temperature. The nucleation of (α-Al) dendrites (refer to point a in Fig. 1) which then grow and form the matrix as the alloy is cooled into the L + (α-Al) region. The beta intermetallic phase reaction L → (α-Al) + β-Al_5FeSi (point b) follows when the interdendrite regions have been enriched in iron, and solidification ends (point c) with the so-called silicon eutectic which should be the ternary L → (α-Al) + β-Al_5FeSi + Si eutectic.

The characteristic temperatures recorded on the DTA thermograms obtained upon cooling are plotted in Fig. 2 as a function of the cooling rate. Doted lines have been drawn through the points at low cooling rate to ease reading of the figure. It is seen that the thermal arrests shift to lower temperature as the scanning rate is increased. The main reason for this is heat transfer resistance [8], though phase transformation kinetics may sometimes have an effect.

It is noted in Fig. 2 that the start and peak temperatures for the final eutectic reaction extrapolate to nearly the same temperature. This temperature is 571 °C, which is 5 °C below the assessed eutectic temperature at 576 °C. This difference is certainly due to the DTA cell, and all temperature should be increased by 5 °C. The liquidus of the alloy is thus experimentally found at 616 °C which is close to the value of 617.6 °C that can be calculated according to a previous assessment [9].

It is worth noting that the thermal arrest for beta phase precipitation is shifted close to the final eutectic reaction at high cooling rate such as 40 °C/min. In such a case, the beta phase becomes associated to the ternary eutectic rather than being pre-eutectic according to the definition proposed by Dinnis et al. [1]. Concerning beta precipitation, it was also observed that the onset and the peak temperatures differ by 2 °C for a cooling rate of 0.2 °C/min and by 4 °C

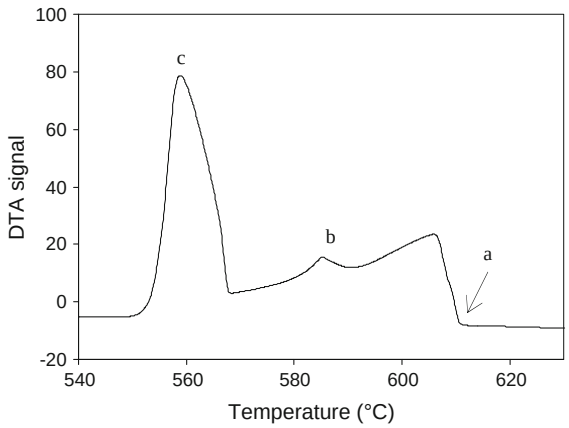

Fig. 1 DTA thermograms recorded upon cooling at 2 °C/min scanning rate

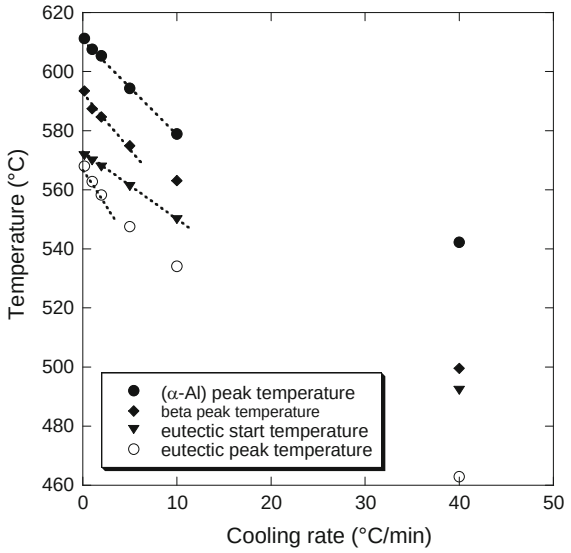

Fig. 2 Effect of scanning rate on characteristic of beta phase formation, liquidus and eutectic temperature

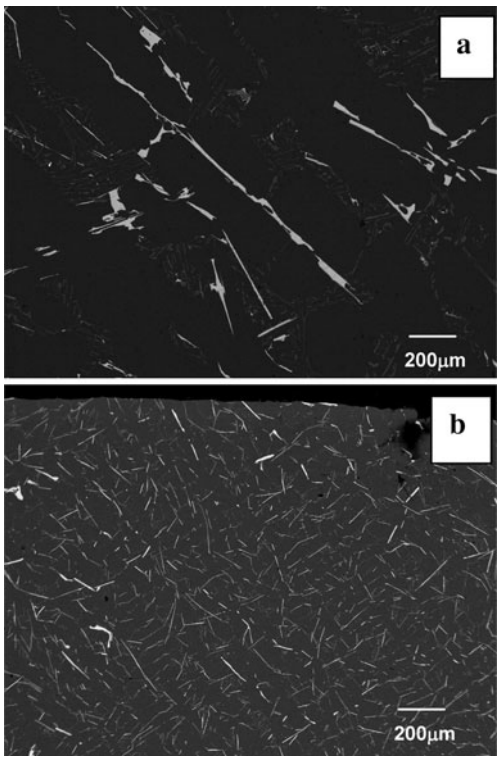

Fig. 3 SEM micrographs taken on DTA samples cooled at (a) 0.2 °C/min, and (b) 40 °C/min (light contrast relates to beta phase)

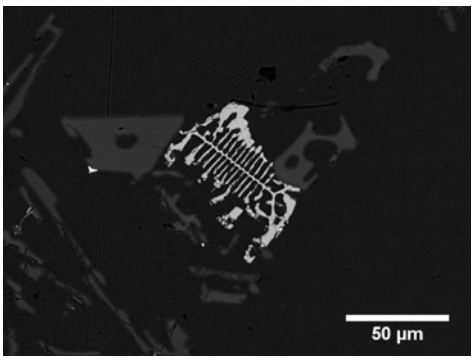

Fig. 4 SEM micrograph showing a precipitate with skeleton appearance similar to that of the alpha phase

for a cooling rate of 10 °C/min. The initial growth of the beta phase is thus very rapid as already reported by Wang et al. [10]. This result shows also that most of the precipitation of beta phase occurs in a narrow temperature window.

Metallographic analysis of the samples showed the presence of beta phase, eutectic (α-Al)-silicon and (α-Al) matrix. The influence of the cooling rate on the morphology of the beta phase is illustrated in Fig 3. For the sample with cooling rate of 0.2 °C/min, the beta phase appears as long and thick needles in 2D view (X-ray tomography showed them to be plates, see below). At 40 °C/min, the size of the beta precipitates is dramatically reduced as seen in Fig. 3b.

Figure 4 shows another iron intermetallic phase forms during solidification at cooling rate of 0.2 °C/min. This precipitation could not be detected on the DTA thermogram. Its skeleton appearance is similar to that reported for alpha phase (Al_8Fe_2Si).

Figure 5 shows the calculated liquidus projection of the Al–Fe–Si phase diagram [9]. The calculated solidification path of the investigated alloy has been superimposed (bold line), it is the same for lever rule and Scheil's model. It is seen that the primary deposition of (α-Al) hits the two-fold (α-Al)–beta line far away from the peritectic reaction $L + Al_8Fe_2Si \rightarrow \alpha\text{-Al} + Al_5FeSi$. Accordingly, the alpha phase would not be expected to appear. The temperature calculated for the start of beta phase precipitation is 606 °C when the maximum value according to the DTA experiments is 600 °C (value read in Fig. 2 plus 5 °C). Beta phase thus appears with a significant undercooling which gives some opportunity for alpha phase to nucleate and grow as a metastable phase. The high undercooling necessary for beta nucleation may be related to the inhibition of the peritectic transformation that leads to enhanced alpha phase precipitation in some alloys [11]. This high sensitivity of iron-bearing phases precipitation to cooling rate is further illustrated by the precipitation of the delta phase (Al_9FeSi_3) instead of the beta phase in directionally solidified Al7Si0.9Fe alloy [12].

Measurements of the 2D volume fraction of beta phase on the DTA samples are reported in Fig. 6 as function of the cooling rate. The bars relate to the standard deviation of the experimental measurements. A slight increase from 2.2 to

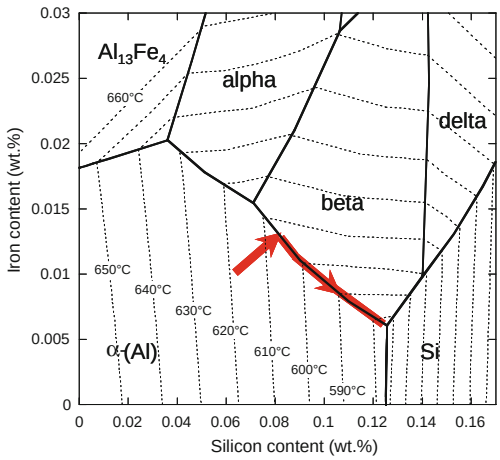

Fig. 5 Part of the ternary Al–Fe–Si phase diagram showing the solidification path for Al-6.5Si-1Fe alloy

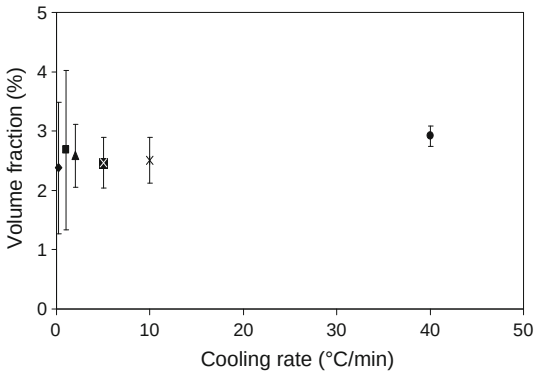

Fig. 6 Evolution of the average volume with the cooling rate

2.9 % can be seen which may not be highly significant considering the high scattering of the data at low cooling rates. This scattering shows that the beta phase was not well distributed throughout the sample for low cooling rates, presumably because of less nucleation sites. The measurement made on the sample cooled at 40 °C/min showed a more constant volume fraction across the cross section, which in turn is indicative of a better spreading of the nucleation events.

For beta phase length calculation, both the average length and the average of the 5 longest particles in each sub-area were considered. This latter method enhances the cooling rate effect on the beta phase morphology as illustrated in Fig. 7. Increasing cooling rate from 0.2 °C/min to 40 °C min reduced the maximum length observed from 1,017–264 µm. The result also showed, as the cooling rate increases, the beta phase appeared more homogeneous in length.

X ray tomography was used to obtain 3D images from the reconstruction series of X-ray images. The images were reconstructed by selecting regions of interest (ROI) from different angles and then geometry calibration was performed.

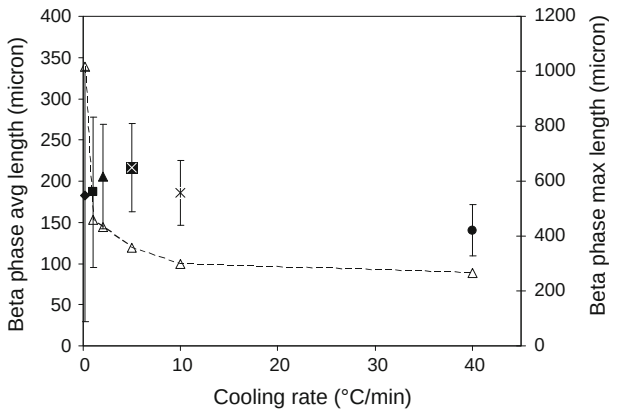

Fig. 7 Evolution of the beta phase average length and maximum length in DTA samples cooled at various cooling rates

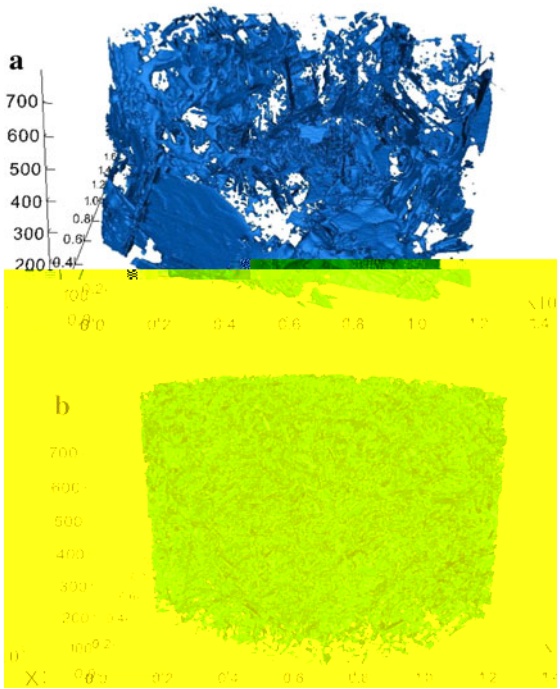

Fig. 8 3D rendering of intermetallic phase in DTA samples for two cooling rates **a** 0.2 °C/min and **b** 10 °C/min. (the scales are in voxel size)

The iron-bearing phase can be extracted due to high difference in atomic weight between Al and Fe and thus X-ray attenuation.

General visualization of the 3D image showed large plates for samples with low cooling rates, as seen in Fig 8. During beta phase growth, the precipitates seem to have bent so as to surround the (α-Al) dendrites that have nucleated and developed earlier in the solidification process. Impingement and branching of large beta phase plates was also observed. Most of the beta phase plates grow laterally, in agreement with previous descriptions by Terzi et al. [13] and Dinnis et al. [14].

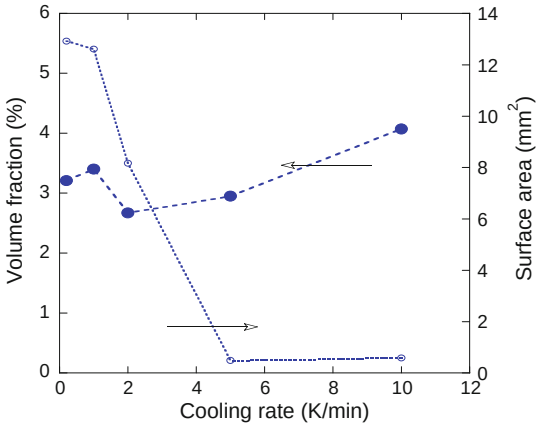

Fig. 9 Beta phase volume fraction (%) and surface area (mm^{-2}) in 3D from different cooling rates. Arrows indicate the relevant Y axis for each curve

The nucleation of the beta phase appeared to occur at the outer surface (skin) of the sample for a cooling rate of 0.2 °C/min, and growth proceeded toward the center. However, with high cooling rate, the initiation appeared dispersed within the volume and the beta particles become much smaller. Observation also showed some small independent beta phase particles that did not develop into large plates. Unfortunately, the image quality and resolution generated by tomography is reduced with smaller size of beta phase.

Figure 9 shows the evolution of the volume fraction and of the surface area as evaluated from 3D images. The volume fraction showed the beta precipitates have a consistant value for cooling rate of 0.2 °C/min and 1 °C/min, while, this value increases at cooling rate higher than 10 °C/min. This is tentatively related to the reduction in image quality. As for beta phase morphology, the results show that the average beta phase surface area decreases with increasing cooling rate, as expected. Nevertheless, this decrease might have been dramatically affected by the noise in the image quality.

4 Conclusion

A study of the effect of cooling rate on the beta intermetallic phase of Al-6.5Si-1Fe alloy by DTA was performed. The characteristic temperatures of the solidification reactions (liquidus, beta precipitation and final eutectic) shifted as the scanning rate changes due to thermal resistance. DTA analysis showed the beta precipitation as pre-eutectic reaction with some undercooling when compared to calculated solidification path. This undercooling may explain that some metastable alpha phase was precipitated during solidification at the lowest cooling rate investigated here. This observation is under further investigation.

Analysis of 3D images show how the beta phase precipitates grow as plates surrounding the primary (α-Al) dendrites. Nucleation initiates from the outer skin surface and growth toward the center for low cooling rates, while the initiation appears dispersed in the bulk as the cooling rate increases.

Acknowledgments Financial support from the European Space Agency (contract #4200014347) through the MICAST program and from the Education Ministry - Republic of Indonesia are greatly appreciated.

References.

1. Dinnis C M, Taylor J A, and Dahle A K, *Mater Sci Eng: A* **425** (2006) 286.
2. Franek A, Pazdernik J, and Hanna A K, *World Aluminum Abstracts,* MCB, Harvard (1974) p 58.
3. Lu L, and Dahle A K, *Metall Mater Transac A* **36** (2005) 819.
4. Samuel A M, Samuel F H, and Doty H W, *J Mater Sci*, **31** (1996) 5529.
5. Khalifa W, Samuel, F H, and Gruzleski, J E, *Metall Mater Transac A* **34** (2003) 807.
6. Shabestari S G, Ghodrat S, *Mater Sci Eng A*, 467 (2007) 150.
7. Fernadez-Calvo A I, Niklas A, and Lacaze J, *Mater Sci Forum* **649** (2010) 493.
8. Boettinger W J, and Kattner U R, *Metall Mater Transac A*, **33A** (2002) 1779.
9. Lacaze J, Eleno L, and Sundman B, *Metall Mater Transac A* **41A** (2010) 2208.
10. Wang J, Lee P D, Hamilton R W, Li M, and Allison J, *Scripta Materialia*, **60** (2009) 516.
11. Belov N A., Eskin D G, Aksenov A A., *Multicomponent Phase Diagrams: Applications for Commercial Aluminum Alloys*, Elsevier Science, Oxford, (2005).
12. Han Y S, Choi J O and Mc Cartney D G, *Metals Mater Int* **10** (2004) 27.
13. Terzi S, Taylor J A, Cho Y H, Salvo L, Suery M, Boller E, Dahle A K, *Acta Materialia* **58** (2010) 5370.
14. Dinnis C M, Taylor J A, *Scripta Materialia* **53** (2005) 955.

Materials Science Forum Vol. 765 (2013) pp 130-134

doi:10.4028/www.scientific.net/MSF.765.130

Study of the Effect of Cooling Rate on Eutectic Modification in A356 Aluminium Alloys

D. Ferdian[1,2,a], J. Lacaze[1,b], I. Lizarralde[3,c], A. Niklas[3,d] and A.I. Fernández-Calvo[3,e]

[1]CIRIMAT, Université de Toulouse, ENSIACET, BP 44362, 31030 Toulouse, Cedex 4, France

[2]Dept. Metallurgy and Material, Universitas Indonesia, Kampus Baru UI Depok, 16424, Indonesia

[3]Engineering and Foundry Processes, IK4-AZTERLAN, Aliendalde Auzunea 6, E-48200 Durango (Bizkaia), Spain

[a]deni@metal.ui.ac.id, [b]jacques.lacaze@ensiacet.fr, [c]ilizarralde@azterlan.es, [d]aniklas@azterlan.es, [e]afernandez@azterlan.es

Keywords: A356 alloy, Thermal analysis, Differential thermal analysis, Eutectic modification

Abstract. In this present work, an assessment of eutectic modification based on thermal analysis was performed on modified A356 alloy. The effect of various cooling rates which were achieved by means of casting samples with various moduli in sand and metallic moulds was investigated. Cooling curves recorded from thermocouples inserted in the centre of the samples showed characteristic undercooling and recalescence associated with (Al)-Si eutectic modification. The results showed that cooling rate has a role in observed modification level. Furthermore, differential thermal analysis was included to determine the eutectic melting temperature.

Introduction

Thermal analysis has been used for a long time in the foundry industry to monitor melt quality prior to casting. In aluminium casting, parameters such as nucleation undercooling and eutectic temperature depression are associated with grain refinement and silicon modification level respectively [1,2]. A356 grade classified as hypoeutectic Al-Si-Mg alloy, is commonly used due to its superior castability and good mechanical properties, especially after heat treatment (T6) owing to precipitation of fine Mg_2Si [3]. This alloy is widely used in permanent die casting and sand casting, e.g. for manufacturing automotive components such as cast wheels and engine blocks. In this paper, an assessment of the effect of cooling rate on eutectic modification of A356 alloy was performed on samples of various thermal moduli cast in sand and metallic moulds at nearly constant Sr level.

Experimental Procedure

Three modified A356 alloys with chemical compositions listed in Table 1 were cast in both sand and metallic moulds following a procedure previously described [4]. These moulds consist of a set of cylinders of different sizes which were designed in such a way that the height of each cylinder was equal to its diameter. Each cylinder was equipped with a thermocouple located at its geometrical centre and the cooling curves were recorded using the Thermolan-Al system [5]. However, some of the cooling curves were not obtained because of thermocouple failure. The thermal modulus (TM) values and the corresponding range of eutectic cooling rates CR_e (see Fig. 1) are listed in Table 2. At the time of casting, a standard cup for thermal analysis (TA) with TM = 0.605 cm was also poured and its cooling curve recorded.

Table 1. Chemical composition (wt.%) of studied A356 alloys and reference temperature T_R (°C).

Sample	Si	Fe	Cu	Mn	Mg	Cr	Ni	Zn	Ti	Sr	T_R
Alloy A	6.90	0.18	<0.01	0.02	0.53	0.01	<0.01	<0.01	0.14	0.011	572.0
Alloy B	6.65	0.17	0.02	<0.01	0.50	<0.01	<0.01	<0.01	0.16	0.013	572.1
Alloy C	6.83	0.14	<0.01	<0.01	0.52	<0.01	<0.01	<0.01	0.13	0.013	572.2

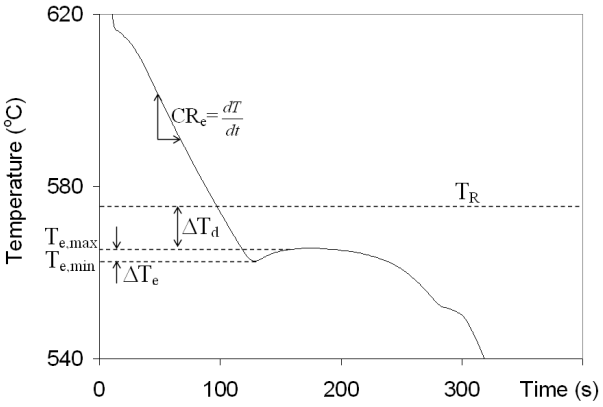

Fig. 1. Parameters taken from thermal analysis cooling curves for characterizing the (Al)-Si eutectic arrest.

Table 2. Thermal moduli (TM) and ranges of eutectic cooling rate (CR_e) of cylinder test samples.

Sand mould	TM [cm]	1.5	1.15	1	0.8	0.6	0.4	-
	CR_e [°C/s]	0.18-0.20	0.22-0.32	0.36-0.38	0.69-0.72	1.1	2.5-2.8	-
Metallic mould	TM [cm]	-	1.15	1	0.8	0.6	0.4	0.3
	CR_e [°C/s]	-	2.6-2.8	3.0	4.2-5.0	5.5-6.5	7.5-11	13-16

This study is focused on parameters related to the (Al)-Si eutectic reaction as obtained from the cooling curves according to the nomenclature shown in Fig. 1. These parameters are defined as follows:

- Minimum eutectic temperature ($T_{e,min}$), maximum eutectic temperature ($T_{e,max}$) and recalescence (ΔT_e). In the case of no recalescence, the $T_{e,max}$ was obtained as the temperature for which the absolute value of the cooling rate (time derivative of the cooling curve) was highest.
- $\Delta T_d = T_R - T_{e,max}$, is the eutectic depression, where T_R is the equilibrium eutectic temperature calculated using an equation obtained by updating the one proposed by Mondolfo [6], where the weight percentage, w_i, of alloying elements i are considered:

$$T_R\left(^{o}C\right) = 577 - \frac{12.5}{w_{Si}} \cdot \left(4.59 \cdot w_{Mg} + 1.37 \cdot w_{Fe} + 1.65 \cdot w_{Cu} + 0.35 \cdot w_{Zn} + 2.54 \cdot w_{Mn} + 3.52 \cdot w_{Ni}\right) \quad (1)$$

Eutectic cooling rate (CR_e) was measured from the slope of the cooling curve (600 °C to 575 °C) after primary (Al) nucleation and prior to the (Al)-Si eutectic reaction.

Furthermore, samples machined out from the cast cylinders were subjected to differential thermal analysis (DTA) using a SETARAM–SETSYS apparatus to evaluate the eutectic temperature. DTA signals were recorded with scanning rates for heating and cooling of 2, 5 and 10 °C/min. Each run used the same sample and low argon flux was used during the entire experiment. Finally, evaluation of the modification level was performed using the AFS chart [2], according to which well-modified structures present an index higher than 3.5.

Results

Microstructure Analysis. Fig. 2 illustrates the as cast microstructure and silicon modification for the two extreme moduli of both moulds. In the case of metallic mould, the eutectic silicon was well modified in all cylinders. However, in the case of large thermal moduli in the sand mould, the silicon modification appeared incomplete. This relates to the low effectiveness of Sr modification which is known at low cooling rates [7]. Observation of the microstructures also revealed other phases such as π-($Al_8FeMg_3Si_6$), Mg_2Si and β-Al_5FeSi phases associated with the so-called final eutectic reaction.

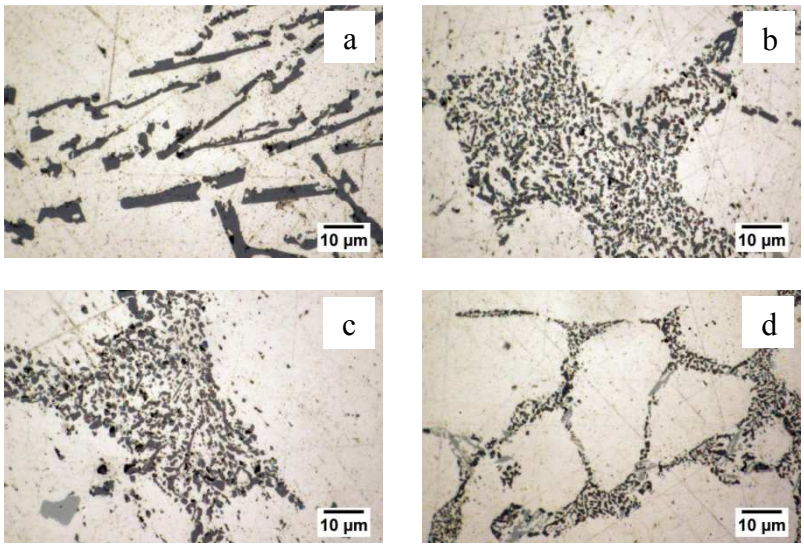

Fig. 2. Microstructure of alloy A samples, cast in sand (a, c) and metallic (b and d) moulds with maximum (a and b) and minimum (c and d) thermal modulus.

Thermal Analysis. Fig. 3 shows the cooling curves in the eutectic region obtained from all records with alloy A. The dashed line represents the TA standard cup record. As the cooling rate increases, the total solidification and eutectic plateau times are reduced. Recalescence of the (Al)-Si eutectic reaction is clearly visible on all sand mould records while it is not visible for the biggest metal mould samples. Observation of the cooling curves revealed also that the final eutectic reaction is visible only in the sand mould at low cooling rates. Correlation between the eutectic cooling rate and maximum eutectic temperature ($T_{e,max}$) is illustrated in Fig. 4a, which shows that the maximum eutectic temperature decreases as the eutectic cooling rate increases. Fig. 4b illustrates that there is no direct correlation or trend between eutectic cooling rate and recalescence (ΔT_e).

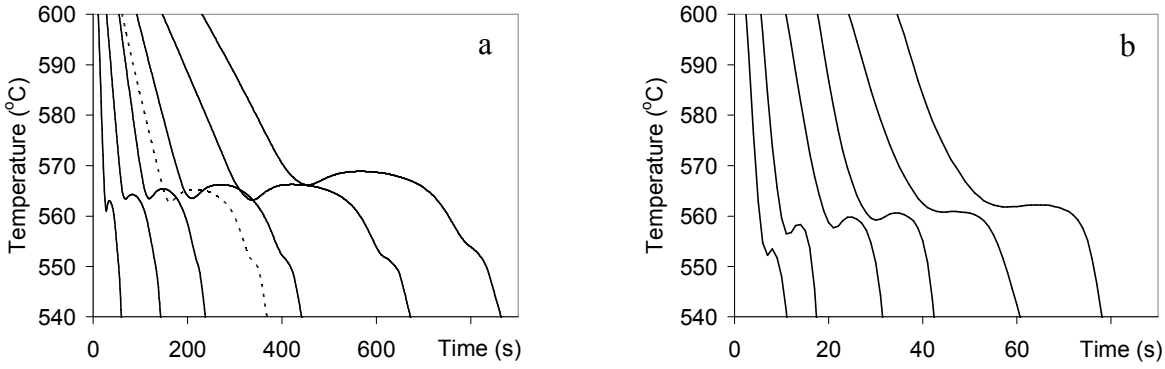

Fig. 3. Cooling curves obtained for cylindrical samples of different thermal moduli with alloy A, cast in sand (a) and metallic (b) moulds.

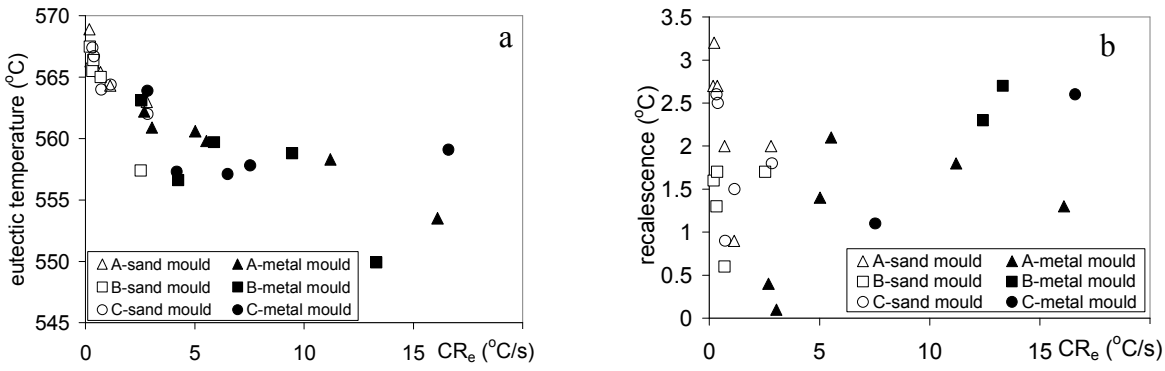

Fig. 4. Correlation between maximum eutectic temperature, $T_{e,max}$ (a) and recalescence, ΔT_e (b) versus eutectic cooling rate.

DTA Results. Fig. 5 presents the DTA record upon cooling and heating alloy A at 2 °C/min. The thermogram shows successive reactions upon solidification: precipitation of (Al) dendrites (1), of the (Al)-Si eutectic (2) and of the final eutectic (3). This latter peak was seen to split in two thermal arrests (3a and 3b) at low scanning rates. Three thermal peaks could similarly be identified on heating records. The start and peak temperatures for (Al)-Si precipitation were evaluated on all the heating and cooling thermograms. These values are plotted versus the scanning rate in Fig. 6 for alloy A, while the results for the two other alloys were nearly superimposed on these ones. The shift of the characteristic temperatures when the scanning rate increases is mainly caused by the thermal resistance in thermocouple measurement of the DTA apparatus [8]. The values obtained by extrapolation to a zero scanning rate are thus expected to be the relevant equilibrium temperatures to be discussed below.

The peak temperature upon heating extrapolates to 574 ^{o}C, only slightly above the calculated T_R values at 572.0-572.2 ^{o}C. This peak temperature is at about 10 ^{o}C above the start temperature upon cooling which shows that modification affects the eutectic reaction temperature at the slow cooling rates achieved in DTA even though the microstructure appeared unmodified. It is interesting to note that the peak temperature on cooling, which represents the end of the (Al)-Si eutectic reaction, extrapolates to about the same temperature as the start temperature on heating. This temperature (559±1 ^{o}C) appears slightly above the final eutectic temperature of about 555 °C [9-11], thus showing the extent of the (Al)-Si eutectic.

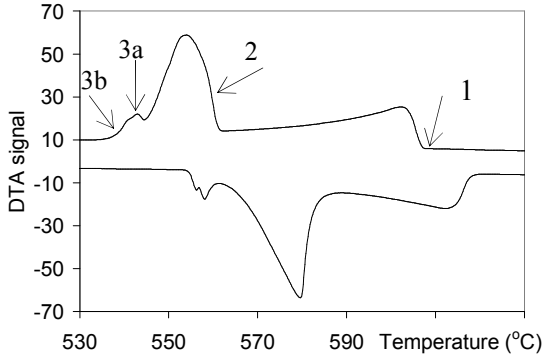

Fig. 5. DTA thermograms recorded upon cooling and heating at 2 °C/min of alloy A (the records were adjusted along the y axis to separate the curves for easier reading).

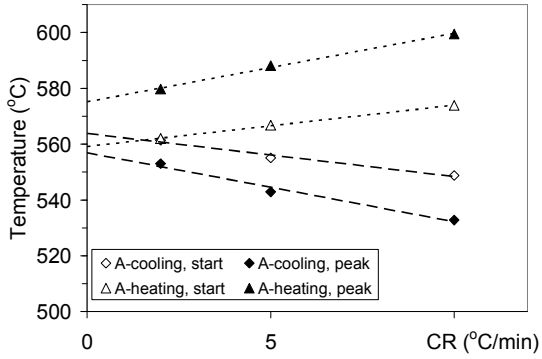

Fig. 6. Effect of scanning rate on the characteristic temperatures of the (Al)-Si eutectic thermal arrest of alloy A.

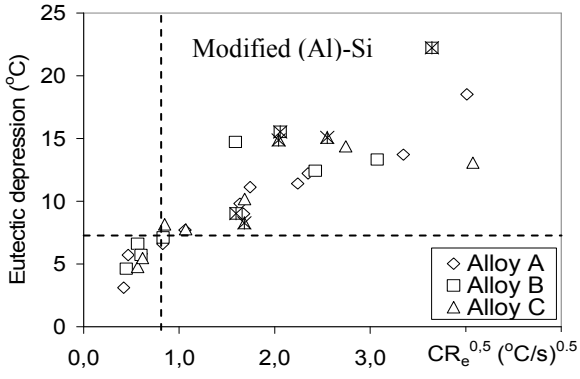

Fig. 7. Evolution of the eutectic depression (ΔT_d) with the square root of the eutectic cooling rate. Crosses represent data without recalescence.

Discussion

Typical solidification sequence for A356 alloy can be referred to in works by Bäkerud et al. [9], Mackay et al. [10], and Closset and Gruzleski [11]. They all reported three thermal arrests as the alloy solidified, which correspond to the major solidification reactions described in relation to

Fig. 5. The degree of silicon modification has been related in the literature to the depression of the (Al)-Si eutectic temperature [12,13], and a value of 5.5 °C has been previously reported as the minimum for efficient modification [2]. The evolution of ΔT_d with the square root of the eutectic cooling rate is shown in Fig. 7 which is indicated the domain where well-modified structures were observed. It is seen that the necessary depression is 7 °C, slightly higher than the value previously reported, and it corresponds to a eutectic cooling rate higher than 0.7 °C/s.

Conclusion

Thermal analysis showed that the (Al)-Si eutectic depression increases with the cooling rate as expected, though only values of cooling rate higher than 0.7 °C/s relate to satisfactory modification of A356 alloy in either sand or metallic moulds.

Acknowledgments

Financial support from the European Space Agency (contract #4200014347) through the MICAST program and from the DGHE- Education Ministry -Republic of Indonesia are greatly appreciated.

References

[1] G.K. Sigworth, Theoretical and practical aspects of the modification of Al-Si alloys, AFS Trans. 91(1983) 7-16.

[2] D. Apelian, G.K. Sigworth, K.R. Whaler, Assessment of grain refinement and modification of Al-Si foundry alloys by thermal analysis, AFS Trans. 92 (1984) 297-307.

[3] A. Lutts, Pre-precipitation of Al-Mg-Ge and Al-Mg-Si, Acta Metall. 9 (1961) 577-586.

[4] A. Niklas, U. Abaunza, A.I. Fernández-Calvo, J. Lacaze, R. Suárez, Thermal analysis as a microstructure prediction tool for A356 aluminium parts solidified under various cooling conditions, China Foundry 8 (2011) 89-95.

[5] P. Larrañaga, J.M. Gutiérrez, A. Loizaga, Thermolan-Al is a system under development that is based on the Thermolan system used for cast irons, AFS Trans. 116 (2008) 547-561.

[6] L.F. Mondolfo, Aluminum alloys, structure and properties, Butterworth, London, 1979.

[7] K. Song, H. Fufii, H. Nakae, H. Yamaura, A study on modification mechanism by Sr in Al-Si eutectic alloy, J. Jpn. Inst. Light Met. 43 (1993) 484-489.

[8] W.J. Boettinger, U.R. Kattner, On differential thermal analysis curves for the melting and freezing of alloys, Metall. Trans. A 33 (2002) 1779-1794.

[9] L. Bäkerud, G. Chai, J. Tamminen, Solidification characteristics of Aluminum alloys, Vol.2, AFS, Illinois, 1990.

[10] R.I. Mackay, J.E. Gruzleski, Quantification of Magnesium in 356 alloy via thermal analysis, Int. J. Cast Met. Res. 10 (1998) 255-265.

[11] B. Closset, J.E. Gruzleski, Mechanical Properties of A356.0 alloys modified with pure strontium, AFS Trans. 90 (1982) 453-464.

[12] S. Gowri, Comparison of thermal analysis parameter of 356 and 359 alloys, AFS Trans. 29 (1994) 503-508.

[13] H. Jiang, J.H. Sokolowski, M.B. Djurdjevic, W.J. Evans, Recent advances in automated evaluation and on-line prediction of Al-Si eutectic modification level, AFS Trans. 23 (2000) 505-510.

Materials Science Forum Vols. 790-791 (2014) pp 367-372
Online available since 2014/May/09 at www.scientific.net

doi:10.4028/www.scientific.net/MSF.790-791.367

Evaluation of (Al)-Si Eutectic Reference Temperature of A3xx alloys

Deni Ferdian[1,2,a], Jacques Lacaze[1,b]

[1]CIRIMAT, Université de Toulouse, ENSIACET, BP 44362, 31030 Toulouse, Cedex 4, France

[2]Dept. Metallurgy and Materials, Universitas Indonesia, Kampus Baru UI Depok, 16424, Indonesia

[a]deni@metal.ui.ac.id, [b]jacques.lacaze@ensiacet.fr

Keywords: Al-Si alloys, modification, thermal analysis, eutectic reference temperature.

Abstract. The modification level of Al-Si alloys is generally evaluated by the depression of the (Al)-Si eutectic temperature which can be recorded by thermal analysis. However, this method requires a reference temperature which should be the eutectic temperature evaluated on the relevant phase diagram. Various methods proposed to account for the effect of low level alloying elements on this reference temperature are reviewed and emphasis is put on the so-called "*Mondolfo's equation*" which is updated. Predictions are compared to experimental information from literature.

Introduction

Thermal analysis became a widespread technique for evaluating melt preparation of aluminum alloys in the 1980's [1]. It is in particular used for checking grain refinement and eutectic modification. Several parameters have been proposed in the literature for characterizing the thermal effects seen on the cooling curves which are associated to nucleation and early growth of (Al) phase (grain refinement) and to the (Al)-Si eutectic (eutectic modification) [2-3]. Concerning eutectic modification, the most used method is to correlate the effectiveness of modification with increased eutectic undercooling or so called "*eutectic depression*". Evaluation of this undercooling requires the knowledge of a eutectic reference temperature which should be given by the relevant phase diagram and has often been evaluated experimentally as the eutectic temperature of the unmodified alloy. However, in many cases, this latter cannot be obtained in a cast shop due the possibility of prior modification treatment to the alloys or the use of returns in the charge.

One of the most used methods to evaluate the reference temperature of the (Al)-Si eutectic was proposed by Apelian et al. [2] who derived an equation expressing the eutectic temperature as a function of alloy's composition from the phase diagram compiled by Mondolfo [4]. The so-called "*Mondolfo's equation*" is still widely accepted as seen in the recent work by Wang and Lu [5]. In the present work, we first reconsider the derivation of the equation and then update it according to more recent assessed phase diagram information. We then review other approaches proposed in the literature and finally compare them to available experimental data from literature.

Prediction of the solidification path of Al-Si-X alloys

Mondolfo's equation. The equation was derived to account for the effect of six elements (Cu, Fe, Mg, Mn, Ni and Zn) on the (Al)-Si eutectic with the binary (Al)-Si eutectic, e_{Si}, set at $w_{e,Si}$=12.5 wt.% Si and $T_{e,Si}$=577°C. The Apelian's method considered that the effect of these elements should be additive, so that the effect of each one could be evaluated based on the related Al-Si-X ternary phase diagram. As an example, Fig.1 shows schematically the projection of the liquidus surface of the Al-Si-Fe system (right part of the diagram) and the evolution of the (Al)-Si eutectic temperature (left part of the diagram), i.e. along the line e_{si}-E_{Fe}, where E_{Fe} is the three phase invariant eutectic point between liquid, (Al), Si and β-Al_5FeSi phase.

Assuming linearity of the temperature change (ΔT_e) along the two-fold (Al)-Si eutectic line, we can write:

$$\Delta T_e = \frac{T_{e,Si} - T_{E,Fe}}{w_{Fe}^{E}} \cdot w_{Fe}^{(Al)-Si} = a_{Fe} \cdot w_{Fe}^{(Al)-Si} \quad (1)$$

where $w_{Fe}^{(Al)-Si}$ is the iron weight content along the (Al)-Si eutectic line.

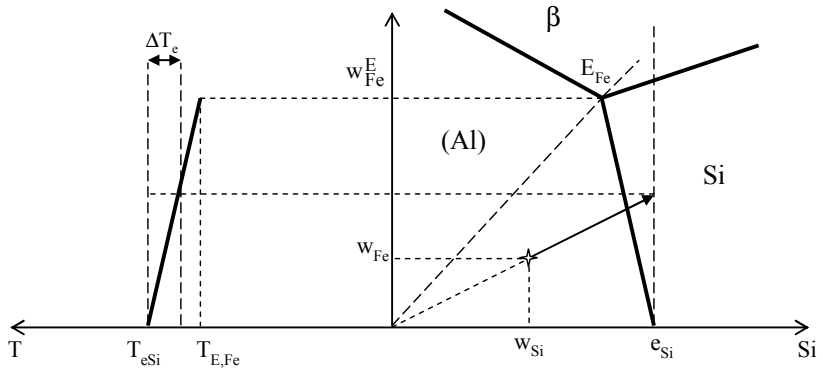

Fig. 1. Schematic Al corner of the ternary Al-Si-Fe system

For any alloy with composition (w_{Si}, w_{Fe}) such as the one represented with the cross in the right side of Fig. 1, the method assumes that solidification of the (Al) primary phase leads to a liquid enrichment in Fe in proportion of $\frac{w_{e,Si}}{w_{Si}}$ namely that $\Delta T_e = a_{Fe}.w_{Fe}.\frac{w_{e,Si}}{w_{Si}}$. This is graphically represented with the arrow in the graph. As mentioned above, the method assumes further that the effect of alloying elements is additive, therefore the reference temperature for the start of the (Al)-Si eutectic reaction of an aluminum-silicon alloy is given as:

$$T_e = T_{e,Si} - \frac{w_{e,Si}}{w_{Si}} \cdot \sum_X (a_X \cdot w_X) \quad (2)$$

with the sum is extended to all X alloying elements and the a_X are defined as for Fe in equation (1).

Ternary Al-Si-X phase diagrams where X is Fe, Mg, Mn or Ni, are very similar, i.e with a e_{si}-E_X line that is at nearly constant Si. Data relative to these diagrams and relevant to the present work are listed in Table 1, where $w_{Si}^{E,X}$ and $w_X^{E,X}$ are the Si and X weight content of the ternary invariant eutectic, $w_X^{E,(Al)}$ is the X weight content in solid (Al) in equilibrium with the ternary eutectic liquid and $T_{E,X}$ is the three-phase eutectic temperature of the Al-Si-X system. The partition coefficients between (Al) and the liquid, k_X, have been evaluated with the ternary eutectic data and are also listed in the table. Mondolfo selected ternary phase diagrams mostly according to the extensive work by Phillips [6]. Recent assessment of the diagrams with Fe, Mg and Ni agree with this latter while an updated version was considered for the Al-Si-Mn [7], Al-Si-Cu [8] and Al-Si-Zn [9,10] systems. For these three systems, original data according to Mondolfo's assessment are listed between brackets in Table 1.

While the method assumed the silicon content to be constant along the eutectic line, at 12.5 wt.%, a correction is proposed here which is an attempt to account for the difference in the silicon content of the binary and ternary eutectic invariant points. Accordingly, the a_X value will be calculated in the present work as:

$$a_X = \frac{T_{e,Si} - T_{E,X}}{w_X^{E}} \cdot \frac{w_{Si}^{E,X}}{w_{e,Si}} \quad (3)$$

Using the partition coefficients in Table 1, one can calculate the solidification path of Al-Si-X ternary alloys according to lever rule and Scheil's model. This is illustrated in Fig. 2a in the case of Ni, where is seen that Scheil and lever rule solidification paths are nearly superimposed and lie very close to Apelian's method (arrow). These observations also apply to the other three elements, Mg,

Fe and Mn. However, it is also clear from the graph in Fig. 2 that the method applies only to Al-Si alloys having their composition in the triangle Al-e_{Si}-E_X. Thus, this method should be restricted to alloys with a maximum content in X such that the (Al)-Si eutectic precipitates before any other secondary eutectic phase. This maximum, w_X^{max}, depends on the alloy's Si content and is roughly given as:

$$w_X^{max} = \frac{w_{Si}}{w_{Si}^{E,X}} \cdot w_X^{E,X} \quad (4)$$

Table 1. Ternary eutectic points data of selected Al-Si-X ternary systems. See the text for definitions; compositions are in wt.% and temperature in Celsius. Values assessed by Mondolfo are between brackets when they have been updated.

Element	$w_{Si}^{E,X}$	$w_X^{E,S}$	$w_X^{E,(Al)}$	k_X	$T_{E,X}$	Original factor a_x	$\frac{w_{Si}^{E,X}}{w_{e,Si}}$	Present work factor a_x
Mg	12.95	0.85	4.96	0.171	555	4.43	1.036	4.59
Fe	12	0.05	0.7	0.071	576	1.43	0.96	1.37
Cu*	6 (5)	4.5	25.6 (27)	0.175	521 (525)	1.93	0.75	1.65
Zn*	4.2 (3)		40 (80)		535 (440)	1.7	0.336	0.35
Mn	12. 7 (12)	0.03	0.4 (1)	0.075	576 (574)	3	1.016	2.54
Ni	11	0.05	5	0.01	557	4	0.88	3.52

* see text

For alloys with low level in alloying elements such as A356 where the total content in elements other than Al and Si is less than 1 wt.%, the accuracy of Apelian's method is quite good in predicting the (Al)-Si eutectic reference temperature. However, the equation fails to predict it correctly for aluminum-silicon alloys with high Cu alloying content such as A319 [3]. The reason for this is evidenced when considering the Al-Si-Cu phase diagram in Fig. 2b drawn according to He et al. [8]. It is seen that the (Al)-Si eutectic line moves far away to the left of the line at 12.5 wt. %Si along with increasing copper content. This leads to copper contents as estimated by the method much higher than the one when the solidification path reaches the (Al)-Si eutectic line. The maximum overestimation of the copper content is obtained for the ternary eutectic point when the method would give 2.5 (i.e. 12.5/5.0) times too high copper content. This means that the a_{Cu} coefficient as listed in Table 1 as "original factor" should be multiplied by 0.4. Because the actual copper contents in the Al-Si alloys are much lower than the value at the ternary eutectic point, the correction can not be that dramatic in all practicality. With the experimental data analyzed below, it has been found that a multiplication factor of 0.75 gives appropriate results, i.e. a_{Cu} was set to 1.65 after accounting for the effect of Si ternary eutectic content, see Table 1. The Al-Si-Zn phase diagram is somehow similar to the Al-Si-Cu one in that the ternary invariant eutectic is located far away from the binary (Al)-Si eutectic, and in fact is very close to the Zn-rich corner of the phase diagram. For this system and owing to the low Zn levels in A3xx alloys, it seemed wiser to use the reported isopleth section at 5.3 at.%Si [9,10] to estimate the effect of Zn on the two-fold (Al)-Si saturation line. The corresponding data is shown in Table 1 where it is seen that the final estimate of a_{Zn} differs greatly from the one assessed with the Apelian's method.

To sum up, the following equation is proposed that incorporates the changes of silicon content along the eutectic lines as well as an updating of the ternary phase diagrams:

$$T_e(^oC) = 577 - \frac{12.5}{w_{Si}} \cdot \left(4.59 \cdot w_{Mg} + 1.37 \cdot w_{Fe} + 1.65 \cdot w_{Cu} + 0.35 \cdot w_{Zn} + 2.54 \cdot w_{Mn} + 3.52 \cdot w_{Ni}\right) \quad (5)$$

This equation itself shows it is restricted to silicon content higher than 1 wt.%. Therefore, the equation should be limited to silicon contents in the range 1 to 12.5 wt.% and to alloying additions that depend on the silicon content, see Eq. 4, and are at most (wt.%) 4.9 for Mg, 0.7 for Fe, 5 for Cu, 5 for Zn, 0.4 for Mn and 5 for Ni.

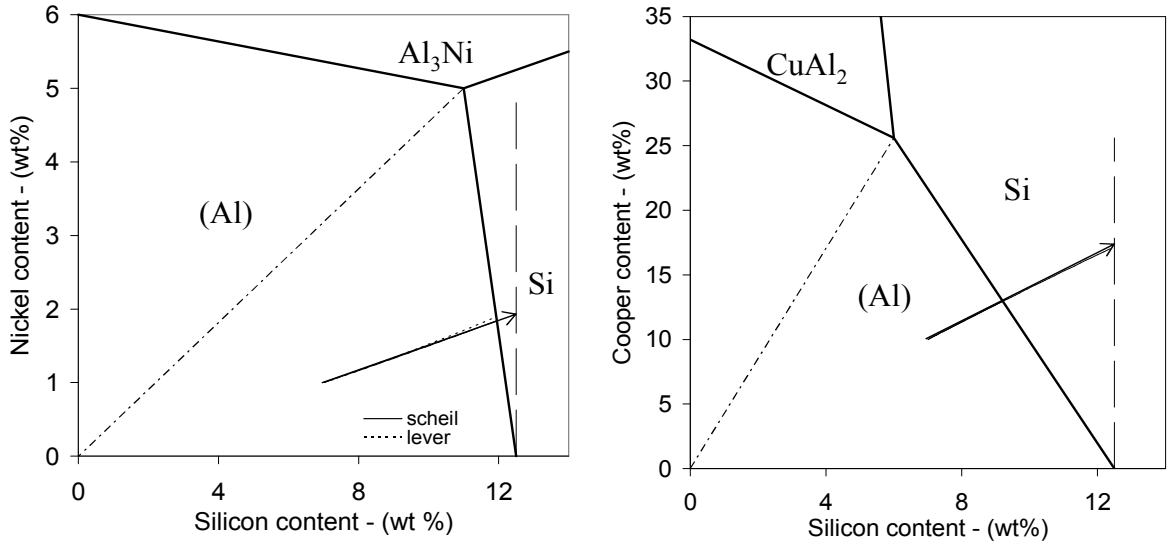

Fig. 2. Solidification path plotted onto the liquidus projection of the ternary Al-Si-Ni (a) and Al-Si-Cu (b) phase diagrams. Arrows illustrates Apelian's method, while Scheil's and lever rule paths are hindered below them.

Other equations. There are several other approaches proposed to calculate the reference eutectic temperature. Studies by Joenoes and Gruzleski [11] which focused on the magnesium effect, proposed a series of empiric calculations with a coefficient depending on the Si content in the alloys. While those equations only consider one element in the calculation and are limited to one type of chemical composition, Sthuldreier et al. [12] considered 3 major elements, Mg, Cu and Fe based on their experimental data. A different approach was used by Djurdjevic and collaborators [13, 14] who described the (Al) liquidus with second order polynomial for binary Al-X systems of interest and then defined a silicon equivalent (Si_{eq}) for each element X. Then, the enrichment of the liquid is described as with the Apelian's method and the eutectic temperature writes as follows:

$$T_e = 660.452 - \left(6.11 \cdot Si_{eq} + 0.057 \cdot Si_{eq}^2\right) \cdot \left(\frac{12.3}{w_{Si}}\right) \quad (6)$$

Result and Discussion

A comparison of reference temperatures predicted with equations from the present work, Apelian et al. [2], Stuhldreier et al. [12] and Djurdjevic [14], with thermal analysis data from literature [2,14-25] is shown in Figure 3a. In addition, comparison with calculations made with Thermo-Calc and the TCAL1 database [26] according to Scheil's model are also shown in Fig. 3b. In the literature data, two different methods are used to extract the eutectic temperature from the cooling curves which relate to recording the plateau temperature, $T_{E,G}$, and the nucleation temperature, $T_{E,Nuc}$ respectively. The method using the nucleation temperature gives systematically much higher temperatures than that predicted by CALPHAD calculations. Though such an observation may need further investigation, it suggests that the change in the cooling rate as recorded with thermal analysis cups and associated to nucleation in the central part of the cup, may relate in fact to the heat released by the outer part of the cup where the eutectic transformation has started. In a way, the reading of thermocouple would be influenced by the heat flux released from the outer shell of the thermal analysis cup.

The graph shows that at high eutectic temperature with low alloying additions, equations by Apelian et al. [2] and Stuhldreier et al. [12] present a low deviation from the bisector line. However, their predictions become scattered as the eutectic temperature is lowered due to higher alloying element. Moreover, the silicon equivalent method proposed by Djurdjevic [14] predicts values significantly above the experimental results in all the composition ranges investigated.

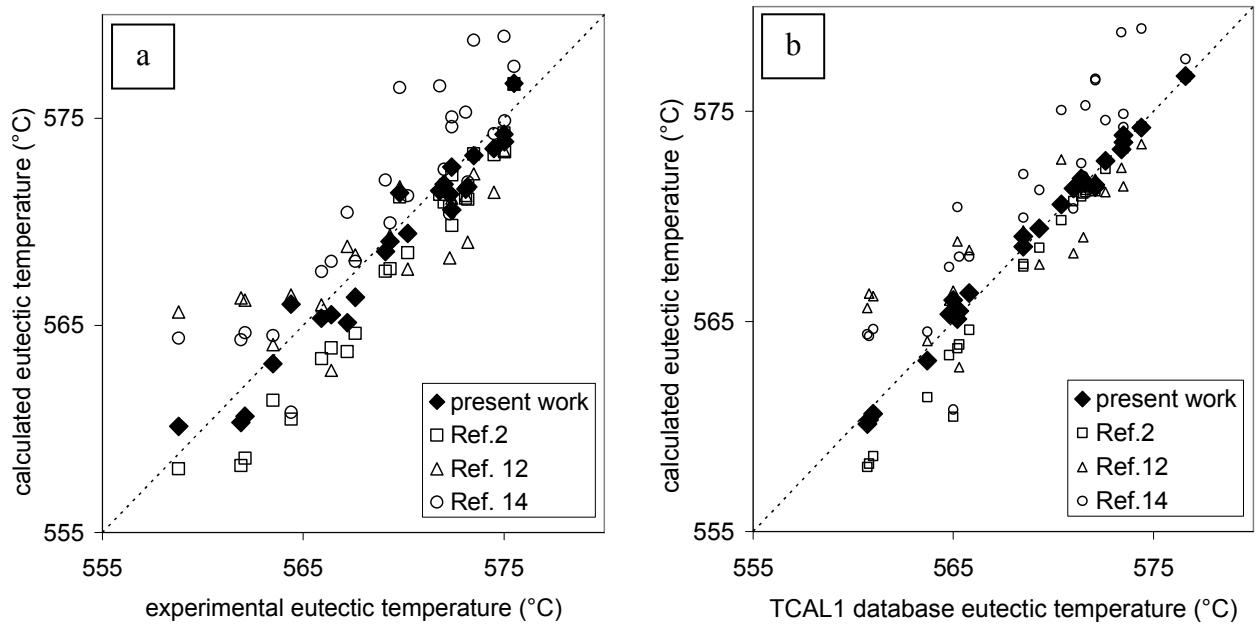

Fig. 3. Graph showing the correlation between experimental data (a), TCAL1 database (b) and calculated eutectic temperatures according to present work, Apelian et al. [2], Stuhldreier et al. [12] and Djurdjevic [14]. The dotted line are bisectors.

Conclusion

The so-called Mondolfo's equation derived by Apelian et al. [2] does agree quite well with the experimental and CALPHAD results for low Cu alloys, while giving too low values otherwise. The present approach that accounts empirically of the effect of Cu does closely follow CALPHAD-type predictions. It is finally seen that the proposed equation shows a better agreement with the experimental data than other equations in the whole range of compositions.

Acknowledgments

The authors wish to acknowledge the financial support received from the European Space Agency (contract #4200014347) through the MICAST program and DGHE – Indonesia Education Ministry.

References

[1] B.L. Tuttle, Principle of thermal analysis for molten metal process control, Proc. AFS/CMI Conf., Rosemont, IL, USA (1984) 1-37.

[2] D. Apelian, G.K. Sigworth, K.R. Whaler, Assessment of grain refinement and modification of Al-Si foundry alloys by thermal analysis, AFS Trans. 92 (1984) 297-307.

[3] J.E. Gruzleski, B.M. Closset, The treatment of liquid aluminum-silicon alloys, AFS Inc., Des Plaines, Illinois, 1990.

[4] L.F. Mondolfo, Aluminum alloys: structure and properties, Butterworth, London, 1976.

[5] R.Y. Wang, W. Lu, Spheroidization of eutectic silicon in direct-electrolytic Al-Si Alloy, Metall. Mater. Trans. A, 44 (2013) 2799-2809.

[6] H.W.L. Phillips, Annotated equilibrium diagrams of some aluminium alloy systems, Monograph No. 25, Inst. Met., London, 1959.

[7] Y. Du, Z. Jin, B. Huang, W. Gong, H. Xu, Z. Yuan, J.C. Schuster, F. Weitzer and N. Krendelsberger, A thermodynamic description of the Al-Mn-Si system over the entire composition and temperature ranges, Metall. Mater. Trans. A. 35 (2004) 1613-1628.

[8] C.Y. He, Y. Du, H.L. Chen, and H. Xu, Experimental investigation and thermodynamic modeling of the Al–Cu–Si system, CALPHAD 33 (2009) 200-210.

[9] K. Suzuki, M. Kagayama, Y. Takeuchi, Eutectic phase equilibrium of Al-Si-Zn system and its applicability for lower temperature brazing, J. Jpn. Inst. Light Met. 43 (1993) 533-538. (in Japanese)

[10] M.H.G. Jacob and P.J. Spencer, A critical thermodynamic evaluation of the systems Si-Zn and Al-Si-Zn, CALPHAD 20 (1996) 307-320.

[11] A.T. Joenoes and J.E. Gruzleski, Magnesium effects on the microstructure of unmodified and modified Al-Si alloys, Cast met. 4 (1991) 62-72.

[12] G. Stuhldreier, E. Mettingen, K.W. Stoffregen, Erfahrungen mit thermischen analyse von G-AlSi-legierungen, Giesserei.68 (1981) 404-409.

[13] F.C. Robles Hernandez, M.B. Djurdjevic, W.T. Kierkus, J.H. Sokolowski, Calculation of the liquidus temperature for hypo and hypereutectic aluminum silicon alloys, Mater. Sci. Eng., A. 396 (2005) 271–276.

[14] M.B. Djurdjevic, Thermal description of hypoeutectic Al-Si-Cu alloys using silicon equivalency, Military Technical Courier. 60 (2012) 152-168.

[15] J. Charbonnier, Microprocessor assisted thermal analysis testing of aluminum alloy structure, AFS Trans.92 (1984) 907-921.

[16] S. Gowri, F.H. Samuel, Effect of alloying elements on the solidification characteristics and microstructure of Al-Si-Cu-Mg-Fe 380 alloy, Metall. Mater. Trans. A, 25A (1994) 437-448.

[17]. M.B. Djurdjevic, H. Jiang, J. Sokolowski, Online prediction of aluminum-silicon eutectic modification level using thermal analysis, Mater. Charact., 46 (2001) 31-38.

[18] S. Thompson, S.L. Cockroft, M.A. Wells, Advance light metals casting development: solidification of aluminum alloy A356, Mater. Sci. Technol. 20 (2004) 194-200.

[19] M.B. Djurdjevic, G. Huber, Z. Odanovic, Synergy between thermal analysis and simulation, J. Therm. Anal. Calorim.111 (2013) 1365-1373.

[20] S. Farahany, A. Ourdjini, M.H. Idrsi, S.G. Shabestari, Evaluation of the effect of Bi, Sb, Sr and cooling condition on eutectic phases in Al-Si-Cu alloy (ADC12) by in situ thermal analysis, Thermochim. Acta, 2013, vol.553, pp. 59-68

[21] Y.M. Han, A.M. Samuel, F.H. Samuel, H.W. Doty, Microstructure characteristics in non-modified and Sr modified Al–Si–Cu–Mg 319 type alloys, Int. J. Cast Met. Res, 2008, vol.21, pp. 371-380.

[22] S. Thompson, S.L. Cockroft, M.A. Wells, Advanced light metals casting development: solidification of aluminium alloy A356, Mater. Sci. Technol., 2004, vol.20, pp.194-200.

[23] S.D. McDonald, A.K. Dahle, J.A. Taylor, D.H. StJohn, Eutectic grains in unmodified and strontium-modified hypoeutectic aluminum-silicon alloys, Metall. Mater. Trans. A, 2004, Vol.35A, pp. 1829-1873.

[24] M.B. Djurdjevic, G. Huber, Z. Odanovic, Synergy between thermal analysis and simulation, J. Therm. Anal. Calorim., 2013, vol.111, pp. 1365-1373

[25] M.B. Djurdjevic, Z. Odanovic, N. Talijan, Characterization of the solidification path of AlSi5Cu(1–4 wt.%) alloys using cooling curve analysis, JOM, 2011, vol.63, pp. 1-7.

[26] Thermo-Calc Software, TCAL1 database version 1.0, http://www.thermocalc.com (Accessed 29 March 2013).

Solidification and Gravity VI
10.4028/www.scientific.net/MSF.790-791

Evaluation of (Al)-Si Eutectic Reference Temperature of A3xx Alloys
10.4028/www.scientific.net/MSF.790-791.367

DOI References
[8] C.Y. He, Y. Du, H.L. Chen, and H. Xu, Experimental investigation and thermodynamic modeling of the Al-Cu-Si system, CALPHAD 33 (2009) 200-210.
http://dx.doi.org/10.1016/j.calphad.2008.07.015
[9] K. Suzuki, M. Kagayama, Y. Takeuchi, Eutectic phase equilibrium of Al-Si-Zn system and its applicability for lower temperature brazing, J. Jpn. Inst. Light Met. 43 (1993) 533-538. (in Japanese).
http://dx.doi.org/10.2464/jilm.43.533
[10] M.H.G. Jacob and P.J. Spencer, A critical thermodynamic evaluation of the systems Si-Zn and Al-Si-Zn, CALPHAD 20 (1996) 307-320.
http://dx.doi.org/10.1016/S0364-5916(96)00033-8
[18] S. Thompson, S.L. Cockroft, M.A. Wells, Advance light metals casting development: solidification of aluminum alloy A356, Mater. Sci. Technol. 20 (2004) 194-200.
http://dx.doi.org/10.1179/026708304225011199
[19] M.B. Djurdjevic, G. Huber, Z. Odanovic, Synergy between thermal analysis and simulation, J. Therm. Anal. Calorim. 111 (2013) 1365-1373.
http://dx.doi.org/10.1007/s10973-012-2389-0

71st BILBAO 2014 WORLD FOUNDRY CONGRESS
Advanced Sustainable Foundry
19-21 May 2014 • Palacio Euskalduna, BILBAO

IMPROVED GRAIN SIZE PREDICTION IN ALUMINIUM-SILICON ALLOYS BY THERMAL ANALYSIS

(J. Lacaze)
CIRIMAT, Université de Toulouse, ENSIACET, Toulouse, France

(D. Ferdian)
CIRIMAT, Université de Toulouse, ENSIACET, Toulouse, France

(I. Lizarralde)
Veigalan Estudio 2010 S.L.U., Durango, Spain

(A. Niklas)
IK4-AZTERLAN, Engineering, R&D and Metallurgical Processes, Durango, Spain

(S. Eguskiza)
IK4-AZTERLAN, Engineering, R&D and Metallurgical Processes, Durango, Spain

(A.I. Fernández-Calvo)
IK4-AZTERLAN, Engineering, R&D and Metallurgical Processes, Durango, Spain

ABSTRACT

Grain refinement is a common practice in aluminium casting alloys, being Ti and/or B the most popular refining additions. The effectiveness of these additions may be controlled by thermal analysis consisting in analysing the cooling curve during solidification of a sample cast in an instrumented standard cup. This assessment is based on the use of a pre-established relationship between some characteristic parameters of the cooling curve and the microstructure features measured either on the cup or on a standard sample cast at the same time.

Previous works showed there is still a need for improving the prediction in the range of small grain sizes in case little or no recalescence is observed. $t_{f,Th\text{-}Al}$, the recalescence time or the time during which temperature remains constant, has been established as an appropriate parameter to take into account high nucleation potential of the melts.

This work reports a statistical analysis performed on the characteristic features of the cooling curves of 110 melts of AlSi7Mg alloy. A first analysis gave a simple linear relation between grain size and $t_{f,Th\text{-}Al}$ with a correlation coefficient R^2 of 0.91, that shows a satisfactory agreement for the fine and medium grains (up to 1 mm) while being less good for very coarse grains. However, coarse grains are easily detected; thus, corrective actions can then be taken in order to improve the metallurgical quality in terms of grain size refinement before casting.

Further analysis led to express $t_{f,Th\text{-}Al}$ as a function of recalescence and of the grain size, its square and cube. The correlation coefficient is much better at 0.96 with an improved description in both small and large grain domains.

Keywords: AlSi7Mg alloys, thermal analysis, grain refinement, multivariate analysis, nucleation potential

INTRODUCTION

Aluminium-silicon alloys are the most widely used alloys for production of aluminium castings because they have very good foundry properties and may be adapted to span a large range of mechanical properties. Their mechanical properties are largely influenced by the melt treatment,

which schematically comprises four main operations: cleaning (i.e. oxide removal), degassing (i.e. hydrogen removal), eutectic modification and grain refinement[1-3]. The three former have an obvious direct impact on the mechanical properties. The grain size does not have such direct impact in the case of hypoeutectic Al-Si alloys, with 5 to 11% silicon, but it has a very clear effect on the shrinkage behavior: well refined alloys tend to display less and more finely dispersed shrinkage[3]. Consequently in those parts which comprise zones difficult to feed adequately a good grain refinement can decisively reduce porosity.

Grain refinement is also well known to reduce the tendency to hot tearing in 2XXX, 5XXX and 7XXX alloys, but this is usually not an issue in the considered industrial Al-Si cast alloys. Thus, although not mandatory if the casting design ensures an excellent feeding, grain refinement is a very common treatment for safety critical or pressure tight parts in which very little porosity is allowed. In industrial practice, Ti and/or B are added to the melt prior to casting in order to increase the nucleation potential of the melt.

It should be pointed out that there is no simple relation between the chemical composition in terms of Ti and/or B and the nucleation potential of the melt. The effectiveness of grain refinement depends not only on the nature of the Ti- and/or B-bearing particles contained in the refining master alloy, but also on the content of the melt in both elements before addition[4-7]. The quality of melt preparation can be assessed by means of thermal analysis which has been regularly applied to aluminium-silicon alloys and more particularly to AlSi7Mg alloys during the past decades[3-18]. This assessment is based on the use of a pre-established relationship between characteristic parameters of the cooling curve obtained on an instrumented thermal analysis (TA) cup and microstructure features measured either on the cup or on a standard sample cast at the same time[3-21].

In general, a slow cooling rate is required to obtain a well defined cooling record by TA. As a consequence, Spittle[6] pointed out that the method may not be appropriate to predict grain size in actual castings where the cooling rate is generally high. In literature, very few works dealt with microstructure prediction in real parts which most generally present variations in local cooling rate, which are essentially determined by the so-called thermal modulus of the part and by the type of mould used[12-13]. These few available works[22-23] showed very little predictive capabilities. However, recent works[16-19] demonstrated that it is possible to predict the grain size in real aluminium castings when knowing the cooling rate of the selected zone in the casting and the grain refining potential of the melt. This latter is evaluated by using thermal analysis curve in a standard sand cup. Thus, it is of great importance to have an accurate method of prediction from standard cup records.

The effect of grain refinement on the cooling and solidification curves relate to parameters associated with solidification of the primary (Al) phase such as undercooling, recalescence and solidification time[13-15]. However, there is still a need for improving the prediction in the range of small grain sizes in case no recalescence is observed. In the present work, 110 AlSi7Mg alloy melts with different grain refiner additions (B or Ti-B) have been analysed in terms of thermal analysis record and metallographic grain size evaluation of standard sand cup. More than half of the tests were done in the very fine grain size range in which no recalescence is observed. 40 tests were done in a small pilot plant with a furnace of 50 kg, while the rest are industrial melts prepared at five different foundries. In this work, a statistical analysis is performed to relate the characteristic features of the cooling curves and the grain size measured on the TA cups.

DESIGN OF EXPERIMENTS

110 melts of AlSi7Mg type alloy with Mg contents varying from the AlSi7Mg0.3 to the AlSi7Mg0.6 standards were tested. Some of the melts were prepared using pure ingots while others contained internal scraps, varying between 20 and 80 percent of the melt charge.

70 tests were performed with real industrial melts and the other ones have been performed in TQC Technologies pilot plant under conditions comparable to manufacturing conditions encountered in industry. Although Si modification is not the objective of this work, some of the melts had Na or Sr addition for modification of the (Al)-Si eutectic. Varying grain size was achieved by adding various amounts of grain refiner. Two different grain refiners have been used: Al-5%Ti-1%B (wt. %) master alloy in bars and boron tablets. Also, several tests have been carried out without addition of grain refiner. Due to the use of scraps, the actual nucleation potential of the melt may not be simply related to refining additions.

For the thermal analysis tests, each cup was instrumented with a thermocouple located at the centre for recording the temperature during cooling and solidification. A data

recording system was used for registration of the cooling curve, plotting and evaluation of the most important features. 5-6 data per second were recorded. Figure 1 is a typical example of cooling curve recorded for AlSi7Mg alloy during its solidification. The insert shows an enlarged view of the part related to the beginning of solidification where several of the parameters considered as characteristic of nucleation of the (Al) primary phase are illustrated. The parameters are defined as[13,14,16]:

- ΔT_{Al} is the recalescence, i.e. the difference between the maximum T_{max} and minimum T_{min} temperatures;
- KF16 is defined as the difference between the temperature at which the cooling rate of the liquid slows down to 2°C/s and the temperature recorded 16 s later;
- $t_{f,Th\text{-}Al}$ is the time difference between the moment corresponding to the minimum in temperature and the time at which that temperature is again reached after recalescence. In absence of recalescence, $t_{f,Th\text{-}Al}$ is the time during which temperature remains constant.

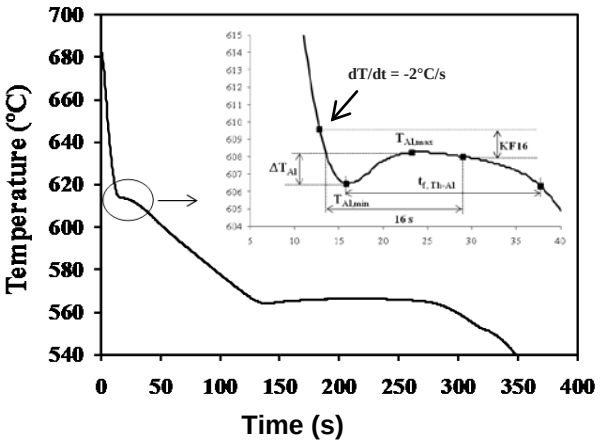

Figure 1. Example of cooling curve with definition of characteristic parameters for primary (Al) growth shown in the enlarged view of the insert.

In their early works, Apelian et al.[12] and Charbonnier[20] avoided the use of the liquidus undercooling because it needs a very accurate temperature record that cannot be ascertained with usual on-floor facilities. These authors preferred to use the amplitude of recalescence ΔT_{Al}. Some of the parameters mentioned above have been compared by Bekaert and Wettinck[4] using statistical analysis. These authors concluded that a third-order polynomial expression of one single parameter does have the same capabilities than more complex equations using several parameters. Following the same line, the parameters selected for statistical analysis in this study were:

- The amplitude of recalescence ΔT_{Al} when present.
- The time parameter $t_{f,Th\text{-}Al}$.
- The KF16 parameter.

All the thermal cups were cut and prepared for metallographic observation at their centre, i.e. close to the thermocouple junction. Grains were revealed by optical microscopy under polarized light after electrolytic Barker etching of the samples. The grain size GS was then determined by the linear intercept method. Fifty grains were measured for each cup from which the average GS value was evaluated.

RESULTS AND DISCUSSION

The effect of grain refinement on the microstructure of standard thermal cups is illustrated in figure 2 where the grain size changes from 0.39 to 1.3 mm in the standard sand cup depending on the nucleation potential of the melt.

Figure 3 shows the cooling curves recorded with the thermal analysis cups for the test samples selected in figure 2, and Table 1 lists the thermal analysis parameters. For the sample with coarsest grains of 1.3 mm, a marked recalescence is observed associated with the very low number of nuclei. All the three thermal analysis parameters ΔT_{Al}, KF16 and $t_{f,Th\text{-}Al}$ are high. In the medium refined melt, the recalescence peak is noticeable, though recalescence is limited to 0.2 ºC. Finally, for the finest grain size at 0.39 mm in the cup, no recalescence is observed in the solidification curve and $t_{f,Th\text{-}Al}$ is only 1 s.

Figure 3 illustrates also that absolute temperature or liquidus undercooling could not be used as relevant parameters. As a matter of fact, it is seen that solidification starts in the case of the best refined alloy at a lower temperature than for the medium refined alloy, and this is attributed to the composition difference between these alloys, particularly in silicon.

Table 1: Grain size and thermal analysis parameters for the cooling curves shown in Figure 3.

GS (mm)	ΔT_{Al} (ºC)	KF16 (ºC)	$t_{f,Th\text{-}Al}$ (s)
1.3 ± 0.2	1.8	1.7	15.2
0.75 ± 0.1	0.2	4.4	6.5
0.39 ± 0.06	0	5.5	1

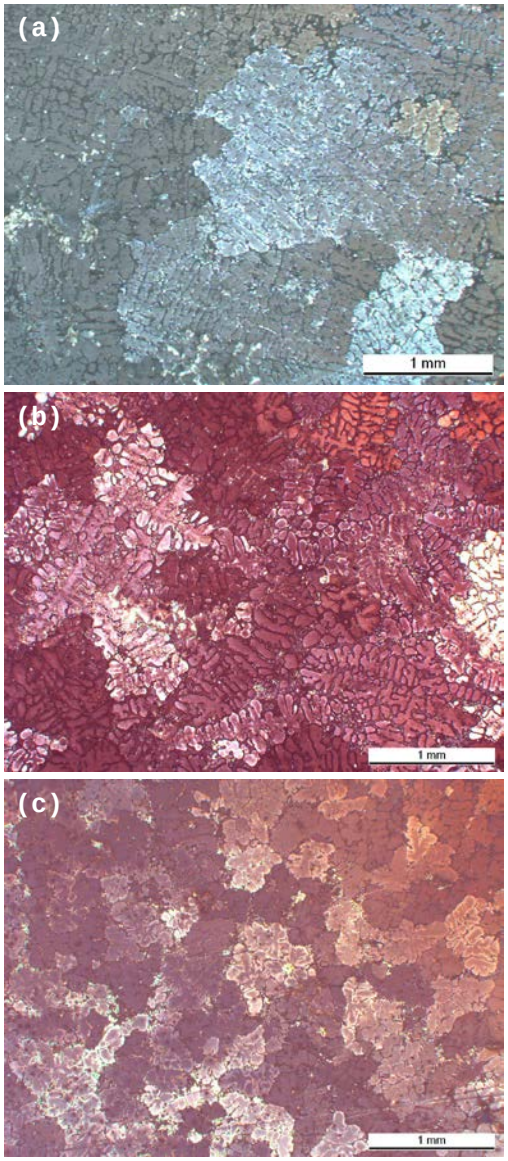

Figure 2. Micrographs illustrating the range of grain size observed in thermal cups: (a) GS = 1.3 mm, (b) GS = 0.75 mm; and (c) GS = 0.39 mm.

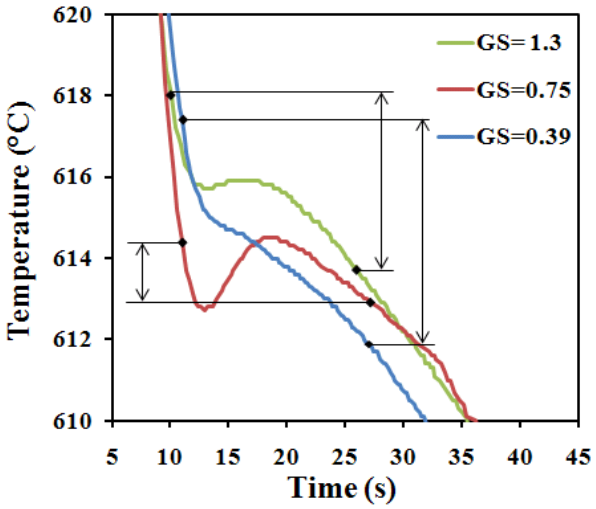

Figure 3. AlSi7Mg alloy cooling curves for the different grain size refinements of Figure 2. The curves are labeled with the corresponding grain size. KF16 is indicated on each curve.

Figures 4-6 show the GS values as function of the three thermal analysis parameters, differentiating between B and Ti-B refined alloys. In these graphs, the industrial trials and those carried out at the pilot plant are also distinguished. It is noticeable that highly similar tendencies are observed for the different refiner additions and also for the industrial trials versus pilot plant results. Comparing the three graphs, it is seen that ΔT_{Al} and KF16 parameters show high scatter in comparison with $t_{f,Th\text{-}Al}$.

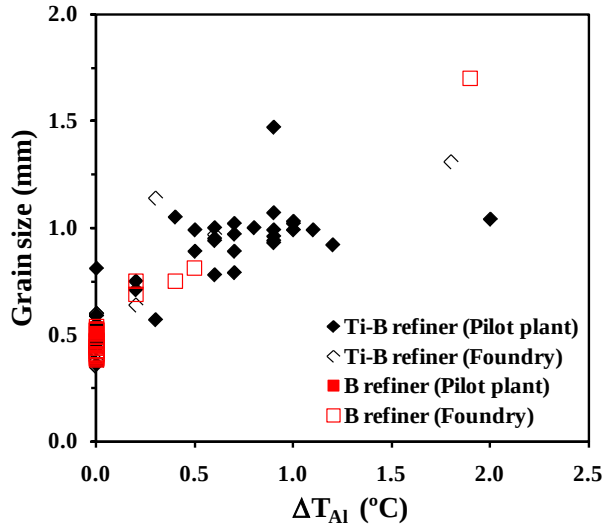

Figure 4. Relationship between grain size and recalescence.

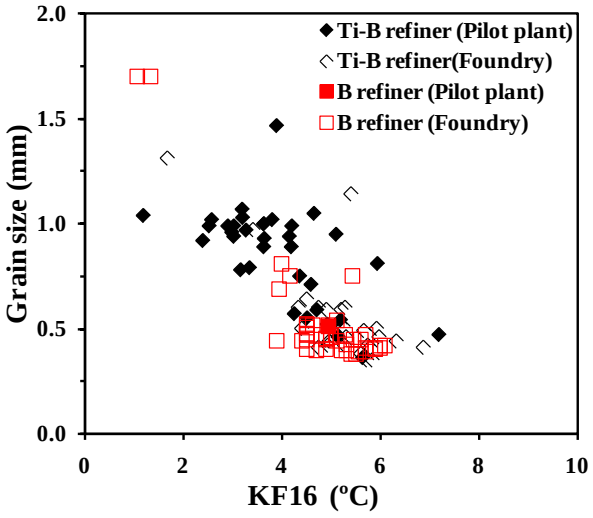

Figure 5. Relation between grain size and KF16 parameter.

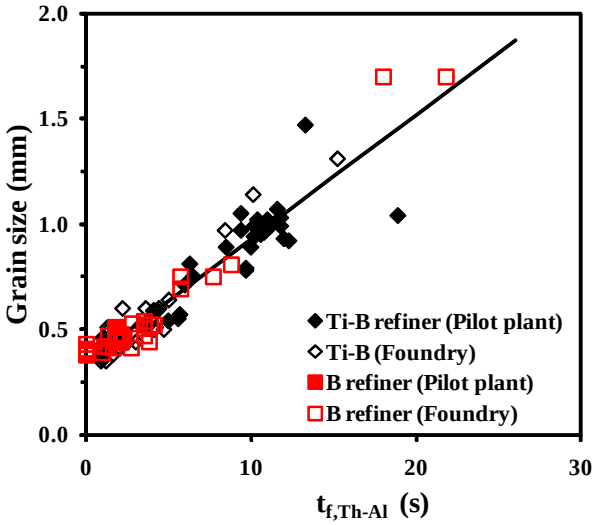

Figure 6. Relation between grain size and $t_{f,Th-Al}$ parameter.

Further, the strong correlation between either ΔT_{Al} and KF16 parameters and $t_{f,Th-Al}$ is illustrated in figure 7 and figure 8, respectively. The highest is the value of $t_{f,Th-Al}$ the lowest is the KF16 parameter; the highest is the value of $t_{f,Th-Al}$ the highest is ΔT_{Al}.

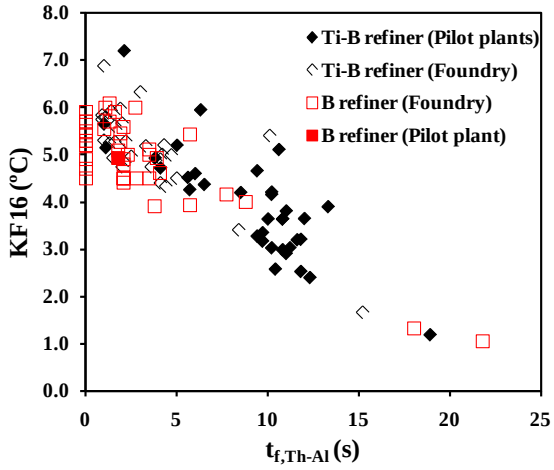

Figure 7. Relation between KF16 and $t_{f,Th-Al}$ parameter.

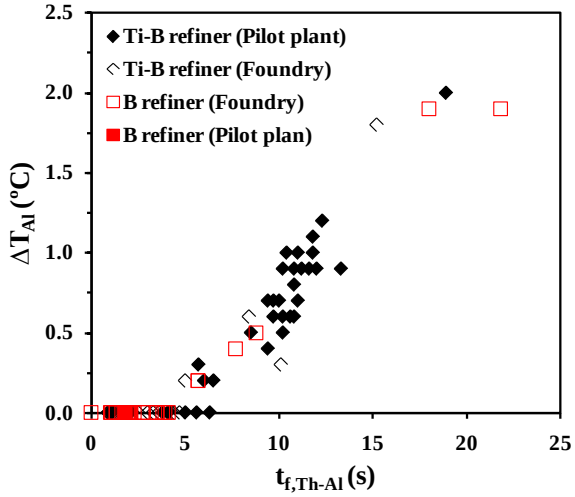

Figure 8. Relation between recalescence and $t_{f,Th-Al}$ parameter.

A linear statistical analysis was performed that showed $t_{f,Th-Al}$ was the only relevant parameter. GS data could then be expressed as indicated by Eq. (1):

$$GS = 0.0589 \cdot t_{f,Th-Al} + 0.344 \qquad \text{Equation 1}$$

The correlation coefficient R^2 is quite high at 0.91. Figure 9 compares predicted values versus measured ones, and it is seen that the scattering is quite small except for large grain sizes.

However, looking closer to the so-called residues, i.e. the difference between predicted and experimental values, it appeared that they present a wavy behaviour as the grain

size increases: at very low grain sizes (GS < 0.5 mm) measured values tend to be higher than predicted ones, then the difference decreases (0.5 < GS < 0.7 mm) and finally increases again for intermediate values (GS > 0.7 mm). To account for this, attempts to improve the statistical description of GS by looking at interaction between the three selected parameters failed. It was finally realized that $t_{f,Th\text{-}Al}$ could be used as output variables, using GS, ΔT_{Al} and KF16 as variables. The Eq. (2) was finally found in which the statistical relevance of each coefficient was very high. KF16 was not found to be statistically significant whilst the correlation coefficient R^2 was increased to 0.96.

$$t_{f,Th\text{-}Al} = -11.39 + 4.78 \cdot \Delta T + 43.73 \cdot GS - 35.64 \cdot GS^2 + 10.35 \cdot GS^3 \quad \text{Equation 2}$$

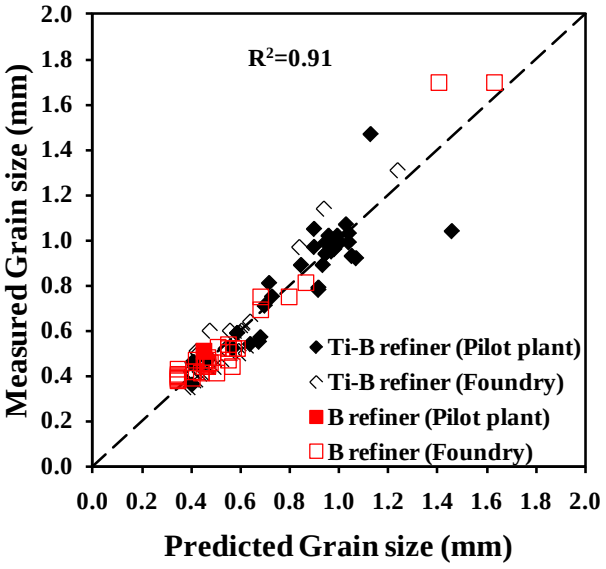

Figure 9. Plot of predicted versus measured GS values using Eq. (1). The interrupted line is the bisector.

Figure 10 compares predicted and experimental values of $t_{f,Th\text{-}Al}$. It is seen that the prediction is highly satisfactory for both short and large values of $t_{f,Th\text{-}Al}$, and accordingly for both low and high values of GS. Introduction of recalescence compensates for the biases at high values while the power terms in GS account for the wavy behaviour mentioned above. It is clearly seen that the residues are now uniformly dispatched on both side of the bisector.

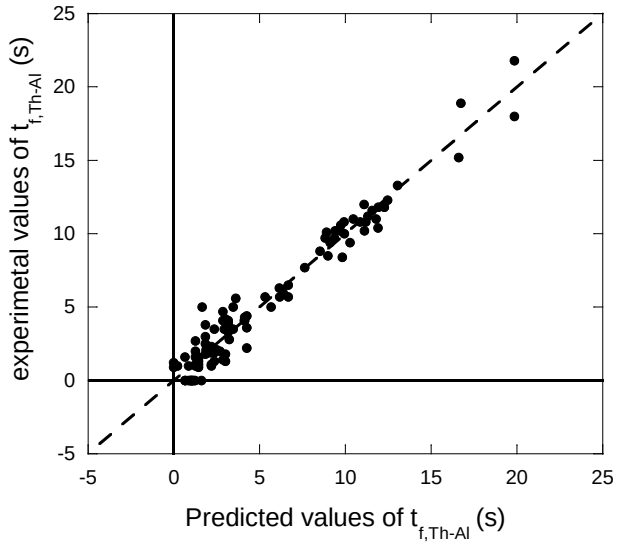

Figure 10. Plot of predicted versus measured $t_{f,Th\text{-}Al}$ values using Eq. (2). The interrupted line is the bisector.

The polynomial in GS is increasing monotonously from GS equal to zero so that it will be easy to use (Eq. 2) to determine GS from the values of $t_{f,Th\text{-}Al}$ and ΔT_{Al} read on the TA cooling curve.

CONCLUSIONS

The effect of B and Ti-B refiner addition on grain size and thermal analysis parameters of standard sand cup has been studied. 110 tests samples of AlSi7Mg alloys cast in five different foundries and in a pilot plant have been considered in this study. The most important conclusions are:

- no recalescence is observed in the cooling curve of standard sand cups when the nucleation potential is very high, meaning that recalescence is not a useful parameter in the range of very fine grains.
- $t_{f,Th\text{-}Al}$, defined as the recalescence time or the time during which temperature remains constant when there is no recalescence, is a good parameter when the nucleation potential of the melt is high.

Two equations that predict grain size as a function of thermal analysis parameters have been assessed which are both highly satisfactory, and in particular show excellent capability for predicting small and medium grain sizes.

ACKNOWLEDGMENTS

Acknowledgments are due to the Basque government for its financial support (Project ProFUTURE-II, Etorkek 2011).

REFERENCES

1. ASM Int., "ASM Metals HandBook Vol. 15, Castings", 9th Ed., Materials Park, Ohio, USA, (1992).
2. Gilbert Kaufman, J., Rooy, E.L., "Aluminum alloy castings: Properties, Processes and Applications", AFS, ASM Int., Materials Park, Ohio, USA, (2005).
3. Gruzleski, J.E., Closset, B.M. "The treatment of liquid aluminum-silicon alloys", The American Foundrymen`s Society Inc., Des Plaines, Illinois, USA, (1990).
4. Bekaert, F., and Wettinck, E., *Aluminium 72*, pp. 442-47 (1996).
5. Sigworth, G.K., Kuhn, T.A., *International Journal of Metalcasting*, pp. 31-40 (Fall 2007).
6. Spittle, J.A. *IJCMR* 19, pp. 210-22, (2006).
7. Spittle, J.A. *FTJ*, pp. 308-314 (2008).
8. Menk, W., Speidel, M., Döpp, R., *Giesserei*, vol. 79 p. 125, (1992).
9. MacKay, R.I., Djurdjevic, J.H., Sokolowski, J.H., Evans, W.J., *AFS Transaction*, vol. 108 p. 511, (2000).
10. Jiang, J., Sokolowski, J.H., Djurdjevic, M.B., Evans, W.J., *AFS Transaction*, vol. 108, p. 505 (2000).
11. Heusler, L., *Giesserei*, vol. 82 p. 66 (1997).
12. Apelian, A., Sigworth, G.K., Whaler, K.R., *AFS Transaction*, vol. 92 p. 297 (1984).
13. Günther, B., Jürgens, H., *Giesserei*, vol. 71 p. 928 (1984).
14. Ibarra, D.G., "Control of grain refinement of Al-Si-alloys by thermal analysis", PhD thesis, McGill University of Montreal, Canada, (1999).
15. Niklas, A., Abaunza, U., Fernández-Calvo, A.I., Lacaze, J., Suárez, R., China Foundry, vol. 8 (1), pp. 89-95 (2011).
16. Argyropoulos, S., Closset, B., Gruzleski, J.E., Oger, H., *AFS Transaction*, vol. 91, p. 350 (1983).
17. Niklas, A., Abaunza, U., Fernández-Calvo, A.I., Lacaze, J., *3rd Int. Conf. on Advances in Solidification Processes*, *IOP Conf. Series*, Mater. Sci. and Eng. 27 012003, (2011).
18. Lizarralde, I., Niklas, A., Fernández-Calvo, A.I., Lacaze, J., *Light Metals*, pp. 327-331, (2013).
19. Lizarralde, I., Eguskiza, S., Santos, F., Niklas, A., Fernández-Calvo, A.I., 71st WFC 2014.
20. Charbonnier, J., *AFS Transaction*, Vol. 92 pp. 907-22 (1984).
21. Gädke, A.F., Eigenfeld, W., Klos, R.K., Koch H, Knoche, D., Lang, H., *Giesserei*, vol. 93 pp. 18-25 (2006).
22. Gowri, S., *AFS Transaction*, vol. 102 pp. 503-08 (1994).
23. Emadi, D., Whiting, L.V., *AFS Transaction*, vol. 110 pp. 285-296 (2002)

Résumé en Français

Effet de la vitesse de refroidissement sur la taille de grain, la modification eutectique et la précipitation de phases riches en fer dans des alliages Al-Si hypoeutectiques.

Résumé

Les alliages aluminium-silicium sont les alliages d'aluminium les plus courants en moulage du fait de leur fluidité et de leurs propriétés mécaniques raisonnables associées à une faible densité. Les propriétés mécaniques des alliages hypo-eutectiques peuvent être améliorées par affinage du grain et modification morphologique des précipités de silicium eutectique. Cependant, le problème majeur est associé à l'apparition fréquente de phases intermétalliques riches en fer, qui abaissent la résistance à la traction et la ductilité, dont la phase beta $Al_9Fe_2Si_2$ qui se présente habituellement sous forme de plaquettes fines. Diverses méthodes pour atténuer les effets néfastes de la phase beta ont été proposées, et des efforts ont été faits pour comprendre le mécanisme de sa croissance.

L'objectif de cette étude est d'établir la relation entre la vitesse de refroidissement et les caractéristiques microstructurales d'alliages Al-Si hypo-eutectiques. Dans les pièces coulées, la vitesse de refroidissement locale est un facteur qu'il n'est pas facile à prédire parce que lié à la géométrie des pièces tout autant qu'au procédé de coulée. Les variations de vitesse de refroidissement affectent le processus de solidification, ce qui est rendu évident par les changements des températures caractéristiques des courbes de refroidissement enregistrées en différents endroits d'une pièce instrumentée. Les relations entre les caractéristiques des courbes de refroidissement, d'une part, et la taille des grains et la modification du silicium eutectique, d'autre part, sont présentées dans le cas d'alliages industriels. Ces relations sont aussi explicitées sous forme de corrélations statistiques.

Cette étude comprend également des résultats sur l'effet de la vitesse de refroidissement sur la morphologie de phase beta dans le cas d'un alliage ternaire Al-Fe-Si hypo-eutectique. L'étude de la croissance de la phase beta a été réalisée par analyse thermique différentielle et tomographie post-mortem des échantillons, complétée par un essai de tomographie in situ. Les essais d'analyse thermique différentielle ont permis d'observer qu'à très faible vitesse de refroidissement la phase beta peut adopter une forme en écriture chinoise qui se substitue, au moins partiellement, à la forme en plaquette.

Enfin, aux vitesses de refroidissement les plus élevées atteintes en analyse thermique différentielle, des structures dites en rosettes ont été observées et analysées. Ces structures désignent une microstructure eutectique multi-phasée extrêmement fine qui est observée dans des zones arrondies et convexes de petites tailles (quelques microns) et correspondent à la structure de solidification de poches de liquide qui ont été isolées à l'intérieur des dendrites durant le dépôt primaire. L'observation de ces rosettes a permis de mettre en évidence deux résultats particulièrement intéressants : 1) la germination de phases métastables est rendue possible du fait des surfusions atteintes dans ces poches ; 2) la présence d'un précipité de phase beta en contact avec une rosette n'apparaît pas avoir stimulé la germination du silicium eutectique, contrairement à ce qui a pu être reporté dans la littérature.

1. Introduction

Les alliages d'aluminium sont largement employés pour des applications allant de l'aéronautique, les façades d'immeubles, les pièces automobiles. Pour ce qui concerne les composants pour l'automobile, la plupart sont obtenus par coulée du fait que cette méthode

permet de grandes variations de formes et de tailles, et est bien adaptée à la production en grandes séries. La quantité moyenne d'aluminium par voiture a ainsi augmenté de 50 Kg en 1990 à 132 Kg en 2005 [1]. Malheureusement, la consommation d'énergie pour produire l'aluminium est l'une des plus élevée parmi tous les procédés d'extraction : la consommation électrique moyenne d'une installation de production d'aluminium varie de 13 à 16 KWh/kg [2]. Dans le cas du recyclage, la consommation n'est que de 2,8 KWh/kg, soit 18% de l'énergie consommée pour la fabrication d'aluminium primaire [3]. Cette différence rend le recyclage particulièrement intéressant sinon nécessaire.

En général, les alliages de silicium et d'aluminium peuvent être classés en trois groupes en fonction de leur teneur en silicium, ce sont les alliages hypo-eutectiques, eutectiques et hyper-eutectiques. En tant qu'élément principal, le silicium augmente la fluidité et réduit le retrait de solidification. D'autres éléments peuvent être ajoutés intentionnellement comme le cuivre, le magnésium ou le manganèse pour améliorer les propriétés mécaniques des alliages, alors que d'autres peuvent être présents en tant que traces ou impuretés. Enfin, l'addition à faible taux de strontium ou de sodium permet de modifier le silicium de l'eutectique, et donc d'améliorer la ductilité et la résistance mécanique.

L'addition d'affinant du grain augmente le nombre de sites de germination de la phase primaire (Al), favorisant ainsi la croissance équiaxe plutôt que colonnaire. Plusieurs modèles ont été proposés pour décrire cette étape de germination et d'affinement des grains. Le modèle de Maxwell et Hellawell [4] suppose que les grains apparaissent de manière similaire dans tout le liquide à température homogène, et que la germination cesse quand il y a recalescence, tous les sites effectifs ayant été consommés. Greer et coll. [5] ont proposé un modèle tenant compte de la distribution en taille des particules servant à la germination. D'après Lee et coll. [6], l'efficacité de l'affinage dépend de la teneur en silicium, elle est meilleure pour des teneurs inférieures à une valeur critique déterminée par le facteur de restriction de croissance (teneur en silicium critique d'environ 3 % dans un alliage non raffiné), alors que la taille de grain reste la même quel que soit le montant d'affinant ajouté à l'alliage au-delà de cette valeur critique.

L'eutectique (Al)-Si est un eutectique irrégulier dont la phase Si est facettée, sous forme de lamelles relativement grossières. La modification de l'eutectique transforme ces lamelles en une structure fibreuse beaucoup plus fine. Cette modification peut être réalisée par l'addition d'éléments modificateurs [7-10] ou générée par refroidissement rapide [11]. Différentes théories ont été proposées pour expliquer le mécanisme de modification, dont la croissance à partir de l'angle ré-entrant entre deux macles (twin plane re-entrant edge, TPRE) [12] et le maclage induit par des impuretés (impurity induced twinning, IIT) [13]. Une autre approche a été proposée par Yilmaz et coll. [14] qui suggèrent que la modification du silicium est due au blocage des sites de croissance plutôt que par l'empêchement de la germination, en accord avec des travaux anciens de Kobayashi and Hogan [15].

Au recyclage est associée une perte de la qualité du métal du fait de l'accumulation des impuretés, éléments d'alliage et de traitement (affinage, modification). L'un des éléments mineurs les plus couramment trouvés dans les alliages commerciaux d'aluminium est le fer qui a une très faible solubilité dans la solution solide (Al), de l'ordre de 0.052% mass. à 660°C [16] et qui diminue avec la température. Des traces de fer conduisent ainsi facilement à l'apparition d'intermétalliques lors de la solidification, qui sont alors associés avec une diminution des propriétés mécaniques. D'après le diagramme de phases Al-Fe-Si, les intermétalliques qui peuvent apparaître en équilibre avec le liquide et (Al) sont les phases Θ-$Al_{13}Fe_4$ (phase theta), α-Al_8Fe_2Si (phase alpha) et β-$Al_9Fe_2Si_2$ (phase beta). Ces deux dernières phases sont celles qui sont observées dans les alliages Al-Si de fonderie du fait de leur teneur en silicium.

Généralement, l'identification des intermétalliques est basée sur leur composition chimique et leur morphologie. Les phases α-Al_8Fe_2Si et β-$Al_9Fe_2Si_2$ peuvent être différenciées l'une de l'autre par le rapport Fe/Si qui est supérieur à 3 pour la première et de l'ordre de 1,8 à 2 pour la seconde. Cependant, Kral [17,18] insiste sur le fait que l'identification des nombreux intermétalliques pouvant être présents dans les alliages d'aluminium ne peut pas être uniquement basée sur l'analyse chimique ou des observations morphologiques.

L'influence de la vitesse de refroidissement sur la croissance de la phase beta a été décrite par Khalifa et coll. [19]. D'après ces auteurs, la fraction de phase beta augmente quand la vitesse de refroidissement diminue, donnant de très grands précipités. Ils notent aussi que l'intervalle de solidification augmente quand la vitesse de refroidissement diminue du fait de l'apparition d'un eutectique à trois phases dans lequel intervient la phase beta. Narayanan et coll. [20] ont observé que la température de début de précipitation de la phase beta décroit quand la vitesse de refroidissement augmente.

La phase beta est connue pour avoir un effet préjudiciable par rapport aux autres phases intermétalliques riches en fer. Des études menées par Gowri et coll. [21] ont montré que cette phase réduit la fluidité du métal liquide sans abaisser la tension superficielle. Des travaux de Elsebaei et coll. [22] ont révélé que les précipités de phase de bêta agissent comme amorce de fissuration et fournissent un chemin de propagation de la fissure lors de tests d'impact. De nombreuses recherches ont également montré que cet effet néfaste peut être attribué à la morphologie de la phase de beta [23-26]. En raison de la nocivité de cette phase bêta, plusieurs méthodes ont été développées pour minimiser sa présence, comme les méthodes physiques avec effet gravitationnel [27-31] et la surchauffe du métal liquide au-dessus de la température de liquidus [32 ,33]. Cependant, la méthode la plus couramment employée pour réduire les effets nocifs de la phase bêta consiste en l'ajout de faibles quantités d'éléments d'alliage. En effet, plusieurs éléments permettent d'éliminer la précipitation de la phase beta qui est remplacée par une phase en écriture chinoise, plus compacte et donc moins préjudiciable pour les propriétés mécaniques [34-38].

L'objectif principal de cette étude est d'établir la relation entre la vitesse de refroidissement et les caractéristiques de la microstructure des alliages Al-Si. Un intérêt particulier a donc été porté dans le cadre de ce travail à l'effet de la vitesse de refroidissement sur la taille des grains et la modification du silicium, et ce en lien avec les températures caractéristiques lues sur les enregistrements thermiques en cours de solidification. Cette étude comprend également la caractérisation de l'effet de la vitesse de refroidissement sur la morphologie de la phase beta et sur les mécanismes qui contrôlent sa croissance, qui sont encore largement inconnus. Enfin quelques écarts aux chemins de solidification attendus ont été observés qui seront discutés.

2. Matériaux et méthodes expérimentales

Les alliages d'aluminium employés dans cette étude sont un alliage commercial et un alliage synthétique. L'alliage A356 commercial a été fourni par Azterlan (Durango, Espagne), alors que l'alliage synthétique Al-6.5Si-1FE a été préparé par Hydro Aluminium Deutschland GmbH à partir de métaux de haute pureté et extrudé à chaud en tiges de 10 mm de diamètre.

La prédiction de la taille des grains à partir des caractéristiques de la courbe de refroidissement obtenue par analyse thermique est habituellement reliée à la surfusion et la recalescence pendant la germination, l'absence de recalescence indiquant une germination efficace associée à des grains de petite taille [39]. L'analyse thermique peut également être utilisée pour prédire le niveau de modification de l'alliage par l'analyse des courbes de refroidissement et en particulier de l'abaissement de la température eutectique.

L’analyse des courbes de refroidissement a été réalisée pour une série d'alliages d'A356 en utilisant le système Thermolan-Al. La procédure expérimentale consistait à couler le métal dans des moules en sable et métalliques contenant des cavités cylindriques de différents modules (rapport surface/volume). Ces cavités étaient telles que leur diamètre Ø est égal à leur hauteur h. Les paramètres caractéristiques obtenus à partir des courbes de refroidissement ont été extraits selon la nomenclature décrite en figure 1.

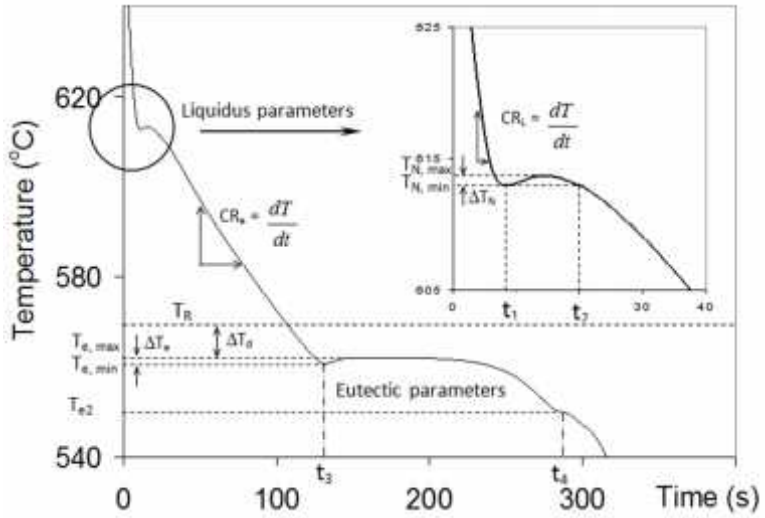

Figure 1. Paramètres sélectionnés pour caractériser les courbes de refroidissement durant la formation des grains primaires d’(Al) et de l’eutectique (Al)-Si.
L’insert est un zoom autour du liquidus.

Quelques enregistrements n’ont pas pu être exploités du fait de la rupture du thermocouple. Par ailleurs, les fortes vitesses de refroidissement correspondant aux plus petits modules ne permettaient pas toujours d’enregistrer convenablement le début des courbes. Pour vérifier la qualité des enregistrements, quelques paramètres caractéristiques du processus complet de solidification ont été sélectionnés. A partir de cette analyse, tous les essais dont la température initiale était inférieure à 620°C ont été éliminés.

L’analyse thermique différentielle (ATD, appareil SETSYS de Setaram) a été employée pour caractériser les transformations de phases des alliages au chauffage et au refroidissement, et relier changement morphologiques et vitesses de refroidissement. Sur les thermogrammes, les températures caractéristiques de transformation sont relevées : au refroidissement les températures de début de transformation et de pic ont été considérées, alors qu’au chauffage seules les températures de pic ont été employées. Les échantillons d’ATD ont ensuite été préparés pour observations métallographiques standards sur section polie par microscopie optique et électronique à balayage (MEB). Dans quelques cas, des attaques profondes (solution de HCl 10% dans de l’alcool, 30 à 40 minutes) ont été réalisées pour dissoudre la matrice (Al).

Dans ce travail, deux types de tomographie X ont été employés, post-mortem et in-situ, afin de caractériser la phase beta. La tomographie post-mortem a été réalisée avec un appareil GE Phoenix Nanotom équipé d’un tube alimenté à 180 kV et fournissant 15 W. Le faisceau monochromatique émis permet d’acquérir 1440 images lors de la rotation de l’échantillon de 360° autour de son axe vertical. Pour les conditions employées, la taille du voxel est de 2,5 µm. Les images sont ensuite empilées afin de reconstruire le volume à l’aide des logiciels Datos X (GE Sensing and Inspection GmbH) et VG Studio Max (Volume Graphic GmbH, Germany). Les essais in-situ ont été réalisés à l’European Synchrotron Radiation Facility (ESRF) sur la ligne ID-19 équipée d’un four mis au point au SiMaP,

Grenoble. L'échantillon consistait en un cylindre de 1 mm de diamètre et de 3 mm de hauteur, percé par le bas d'un trou de 0,55 mm de diamètre destiné à insérer un thermocouple. Un faisceau blanc de 17,6 KeV a été employé qui a permis l'acquisition de 700 projections avec un pas de temps de 0,75 s, soit au total 36 tomographies complètes (180°) pour une taille de voxel de 1,1 µm, et une vitesse de refroidissement de 10°C/min.

Les analyses d'images ont été réalisées à l'aide des logiciels ImageJ (National Institute of Health –USA) et Aphelion™ Dev software (ADCIS, France). Ces logiciels ont été employés pour traiter aussi bien les images de MEB que les images de tomographie de la phase beta. Des séries d'opérations telles que le filtrage médian et le seuillage ont été employées pour séparer la phase beta de la matrice (Al). La fraction de phase beta et les caractéristiques de taille de ses précipités ont ensuite été estimées à partir des images binarisées. Ces logiciels ont aussi été employés pour faire les reconstructions 3D à partir des images de tomographie et calculer les caractéristiques en volume de la phase beta.

3. Resultats et Discussion

3.1. Effet de la vitesse de refroidissement sur la taille des grains et la modification eutectique.

La figure 2 présente la microstructure à l'état brut de coulée en moules en sable et métalliques, et pour deux modules thermiques. La microstructure fait apparaître essentiellement une matrice (Al) et de larges plages d'eutectique (Al)-Si, mais aussi d'autres phases : la phase π ($Al_8FeMg_3Si_6$) qui a une forme en écriture chinoise, Mg_2Si qui apparaît sous la forme de précipités noirs localisés près des précipités de silicium, et enfin la phase beta (β-$Al_9Fe_2Si_2$).

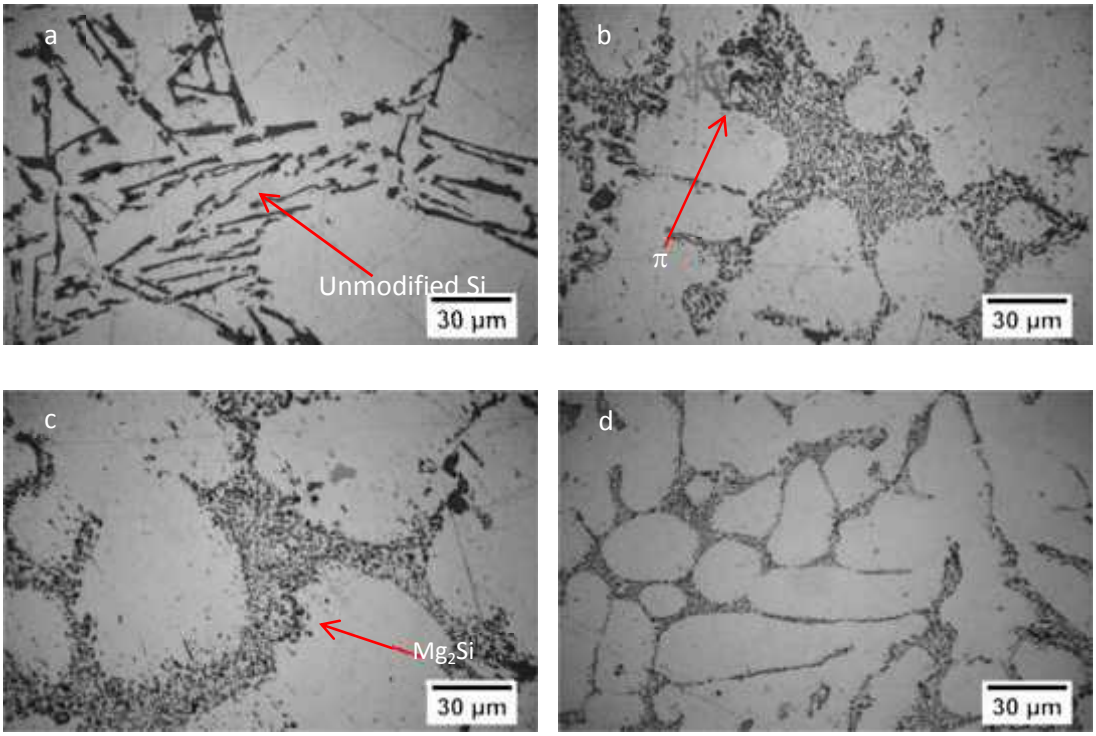

Figure 2. Microstructure de l'alliage A356 coulé en sable (a, c) et en moule métallique (b et d) pour les modules thermiques extrêmes, maximum (a et b) et minimum (c et d).

L'effet de la vitesse de refroidissement sur la taille des grains et la modification eutectique de silicium a été étudié pour l'alliage industriel A356 à partir des enregistrements

de la température en fonction du temps. La figure 3 présente des enregistrements typiques obtenus pour les coulées en sable et en moule métallique. Les courbes les plus extrêmes à droite et à gauche représentent respectivement les cylindres de plus grand et plus petit module, tandis que la courbe en pointillés correspond à l'enregistrement effectué sur un creuset d'analyse thermique standard utilisé industriellement pour le contrôle du métal avant coulée.

On note que l'intervalle de solidification augmente avec la vitesse de refroidissement, ce qui est bien visible si l'on considère la différence de température entre l'arrêt correspondant au liquidus et la réaction eutectique (Al)-Si (palier variant entre 550 et 570°C). En dehors des accidents thermiques associés à ces deux transformations, on note la présence d'un troisième accident thermique à plus basse température sur les courbes des trois plus gros modules du moulage en sable, ainsi que sur la courbe correspondant à l'enregistrement en creuset d'analyse thermique (courbe en pointillé). Cet accident correspond à des eutectiques terminaux où apparaissent les phases Mg_2Si et π. La température de ces réactions diminue avec la vitesse de refroidissement, et la surfusion correspondante doit être due à l'étape de germination de ces phases minoritaires, mais pourrait aussi être affectée par la sensibilité des thermocouples.

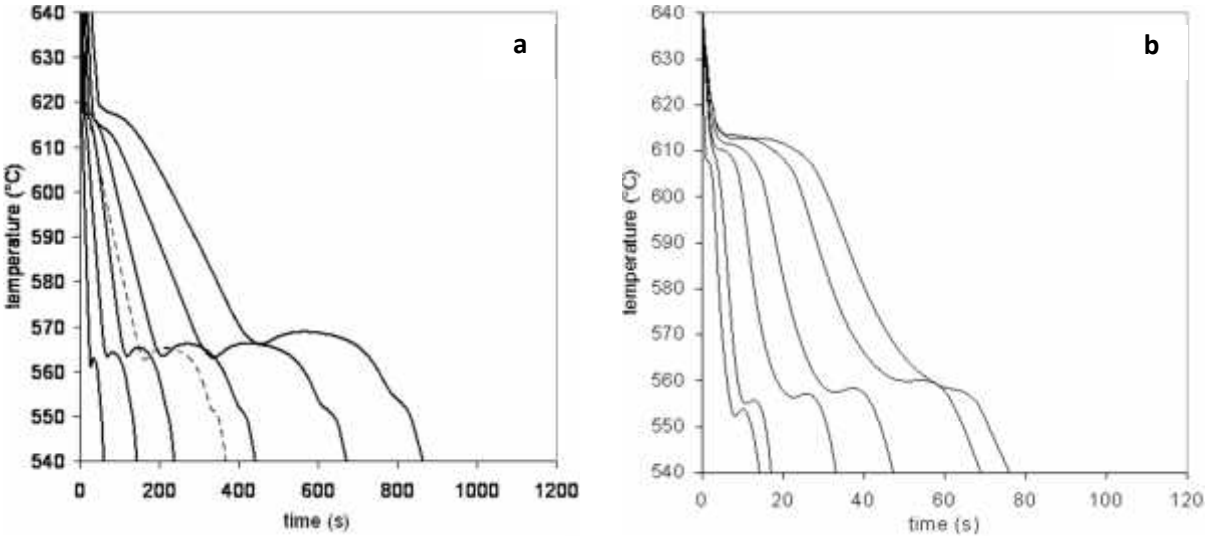

Figure 3. Exemple de séries d'enregistrements thermiques réalisés lors de la coulée en moule en sable (a) et métallique (b). La courbe en pointillé correspond à la courbe de refroidissement du creuset d'analyse thermique standard utilisé industriellement pour le contrôle de la préparation du métal liquide.

Il est généralement admis que la recalescence lors de la germination des grains d'(Al) observée sur l'enregistrement d'analyse thermique standard – c'est-à-dire à vitesse de refroidissement donnée - peut servir pour estimer la taille finale du grain dans le creuset d'analyse thermique standard. Cependant, la corrélation obtenue entre cette recalescence et la taille des grains pour tout un ensemble de vitesses de refroidissement montre que, en l'absence de recalescence, la taille des grains peut varier de 0,2 à 0,7 mm. Ceci démontre que la recalescence seule ne peut pas être utilisée pour déterminer le degré d'affinement du grain. D'autres corrélations ont été recherchées, par exemple entre la taille des grains et le temps de recalescence ($\Delta t_N = t_2 - t_1$), quelquefois appelé temps de germination. L'augmentation de ce temps est associée à un accroissement de la taille des grains, en accord avec des études précédentes de Charbonnier [39] et Apelian et al. [40] dont les résultats concernaient des analyses thermiques standard.

Une analyse statistique a été réalisée avec comme objectif d'établir une relation entre la taille des grains et des paramètres issus des enregistrements thermiques. Le meilleur résultat obtenu permet de relier la vitesse de refroidissement eutectique (CR_e), le temps de germination (Δt_N), l'espacement entre bras dendritiques (DAS), et le produit Δt_N•DAS. Notons que le DAS peut être exprimé en fonction du temps de coalescence ($t_{coales}=t_3-t_1$) selon l'expression $DAS=11,5*t_{coales}^{0,33}$ (µm). L'expression suivante a finalement été obtenue :

$$GS = 0,614 - 0,1688 \log CR_e - 0,0046\ DAS + 0,0112(\Delta t_N * DAS)^{0,5} - 0,0012\ \Delta t_N$$

Cette expression correspond à une valeur assez faible du coefficient de régression R^2 à 0,68, ce qui indique que les variables retenues ne sont certainement pas suffisantes. Des essais complémentaires sont nécessaires pour préciser ce point ; la comparaison entre prédictions et mesures est malgré tout présentée en figure 4.

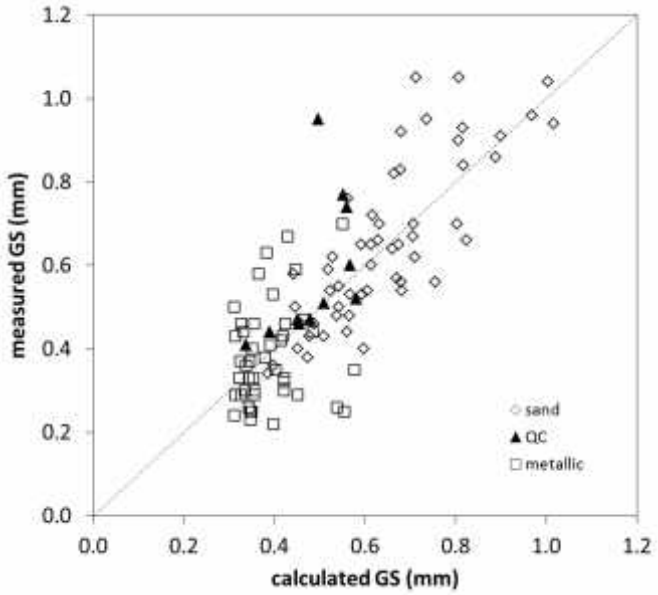

Figure 4. GS calculé vs. mesuré, la ligne en pointillés est la bissectrice.

De la même manière, une analyse statistique a été réalisée sur la modification du silicium afin d'établir une relation entre le niveau de modification atteint ML et des variables d'entrée telles que le module thermique, la vitesse de refroidissement pré-eutectique (CR_e/°C.s^{-1}), la surfusion eutectique (ΔT_d/°C), le temps de réaction eutectique ($t_{eut}= t_4-t_3$/s) et la recalescence eutectique (ΔT_e/°C). Lors d'un travail précédent [41], nous avions mis l'accent sur le rôle de la surfusion eutectique mais avions trouvé un coefficient de corrélation assez faible, inférieur à 0,8. De ce fait, cette variable a été exclue de cette seconde analyse, et l'expression suivante a finalement été obtenue :

$$ML = 3,615 + 1,5 \log CR_e + 0,0023\ t_{eut} - 0,0012\ (t_{eut} * \Delta T_e)$$

Cette expression correspond à un coefficient de corrélation R^2 de 0,83, et est illustrée en figure 5. On note une meilleure adéquation pour les résultats obtenus en moules métalliques, et une grande variabilité des résultats relatifs aux analyses thermiques standards. Ce dernier point semble indiquer qu'il a manqué à l'analyse une information sur d'autres paramètres pertinents, tel que le niveau d'ajout du strontium.

L'observation des résultats relatifs aux moules métalliques révèle que le silicium eutectique a été bien modifié. Au contraire, dans le cas de forts modules thermiques en moule

en sable, la modification du silicium n'est que partielle, en accord avec le fait connu que la modification par le strontium est moins efficace à faible vitesse de refroidissement.

Des analyses complémentaires de la température eutectique réalisées par ATD ont mis en évidence des résultats intéressants. La température de début de fusion au chauffage peut être extrapolée à 564°C pour l'alliage étudié, soit 8°C en dessous de la température calculée pour l'eutectique (Al)-Si (572°C), sachant que la température expérimentale a été augmentée de 3°C en accord avec la calibration de la cellule d'ATD précédemment réalisée [42]. Ceci montre que les éléments d'alliage ont un effet notable sur le début de fusion de l'eutectique (Al)-Si au chauffage, et donc certainement sur la fin de son dépôt au refroidissement.

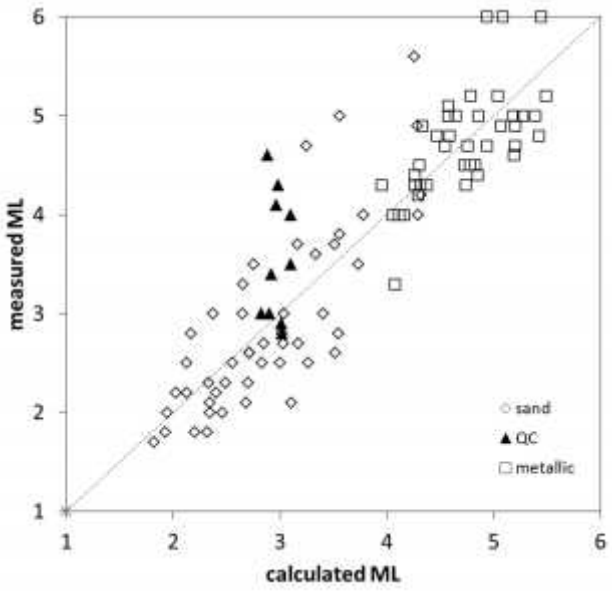

Figure 5. Corrélation entre valeurs calculées et expérimentales du niveau de modification de l'eutectique, ML. La droite en pointillés est la bissectrice.

3.2. Effet de la vitesse de refroidissement sur la précipitation de la phase beta.

La figure 6 présente la projection du liquidus dans le coin riche en aluminium du système Al-Fe-Si. Le chemin de solidification de l'alliage ternaire Al-6,5Si-1Fe étudié est illustré par les flèches. Des essais d'analyse thermique différentielle ont été réalisés pour différentes vitesses de chauffage, 0,2, 1, 2, 5, 10 and 17,5°C/min, et de refroidissement of 0,2, 1, 2, 5, 10 and 40°C/min.

Sur chaque thermogramme, les températures caractéristiques (début et pic) ont été évaluées pour chacune des réactions se produisant au chauffage ou au refroidissement.

Les échantillons d'ATD ont été préparés pour observations métallographiques qui ont permis de mettre en évidence des dendrites de (Al), des précipités de phase beta et de silicium. Les micrographies de la figure 7 illustrent l'effet de la vitesse de refroidissement sur la morphologie de la phase beta. Dans le cas de l'échantillon refroidi à 0,2°C/min, la phase beta apparaît en 2-D sous forme d'aiguilles longues et relativement épaisses, qui sont beaucoup plus fines dans le cas d'un refroidissement à 40°C/min.

La teneur moyenne en phase beta varie entre 2,4 and 2,9% vol. pour les différentes vitesses de refroidissement, avec les valeurs les plus élevées correspondant aux vitesses de refroidissement les plus lentes. La longueur des précipités de phase beta a été estimée dans les mêmes zones que celles employées pour mesurer la fraction volumique, à l'aide du diamètre de Féret maximum. Seules les 5 plus grandes valeurs ont été retenues afin d'amplifier les

différences entre les échantillons, c'est-à-dire selon la vitesse de refroidissement. La taille des précipités de phase beta décroît ainsi de 1017 µm à 264 µm quand la vitesse de refroidissement change de 0,2°C/min à 40°C/min.

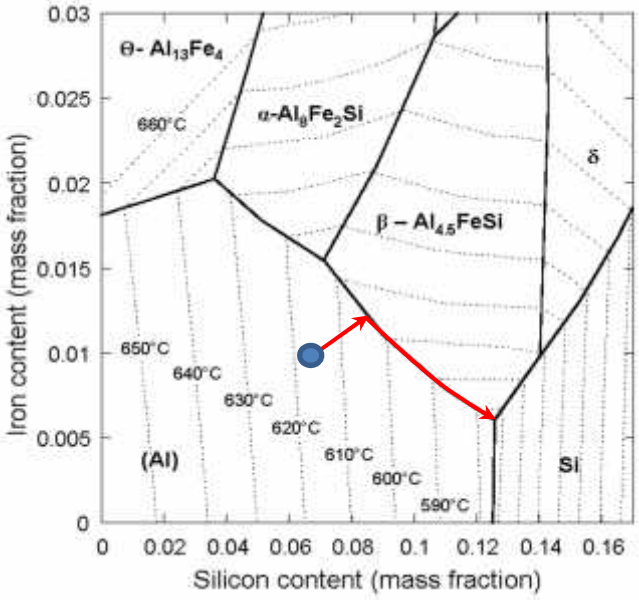

Figure 6. Projection du liquidus du coin riche en aluminium du système ternaire Al-Fe-Si.

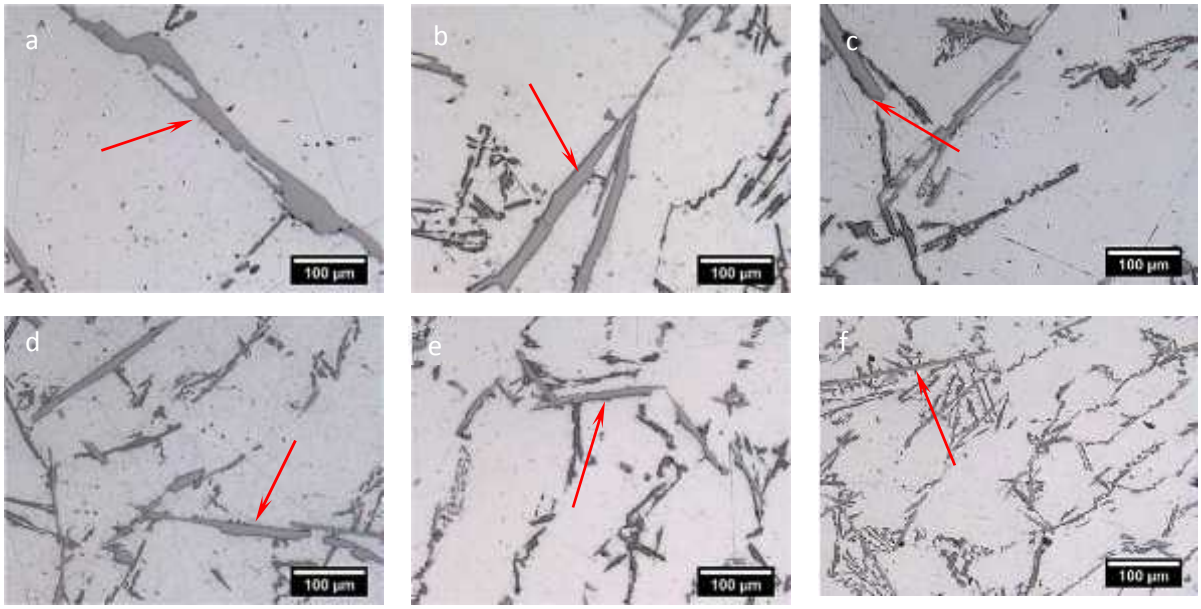

Figure 7. Micrographies des échantillons d'ATD refroidis à différentes vitesses : (a) 0,2°C/min, (b) 1°C/min, (c) 2°C/min, (d) 5°C/min, (e) 10°C/min et (f) 40°C/min. Les flèches pointent sur des précipités de phase beta, tandis que les précipités légèrement plus sombres sont du silicium.

Les observations en tomographie post-mortem ont été réalisées sur tous les échantillons d'ATD à l'exception de celui refroidi le plus vite du fait de la limitation en résolution spatiale de l'appareil. L'évaluation de la fraction volumique de phase beta a été faite en divisant le volume en 8 secteurs de 100 voxels d'épaisseur (direction Z) chacun. Aux vitesses les plus faibles, la phase beta apparaît comme de larges plaquettes, et dans tous les échantillons il a été observé que, quand le développement de ces plaquettes est bloqué par une dendrite d'(Al), elles la contournent. La jonction de plaquettes entre elles de même que le branchement des plaquettes ont pu être facilement observés sur les grandes plaquettes. Enfin, les observations montrent que la croissance des plaquettes de phase beta se fait essentiellement latéralement, en accord avec les résultats de Dinnis et coll. [43].

La figure 8 représente la fraction volumique de phase beta et l'aire surfacique par plaquette de phase beta estimées à partir des images 3-D. La fraction volumique est semblable pour les vitesses de refroidissement de 0,2°C/min et de 1°C/min, elle augmente pour la vitesse de refroidissement de 10°C/min. Ceci est certainement lié à la réduction de la qualité de l'image tomographique qui provoque l'apparition de plaques de phase beta plus grandes que leur taille réelle. L'évaluation de l'aire de la surface de chacune des 5 plus grosses particules de chaque échantillon montre une décroissance avec la vitesse de refroidissement. Ceci indique que les particules de phase beta sont d'autant plus petites que la vitesse de refroidissement augmente.

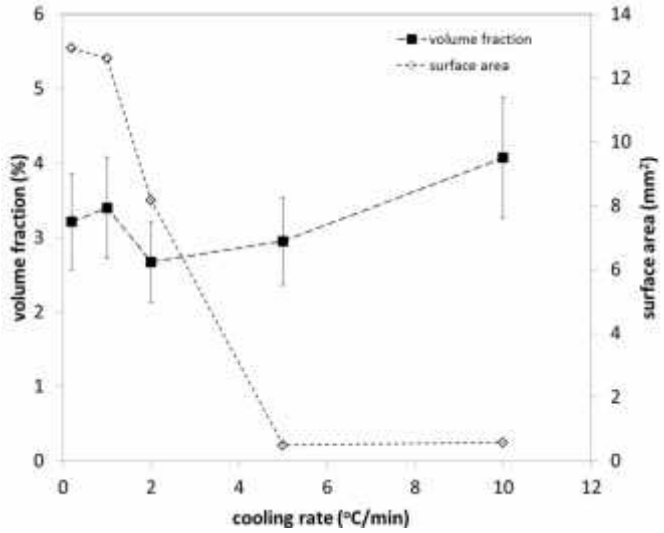

Figure 8. Fraction volumique de phase beta et aire des cinq plus grandes plaquettes de phase beta en fonction de la vitesse de refroidissement, mesurées à partir de la reconstruction des images 3-D.

Les analyses post-mortem semblent montrer que la germination de la phase beta se produit sur la couche d'oxyde externe, suivie d'une croissance radiale des plaquettes vers le centre de l'échantillon. Ceci est illustré dans le cas du refroidissement à 0,2°C/min en figure 9. Les observations tomographiques réalisées sur les échantillons refroidis lentement ont montré une très faible quantité de précipités de phase beta non reliés aux plaquettes formées sur la surface. Il a été noté que le chemin suivi par les plaquettes ne présente pas de directions privilégiées, certainement du fait de l'espace limité laissé par les dendrites de (Al). En accord avec cette observation, les précipités de phase beta apparaissent souvent courbés et présentent de nombreux changements de direction durant leur croissance. Le branchement des plaquettes semble pouvoir être associé au blocage de leur croissance par des dendrites de (Al). Notons

enfin que des particules de phase beta qui ne se sont pas développées en larges plaquettes ont été observées dans l'échantillon refroidi à 0,2°C/min, ce qui sera discuté plus loin.

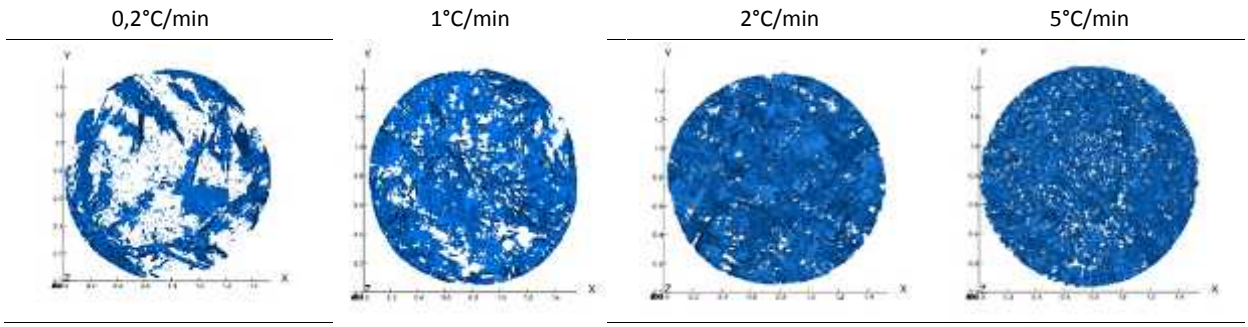

Figure 9. Représentation 3D d'images obtenues en tomographie post-mortem sur des échantillons refroidis à différentes vitesses (taille du voxel : 2.5 µm)

La tomographie in-situ a été réalisée pour une vitesse de refroidissement constante de 10°C/min, de l'état liquide à 618°C jusqu'à la température de 575°C qui se situe légèrement au-dessus de la température de la réaction eutectique (Al)-Si. L'observation des images 3-D du volume après reconstruction montre que la précipitation des dendrites primaires se produit à 608°C, et que la germination de la phase beta a eu lieu en plusieurs endroits et a commencé à 593°C. La croissance de la phase beta se déroule dans les régions inter-dendritiques en même temps que la croissance continue et le grossissement des dendrites d'(Al) primaires se poursuivent. En raison du contraste très proche de la phase beta et de la peau d'oxyde, on a ajouté au traitement des images une opération de masquage consistant en un filtrage gaussien-flou, seuillage, érosion et dilatation, pour éliminer la couche externe d'oxyde. L'analyse de la germination de la phase beta a pu finalement être réalisée sur une région de 1008x1008x500 voxels. La figure 10 présente des exemples de rendu volumique pour différentes températures durant le refroidissement.

La germination de la phase beta semble s'être produite ici aussi sur la couche d'oxyde de la surface extérieure de l'échantillon. La figure 10 montre que la croissance des plaquettes peut être parfois bloquée par un bras primaire de (Al), mais qu'elle se poursuit par contournement de la dendrite et que certains des précipités se reconnectent après passage de l'obstacle. Au cours de la croissance, flexion et dédoublement des plaquettes ont également été observés. Les branchements ont été remarqués durant l'étape intermédiaire de la croissance, alors que les reconnexions se produisent plus avant dans la solidification et conduisent à des amas de grandes plaquettes.

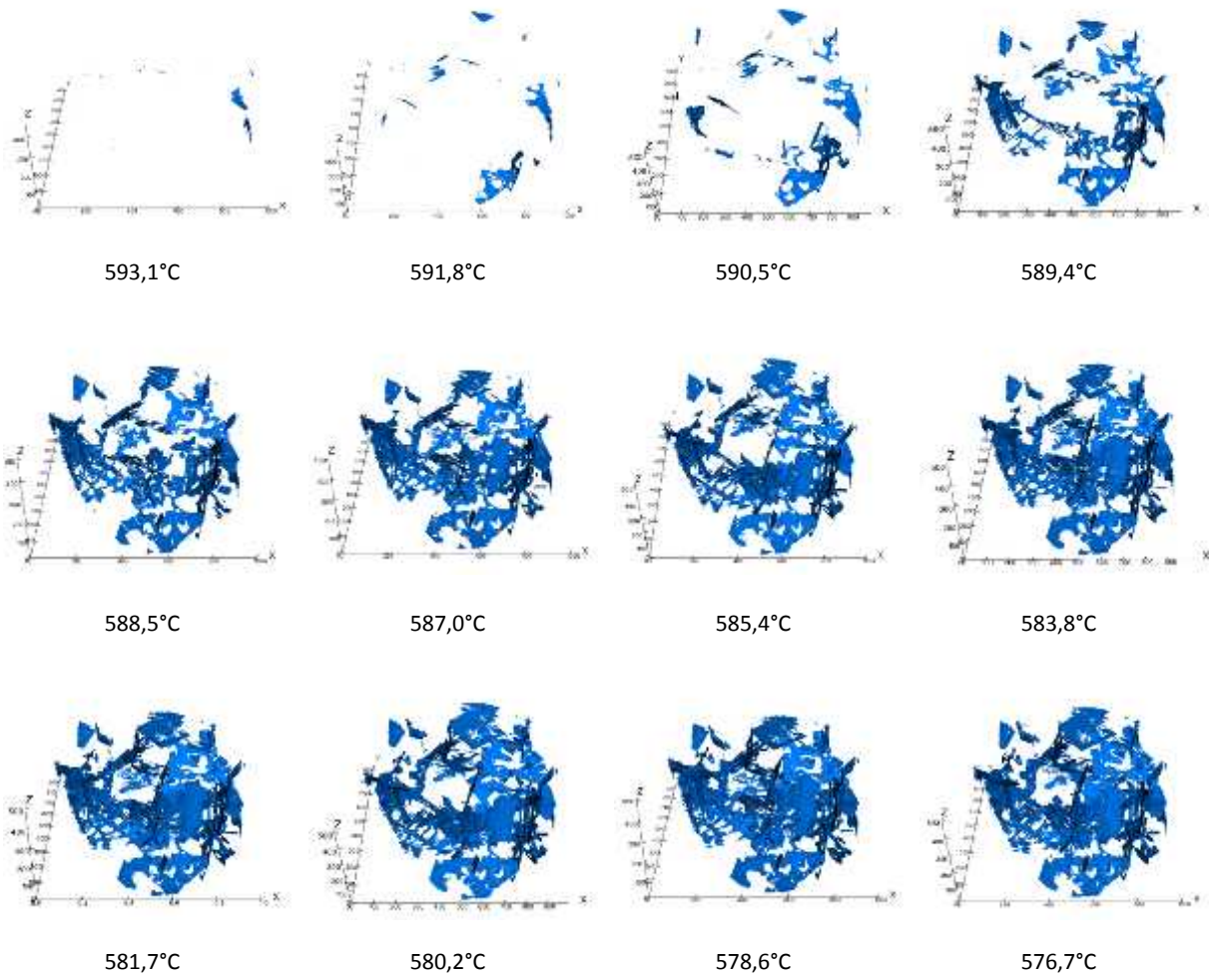

Figure 10. Série d'images 3-D in-situ reconstruites correspondant à différentes températures durant le refroidissement et illustrant la croissance de la phase beta.

Les mesures des longueurs latérales ont été réalisées en suivant plusieurs précipités de phase beta sur les reconstructions tomographiques successives. A partir de ces mesures de longueur, cinq particules de phase beta numérotées de 1 à 5 ont été sélectionnées parmi celles apparues tôt durant l'expérience, ce afin de réaliser une analyse approfondie de leur cinétique de croissance. Trois de ces particules étaient apparues au même pas de temps et les deux autres au pas de temps suivant. La complexité de la morphologie de la phase bêta et ses orientations de croissance rendent difficiles la mesure et la localisation de l'extension maximum des précipités. De plus, une partie des particules fusionnent au cours de la solidification et ne peuvent pas être utilisées pour l'évaluation de la cinétique de croissance. Pour résumer, nous avons pu distinguer trois étapes de croissance sur la base de la forme de la courbe donnant la longueur des précipités en fonction du temps (figure 11) : étape initiale de développement accéléré (I), croissance à vitesse sensiblement constante (II) et étape de saturation (III).

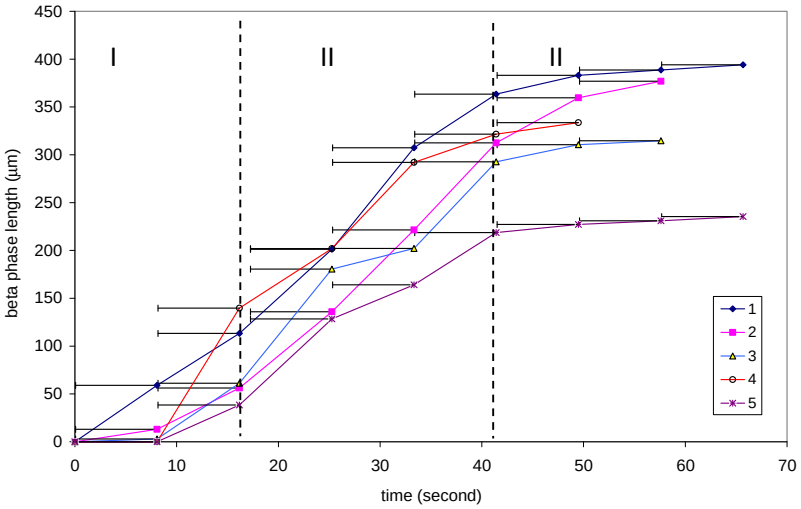

Figure 11. Evolution temporelle de la longueur maximum de 5 précipités de phase beta suivis au cours de la solidification de l'échantillon de tomographie in-situ.

Notons que le suivi de la croissance des plaquettes de phase beta au cours de la solidification par tomographie in-situ peut être biaisé. En effet, l'acquisition est faite durant une rotation de 180° de l'échantillon, pendant laquelle la phase beta continue de croître ce qui peut biaiser la corrélation temporelle [44]. Par conséquent, la croissance latérale réelle de la phase beta peut être plus rapide que celle évaluée ci-dessus. Une barre d'erreur a donc été définie le long de l'axe des temps (et systématiquement reportée en figure 11) en supposant que les précipités croissent de façon continue au cours de la rotation de 180°.

Le mécanisme d'épaississement de la phase beta apparaît lié à la présence de marches de croissance macroscopiques, ce qui pourrait indiquer qu'une certaine épaisseur de marche est requise avant que la croissance latérale ne progresse. L'épaisseur des précipités de phase beta a été mesurée sur les images 3D en utilisant ImageJ avec le plug-in d'épaisseur locale [45] développé sur la base du travail de Hildebrand et Rüegsegger [46]. La classe de taille de 2 à 2,49 µm est la valeur minimale qui puisse être reportée en raison de la limitation en taille des voxels. Sur la figure 12, on remarque que les épaisseurs allant de 3,5 à 5,99 µm sont les plus courantes, et ce domaine de taille pourrait être identifié comme un seuil pour l'épaississement de la phase beta. L'évolution en épaisseur des plaquettes de phase beta ne montre aucun changement de la position du pic caractéristique, et cela pourrait indiquer qu'une valeur critique minimum de l'épaisseur est nécessaire pour la poursuite de la croissance latérale de la phase. L'épaississement de la phase est plus marqué en fin de solidification, certaines des plaquettes atteignant des épaisseurs de 9,5 à 9,99 µm et plus.

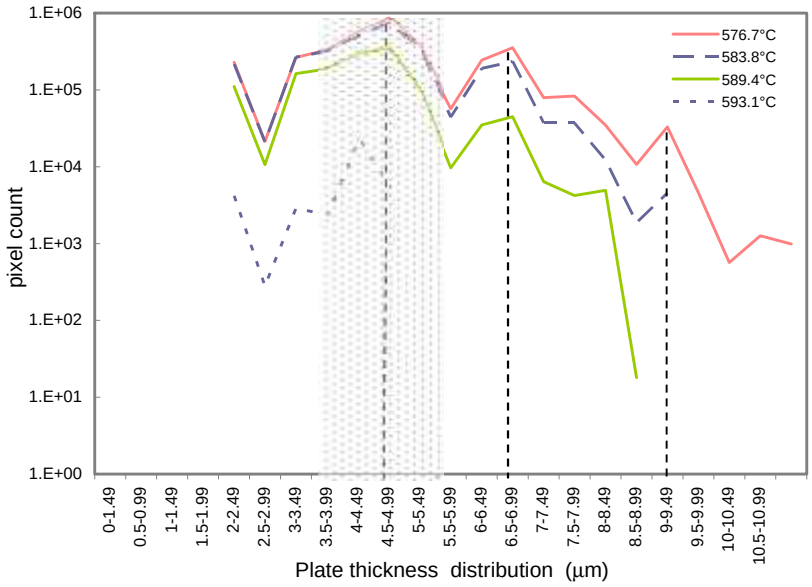

Figure 12. Distribution de l'épaisseur des plaquettes de phase beta pour différentes températures dans l'intervalle de solidification.

L'observation en MEB de l'échantillon attaqué profondément est illustrée à la figure 13. Nous pouvons y voir que la phase beta peut présenter des branchements d'angles quelconques. Le silicium eutectique apparaît attaché à la phase beta, mais il n'y a aucune évidence que la phase beta lui serve de site de germination puisque les directions de croissance des plaquettes de silicium sont quelconques. Dans certains cas, nous avons pu observer que le silicium présente en présence d'une plaquette de phase beta une morphologie d'eutectique modifié qui indique qu'il s'est développé à une surfusion notable, certainement depuis un liquide emprisonné dans une poche de liquide isolée du reste des espaces inter-dendritiques (voir plus loin).

La vitesse d'épaississement a été mesurée sur les plaquettes les plus épaisses à chaque pas de reconstruction tomographique. Il a ainsi été estimé que la vitesse d'épaississement est de l'ordre de 1,5 µm/s après l'étape de germination, ralentit à 0,4 µm/s durant la seconde étape et à 0,2 µm/s durant la troisième. Ces valeurs sont beaucoup plus élevées que celles reportées par Terzi et coll. [47] qui ont estimé cette vitesse à ~2 µm/min lors d'un essai réalisé à 1.4°C/min, alors que dans le cas présent la vitesse de refroidissement était de 10°C/min.

L'épaississement des plaquettes apparaît bloqué durant leur développement latéral qui est 10 fois plus rapide en moyenne. La figure 14 montre ainsi que le développement latéral est dominant durant la première partie de la précipitation de la phase beta, avec de très fortes vitesses de croissance latérale qui, ensuite, diminuent quand la fraction de liquide décroît en laissant moins de place pour les plaquettes.

Cependant, il a aussi été noté que la vitesse d'épaississement n'augmente pas notablement une fois que l'extension latérale ralentit, certainement du fait d'une décroissance de la force motrice de précipitation. Des mesures effectuées, nous pouvons voir que le maximum en aire de l'épaisseur des plaquettes se situe à 4,5 - 5 µm, et que l'écart au pic suivant dans la distribution est d'approximativement 1,5 - 2 µm. L'épaississement relativement rapide aux temps courts de croissance de la phase beta pourrait être lié au blocage de l'extension latérale des plaquettes par les dendrites.

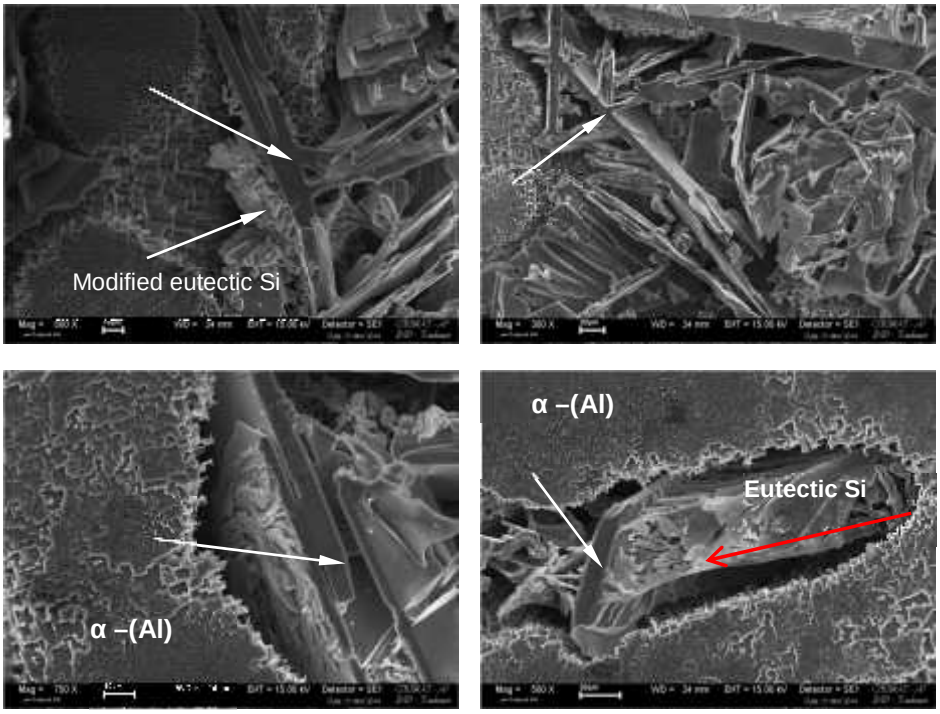

Figure 13. Micrographies MEB d'échantillons attaqués profondément pour permettre de visualiser les branchements de la phase beta et le lien avec le silicium eutectique.

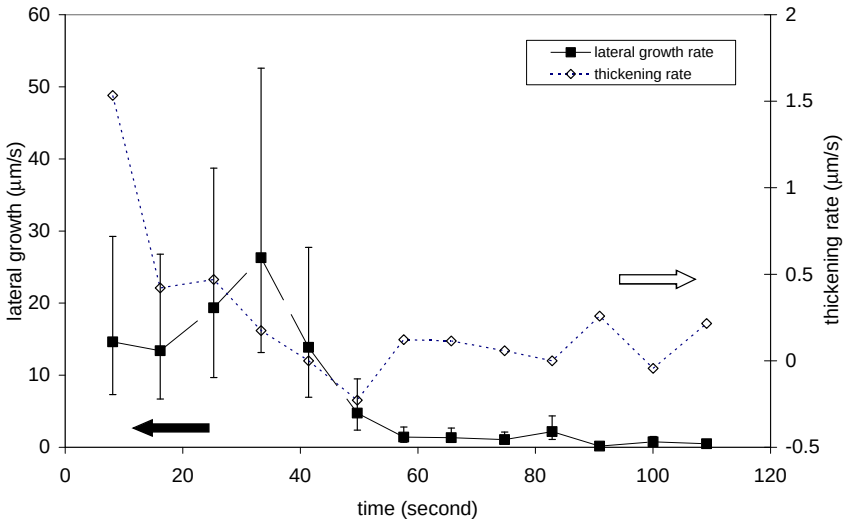

Figure 14. Comparaison des vitesses de croissance latérale et d'épaississement des plaquettes de phase beta (les valeurs de croissance latérale concernent une seule plaquette).

Un modèle de croissance des plaquettes de phase beta, inspiré du travail de Amini et Abbaschian [48] sur les lamelles de graphite dans les fontes, est illustré en figure 15, où V est la vitesse de croissance latérale et r* le rayon critique d'une plaquette.

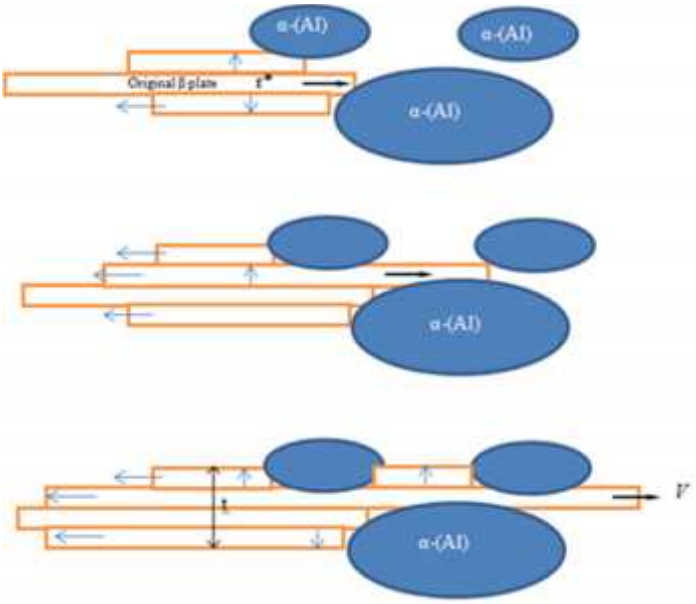

Figure 15. Modèle de croissance latérale et d'épaississement des plaquettes de phase beta.

La croissance latérale de la phase beta est certainement contrôlée par la diffusion des éléments à la pointe des plaquettes, et l'on peut penser que la diffusion du fer est la moins rapide et donc contrôle cette cinétique. Par ailleurs, il est proposé ici que l'épaississement soit dû à la formation de nouvelles couches de phase beta, par maclage ou bien par germination quand le rayon critique est atteint. Il serait sûrement de grand intérêt de poursuivre des travaux pour préciser le mécanisme d'épaississement de la phase beta.

3.3 Variantes du chemin de solidification d'un alliage Al-Si-Fe de haute pureté.

Un travail préliminaire [49] sur l'effet de la vitesse de refroidissement sur la morphologie de la phase beta dans l'alliage Al-6.5Si-1Fe avait mis en évidence une anomalie dans la précipitation de cette phase. L'examen métallographique d'un échantillon d'ATD refroidi à 0,2°C/min a montré la présence d'un précipité en écriture chinoise inattendu en ce que cette forme est généralement associée à la phase hexagonale alpha-AlFeSi. Sur cette base, des essais d'ATD complémentaires ont été réalisés dans l'objectif de mieux comprendre la précipitation de ces précipités en forme d'écriture chinoise qui apparaît aux très faibles vitesses de refroidissement. Ces essais d'ATD prévoyaient un refroidissement lent, à 0,02, 0,05 ou 0,1°C/min, de 620 à 590°C, c'est à dire débutant à une température supérieure à celle du liquidus et allant jusqu'à une température où l'essentiel du dépôt de phase beta peut être considéré comme achevé. Avant le refroidissement, les échantillons étaient maintenus 30 min à 620°C pour homogénéisation.

Les observations métallographiques ont montré la présence de précipités en écriture chinoise dans tous les échantillons illustrés en figure 16. Ces précipités en arête de poisson ou en écriture chinoise sont observés dans des zones inter-dendritiques, aussi bien au milieu que près de la surface des échantillons. Leur taille varie mais est limitée à 100 µm en longueur en section 2-D, mais le plus intéressant est que les précipités en plaquettes sont généralement absents des zones de précipitation en écriture chinoise. Ajoutons enfin que des analyses EDX et WDX ont montré que ces précipités ont la même composition que les précipités de phase beta en plaquettes.

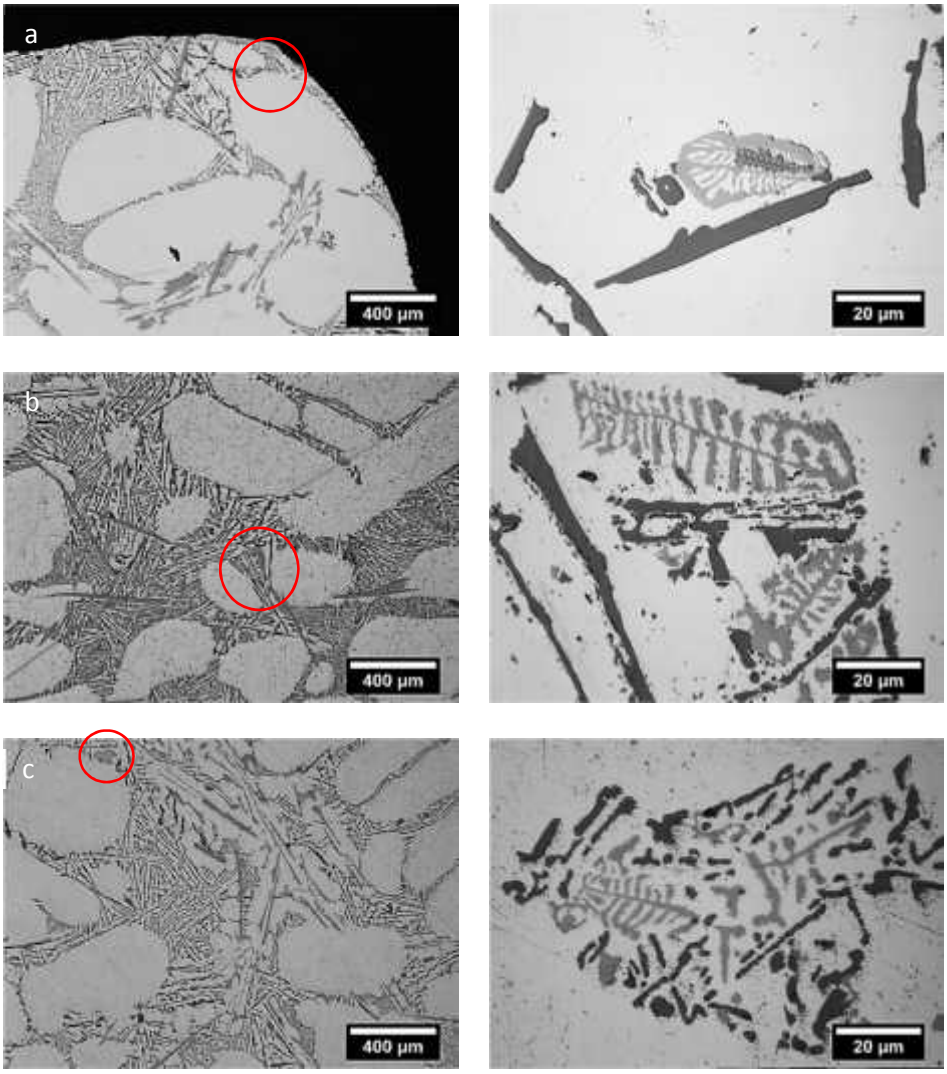

Figure 16. Micrographies des échantillons d'ATD refroidis à différentes vitesses et présentant des précipités en écriture chinoise : (a) 0,02°C/min, (b) 0,05°C/min, et (c) 0,1°C/min. Les images de la colonne de droite sont des vues agrandies des zones cerclées dans la colonne de gauche.

Les thermogrammes ATD de la figure 17 montrent des accidents thermiques bien identifies associés à la germination et la croissance des dendrites d'(Al) (flèche bleu), de la phase beta dans la réaction eutectique L→(Al)+beta (flèche rouge). Entre les deux, un pic de faible intensité (flèche noire) peut aussi être détecté dans le cas de l'échantillon refroidi à 0.05°C/min qui pourrait être associé à la précipitation de la phase en écriture chinoise.

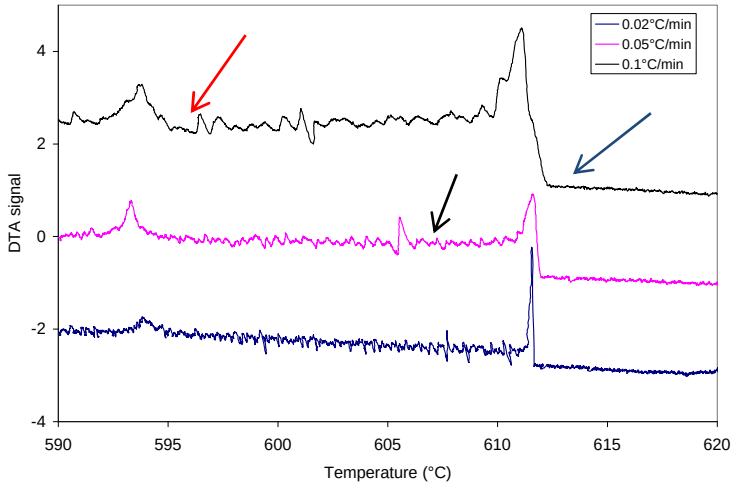

Figure 17. Thermogrammes d'ATD enregistrés pour différentes mais faibles vitesses de refroidissement indiquées dans la légende; les enregistrements ont été décalés le long de l'axe y pour faciliter la lecture.

Des analyses aux rayons X ont été réalisées en utilisant un micro-faisceau (Bruker Advance D8). Du fait du micro-faisceau, le flux de rayons X générés est très faible, les pics ne sont pas marqués et de longs temps d'acquisition sont nécessaires pour que les diffractogrammes soient exploitables. Sur la base des données structurales disponibles, les pics obtenus ne peuvent pas être indexés en relation avec la phase alpha hexagonale. Des analyses complémentaires en EBSD ont été faites qui ont permis l'identification des précipités en écriture chinois comme étant de la phase monoclinique β-$Al_9Fe_2Si_2$ alors qu'elles ne peuvent pas correspondre à la phase hexagonale α-Al_8Fe_2Si. La méthode de moyenne de l'angle de déviation (median angular deviation, MAD) donne un indice de 0,76 pour 10 raies qui permet de conclure que les précipités en écriture chinoise sont bien constitués de phase beta.

Les observations métallographiques ont montré qu'il n'y a pas de précipités de phase beta en plaquettes dans les régions où apparaît la phase en écriture chinoise. Pour vérifier que les précipités en écriture chinoise ne sont pas de simples figures associées aux branchements de la phase en plaquette, des attaques profondes des échantillons ont été réalisées qui sont illustrées par les micrographies de la figure 17. Dans tous les cas, il a été observé que la phase en écriture chinoise est entourée de plaquettes de silicium eutectique et jamais connectée à une plaquette. On peut donc imaginer que l'une des formes de phase beta exclut l'autre, certainement parce que son apparition et sa croissance consume rapidement la sursaturation en fer du liquide.

Une autre observation faite sur les échantillons d'ATD est celle de rosettes illustrée en Figure 18. Ce type de morphologies est reconnaissable par ses frontières convexes et lisses et le fait qu'elles présentent une très fine structure multi-phasée. Les formes en ellipse ou en chou-fleur quelquefois observées indiquent que ces poches suivaient les contours des bras dendritiques.

Kim et Cantor [50] ont étudié la formation de rosettes aux contours presque parfaitement sphériques, et notent qu'elles doivent s'être formées dans des conditions de minimisation de l'énergie de surface pour avoir ces formes globulaires. D'autres travaux ont conclu à ce que la formation des rosettes procède par l'isolement de poches de liquide du fait de la coalescence de bras dendritiques [51] ou de la division à la pointe de cellules [52]. D'après Lacaze et coll. [51], la finesse de la microstructure est due à ce que ces poches de

liquide doivent être surfondues notablement pour que la germination de nouvelles phases puisse se produire leur permettant de se solidifier.

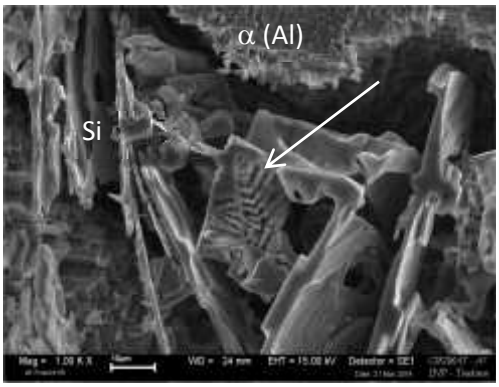

Figure 18. Précipités en écriture chinoise entourés de plaquette de silicium eutectique dans un espace inter-dendritique, observés après attaque profonde.

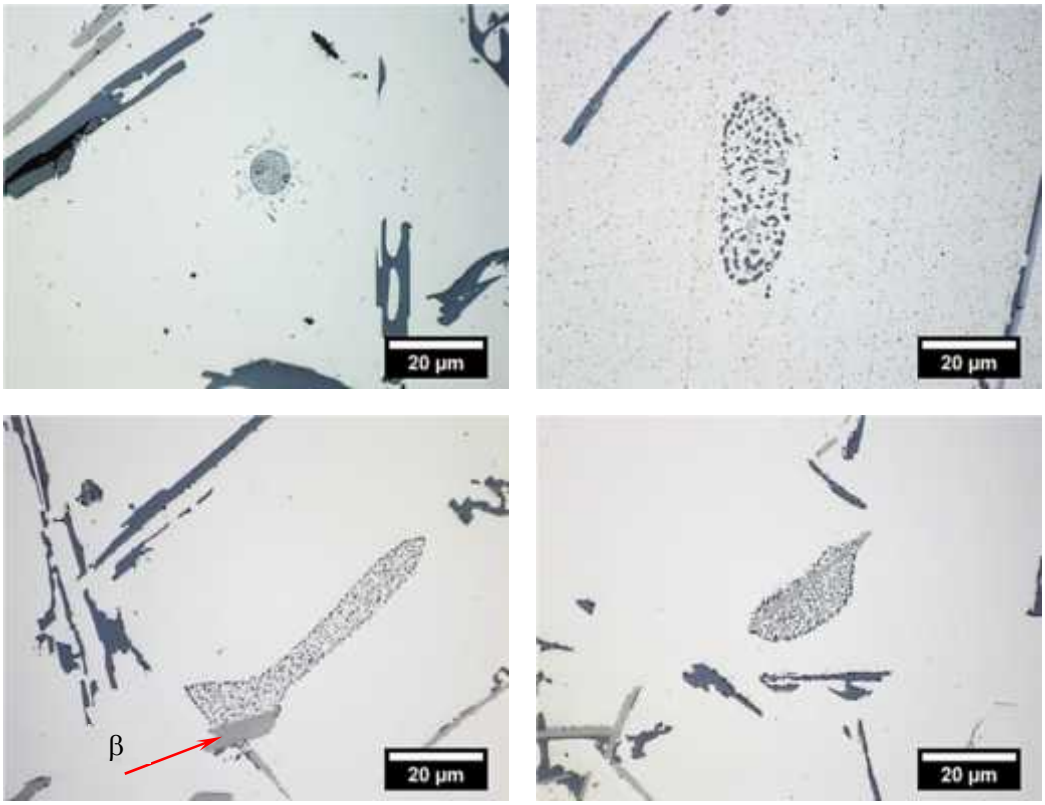

Figure 19. Micrographie de quelques rosettes observées en microscopie optique sur des échantillons d'ATD refroidis à 5°C/min et 40°C/min. (la flèche rouge pointe sur un précipité de phase beta).

Des analyses à la microsonde électronique ont été réalisées sur deux échantillons en suivant deux protocoles de mesure, en série de pointés selon une ligne et par intégration sur une zone de petite taille. Les deux types d'analyses ont conduit à des sommes des teneurs des éléments présents variant de 89 to 96%, bien inférieures à 100%, certainement en relation avec la nature multi-phasée des rosettes [53, 54].

La finesse de la structure des rosettes est associée à une surfusion significative lors de leur solidification. Du fait que la solidification de la phase primaire se poursuit durant cette étape de surfusion, celle-ci doit correspondre à l'augmentation de la composition du liquide en fer et silicium, et donc en une augmentation moyenne de la composition des rosettes en ces éléments. Ainsi, pour illustrer l'effet de la surfusion, les résultats d'analyse par microsonde normalisés à 100% ont été superposés à la projection du liquidus du système Al-Fe-Si en figure 20. On voit que les compositions estimées sont situées loin des lignes d'équilibre du diagramme, mais aussi qu'elles ne sont pas très éloignées des prédictions que l'on peut faire en utilisant les modèles de la règle du bras de levier ou de Scheil. Par ailleurs, en considérant que le liquidus de la phase primaire (Al) peut être décrit par l'équation T(°C)=660– 6.64•wt%Si– 2.77•wt%Fe, les surfusions atteintes ont pu être estimées entre 80 et 120°C.

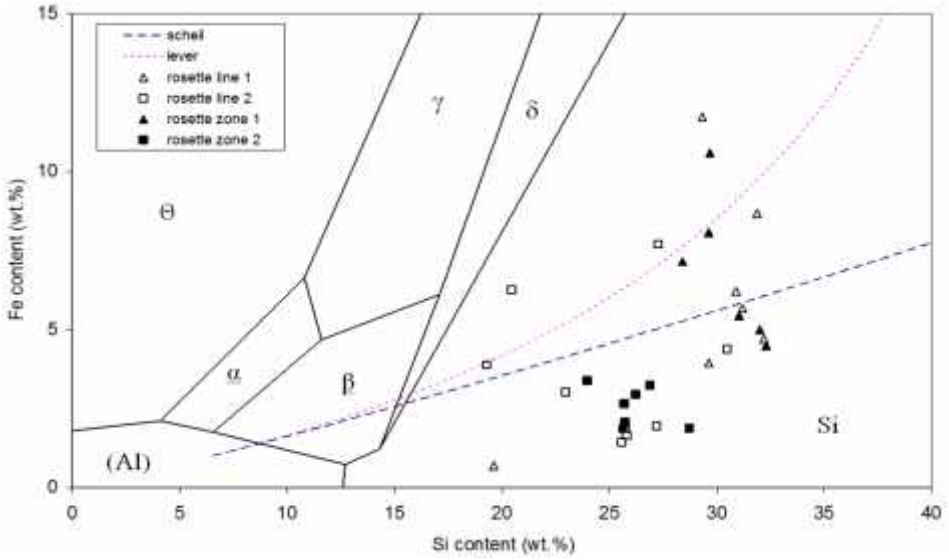

Figure 20. Report sur la projection de liquidus du système Al-Fe-Si de la composition de rosettes mesurée par EPMA (Θ-$Al_{13}Fe_4$, α-Al_8Fe_2Si, β-$Al_9Fe_2Si_2$, ¥-Al_3FeSi, ¢-Al_3FeSi_2).

Les observations des rosettes nous ont amené à faire une constatation intéressante pour ce qui concerne le silicium eutectique. Ainsi, quelques chercheurs ont proposé que la phase beta soit un site préférentiel de germination du silicium eutectique [55, 56], certainement en constatant que le silicium eutectique est situé en contact avec la phase beta. Cependant, les observations telles que celle illustrée par la micrographie de la figure 19 contredisent cette conclusion. On peut voir sur cette micrographie un large précipité de phase beta pénétrant dans une rosette dans laquelle le silicium ne présente pas la forme aiguillée des espaces inter-dendritiques mais la forme fibreuse de l'eutectique (Al)-Si surfondu. Ce résultat est en fait en accord avec des conclusions faites précédemment par Lu and Dahle [57].

Des mesures par EDS sur un autre échantillon ont par ailleurs permis d'observer un précipité de phase riche en fer, de composition correspondant à celle de la phase delta, et enrichi en cérium. L'absence de précipité de cérium pur (figure 21) montre que cet élément se trouvait en substitution dans la phase delta, et qu'il était donc présent dissout dans le liquide. Des observations complémentaires ont été réalisées pour rechercher la présence de cérium dans les échantillons, et l'on a pu trouver quelques précipités riches en cet élément en contact ou même dans la matrice (Al), ce qui semble indiquer qu'ils auraient pu précipiter à l'état solide.

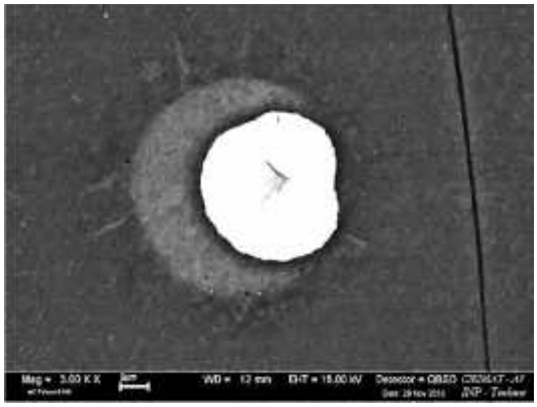

Figure 21. Rosette présentant un précipité riche en cérium et qui apparaît très brillant sur cette image en électrons rétrodiffusés.

Les observations métallographiques ont montré que la finesse de la structure des rosettes décroit avec la vitesse de refroidissement. De cette observation, il pourrait être conclu que les structures les plus fines sont obtenues parce que de plus grandes surfusions sont atteintes avec l'augmentation de la vitesse de refroidissement. Cependant, des essais de maintien à l'état mi-liquide mi-solide pour différentes durées ont montré que la structure des rosettes est plus grossière après maintien que sans, à vitesse de refroidissement donnée. Cette observation n'est pas comprise à ce jour.

4. Conclusion

L'objectif de ce travail était d'étudier quelques aspects de la coulée et de la solidification des alliages Al-Si qui sont couramment employés, en particulier dans l'industrie automobile. L'analyse des courbes de refroidissement enregistrées de manière routinière en analyse thermique standard pour le contrôle de la préparation du métal liquide a été étendu ici pour prendre en compte l'effet de la vitesse de refroidissement sur la germination des grains et la modification eutectique. Des analyses statistiques multi-variables ont été réalisées afin de préciser la possibilité que quelques paramètres évalués sur les courbes de refroidissement puissent décrire de manière statistiquement significative l'affinage des grains et la finesse de l'eutectique (Al)-Si. Des relations ont pu être proposées qui présentent des coefficients de corrélation satisfaisants. Dans le futur, il pourrait être intéressant de poursuivre cette étude afin de caractériser les possibilités de l'analyse thermique sur d'autres alliages et sa capacité à différencier des affinants ou des modificateurs.

Par ailleurs, des essais complémentaires en ATD ont été réalisées pour mieux cerner la relation entre vitesse de refroidissement et modification de l'eutectique. Il a été possible de mettre en évidence que la surfusion de l'eutectique observée par analyse thermique n'est pas nécessairement associée à une modification microstructurale. Ce résultat semble montrer que la modification pourrait résulter d'une combinaison de mécanismes bloquant la croissance et limitant la germination du fait de la présence d'éléments modificateurs.

Essentiellement parce qu'il est ajouté intentionnellement dans les alliages coulés sous pression, le fer se retrouve dans les alliages de moulage au sable du fait du recyclage. L'accent a été mis ici sur l'étude de l'intermétallique riche en fer le plus problématique, la phase monoclinique beta $Al_9Fe_2Si_2$. Cette phase apparaît sous forme d'aiguilles en sections 2-D, qui sont des plaquettes fines très étendues selon deux directions en observations tomographiques 3-D. Dans l'alliage ternaire Al-6,5Si-1Fe étudié durant ce travail, la phase beta apparaît entre le dépôt primaire dendritique de (Al) et le dépôt tri-phasé (Al)-beta-Si. La

croissance initiale de la phase beta est très rapide, elle se ralentit ensuite en même temps que les plaquettes commencent à épaissir.

Les expériences de tomographie in-situ ont permis de caractériser le mécanisme de croissance de la phase beta, qui est dominé par la croissance latérale. Les bras dendritiques de phase primaire (Al) limitent l'extension des plaquettes, les obligeant à les contourner et diminuant ainsi leur vitesse d'extension. Après une étape de croissance rapide, les plaquettes se développent plus lentement latéralement, et ne présentent pas de tendance particulière à l'épaississement, probablement du fait de la forte fraction de solide atteinte alors.

A très faible vitesse de refroidissement, il a été observé qu'une partie de la phase beta précipite en forme d'écriture chinoise plutôt que de plaquettes, ce qui devrait correspondre à l'établissement d'une croissance couplée entre (Al) et la phase beta. Cette observation originale confirme que l'identification des phases ne doit pas être basée uniquement sur leur morphologie dans les alliages d'aluminium.

L'observation des échantillons d'ATD a aussi mis en évidence la présence de rosettes, en particulier aux plus fortes vitesses de refroidissement. Ces rosettes sont caractérisées par des formes arrondies et une microstructure multi-phasée très fine, elles correspondent à des poches de liquide qui ont été isolées du liquide inter-dendritique durant la solidification. Pour que ces poches se solidifient, des évènements indépendants de germination de phases riches en Si et Fe doivent s'y produire, ce qui nécessite une surfusion qui peut être élevée, d'où la finesse des structures multi-phasées qui y sont observées. Des analyses chimiques locales ont permis d'évaluer les compositions de ces rosettes et les surfusions correspondantes. Deux résultats originaux peuvent être mentionnés:

- Précipitation de la phase δ, qui n'est pas attendue d'après le diagramme de phase stable, dans l'une de ces rosettes.
- Présence de phase beta de forme compacte et de grande taille dans une rosette en même temps qu'un eutectique (Al)-Si très fin. Ceci est pris comme une indication très forte que la phase beta n'a pas servi de germe au silicium eutectique, contrairement à quelques travaux de la littérature.

Un modèle de croissance de la phase beta a été proposé qui nécessiterait d'être complété par des calculs détaillés et des simulations. Par ailleurs, il pourrait être intéressant d'utiliser la tomographie in-situ pour étudier la modification du silicium, par exemple en utilisant un élément lourd comme le zinc pour augmenter le contraste entre le silicium et (Al).

Remerciements

Le support financier de l'ESA (contrat #4200014347) dans le cadre du programme MICAST et du ministère de l'éducation indonésien sont grandement remerciés. La mise à disponibilité de matériaux par AZTERLAN et de temps de faisceau par l'ESRF ont aussi été essentielles. L'auteur désire encore remercier C. Tenailleau et L. Salvo pour leur aide dans les analyses des essais de tomographie.

Références

1. European Aluminium Association, Aluminium in cars, 2008, available in www.alueurope.eu/pdf/Aluminium_in_cars_Sept2008.pdf, accessed in 24 March 2014.
2. Z. Luo, A. Soria, Prospective study of the world aluminium industry, European Commission-Joint Research Centre, Institute for Prospective Technological Studies, 2007.
3. J.A.S. Green, Aluminum recycling and processing for energy conservation and sustainability, ASM International, 2007.

4. Maxwell, A. Hellawell, The constitution of the system Al-Ti-B with reference to aluminum-base alloys, Metallurgical Transaction, 3, (1972), 1487-1493.
5. A.L. Greer, A.M. Bunn, A. Tronche, P.V. Evans, D.J. Bristow, Modelling of inoculation of metallic melts: application to grain refinement of aluminium by Al-Ti-B, Acta Materialia, 48, (2000), 2823-2835.
6. Y.C. Lee, A.K. Dahle, D.H. StJohn, J.E.C. Hutt, The effect of grain refinement and silicon content on grain formation in hypoeutectic Al-Si alloys, Materials Science and Engineering A, 259, (1999), 43-52.
7. R.W. Smith, Modification of aluminium-silicon alloys, The Solidification of Metals, The iron and steel institute, London, (1968), 224-237.
8. H. Fredriksson, M. Hillert, N. Lange, The modification of aluminium-silicon alloys by sodium, Journal of the institute of metals, 101, (1973), 285-299
9. D.C. Jenkinson, L.M. Hogan, The modification of aluminium-silicon alloys with strontium, Journal of Crystal Growth, 28, (1975), 171-187.
10. Q. Liu, Q. Li, Q. Liu, Modification of Al-Si alloys with sodium, Acta Metall. Mater, 39, (1991), 2497-2502.
11. S. Khan, R. Elliott, Quench modification of aluminium-silicon eutectic alloys, Journal of Materials Science, 31, (1996), 3731-3737.
12. D.R. Hamilton, R.G. Seidensticker, Propagation mechanism of germanium dendrites, Journal of Applied Physics, 31, (1960), 1165-1168.
13. S.Z. Lu, A. Hellawell, The mechanism of silicon modification in aluminum-silicon alloys: Impurity induced twinning, Metallurgical Transactions A, 18, (1987), 1721-1733.
14. F. Yilmaz, O.A. Atasoy, R. Elliott, Growth structure in alumium-silicon alloys II. The influence of strontium, Journal of Crystal and Growth, 118, 1992, 377-384.
15. K.F. Kobayashi, L.M. Hogan, The crystal growth of silicon in Al-Si alloys, Journal of Materials Science, 20, (1985), 1961-1975.
16. J.R. Davis, ASM Speciality handbook aluminum and aluminum alloys, ASM International, 2003.
17. M.V. Kral, A crystallographic identification of intermetallic phases in Al-Si alloys, Materials Letters, 59, (2005), 2271 – 2276.
18. M.V. Kral, P.N.H. Nakashima, D.R.G. Mitchell, Electron microscope studies of Al-Fe-Si intermetallics in an Al-11% Si alloy, Metall. Mater. Trans A, 37A, (2006), 1987–1997.
19. W. Khalifa, F.H. Samuel, J.E. Gruzleski, Iron intermetallic phases in the Al corner of the Al-Si-Fe system, Metall. Mater. Trans. A, 34, (2003), 807 – 825.
20. L.A. Narayanan, F.H. Samuel, J.E. Gruzleski, Crystallization behavior of iron-containing intermetallic compounds in 319 aluminum alloy, Metall.Trans, 25A, (1994), 1761-1773.
21. S. Gowri, F.H. Samuel, Effect of Alloying Element on the Solidification Characteristics and Microstructure of Al-Si-Cu-Mg-Fe 380 Alloy, Metall. Trans.A., 25, (1994), 437-448.
22. O. Elsebaie, A. M. Samuel and F. H. Samuel, Effects of Sr-modification, iron-based intermetallics and aging treatment on the impact toughness of 356 Al–Si–Mg alloy, Journal of Materials Science, 46, 3027-3045
23. S.Belmares-Perales, M.Castro-Román, M.Herrera-Trejo, L.E Ramírez-Vidaurri, Effect of cooling rate and Fe/Mn weight ratio on volume fractions of α-AlFeSi and β-AlFeSi phases in Al-7.3Si-3.5Cu alloy, Metals and Materials International, 14, (2008), 307-314.
24. S. Murali, K. S. Raman and K. S. S. Murthy, Effect of magnesium, iron (impurity) and solidification rates on the fracture toughness of Al-7Si-0.3Mg casting alloy, Materials Science and Engineering: A, 151, (1992), 1–10.
25. M.A. Moustafa, Effect of iron content on the formation of β-Al_5FeSi and porosity in Al–Si eutectic alloys, Journal of Materials Processing Technology, 209, (2009), 605–610.

26. J.Z. Yi, Y.X. Gao, P.D. Lee, T.C. Lindley, Effect of Fe-content on fatigue crack initiation and propagation in a cast aluminum–silicon alloy (A356–T6), Materials Science and Engineering A, 386 (2004) 396–407.
27. S.G. Shabestari, J.E. Gruzleski, Gravity segregation of complex intermetallic compounds in liquid aluminum-silicon alloys, Metall. Mater. Trans. A, 26, (1995), 999 – 1006.
28. J. Šerák, D. Vojtech, P. Novák, K. Dám, T. Janoušek, The influence of annealing conditions on microstructure Of AlSiCuMgFe Alloys, METAL 2009 - 18th International Metallurgical & Material Conference, Hradec nad Moravicí, Czech Republic, May 19-21 2009.
29. H.L. de Moraes, J.R. de Oliveira, D.C. Romano-Espinosa1 and J.A. Soares-Tenório, Removal of iron from molten recycled aluminum through intermediate phase filtration, Materials Transactions, 47, (2006), 1731-1736.
30. J.W. Gao, D. Shu, J. Wang, B.D. Sun, Effects of $Na_2B_4O_7$ on the elimination of iron from aluminum melt, Scripta Materialia, (2007), 57.
31. J.W. Gao, D. Shu, J. Wang, B.D. Sun, Study on iron purification from aluminium melt by $Na_2B_4O_7$ flux, Materials Science and Technology, 25, (2009), 619-624.
32. L.F. Mondolfo and *J.G.* Barlock, Effect of some superheating on structure aluminum alloys, Metallurgical Transactions B, 6, (1975), 565- 572.
33. Y. Awano, Y. Shimizu, Non-equilibrium crystallization of AlFeSi compound in melt-superheat Al–Si alloy castings, AFS Trans., 98, (1990), 889–895.
34. H.W.L. Phillips, P.C. Varley. JIM, 69, (1943), 317.
35. M. Mahta, M. Emamy, A. Daman, A. Keyvani, J. Campbell, Precipitation of Fe rich intermetallics in Cr- and Co-modified A413 alloy, International Journal of Cast Metals Research, 18, (2005), 73-79.
36. S.S. Sreeja Kumari, R.M. Pillai, B.C. Pai, K. Nogita and A.K. Dahle, Influence of calcium on the microstructure and properties of an Al-7Si-0.3Mg-xFe alloy, Metallurgical and Materials Transactions A, 37, (2006), 2581-2587.
37. T. Kobayashi, H.J. Kim, M. Niinomi, Effect of calcium on mechanical properties of recycled aluminium casting alloys, Materials Science and Technology 13, (1997), 497-502.
38. M. Hosseinifar and D.V. Malakhov, Effect of Ce and La on microstructure and properties of a 6XXX series type aluminum alloy, Journal of Materials Science, 43, (2008), 7157-7164.
39. J. Charbonnier, Microprocessor assisted thermal analysis testing of aluminum alloy structure, AFS Trans., 92, (1984), 907-921.
40. D. Apelian, G.K. Sigworth, K.R. Whaler, Assessment of grain refinement and modification of Al-Si foundry alloys by thermal analysis, AFS trans., 92, (1984), 297-307.
41. D. Ferdian, J. Lacaze, I. Lizarralde, A. Niklas, A.I. Fernández-Calvo, Study of the effect of cooling rate on eutectic modification in A356 aluminium alloys, Material Science Forum, Vol 765- Light Metals Technology 2013, pp. 130-134
42. J. Lacaze, L. Eleno, B. Sundman, Thermodynamic assessment of the aluminum corner of the Al-Fe-Mn-Si system, Metallurgical and Materials Transaction A, 41, (2010), 2208-2215.
43. C.M Dinnis, J.A Taylor, A.K. Dahle, As cast morphology of iron intermetallic in Al-Si foundry alloys, Scripta Materialia, 53, (2005), 955-958.
44. Private communication with Luc Salvo, March 2014.
45. R.P. Dougherty and K-H Kunzelmann, Computing local thickness of 3D structures with ImageJ, Microscopy & Microanalysis, 13, supplement S02, (2007), 1678-1679

46. T. Hildebrand and P. Rüegsegger, A new method for the model-independent assessment of thickness in three-dimensional images, Journal of Microscopy, 185, (1997), 67-75.
47. S. Terzi, J.A. Taylor, Y.H. Cho, L. Salvo, M. Suéry, E. Boller, A.K. Dahle, Insitu study of nucleation and growth of the irregular -Al/β Al_5FeSi eutectic by 3D synchrotron X-ray microtomography, Acta Materialia, 58, (2010), 5370-5380.
48. S. Amini, R. Abbaschian, Nucleation and growth kinetics of grapheme layers from a molten phase, Carbon, 51, (2013), 110-123.
49. D. Ferdian, B. Suharno, B. Duployer, C. Tenailleau, L. Salvo, J. Lacaze, Differential thermal analysis assessment of beta phase precipitation in Al-6.5Si-1Fe alloy, Transactions of the Indian Institute of Metals, 65, (2012), 821-825.
50. W.T. Kim and B.Cantor, Heterogeneous nucleation of Al_2Cu in Al-Cu eutectic liquid droplets embedded in an Al matrix, Acta Metall. Mat., 42, 9 (1994), 3045-3053.
51. J. Lacaze, G. Lesoult, I. Ansara, Rosettes in Al-Cu-Mg-Si aluminium alloys, Materials Science Forum, 217-222, (1996), 171-176.
52. D.T.L. Alexander and A.L Greer, Formation of eutectic intermetallic rosettes by entrapment of liquid droplets during cellular columnar growth, Acta Materialia, 52, (2004), 5853-5861.
53. S. Ahrweiler, L. Ratke, J. Lacaze, Microsegregation and microstructural features of directionally solidified AlSi and AlSiMg alloys, Advanced Engineering Materials, 5, (2003) 17-23.
54. J. Lacaze, P. Benigni, A. Howe, Some issues concerning experiment and models for alloy microsegregation, Advanced Engineering Materials, 5, (2003) 37-46.
55. J.A. Taylor, G.B. Schaffer, D.H. StJohn, The role of iron in the formation of porosity in Al-Si-Cu-based casting alloys: Part III. A microstructural model, Metallurgical and Materials Transactions A, 30, (1999), 1657-1662.
56. L. Liu, A.M. Samuel, F.H. Samuel, H.W. Doty, and S. Valtierra, Role of iron in relation to silicon modification in Sr-treated 319 and 356 alloys, Int. J. Cast Met. Res, 16, (2003), 397–408.
57. L. Lu, A.K. Dahle, Iron-rich intermetallic phases and their role in casting defect formation in hypoeutectic Al−Si alloys, Metallurgical and Materials Transactions A, 36, (2005), 819-835.